

ALMA MATER STUDIORUM · UNIVERSITÀ DI BOLOGNA

---

SCUOLA DI SCIENZE  
Dipartimento di Fisica e Astronomia “A. Righi”  
Corso di Laurea Magistrale in Astrofisica e Cosmologia

# Void Weak Lensing in modified gravity simulations

Tesi Magistrale

**Candidato:**  
Leonardo Maggiore

**Relatore:**  
Prof. Lauro Moscardini

**Co-relatori**  
Dott. Sofia Contarini  
Dott. Carlo Giocoli

---

Sessione V  
Anno Accademico 2022-2023



# Indice

Abstract . . . . .	i
Sommario . . . . .	iii
Introduction . . . . .	v
<b>1 Theoretical cosmological framework</b>	<b>1</b>
1.1 Fundamentals of Modern Cosmology . . . . .	1
1.1.1 The Cosmological Principle . . . . .	1
1.1.2 Theory of General Relativity . . . . .	2
1.2 Friedmann-Lemaître-Robertson-Walker metric . . . . .	3
1.2.1 Hubble-Lemaître’s law and redshift . . . . .	4
1.2.2 Observable cosmological distances . . . . .	5
1.3 Friedmann equations . . . . .	7
1.3.1 Cosmological constant $\Lambda$ . . . . .	8
1.3.2 The components of the Universe and their evolution . . . . .	9
1.3.3 Big Bang and cosmological horizon . . . . .	10
1.4 The standard cosmological model $\Lambda$ CDM . . . . .	12
1.5 Formation of Cosmic Structures . . . . .	14
1.5.1 Primordial fluctuations . . . . .	14
1.5.2 Linear evolution . . . . .	18
1.5.3 Nonlinear evolution . . . . .	24
<b>2 <math>\Lambda</math>CDM tensions and modified gravity</b>	<b>31</b>
2.1 Modified gravity theories . . . . .	33
2.1.1 Higher derivative theories of gravity . . . . .	33
2.1.2 Scalar-tensor theories of gravity . . . . .	34
2.1.3 $f(R)$ gravity . . . . .	35
2.1.4 Massive neutrinos . . . . .	38
<b>3 Cosmic voids and gravitational lensing</b>	<b>41</b>
3.1 Definition and void finding . . . . .	42
3.1.1 2D voids . . . . .	44
3.2 Statistical properties of voids . . . . .	46
3.2.1 Size function . . . . .	47
3.2.2 Density profile . . . . .	52
3.3 Weak gravitational lensing . . . . .	54
3.3.1 Lens equation . . . . .	54
3.3.2 Convergence and shear . . . . .	55
3.3.3 Weak-lensing signal from observed ellipticity . . . . .	57
3.3.4 Tangential and cross shear . . . . .	58
3.3.5 Weak lensing from multiple lenses . . . . .	59

3.3.6	Weak-lensing in 2D voids . . . . .	61
3.3.7	Weak lensing in $f(R)$ gravity . . . . .	63
<b>4</b>	<b>2D void finder</b>	<b>65</b>
4.1	Connected regions detection . . . . .	66
4.1.1	Peaks/Valleys reconstruction . . . . .	66
4.2	Center identification . . . . .	69
4.2.1	Weighted centroids vs absolute minima . . . . .	70
4.3	Final radius assignment . . . . .	72
4.4	Void cleaning . . . . .	73
<b>5</b>	<b>Simulated Weak-lensing maps</b>	<b>77</b>
5.1	DUSTGRAIN- <i>pathfinder</i> simulations . . . . .	77
5.2	The halo catalogs . . . . .	79
5.3	Weak-lensing past light-cones . . . . .	80
5.3.1	Multiplane rays-tracing . . . . .	82
<b>6</b>	<b>Results</b>	<b>85</b>
6.1	Void catalogs from WL maps . . . . .	86
6.1.1	$\Lambda$ CDM 2D void size functions . . . . .	88
6.1.2	$\Lambda$ CDM tangential shear profile from void . . . . .	89
6.2	Comparison with alternative gravity scenarios . . . . .	93
6.3	Modeling the tangential shear profiles . . . . .	97
6.3.1	Integration of 3D void density profiles . . . . .	97
6.3.2	A new parametric formula . . . . .	99
6.4	Bayesian statistical analysis . . . . .	100
<b>7</b>	<b>Conclusions</b>	<b>107</b>
7.1	Future perspectives . . . . .	110
	<b>Bibliography</b>	<b>111</b>



## Abstract

A modern solution to investigate the modified gravity (MG) theories is to search for deviations from GR in matter underdensities, i.e., *cosmic voids*. Voids are extended and underdense regions that constitute the predominant volume of the Universe large-scale structure (Cautun et al. 2014). Due to their low-density interiors and large sizes spanning tens of megaparsecs, voids serve as natural laboratories for testing alternative MG models, but also to explore the nature of dark energy, and to study the effects of elusive components like massive neutrinos (Sánchez et al. 2017; Cautun et al. 2018; Contarini et al. 2021, 2022b). In this study, we focus on the class of MG models known as  $f(R)$  (Hu & Sawicki 2007), that mimic the  $\Lambda$ CDM scenario in the high-redshift regime (well-tested by the cosmic microwave background analyses of e.g., Planck Collaboration et al. 2020a), producing the Universe accelerated expansion similarly to  $\Lambda$ CDM, but without a cosmological constant at low redshift.

One of the most promising studies that can be used to investigate MG models in voids is related to the phenomenon of *gravitational lensing*. Lensing refers to the deflection of photons emitted by distant galaxies as they travel towards the observer, caused by matter fluctuations along the line of sight (Sereno & Umetsu 2011). The analysis of the weak lensing (WL) from voids concerns, therefore, the small distortions of background light sources caused by underdense regions. Besides its promising application to study MG models, this kind of statistic has already been demonstrated to be very sensitive to the growth rate of the large-scale structure and to the expansion history of the Universe (Bartelmann 2010; Troxel & Ishak 2015).

The main goal of this work is to measure the mean tangential shear profile,  $\gamma_t(r)$ , of voids identified in cosmological simulations implementing the  $f(R)$  models. Then, we aim at estimating the differences between the shear profiles in  $f(R)$  cosmologies with respect to the standard  $\Lambda$ CDM profile. In order to maximize the lensing signal from the mock data, it is fundamental to identify cosmic voids in the 2D distribution of matter (Davies et al. 2021b). Therefore, we build an efficient pipeline for the extraction and analysis of 2D voids. In particular, we develop a novel finding algorithm for 2D voids based on density and geometrical criteria, aimed at maximizing the void tangential shear signal. To do this, we take into account the findings of Cautun et al. (2018) and Davies et al. (2021b) and implement an accurate and stable procedure of void center finding and radius assignment.

We apply this pipeline to the data extracted from the DUSTGRAIN-*pathfinder*, a set of  $N$ -body simulations including several models with  $f(R)$  gravity and massive neutrinos (Giocoli et al. 2018a; Hagstotz et al. 2019a). We build independent mock light cones by randomizing the snapshots of the simulation and we construct, for each cosmological model, 256 realizations of the convergence and signal to noise ratio (SNR) maps. This is done using the technique of ray-tracing for multiple lens planes (Giocoli et al. 2014, 2016, 2017). These maps assume a background source of galaxies located at  $z = 1$  and take into account a realistic galaxy shape noise. From each SNR convergence maps, we extract a sample of 2D voids. These are the regions of negative SNR resulting from the alignment of several 3D voids intercepting the line of sight and are commonly named *tunnel of voids* (Nadathur & Hotchkiss 2015a; Davies et al. 2021b). They are therefore the ideal objects to study the shear signal produced by underdensities (Sánchez et al. 2017).

To compute the shear profiles of 2D voids we measure the value of the convergence in different shells around their centers, up to ten times the void radii. Then, for each value of the tangential shear around the void, we associate an uncertainty that is a combination of statistical and observational errors, the latter derived by imposing a setting targeted for realistic surveys like those planned by ESA mission *Euclid*. The resulting tangential shear

profiles exhibit values statistically lower than zero, as expected for underdense regions. Dividing the void sample according to the void size, we demonstrate how smaller voids are characterized by deeper and more rapidly rising signals compared to larger voids, consistently to what expected from the already-known behavior of density profiles (Hamaus et al. 2014; Voivodic et al. 2020).

We then move on to the analysis of the differences between the tangential shear profiles measured in alternative models and those in the standard  $\Lambda$ CDM. We show how, in models where MG is present, voids exhibit more negative shear profiles, precisely because the fifth force accentuates their evolution, leading to a more efficient emptying of their interior. Conversely, we verify how the presence of massive neutrinos gives rise to less deep shear profiles, as in this case the growth of structures is dampened because of the neutrino free-streaming effect, and therefore the void density profiles appear shallower.

The last objective of our analysis concerns the modeling of the shear profile. We first tested the use of popular functional forms to represent the density profiles of voids, namely those introduced by Hamaus et al. (2014) and Boschetti et al. (2023). We integrated these two parametric formulas along the line of sight and used the resulting model to fit our tangential shear profiles. However, even by leaving free all the coefficients of these parametric formulas, both model fail to reproduce our data. This happens because the density profiles considered are suitable only for representing isolated 3D voids and not tunnel voids, which result from the complex projection of different underdensities.

To overcome this issue, we propose and validate a new parametric formula for void tangential shear profiles. We take care of minimizing free parameters of this model while requiring an accurate representation of the data for different void sizes and cosmological models. Finally, we use this functional form as a model to perform a Bayesian analysis. We constrain the five free parameters of the formula and we analyze their correlation, the effects of their variation and their sensitivity to the cosmological model. Then we focus on the possibility to statistically distinguish the results for the  $\Lambda$ CDM case from those obtained for alternative models, i.e. featuring MG or massive neutrinos. We show that, even for the most extreme scenarios, the uncertainty associated to our measurements prevent us from disentangling these models. We conclude that the mitigation of the observational errors is key in the perspective of effectively exploiting this probe for future studies.

As a future development of this work, we aim at applying our pipeline to larger simulations, eventually featuring different cosmological scenarios, in order to improve the void statistics and study the behavior also of larger underdensities. We will explore also the feasibility of this kind of study on real data catalogs. For instance, we aim at utilizing the data of the Kilo-Degree Survey (KiDS de Jong et al. 2013a,b) and, in the near future, of the *Euclid* survey (Laureijs et al. 2011; Amendola et al. 2018; Euclid Collaboration: Blanchard et al. 2020).

## Sommario

Una soluzione moderna per investigare le teorie di gravità modificata (MG) consiste nel cercare deviazioni dalla Relatività Generale (GR) nella materia sottodensa, ovvero nei *vuoti cosmici*. I vuoti sono regioni estese e sottodense che costituiscono il volume predominante della struttura su larga scala dell'Universo (Cautun et al. 2014). Grazie ai loro interni sottodensi e alle loro dimensioni estese che si estendono per decine di megaparsec, i vuoti fungono da laboratori naturali per testare modelli alternativi di MG, ma anche per esplorare la natura dell'energia oscura e studiare gli effetti di componenti elusive come i neutrini (Sánchez et al. 2017; Cautun et al. 2018; Contarini et al. 2021, 2022b). In questo studio, ci concentriamo sulla classe di modelli di MG conosciuti come  $f(R)$  (Hu & Sawicki 2007), che imitano lo scenario  $\Lambda$ CDM nel regime ad alto redshift (ben testato dalle analisi del fondo cosmico a microonde, ad esempio Planck Collaboration et al. 2020a), producendo un'espansione accelerata dell'Universo in modo simile a  $\Lambda$ CDM, ma senza una costante cosmologica a basso redshift.

Uno degli studi più promettenti che può essere utilizzato per investigare i modelli di MG nei vuoti è legato al fenomeno del *lensing gravitazionale*. Il lensing si riferisce alla deviazione dei fotoni emessi da galassie lontane mentre viaggiano verso l'osservatore, causata dalle fluttuazioni di materia lungo la linea di vista (Serenio & Umetsu 2011). L'analisi del lensing debole (WL) dai vuoti riguarda, quindi, le piccole distorsioni delle sorgenti di fondo causate dalle regioni sottodense. Oltre alla sua promettente applicazione nello studio dei modelli di MG, questo tipo di statistica è già dimostrato essere molto sensibile al tasso di crescita della struttura su larga scala e alla storia dell'espansione dell'Universo (Bartelmann 2010; Troxel & Ishak 2015).

L'obiettivo principale di questo lavoro è misurare il profilo medio di shear tangenziale,  $\gamma_t(r)$ , dei vuoti identificati nelle simulazioni cosmologiche che implementano modelli  $f(R)$ . Successivamente, miriamo a stimare le differenze tra i profili di shear nei modelli cosmologici  $f(R)$  rispetto al profilo del modello standard  $\Lambda$ CDM. Per massimizzare il segnale di lensing dai dati simulati, è fondamentale identificare i vuoti cosmici nella distribuzione 2D di materia (Davies et al. 2021b). Pertanto, sviluppiamo una pipeline efficiente per l'estrazione e l'analisi dei vuoti 2D. In particolare, sviluppiamo un algoritmo di ricerca per i vuoti 2D basato su criteri di densità e geometria, mirato a massimizzare il segnale di shear tangenziale dei vuoti. Per fare ciò, teniamo conto dei risultati di Cautun et al. (2018) e Davies et al. (2021b) e implementiamo una procedura accurata e stabile per la ricerca del centro del vuoto e l'assegnazione del raggio.

Applichiamo questa pipeline ai dati estratti dalle DUSTGRAIN-*pathfinder*, un insieme di simulazioni  $N$ -body che includono diversi modelli con gravità  $f(R)$  e neutrini massivi (Giocoli et al. 2018a; Hagstotz et al. 2019a). Costruiamo coni di luce mock indipendenti randomizzando gli snapshot della simulazione e costruiamo, per ogni modello cosmologico, 256 realizzazioni delle mappe di convergenza e del rapporto segnale-rumore (SNR). Questo viene fatto utilizzando la tecnica del tracciamento dei raggi per multipli piani di lenti (Giocoli et al. 2014, 2016, 2017). Queste mappe assumono delle galassie come sorgenti di fondo situate a  $z = 1$  e tengono conto di uno shape noise realistico sulla distribuzione di ellitticità delle galassie. Da ciascuna mappa SNR di convergenza, estraiamo un campione di vuoti 2D. Queste sono le regioni di SNR negativo risultanti dall'allineamento di diversi vuoti 3D che intercettano la linea di vista e sono comunemente chiamate *tunnel di vuoti* (Nadathur & Hotchkiss 2015a; Davies et al. 2021b). Sono quindi gli oggetti ideali per studiare il segnale di shear prodotto dalle sottodensità (Sánchez et al. 2017).

Per calcolare i profili di shear dei vuoti 2D, misuriamo il valore della convergenza in diverse shell attorno al loro centro, fino a dieci volte il raggio del vuoto. Poi, per ogni valore dello

shear tangenziale intorno al vuoto, associamo un'incertezza che è una combinazione di errori statistici e osservativi, questi ultimi derivati imponendo un'impostazione mirata a survey realistiche come quelli previsti dalla missione Euclid dell'ESA. I profili di shear tangenziale risultanti presentano valori statisticamente inferiori a zero, come previsto per le regioni poco dense. Dividendo il campione di vuoti in base alla loro dimensione, dimostriamo come i vuoti più piccoli siano caratterizzati da segnali più profondi e più rapidamente crescenti rispetto ai vuoti più grandi, coerentemente con quanto ci si aspetta dal comportamento già noto dei profili di densità (Hamaus et al. 2014; Voivodic et al. 2020).

Passiamo poi all'analisi delle differenze tra i profili di shear tangenziale misurati nei modelli alternativi e quelli in  $\Lambda$ CDM. Mostriamo come, nei modelli in cui è presente la MG, i vuoti presentino profili di shear più negativi, proprio perché la quinta forza ne accentua l'evoluzione, portando ad uno svuotamento più efficiente del loro interno. Viceversa, verificiamo come la presenza di neutrini massivi dia luogo a profili di shear meno profondi, poiché in questo caso l'accrescimento delle strutture viene smorzato a causa dell'effetto di free-streaming dei neutrini, e quindi i profili di densità dei vuoti appaiono meno profondi.

L'ultimo obiettivo della nostra analisi riguarda la modellazione del profilo di shear. Abbiamo innanzitutto testato l'uso di forme funzionali popolari per rappresentare i profili di densità dei vuoti, ovvero quelle introdotte da Hamaus et al. (2014) e Boschetti et al. (2023). Abbiamo integrato queste due formule parametriche lungo la linea di vista e abbiamo utilizzato il modello risultante per adattare i nostri profili di shear tangenziale. Tuttavia, anche lasciando liberi tutti i coefficienti di queste formule parametriche, entrambi i modelli non riescono a riprodurre i nostri dati. Questo accade perché i profili di densità considerati sono adatti solo a rappresentare vuoti 3D isolati e non tunnel di vuoti, che risultano dalla complessa proiezione di diverse sottodensità.

Per superare questo problema, proponiamo e convalidiamo una nuova formula parametrica per i profili di shear tangenziale dei vuoti. Ci preoccupiamo di minimizzare i parametri liberi di questo modello, pur richiedendo una rappresentazione accurata dei dati per diverse dimensioni dei vuoti e modelli cosmologici. Infine, utilizziamo questa forma funzionale come modello per eseguire un'analisi bayesiana. Vincoliamo i cinque parametri liberi della formula e analizziamo la loro correlazione, gli effetti della loro variazione e la loro sensibilità al modello cosmologico. Ci concentriamo poi sulla possibilità di distinguere statisticamente i risultati per il caso  $\Lambda$ CDM da quelli ottenuti per modelli alternativi, cioè caratterizzati da MG o da neutrini massicci. Mostriamo che, anche per gli scenari più estremi, l'incertezza associata alle nostre misure ci impedisce di distinguere questi modelli. Concludiamo che la mitigazione degli errori osservativi è fondamentale nella prospettiva di sfruttare efficacemente questa sonda per studi futuri.

Come futuro sviluppo di questo lavoro, ci proponiamo di applicare la nostra pipeline a simulazioni più ampie, eventualmente caratterizzate da diversi scenari cosmologici, al fine di migliorare le statistiche dei vuoti e studiare il comportamento anche di sottodensità più grandi. Esploreremo anche la fattibilità di questo tipo di studio su cataloghi di dati reali. Ad esempio, intendiamo utilizzare i dati della Kilo-Degree Survey (KiDS de Jong et al. 2013a,b) e, nel prossimo futuro, della survey *Euclid* (Laureijs et al. 2011; Amendola et al. 2018; Euclid Collaboration: Blanchard et al. 2020).

## Introduction

Nowadays, the standard cosmological framework is the  $\Lambda$ -cold dark matter ( $\Lambda$ CDM) concordance model (Heavens et al. 2017). It relies on the theory of General Relativity (GR) and Cosmological Principle, and describes the accelerated expansion of the Universe by means of an extra component called *cosmological constant*,  $\Lambda$ . According to this model, the structure formation follows a bottom-up hierarchical scenario, resulting in the filamentary pattern known as *cosmic web* (van de Weygaert & Schaap 2009; Cautun et al. 2014). In this scenario, collapsed structures originate from positive primordial fluctuations in the initial density field, whereas voids arise from their negative counterparts.

Despite the prevalence of the  $\Lambda$ CDM model in the scientific community, numerous alternative cosmological scenarios have emerged over the years in an effort to provide the best agreement between theoretical predictions and survey observations (Clifton et al. 2012). One possible explanation for the observed tensions in the  $\Lambda$ CDM (see Carroll 2001; Martin 2012; Moresco & Marulli 2017a), is the inadequacy of GR on cosmological scales (see Dolgov & Kawasaki 2003; Clifton et al. 2012; Joyce et al. 2015; Ishak 2019). In response, a number of models based modified gravity (MG) theories has been proposed. Among them, one of the most studied is the class of  $f(R)$  models, which incorporate an additional force, often referred to as the *fifth force*, to replicate the effects of the cosmological constant on the expansion history of the Universe (Joyce et al. 2015). Additionally, these models typically employ a *screening mechanism* to restore the predictions of GR on small scales and weaken the influence of the fifth force within high-density regions (Bertotti et al. 2003; Will 2005; Hinterbichler & Khoury 2010; Brax & Valageas 2013).

Due to their similarities with the standard model across various scales, MG theories are challenging to constrain to a level where they can be statistically distinguished from the  $\Lambda$ CDM model. A quite innovative strategy is to search for deviations from GR in matter underdensities, i.e., *cosmic voids*. Voids are extended and underdense regions that cover the majority of the Universe volume (Cautun et al. 2014). Unlike galaxy clusters, voids are weakly affected by screening mechanisms because of their low-density interiors and very large sizes. This makes them perfect laboratories to detect the gravitational effects produced by the fifth force (Barreira et al. 2015; Baker et al. 2018). Thanks to these unique features, cosmic voids have started to be exploited as cosmological probes, not only to test MG models, but also to explore the nature of dark energy, and study the effects of elusive components like neutrinos (Sánchez et al. 2017; Cautun et al. 2018; Contarini et al. 2021, 2022b).

One of the most promising approaches for exploring MG models in cosmic voids involves the analysis of the weak lensing (WL) signal. This involves studying the subtle deflection in the trajectory of photons emitted by background sources as they pass through matter fluctuations (Sereno & Umetsu 2011). Underdense regions along the line of sight cause therefore a peculiar distortion of the light sources in background, that can be quantified by the complex quantity called *cosmic shear*,  $\gamma$ , that defines the direction of this distortions, and convergence,  $\kappa$ , which represents the magnification of the sources (see Bartelmann & Schneider 2001; Kilbinger 2015a; Ishak 2019; Umetsu 2020). Besides its promising application to study MG models, this kind of statistic has already been demonstrated to be very sensitive to the growth rate of large-scale structure and the expansion history of the Universe (Bartelmann 2010; Troxel & Ishak 2015).

The goal of this Thesis work is to analyze the potentiality of the WL from cosmic voids as a cosmological probe. We aim at developing an effective pipeline that can be applied to simulations or real data, enabling the identification of cosmic voids in convergence maps and the subsequent extraction of the shear signal generated by underdensities. The building

of this pipeline is significant for the scientific community, as it offers an innovative method to investigate the fundamental properties of the Universe, including the presence of massive neutrinos and modifications to the theory of gravity.

This Thesis is designed to accompany the reader through the foundational knowledge necessary to understand its core topics, delving into the relatively novel research area of WL by cosmic voids. The structure of the work is organized as follows:

- In Chapter 1, we provide a comprehensive description of the theoretical framework of modern cosmology. We covered its pillars such as General Relativity and the Cosmological Principle, and delved into understanding the Friedmann Equations. We introduce the main features of the currently adopted standard cosmological model, the  $\Lambda$ CDM, including its strengths and weaknesses. Finally, we provide a brief overview on the formation and growth of large-scale structures in the Universe.
- In Chapter 2, we offer a brief analysis of the issues related to the  $\Lambda$ CDM model, as the current tensions afflicting the cosmological constraints derived with low and high-redshift observables. Then, we present the main alternatives to  $\Lambda$ CDM model, focusing in particular on the description of scenarios featuring MG and massive neutrinos.
- In Chapter 3, we entered the core of our research by introducing the object of our study: cosmic voids. We describe the main statistics used to analyze these objects and we provide the theoretical framework needed to describe the phenomenon of weak gravitational lensing. We focus in particular on the modeling of the WL signal from cosmic voids and on the expected effects in MG scenarios.
- In Chapter 4, we present one of the main outcomes of this work: the development of a new 2D void finder. We provide a detailed description of our pipeline, analyzing the algorithm step by step, from pre-processing to the final 2D void catalog. We demonstrate the effectiveness of our algorithm and we highlight its main qualities.
- In Chapter 5, we illustrate the preparation of the data catalogs used in our analysis. We describe the *DUSTGRAIN-pathfinder*, a set of simulations featuring different cosmological models, including those characterized by MG. Then we present the procedure followed to build the halo catalog and light-cones, up to the processes of generating the convergence WL maps used as input for our finder.
- In Chapter 6, we showcase all the results achieved. We make use of our void finding algorithm to analyze 2D voids and extract their main properties. We first discuss the abundance of voids in different cosmologies, then we measure and analyze their shear profiles. Finally, we propose a new parametric formula to model the mean void shear profile, effective also to encapsulate the variations caused by MG and massive neutrinos. We constrain the free parameters of this model through a Bayesian analysis and we focus on the cosmological dependency of void shear profiles.
- In Chapter 7, we provide a final overview of this Thesis work and outline the future perspective of the project.



# Chapter 1

## Theoretical cosmological framework

In this first Chapter, we present the basis of the Standard cosmological model. We discuss the theoretical framework, its observational counterpart, and the resulting interpretations moving from the general theory of gravity and the principles on which it is based to the evolution of density perturbations and the specific physical properties of the Universe. In particular, we define the spacetime metric, we introduce cosmological distances such as the definition of redshift, and we discuss the Friedmann Equations as solutions to the Einstein's Field Equation. In addition, we detail the formation of the large-scale structure (LSS) and its primary components, such as galaxy clusters and cosmic voids, in order to set the stage for the subsequent analysis in the next Chapters.

### 1.1 Fundamentals of Modern Cosmology

Cosmology investigates the formation and evolution of the Universe on the largest observable scales, describing its physical and statistical properties with suitable models. To construct such models, assumptions must be made from which it is possible to derive the explanation of the observables. The two fundamental pillars of every model are the observer's position inside the Universe and the choice of the theory of gravity. The current cosmological model is mainly based on the *cosmological principle* (CP) and the theory of *General Relativity* (GR), respectively.

#### 1.1.1 The Cosmological Principle

The CP ([Einstein 1917](#)) asserts that the Universe exhibits homogeneity and isotropy on sufficiently large scales. Homogeneity is the property of being identical everywhere in space and it denotes the absence of preferred locations in the Universe, while isotropy is the characteristic of appearing the same in every direction and entails the absence of preferred directions for an observer ([Lemaître 1927](#)). From these two fundamental properties derives the spacetime metric, as described in Sect. 1.2. While at small scales, the present-day observable Universe appears to be quite inhomogeneous, showing galaxies, clusters, and large voids, in its LSS we can recover an isotropic and homogeneous field on scales larger than  $\sim 100$  Mpc. The most important empirical support to CP is the isotropy of the cosmic microwave background (CMB) radiation ([Bennett et al. 1996](#)).

The cosmological principle includes the fair sample principle, described in Sec. 1.5, which states that examining adequately large and independent volumes of the Universe is akin to analyze numerous instances of the Universe. This concerns the non-reproducibility of the Universe, enabling the statistical depiction of the Universe's matter-energy content.

### 1.1.2 Theory of General Relativity

The other fundamental pillar when constructing a model that describes the entire Universe is the theory of gravity. This is because, on the large scales where the CP holds, the total action<sup>1</sup> of a free particle can be approximated by that of gravitational interaction, making gravity dominant over other forces. The total action is determined by integrating the Lagrangian of the system over time, and each term represents a specific contribution:

$$S_{\text{total}}[x^\mu(\lambda)] = \int_{t_i}^{t_f} \mathcal{L}_{\text{system}}(\text{fields}, t) dt = S_{\text{interactions}} + S_{\text{matter}} + \dots \approx S_{\text{gravity}}, \quad (1.1)$$

where  $x^\mu(\lambda)$  is the particle world line,  $\mathcal{L}$  is the Lagrangian density, and  $t_i$  and  $t_f$  are the initial and final times of the system.

The best current theory of gravity on which the standard cosmological model is based is General Relativity (GR) introduced by Einstein in 1915 (Einstein 1915). In GR, gravity is defined as an intrinsic property of spacetime geometry that can deform this geometry in the presence of mass and energy. Space-time is a four-dimensional differentiable manifold that has three space-like and one time-like coordinates, and its features are described by the metric tensor  $g_{\mu\nu}$  that is interpreted as the potential of gravitational forces. The spacetime points are called *events* and the interval between two infinitesimally close events is expressed as<sup>2</sup>

$$ds^2 = g_{\mu\nu} dx^\mu dx^\nu = g_{00} dt^2 + 2g_{0i} dt dx^i - g_{ij} dx^i dx^j, \quad (1.2)$$

where  $x^\mu = (ct, x, y, z)$ , with  $c$  is the speed of light,  $t$  is the proper time<sup>3</sup>, and  $x^\nu = x^\mu + dx^\mu$ .  $ds^2$  is an invariant length for generalized Lorentz transformations called the *mean square distance*,  $g_{00} dt^2$  is the temporal term,  $g_{ij} dx^i dx^j$  is the spatial term, and  $2g_{0i} dt dx^i$  is the mixed term. In a curved spacetime, free particles move along paths called *geodesics*. Following the principle of minimal action, these are the shortest paths between two events, and we can derive it by minimizing  $ds^2$ :

$$\delta \int_{\text{path}} ds = 0. \quad (1.3)$$

By describing the content of the Universe as a perfect fluid with pressure  $p$  and energy density  $\rho c^2$ , we can introduce the energy-momentum tensor as

$$T_{\mu\nu} = (p + \rho c^2) u_\mu u_\nu - p g_{\mu\nu}, \quad (1.4)$$

where  $u_\mu = g_{\mu\nu} u^\nu = g_{\mu\nu} \frac{dx^\nu}{d\lambda}(\lambda)$  is the 4-velocity of the fluid volume element. The metric tensor is influenced by the distribution and by the motion of the matter, so it is related to the energy-momentum tensor  $T_{\mu\nu}$ , through the Einstein's field equations, fundamental pillar of modern Cosmology, expressed as the Einstein's tensor:

$$G_{\mu\nu} = R_{\mu\nu} - \frac{1}{2} g_{\mu\nu} R = \frac{8\pi G}{c^4} T_{\mu\nu}, \quad (1.5)$$

where  $R_{\mu\nu} = R^\alpha_{\mu\alpha\nu}$  and  $R \equiv g^{\mu\nu} R_{\mu\nu}$  are the Ricci tensor the Ricci scalar, respectively, while  $G$  is the Newtonian gravitational constant. The constant factor  $8\pi G/c^4$  ensures to obtain the Poisson's equation  $\nabla^2 \phi = 4\pi G \rho$  in the weak gravitational field limit.

<sup>1</sup>Defined as the functional acting on the phase space, it is a scalar quantity that has dimensions  $[E \cdot t]$  and parameterizes the evolution and state of a system.

<sup>2</sup>Here we use the *Einstein's notation*, a notational convention that implies summation over a set of indexed terms in a formula, it is a notational subset of Ricci's calculus. In general relativity, a common convention is that the Greek alphabet is used for space and time components ( $\mu, \nu = 0, 1, 2, 3$ ), while the Latin alphabet is used for spatial components only ( $i, j = 1, 2, 3$ ).

<sup>3</sup>Defined as the time measured by a clock at rest with respect to the expansion of the Universe.

## 1.2 Friedmann-Lemaître-Robertson-Walker metric

A direct implication of assuming CP and GR is the determination of a metric describing spacetime known as the Friedmann-Lemaître-Robertson-Walker (FLRW) metric. In fact, in comoving coordinates<sup>4</sup>, isotropy is achieved by imposing null the mixed term, i.e.,  $g_{0i} = 0$ . Therefore, Eq. (1.2) is reduced to the following:

$$ds^2 = g_{00}dt^2 - g_{ij}dx^i dx^j = c^2 dt^2 - dl^2, \quad (1.6)$$

where there are only time and space terms. In the time term  $t$  coincides with the proper time, or *cosmic time*, and  $c$  is maintained, which means that the right-hand side (RHS) represents the distance covered at the speed of light, i.e.,  $ds^2 = 0 \rightarrow g_{00} = c^2$ . In the spatial term  $x^i$  and  $x^j$  are two sets of comoving coordinates and, at any instant  $t$ ,  $dl^2$  is identical in all the places and directions.

To find the explicit formula of  $g_{ij}$ , we need to look for a metric in the three-dimensional space which satisfies our assumption of the CP. The only 3D geometries that satisfy the homogeneity and the isotropy are the flat Euclidean space, hyper-spherical space, and the hyperbolic space. Hence, to obtain a generalized formula for the spatial element  $dl^2$ , we

- Use polar comoving coordinates  $(\rho, \theta, \phi)$  with  $0 \leq \rho < \infty$ ,  $0 \leq \theta < \pi$ ,  $0 \leq \phi < 2\pi$ ;
- Define the solid angle as  $d\Omega^2 = d\theta^2 + \sin^2 \theta d\phi^2$ ;
- Consider  $\rho \equiv ar$ , where  $a(t)$  is a factor called *cosmic scale factor* that is expressed as a function of the proper time of comoving observers. It describes the evolution of the space and has the dimensions of a length, while  $r$  is a dimensionless variable ( $0 \leq r < \infty$ );
- Introduce the so-called *curvature parameter*  $K$  that is a dimensionless parameter related to the amount of matter-energy density and it can be used to determine the value of the Gaussian curvature  $C_G = K/a^2$ .  $K$  has only three possible values corresponding to the different shapes of the geometry of the Universe:
  - $K = 1$ : Hyper-spherical geometry, implying a closed space with no boundaries;
  - $K = 0$ : Cartesian flat geometry, implying a pseudo-Euclidean and infinite space;
  - $K = -1$ : Hyperbolic geometry, implying an open and infinite space.

The general expression for  $dl^2$  in three dimensions is then

$$dl^2 = a^2(t) \left[ \frac{dr^2}{1 - Kr^2} + r^2 d\Omega^2 \right]. \quad (1.7)$$

Therefore, substituting Eq. (1.7) into the RHS of Eq. (1.6), we finally stick together the terms of time and space in the limit of the CP, and we get the FLRW metric for the 4D spacetime:

$$ds^2 = c^2 dt^2 - a^2(t) \left[ \frac{dr^2}{1 - Kr^2} + r^2 d\Omega^2 \right], \quad (1.8)$$

---

<sup>4</sup>Coordinates at rest with respect to the frame of the expanding Universe.

### 1.2.1 Hubble-Lemaître's law and redshift

Based on the FLRW metric, we can derive two kinds of fundamental distances:

- the *proper distance*  $d_{pr}$  of a point from the origin of a set of polar coordinates  $(r, \theta, \phi)$  is defined as the geodesic passing through such point. It is the distance measured in the comoving reference frame at fixed time ( $dt=0$ ) and assuming for simplicity  $d\theta = d\phi = 0$  in Eq. (1.8).

$$d_{pr}(r, t) = a(t) \int_0^r \frac{dr'}{\sqrt{1 - Kr'^2}} = a(t)F(r, K), \quad (1.9)$$

where the spatial and temporal parts of the equation have been explicitly separated. The function  $F(r, K)$  does not depend on time and takes different values depending on the value of  $K$ , so it depends on the geometry of the Universe, and we can rewrite it as

$$F(r) = \begin{cases} \sin^{-1}(r) & \text{for } K=1 \\ r & \text{for } K=0 \\ \sinh^{-1}(r) & \text{for } K=-1 \end{cases} ; \quad (1.10)$$

- the *comoving distance*  $d_C$ , is the proper distance computed at the present time  $t=t_0$ <sup>5</sup>:

$$d_C = d_{pr}(t_0) = a(t_0)F(r) = \frac{a_0}{a(t)}d_{pr}(r, t). \quad (1.11)$$

As we can see, here the expansion of the Universe is factored out, so this distance does not change in time even if the space is expanding.

It is not possible to measure proper and comoving distances directly through observations because of the finite speed of light, which in any reference system is the maximum speed at which information from distant objects can be transported. It, therefore, reaches our telescopes after a certain time, limiting our measurements to the set of light paths arriving from our past light cone (Coles & Lucchin 2002).

As we defined in Eq. (1.9), the proper distance has a time dependence in  $a(t)$ . This, together with the observation of an expanding Universe, implies a radial receding velocity between any two points in space. It is obtained by deriving  $d_{pr}$  with respect to time  $t$ , and its expression is the well-known *Hubble-Lemaître's law* (Lemaître 1927; Hubble 1929):

$$v_r = \frac{d}{dt}d_{pr} = \frac{d}{dt}[a(t)F(r)] = \dot{a}(t)F(r) = \frac{\dot{a}(t)}{a(t)}d_{pr} = H(t)d_{pr}, \quad (1.12)$$

where we defined the parameter  $H(t) \equiv \dot{a}/a$ , known as the Hubble parameter. It is a function of time that describes the isotropic expansion rate of the Universe, so it has the same value everywhere at a given cosmic time. Its value today  $H(t_0) = H_0$  is known as the Hubble Constant, and conventionally it is expressed through a dimensionless parameter  $h$  to overcome uncertainties in the value of  $H_0$ :

$$H_0 \equiv 100h [km s^{-1} Mpc^{-1}]. \quad (1.13)$$

In fact, even in the most recent measurements,  $H_0$  remains uncertain, with values around  $70 \text{ km s}^{-1} \text{ Mpc}^{-1}$ . Notable measurements include  $H_0 = 69.13 \pm 2.34 \text{ km s}^{-1} \text{ Mpc}^{-1}$  from BAO measurements (Riess et al. 2019a),  $H_0 = 74.03 \pm 1.42 \text{ km s}^{-1} \text{ Mpc}^{-1}$  from SNIa standard candels (Riess et al. 2019a),  $H_0 = 67.4 \pm 0.5 \text{ km s}^{-1} \text{ Mpc}^{-1}$  from CMB angular spectrum

---

<sup>5</sup>The subscript 0 corresponds to today's value, from here on.

(Planck Collaboration et al. 2020a),  $H_0 = 67.7^{+4.3}_{-0.42}$  km s<sup>-1</sup> Mpc<sup>-1</sup> from gravitational waves (Mukherjee et al. 2020).

In this context, we call the relative collective motion of objects in the Universe, the Hubble Flow. An outcome of this phenomenon is the reddening of the observed spectrum of distant objects, indicating a shift towards longer wavelengths in the electromagnetic spectrum. The further away an object the more it is affected by this effect termed *redshift*. It is properly defined as the relative difference between the wavelength  $\lambda_{\text{em}}$  of radiation emitted at time  $t_{\text{em}}$  from a source, in its reference system, moving along the line of sight (los) of the observer, and the wavelength  $\lambda_{\text{obs}}$  of the radiation which arrives at the observer at time  $t_{\text{obs}}$ .

$$z \equiv \frac{\lambda_{\text{obs}} - \lambda_{\text{em}}}{\lambda_{\text{em}}} = \frac{\Delta\lambda}{\lambda}, \quad (1.14)$$

where  $z < 0$  (*blueshift*) when the source is approaching the observer, or  $z > 0$  (*redshift*) when the object is moving away from the observer. We can derive an important relation for Cosmology by integrating, assuming comoving coordinates, the FLRW metric along the difference between two photon paths<sup>6</sup>. Therefore, for an observer located at the present time  $t_0$  and an emitting source at a generic  $t$ , it is:

$$1 + z = \frac{a_0}{a(t)}. \quad (1.15)$$

In this relation we can see how cosmological redshift depends on the scale factor  $a(t)$  that is a monotonic function of cosmic time, this is why redshift can be considered as a measure of both distance and time. We can use spectroscopy (but also photometry) to measure  $z$  and through this relation infer the distance of extragalactic sources<sup>7</sup>.

## 1.2.2 Observable cosmological distances

As we mentioned, the previous definition represent distances between events happening at the same proper time  $d_{\text{pr}}$ , so they are physically impossible to measure. At this point, it is useful to define other distances that are directly measurable from observables, leveraging their characteristics, as the case of redshift.

- The *luminosity distance*  $d_L$ , which is derived by assuming to have an object with the same intrinsic emitted luminosity ( $L \equiv \frac{dE}{dt} = L_{\text{obs}}[\frac{a_0}{a(t)}]^2$ ) throughout the space-time, like in the standard candle<sup>8</sup> method, and by measuring its flux ( $f = \frac{L_{\text{obs}}}{4\pi d_C^2} = \frac{L}{4\pi a_0^2 r^2} [\frac{a(t)}{a_0}]^2$ ) with the assumption of the flux conservation (see Figure 1.1a). Using the flux-luminosity relationship, we can obtain the following definition:

$$d_L = \sqrt{\frac{L}{4\pi f}} = \frac{a_0^2}{a(t)} r = a_0 r (1 + z). \quad (1.16)$$

- The *angular diameter distance*  $d_A$  is defined in order to preserve the geometric characteristics of an Euclidean space with the distance, in particular the variation of angular

<sup>6</sup>A massless particle like photon move along null geodesics ( $ds^2 = 0$ ).

<sup>7</sup>It is crucial to emphasize that the frequency of light is influenced also by gravitational fields and other relativistic effects (Weinberg 1972).

<sup>8</sup>The term *standard candles* refers to objects with a well-established luminosity, such as SNIa, leading to consistent peaks in their light curves; while *standard rulers* are objects with a known size, i.e., Baryon Acoustic Oscillations (BAO), fluctuations visible in the distribution of baryonic matter on large scales.

size (see Figure 1.1b). Given an object with known physical (transverse) size  $D$ , subtended by a certain angle  $\delta\theta$  in the small-angle approximation ( $\delta\theta \ll 1$ ), its distance is:

$$d_A = \frac{D}{\delta\theta} = a(t)r. \quad (1.17)$$

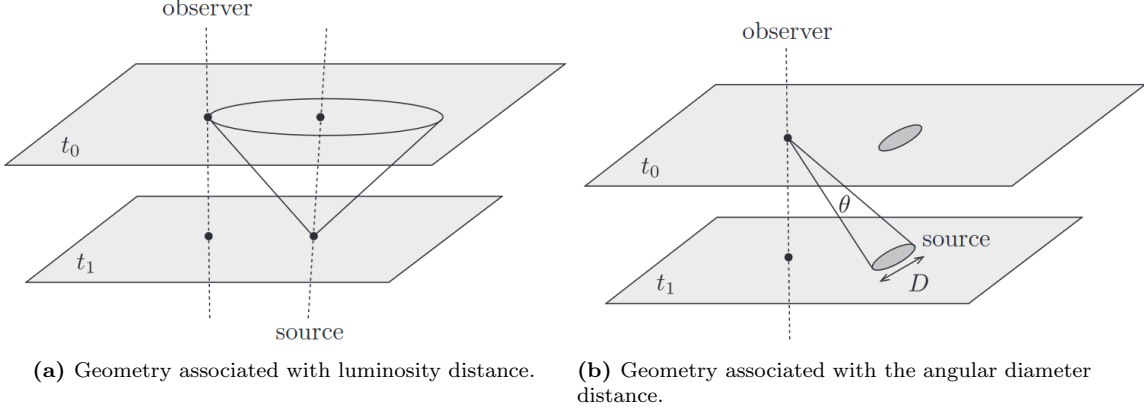


**Figure 1.1:** Left panel (a): A standard candle emits photons at time  $t = t_{\text{em}} = t_1$  at a distance  $z$ . At the time of observation  $t_{\text{obs}} = t_0$ , the observer can measure a flux through the surface area of a sphere centered in its position and inflated by the Universe expansion. Right panel (b): A standard ruler emits photons at time  $t = t_{\text{em}} = t_1$  at a distance  $z$ . At the time of observation  $t_{\text{obs}} = t_0$ , the object appears to subtend an angle  $\theta$ , though the space in-between the observer and the standard ruler has expanded during the photons' travel by a factor of  $(1+z)$ . Credits to: <https://homes.psd.uchicago.edu/~liantaow/my-teaching/dark-matter-472/lectures.pdf>

Assuming a spacetime metric allows us to calculate luminosity and angular diameter distances for any extragalactic source with a known redshift. Utilizing standard candles facilitates testing the FLRW metric using Eq. (1.16) when the source redshift is available. Similarly, standard rulers offer a means to assess the assumed spacetime metric through Eq. (1.17).

We can note that, by their definition, all the cosmological distance definitions are coincident for  $r \rightarrow 0$  and  $t \rightarrow t_0$ :

$$d_{\text{pr}} \approx d_{\text{C}} \approx d_{\text{L}} \approx d_{\text{A}}, \quad (1.18)$$

reproducing the Euclidean behavior at small distances (Hogg 1999).

By comparing the luminosity distance with the angular diameter distance, we obtain the Etherington's reciprocity theorem also well-known as the *duality relation* (Etherington 1933):

$$\frac{d_{\text{L}}}{d_{\text{A}}} = (1+z)^2. \quad (1.19)$$

From this relation we can derive that having a source which is both a standard candle and a standard ruler, its  $d_{\text{A}}$  will be always smaller than its  $d_{\text{L}}$ . Eq. (1.19) provides a robust test to quantify the deviations from the FLRW metric, in particular the assumptions of CP (Li et al. 2011), and consequently it plays an important role in the validation of current cosmological models. Up to now the strongest probes to duality relation are strong gravitational lensing and compact radio sources (see, e.g., Qin et al. (2021); Tang et al. (2023); Li (2023)). These observations have found no divergence from the duality connection, and this means that the standard cosmological model holds.

### 1.3 Friedmann equations

As we mentioned, in a Universe with assumptions of CP and GR, the relationship between the geometry of spacetime and the matter content is governed by the Einstein's field equations (Eq. (1.5)). Assuming the validity of the FLRW metric and considering the energy-momentum tensor as that of a perfect fluid (Eq. (1.4)), we can reduce this set of 10 equations to only two independent equations, called the *first* and the *second Friedmann equations* (Friedmann 1922):

$$\ddot{a} = -\frac{4\pi}{3}G \left( \rho + \frac{3p}{c^2} \right) a \quad (\text{time-time component}), \quad (1.20)$$

$$\dot{a}^2 + Kc^2 = \frac{8\pi}{3}G\rho a^2 \quad (\text{space-space component}). \quad (1.21)$$

These equations provide the time evolution of the scale factor  $a(t)$  and represent the dynamic evolution of the Universe.

In addition, assuming the Universe as a closed system in adiabatic expansion<sup>9</sup>, these equations are related by the *adiabaticity condition*:

$$d\mathcal{U} = -p dV \quad \longrightarrow \quad d(\rho c^2 a^3) = -p da^3, \quad (1.22)$$

where, in the general form,  $\mathcal{U}$  is the internal energy and  $V$  is the volume of the Universe. The density,  $\rho$ , and the pressure,  $p$ , have to be considered as the sum of the densities and the pressures of all Universe's components, respectively. From this relation follows:

$$\dot{\rho} + 3 \left( \rho + \frac{p}{c^2} \right) \frac{\dot{a}}{a} = 0. \quad (1.23)$$

At this point, we can manipulate the second Friedmann equation (1.21) to derive the curvature parameter  $K$  as a function of the Universe's density  $\rho$ . In order to do this, it is convenient to define a density parameter called *critical density*:

$$\rho_{\text{crit}}(t) \equiv \frac{3}{8\pi G} \left( \frac{\dot{a}}{a} \right)^2 = \frac{3H^2(t)}{8\pi G}, \quad (1.24)$$

so the Eq. (1.21) can be reduced to:

$$H^2(t) \left( 1 - \frac{\rho(t)}{\rho_{\text{crit}}(t)} \right) = -\frac{Kc^2}{a^2(t)}. \quad (1.25)$$

For each time, the ratio between the density and the critical density defines the dimensionless *density parameter*:

$$\Omega(t) \equiv \frac{\rho(t)}{\rho_{\text{crit}}(t)} = \frac{8\pi G}{3H^2(t)} \rho(t). \quad (1.26)$$

$\Omega(t)$  is a fundamental cosmological parameter because in this notation it describes the density contribution of each component of the Universe and from its value we can determine the value of  $K$  and then deduce the real geometry and the kind of evolution of the Universe:

- If  $\Omega > 1 \Leftrightarrow \rho > \rho_{\text{crit}} \Leftrightarrow K = 1$ , Hyperspherical geometry, positive curvature (closed) Universe with decelerated expansion followed by a contraction;
- If  $\Omega = 1 \Leftrightarrow \rho = \rho_{\text{crit}} \Leftrightarrow K = 0$ , Flat geometry, null curvature Universe;

---

<sup>9</sup>An expansion in which the system has no energy loss so does not exchange heat with the outside

- If  $\Omega < 1 \Leftrightarrow \rho < \rho_{crit} \Leftrightarrow K = -1$ , Hyperbolic geometry, negative curvature (open) Universe with eternal expansion.

As we can see on Eq. (1.25), the value of the critical density depends from  $H(t)$ . Computed today ( $t = t_0$ ) its value is  $\rho_{crit,0} \simeq 1.9 \times 10^{-26} h^2 \text{ kg m}^{-3} \simeq 2.775 \times 10^{11} h^2 M_\odot \text{ Mpc}^{-3}$ . The most recent estimate of the total density parameter is  $\Omega_0 = 0.9993 \pm 0.0019$  (Lahav & Liddle 2019), obtained assuming the measurements from Planck Collaboration et al. (2020a).

### 1.3.1 Cosmological constant $\Lambda$

From Eq. (1.20) we can deduce that the Universe can not be static otherwise it would have negative pressure or energy density, and this is physically impossible. In order to recover static-Universe solutions from his field equation, Einstein introduced a constant  $\Lambda$ , called the *cosmological constant* that balances the gravity's attractive action on matter. This implies a modification in the field equations:

$$R_{\mu\nu} - \frac{1}{2}g_{\mu\nu}R - \Lambda g_{\mu\nu} = \frac{8\pi G}{c^4}T_{\mu\nu}. \quad (1.27)$$

In fact, by imposing on  $\Lambda$  a sufficiently small value, we can achieve a static model for our Universe and at the same time maintain consistency with the weak field approximation of Newtonian theory. Such a requirement was highly fine-tuned, and, following the discovery of the Universe's expansion through Hubble-Lemaître's law, the concept of a static Universe was abandoned, along with the introduction of the cosmological constant. Nevertheless, from the subsequent discovery of the accelerated expansion of the Universe thanks to the observation of the flux of distant SNIa (Riess et al. 1998; Perlmutter et al. 1999),  $\Lambda$  has been reintroduced into Einstein's field equation.

The current theoretical justification of the cosmological constant is physically well motivated in GR, as its presence naturally descends from the general expression of the gravitational field's second-order action (Bianchi & Rovelli 2010). Its repulsive action on large scales plays a role in the current cosmological model and changes our understanding of gravity's nature itself. Depending on its position in Einstein's field equation, it takes different interpretations:

- **LHS:** interpretation of  $\Lambda$  as a geometrical modification of gravity, i.e. a failure of the standard relativistic theory of gravity, and hence, the GR would need to be revised on cosmological scales;
- **RHS:** interpretation of  $\Lambda$  as an additional energy component in the energy-momentum tensor. It is called *dark energy* (DE), a cosmological fluid with negative pressure, which contrasts the small-scale attractive interactions. Its nature is unknown and it is currently interpreted as the vacuum energy.

The first work that integrates the cosmological constant into the field equations and studies its dynamic solutions and their evolution over time under the assumption of perfect fluid, dates back to A. Friedmann (Friedmann 1922). By defining an effective pressure ( $\tilde{p} = p - \frac{\Lambda c^4}{8\pi G}$ ) and an effective density ( $\tilde{\rho} = \rho + \frac{\Lambda c^2}{8\pi G}$ ), he modified the energy-momentum tensor as

$$\tilde{T}_{\mu\nu} = T_{\mu\nu} + \frac{\Lambda c^4}{8\pi G}g_{\mu\nu} = -\tilde{p}g_{\mu\nu} + (\tilde{p} + \tilde{\rho}c^2)u_\mu u_\nu, \quad (1.28)$$

obtaining the so-called modified Friedmann equations:

$$\ddot{a} = -\frac{4\pi}{3}G \left( \tilde{\rho} + 3\frac{\tilde{p}}{c^2} \right) a, \quad (1.29)$$

$$\dot{a}^2 + Kc^2 = \frac{8}{3}\pi G \tilde{\rho} a^2. \quad (1.30)$$

### 1.3.2 The components of the Universe and their evolution

In order to describe the expansion history of the Universe, it is necessary to know its content and thus the equation of state that characterizes each component.

In the perfect-fluid approximation<sup>10</sup> a general equation of state (EoS)  $p = p(\rho)$  with isotropic pressure (from the adoption of the CP) assumes the form:

$$p = w\rho c^2 \quad \text{with } 0 \leq w \leq 1. \quad (1.31)$$

where  $w$  is the EoS parameter defined from the sound speed like  $c_s \equiv \left(\frac{\partial p}{\partial \rho}\right)_{S=\text{const}}^{1/2} = c\sqrt{w}$ . This parameter is assumed to be constant with time and, to have a physical meaningful<sup>11</sup>, it must belong to the so-called *Zel'dovich interval* given in Eq. (1.31). Depending on the specific component under consideration, differentiating between relativistic and non-relativistic, the constant  $w$  may assume various values:

- $w \simeq 0$  represents a **non-relativistic fluid**, like *matter* (dust):  $p_m = \frac{k_B T}{m_p c^2} \rho_m c^2$  where  $\frac{k_B T}{m_p c^2} \sim 0$ , so its contribution to total pressure can be neglected<sup>12</sup>:  $p_m \approx 0$ ;
- $w = 1/3$  represents an **ultra-relativistic fluid**, like *radiation* or relativistic matter, composed of non-degenerate particles at equilibrium like photons and neutrinos:  $p_r = \frac{1}{3}\rho c^2$ ;
- $w = -1$  represents the **cosmological constant**:  $p_\Lambda = -\rho_\Lambda c^2$ . It is the only value of  $w$  that makes the contribution of  $\Lambda$  constant over time, obtaining  $\rho_\Lambda = \rho_{0,\Lambda} = \text{const}$ .

At this point, by combining the adiabaticity condition, Eq. (1.22), and the general EoS, Eq. (1.31), it is possible to derive the density trend with the cosmic time of an individual component:

$$\rho_w = \rho_{w,0} \left(\frac{a}{a_0}\right)^{-3(1+w)} \propto a^{-3(1+w)} \propto (1+z)^{3(1+w)}, \quad (1.32)$$

It is a function of the scale factor for any value of  $w$ . By computing it for each component, it is clear that they evolve differently. Thus, we can deduce that different components have dominated through the cosmic epochs, with one prevailing over the others.

<sup>10</sup>To make this assumption reasonable, it is sufficient for the particles mean free path of the fluid to be much smaller than the scales of interest. This can be realistic when considering the Universe on a large scales.

<sup>11</sup>We must have a positive (or null) real value for the sound speed, also smaller than the speed of light.

<sup>12</sup>This is because  $k_B T$  (the typical particle thermal energy), with  $k_B$  the Boltzmann constant and  $T$  the fluid temperature, is much lower than  $m_p c^2$  (the particle rest mass).

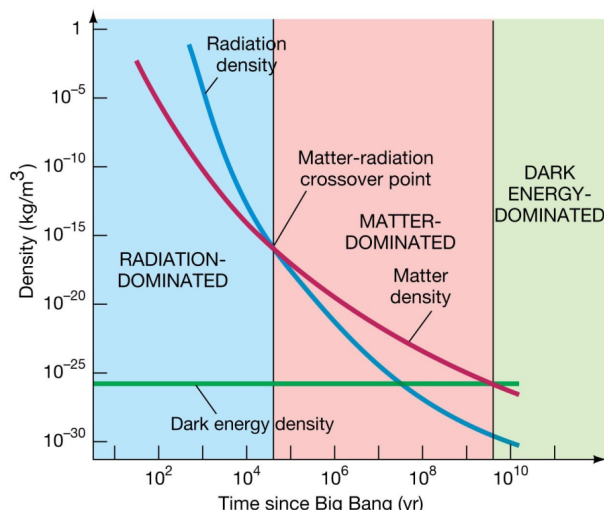


**Figure 1.2:**  $\rho - t$  plot with trends in time of the three main Universe’s components: radiation, matter, dark energy, here in the form of a cosmological constant.

From this, by inserting this relation into Eq. (1.26), we obtain

$$\Omega_{\text{tot}}(t) \equiv \sum_i \Omega_{w_i}(t). \quad (1.33)$$

Generalizing Eq. (1.25) for a multi-component Universe, we obtain the evolution of the Hubble parameter:

$$H^2(z) = H_0^2(1+z)^2 \left[ 1 - \Omega_{0,tot} + \Omega_{0,tot}(1+z)^{(1+3w_i)} \right] \equiv H_0^2 E^2(z), \quad (1.34)$$

where  $H_0$  is the Hubble constant,  $\Omega_{0,K} = 1 - \sum_i \Omega_{0,w_i}$  is the so-called curvature density parameter, and  $E(z)$  is the dimensionless Hubble parameter. For the mono-component Universe, combining all the equations above, we can explicitly describe the evolution of the density parameter over time, or redshift, as:

$$(\Omega_{tot}(z))^{-1} - 1 = \frac{(\Omega_{0,tot})^{-1} - 1}{(1+z)^{1+3w_i}}. \quad (1.35)$$

For “ordinary” fluid components, given  $w = \text{const}$  and in the Zel’dovich interval, the exponent of  $(1+z)$  will be always positive. Therefore, the sign of the RHS of Eq. (1.35) remains constant throughout the expansion of the Universe; consequently, the LHS also remains invariant and the total curvature density parameter can not change its sign over time. This fundamental relation implies that a Universe governed by the Friedmann equations undergoes no changes in its geometry during its evolution.

### 1.3.3 Big Bang and cosmological horizon

From the second Friedmann Eq. (1.25) and from the Hubble’s law observations of the expansion of the Universe, we have  $\dot{a}(t) > 0$ . From the first Friedmann Eq. (1.20) with the perfect-fluid approximation in the Zel’dovich interval, we have  $\ddot{a}(t) < 0$  for any  $t$ .

This information makes us infer the behavior of  $a(t)$  going back in time:

- $\dot{a}(t) > 0 \implies a(t)$  is a monotonically increasing function;
- $\ddot{a}(t) < 0 \implies a(t)$  is a downward concave function without an inflection point.

All possible cosmological models, based on the GR and CP and described by perfect fluids with  $-1/3 < w \leq 1$ , necessarily have some finite time in the past at which it is infinitely small  $a(t) = 0$ , while density, Hubble parameter and temperature diverge:

$$\lim_{t \rightarrow 0} \rho(t) = \lim_{t \rightarrow 0} \left( \frac{a_0}{a(t)} \right)^{-3(1+w)} \rightarrow +\infty. \quad (1.36)$$

This is a singularity because its real physical conditions at the time are unknown and is called the *Big Bang* (BB). It gives the name to the model that currently appears to better describe these conditions and the subsequent evolution: the *Hot Big Bang* (HBB) model. In this context, the evolution of the Universe is illustrated as a thermal history, thus the term “Hot”. As we rewind closer  $t \simeq 0$ , the Universe consistently becomes hotter, but for times  $t < t_p$ , where  $t_p \sim 10^{-43}$  s is the Planck time, it is no longer possible to neglect the quantum effects of gravity which, still to date, has not a universally accepted treatment. Note that the expansion of the universe emerging from the HBB model is a result of the initial conditions.

Understanding the evolution of the scale factor  $a(t)$  enables the derivation of the *cosmological horizon*  $R_H(t)$ . This parameter delineates a sphere centered on a particle, encompassing the volume of the Universe in causal connection with that particle. Specifically,  $R_H(t)$  is defined as follows:

$$R_H(t) = a(t) \int_0^t \frac{c dt'}{a(t')}. \quad (1.37)$$

It is a proper distance, derived from Eq. (1.9), that takes into account the expansion of the Universe for a photon. If the integral remains finite,  $R_H(t)$  defines the so-called *particle horizon*, which encloses the set of events in the space-time that are causally connected to a particle P. From Eq. (1.21), it can be shown that  $a(t) \propto t^\beta$ , with  $\beta > 0$ , for a generic Friedmann model. Therefore, manipulating the Friedmann equations as a function of  $\beta$ , we can derive

$$\beta(\beta - 1) \propto -\frac{4\pi}{3} G t^2 \left( \rho + \frac{3p}{c^2} \right). \quad (1.38)$$

We can note that the condition  $\ddot{a} < 0$  for a Big Bang singularity implies  $0 < \beta < 1$ . Consequently, the presence of a Big Bang ensures the finiteness of  $R_H(t)$ .

Since  $R_H(t)$  is finite, signals originating from sources with comoving proper distances exceeding the particle horizon scale  $d_p(t) > R_H(t)$  cannot have been observed by the observer. It is essential to differentiate between the behaviors before and after  $a_{\text{eq}}$ , representing the scale factor that defines the age of equivalence between radiation and matter:

$$R_H = \begin{cases} a^2 & \text{for } a < a_{\text{eq}} \\ a^{2/3} & \text{for } a > a_{\text{eq}} \end{cases}. \quad (1.39)$$

For a flat Universe, this leads to the exact relation:

$$R_H = 3 \frac{1+w}{(1+3w)} ct = \begin{cases} 2ct & \text{for } t < t_{\text{eq}} \\ 3ct & \text{for } t > t_{\text{eq}} \end{cases}, \quad (1.40)$$

where  $w = 1/3$  for a radiation-dominated Universe and  $w = 0$  for a matter-dominated Universe.

## 1.4 The standard cosmological model $\Lambda$ CDM

Today, the widely accepted model describing the origin of our Universe is the HBB model. It portrays an almost flat Universe characterized by the CP and GR, governed by the Friedmann equations. As we mentioned above, the Universe described in this context underwent a thermal history, so we can trace its evolution studying the changes in temperature. In principle, the Universe's temperature was significantly higher than it is today, while presently the temperature of the photons permeating the Universe is measured at  $T = 2.7255 \pm 0.0006K$  (Fixsen et al. 1996; Planck Collaboration et al. 2020a). This value corresponds to the CMB temperature, a black-body radiation originating from the last scattering surface approximately at redshift  $z \approx 1089$  (about  $3.79 \times 10^5$  yr after the Big Bang). The early Universe was composed of a hot fully ionized high-dense plasma, containing baryons and free electrons. In this fluid, electromagnetic radiation was continuously scattered by high density of baryonic matter, so that the Universe was completely opaque<sup>13</sup> and in thermal equilibrium. This can happen because the continuous expansion led to a cooling effect until, when the temperature falls below  $\simeq 3000K$ , electrons start recombining with protons at  $z \approx 1500$ , allowing photons to propagate freely reaching us, the observers. Subsequently, with the dominance of the matter component, gravitationally bound structures formed, rising to the large-scale structures observed today.

In addition, CMB temperature exhibits very small fluctuations, approximately  $10^{-5}$  K, in any direction across the sky, and this lends empirical support to the isotropy assumption embedded in the CP<sup>14</sup>. Despite the observed causal connection at  $z \simeq 1100$  implied by the isotropy of the CMB temperature, the size of the cosmological horizon predicted by the models at that time suggests that causal connection should not extend beyond approximately  $2^\circ$  on the sky. Cosmic inflation, proposed by Guth (1981), addresses this discrepancy by positing an accelerated expansion characterized by exponential growth of the cosmic scale factor  $a(t)$ , in the early Universe at  $t \simeq t_{GUT}$ , but after the BB. Modern inflationary models, notably based on the *Chaotic Inflation* proposed by Linde (1983), often involve a scalar field with substantial initial potential energy, referred to as the inflaton. In these models, the inflaton eventually decays into particles through quantum fluctuations, establishing the initial conditions for growth of perturbation and the formation of cosmic structures. Additionally, cosmic inflation explains the observed flatness of the Universe's spacetime geometry, as revealed by CMB experiments (de Bernardis et al. 2000).

At now, based on HBB and inflationary models, we describe the total theoretical framework of our Universe with the standard cosmological model, called concordance  $\Lambda$ -cold dark matter ( $\Lambda$ CDM) model. Supported by extensive observational data, this model is the basis of our understanding of structure formation. By making explicit the components of  $\Omega_{tot}$  in (1.35) and expressing with their present-day values:

$$\Omega_{0,tot} = \Omega_{0,m} + \Omega_{0,r} + \Omega_{0,\Lambda} , \quad (1.41)$$

where  $\Lambda$  represents the cosmological constant with  $\Omega_{0,\Lambda} \approx 0.67$ , cold dark matter (CDM), a dust-like type of dark matter with  $\Omega_{0,cdm} \approx 0.28$ , ordinary observable matter (baryons) with  $\Omega_{0,b} \approx 0.05$ , and a radiation component with  $\Omega_{0,r} \approx 10^{-5}$ . These energy density values align with the flatness condition  $\Omega_{0,tot} \approx \Omega_{0,\Lambda} + \Omega_{0,cdm} + \Omega_{0,b} + \Omega_{0,r} \approx 1$ .

As we can see, the dominant component of the standard cosmological model is DE, represented by  $\Lambda$ , and it is vital for explaining the observed accelerated expansion of the Universe.

<sup>13</sup>Photons, within this Universe were essentially confined, incapable of traveling significant distances before interacting with the plasma through Thomson scattering.

<sup>14</sup>Note that these measurements, while confirming the isotropy, do not validate the homogeneity of spacetime, a requirement demanding observations from diverse locations in the Universe.

Combining the Friedmann equation and the perfect fluid EoS, it can be demonstrated that a multi-component universe consisting of a cosmological constant and matter leads to an accelerated expansion ( $\ddot{a} > 0$ ). This acceleration is expressed as  $\ddot{a} = -\frac{4\pi}{3}Ga\rho(1+3w)$ , where a positive  $\Lambda$  is required to account for the accelerated expansion. This implies a positive density and a negative pressure ( $w_\Lambda = -1$ ), and requires imposing the condition  $\Omega_{0,\Lambda} > \Omega_{0,m}/2$ , which is indeed satisfied by the present-day density values. Although  $w_\Lambda = -1$  could avoid a Big Bang singularity introducing a flex in the function  $a(t)$ , the measured energy density associated with  $\Lambda$  is too low, so it occurs. It can be shown that, given the present-day density values, this inversion in the expansion rate occurs at  $z_f \approx 0.67$ . Further mathematical derivations allow us to determine the moment of equivalence between the density corresponding to matter and the cosmological constant, i.e.,  $\Omega_m(z_{\text{eq},\Lambda}) = \Omega_\Lambda(z_{\text{eq},\Lambda})$ . This event occurs at  $z_{\text{eq},\Lambda} \approx 0.33$ , indicating that DE and matter are presently comparable, with the contribution of  $\Lambda$  becoming significant only at recent times. DE density is approximately  $\rho_{0,\Lambda} \approx 7 \times 10^{-27}$  kg m<sup>-3</sup> and it is the highest compared to the other components, but, even now, it is not associated with any known form of energy.

Similarly, due to the inability of direct observations, a physical description of the DM is still lacking. It was introduced in Zwicky (1937) to account for observed gravitational effects that could not be explained by existing gravitational theories without an excess of non-visible mass. DM can be interpreted as particles or small objects interacting solely with matter, including self-interaction, through gravity and possibly the weak force. The existence of DM would now seem to be confirmed by various pieces of evidence, with gravitational lensing by galaxy clusters, redshift-space distortions in large-scale mass distribution, and fluctuations in the density spectrum due to BAO being among the most reliable probes to quantify its effects. From a cosmological point of view DM can be classified into two primary types:

- Hot dark matter (HDM), composed of low-mass relativistic particles, with massive neutrinos being the leading candidates;
- Cold dark matter (CDM), consisting of massive non-relativistic particles, with Weakly Interacting Massive Particles (WIMPs) currently being the most plausible candidates.

Over the past decades, several particle candidates have been proposed and tested. As discussed in the next section, structure formation and evolution models suggest that the majority of the DM component must be cold. CDM is integrated into the standard cosmological model due to its non-relativistic state preceding that of HDM. The intrinsic link between cosmic time and temperature allows us to estimate when a fluid ceases to be relativistic. This is accomplished using the relationship  $k_B T \simeq m_x c^2$ , where  $k_B$  is the Boltzmann constant, and  $m_x$  is the characteristic mass of the fluid particles. CDM particles, being more massive than their hot counterparts, experience the transition to a non-relativistic state earlier. Moreover, CDM, being non-relativistic at the moment of decoupling from the radiation component, facilitates the prompt emergence of gravitational perturbations. This characteristic aligns with the *hierarchical model* for the development of cosmic structure, involving the initial formation of small structures that undergo mergers, leading to the creation of larger gravitationally bound objects.

A comprehensive characterization of the  $\Lambda$ CDM scenario involves defining six fundamental parameters:

- $\Omega_m$ : total matter density parameter,
- $\Omega_b$ : baryonic matter density parameter,
- $H_0$ : Hubble constant,

- $A_s$ : primordial power spectrum amplitude,
- $n_s$ : spectral index of the primordial power spectrum,
- $\tau$ : reionization optical depth.

Here,  $\Omega_m$  and  $\Omega_b$  are typically expressed with their present-day values, while, in a flat Universe, the DE density parameter is expressed as  $\Omega_\Lambda = 1 - \Omega_m$ . The matter power spectrum depends on  $A_s$  and  $n_s$ .

The strongest constraints on these parameters are derived from the analysis of the CMB angular power spectrum observations. From the combination of CMB temperature fluctuations and lensing, [Planck Collaboration et al. \(2020a\)](#) derived the following constraints:  $\Omega_m h^2 = 0.1430 \pm 0.0011$ ,  $\Omega_b h^2 = 0.02237 \pm 0.00015$ ,  $H_0 = 67.36 \pm 0.54 \text{ km s}^{-1} \text{ Mpc}^{-1}$ ,  $10^9 A_s = 2.100 \pm 0.030$ ,  $n_s = 0.9649 \pm 0.0042$ ,  $\tau = 0.0544 \pm 0.0073$ . The CDM density parameter is defined as  $\Omega_c = \Omega_m - \Omega_b$ , and from these results we can note that it is the contribution that dominates  $\Omega_m$ .

## 1.5 Formation of Cosmic Structures

According to the Standard Cosmological Model, after the BB, the Universe evolved from a homogeneous state into a complex network of structures called *cosmic web* that we can now observe. This term refers to the LSS of the Universe, characterized by a hierarchical-organized system consisting of voids, filaments, walls, and nodes. This intricate network has evolved from primordial fluctuations that originated in the final phase of inflation at very high redshifts ([Bacon et al. 2021](#)). The  $\Lambda$ CDM model posits a bottom-up scenario for the formation of cosmic structures. In this model, DM particles collapse into DM haloes, forming potential wells where baryons can subsequently accumulate through a process known as *baryon catch-up*. The initial appearance of small DM haloes and baryonic structures precedes the formation of larger structures through aggregation.

As these structures emerged, the Universe displayed inhomogeneity on smaller scales, approximately tens of megaparsecs. So, to comprehend the Universe’s homogeneity today, observations must extend to scales larger than  $\sim 100 \text{ Mpc}$ . In fact, when the cosmic field is smoothed across sufficiently large regions, the Friedmann equations can still effectively describe the dynamics of the Universe. The formation and evolution of cosmic structures are intricately tied to cosmological parameters that encapsulate both the geometry and constituents of the Universe. Consequently, the statistics of LSS offers powerful insights, guiding us toward a deeper understanding of the Universe we inhabit. In this section, we will delve into both the linear (1.5.2) and nonlinear (1.5.3) evolution of cosmic structures.

### 1.5.1 Primordial fluctuations

Currently, the widely accepted theory of cosmic structure formation is grounded in a homogeneous background of the primordial Universe, perturbed by mechanisms such as initial scalar metric-fluctuations (quantum vacuum fluctuations) that might have expanded into “macroscopic” cosmological perturbations during cosmic inflation ([Langlois 2005](#)). They are produced by the oscillation of the inflaton field and in Newtonian approximation correspond to fluctuations  $\delta_\Phi$  of gravitational potential  $\Phi$ . Assuming that just after inflation there are no privileged scales on which such perturbations occur, the initial model of  $\delta_\Phi$  is called *scale-free*. Due to that, at any scale  $R$  fixed, this phenomenon generated primordial density perturbations  $\delta_\rho$  through the relationship  $\delta_\Phi \propto \frac{G\delta_M}{R} \propto \delta_\rho GR^2$ , consisting in small fluctuations in the density field of the primordial fluid (see [Mukhanov 2005](#), for a detailed description).

The effects of these perturbations can be observed in the temperature fluctuations of the CMB maps and the discovery of these anisotropies (Smoot et al. 1992) provided a crucial observational confirmation of the HBB model. Under the adiabatic condition (1.22), we can express  $\delta T/T \approx \delta\rho/\rho \approx 10^{-5}$ , where  $T = T_{0,\text{CMB}}$ . As of today ( $z = 0$ ), the measured density contrast within virialized cosmic structures ranges from 100 to 1000, while at  $z \approx 1100$  it was less than approximately seven orders of magnitude. The goal of Cosmology is to provide an explanation for this significant growth. In this section we provide the theoretical basis for the study of the density fluctuations.

The *point density contrast field*,  $\delta(\mathbf{x})$ , is a dimensionless quantity defined as:<sup>15</sup>

$$\delta(\mathbf{x}) \equiv \frac{\delta\rho}{\rho} = \frac{\rho(\mathbf{x}) - \bar{\rho}}{\bar{\rho}}, \quad (1.42)$$

where  $\rho(\mathbf{x})$  is the point density field, and  $\bar{\rho}$  is the mean density of the background Universe. Since density is always positive,  $-1 \leq \delta < +\infty$ , encompassing both overdense and underdense regions.

As we mentioned, the seeds of density perturbations are believed to be produced in the final phases of the inflationary era, through a spiraling motion of the inflaton in phase space, which is a stochastic process. This implies that the generated metric fluctuations are random, meaning they exhibit a lack of phase correlation in Fourier space<sup>16</sup>. Therefore, because they are generated by stochastic processes, is not possible to describe the density contrast field deterministically. Alternatively, it is possible to describe the condensed statistical characteristics of the field<sup>17</sup>. To have a precise measure of a statistic, it is necessary to probe a large enough sample that is reproducible. This is not the case in our Universe, for which the sample consists of only one element, itself, that is the only possible realization. Here the space-like *Ergodic hypothesis* (EH) plays a fundamental role, stating that the average between multiple Universes equals the spatial average between sufficiently large and non-overlapping sub-volumes of a single Universe. The EH is based on the idea that sufficiently large and separated regions of the Universe are statistically independent of each other and are therefore equivalent to different statistical realizations of the same stochastic process, and in case of Gaussian distribution the it becomes a provable theorem. In this sense, the EH combined with CP is called the *Fair Simple Principle* (Coles & Lucchin 2002).

In Fourier space, when random phases are present, we can assume that the distribution of probability  $P(\delta)$  of having a given  $\delta$ , approximatly grows as a Gaussian<sup>18</sup> due to the homogeneity and isotropy of the Universe. So, given the non-negative definition of density, the real initial distribution of  $P(\delta)$  is considered a truncated Gaussian centered around the mean value of  $\delta$ . This implies that all odd moments are null, and all even moments are powers of the variance of the distribution (second momentum). Therefore,  $P(\delta)$  is a 3D Gaussian field and its variance is defined as  $\sigma^2 \equiv \langle |\delta|^2 \rangle - \langle \delta \rangle^2 = \langle |\delta|^2 \rangle$ , where the last equality follows from the null mean (momentum 0).

At this point, we expect that density fluctuations will be present across a range of mass and spatial scales, implying that the eventual collapsed structures will be influenced by the evolution of various perturbations spanning different scales. To perform a statistical analysis of the fluctuations and accurately depict the growth of structures, deriving from the

<sup>15</sup>In the notation used here, elements in bold represent vectors

<sup>16</sup>It is an abstract space into which the Fourier transform maps a function, consisting of the amplitude and phase of the sine function at various frequencies (or wavelengths) that sum to produce the same shape.

<sup>17</sup>It should be noted that the probabilistic approach does not predict the formation of a structure but provides the probability of similar structures occurring.

<sup>18</sup>This assumption is consistent with the CP. It means that if it could be measured the value of  $\delta$  at different positions, the probability  $P(\delta)$  at a given point would follow a Gaussian distribution.

result of linear theory (Sect. 1.5.2), it is convenient to express the density perturbations as a combination of plane waves, each evolving independently of the others. In order to describe properly  $\sigma^2$ , working in either real space and Fourier space, we can deconstruct  $\delta(\mathbf{x})$  into infinite plane waves, each with an amplitude  $\hat{\delta}(\mathbf{k})$  and a wave-vector  $\mathbf{k}$ , and reconstruct the field by summing up to infinity. Given the real-space density contrast field  $\delta(\mathbf{x})$ , its spatial Fourier transform<sup>19</sup> (FT) is given by:

$$\hat{\delta}(\mathbf{k}) = \frac{1}{(2\pi)^3} \int \delta(\mathbf{x}) e^{-i\mathbf{k}\cdot\mathbf{x}} d^3\mathbf{x}, \quad (1.43)$$

where  $\mathbf{k} = 2\pi/\mathbf{x}$  is the *wave-vector*. It is a complex field with dimensions of a volume. Following the Fourier inversion theorem<sup>20</sup> its inverse Fourier transform (FT<sup>-1</sup>) is:

$$\delta(\mathbf{x}) = \frac{1}{(2\pi)^3} \int \hat{\delta}(\mathbf{k}) e^{i\mathbf{k}\cdot\mathbf{x}} d^3\mathbf{k}. \quad (1.44)$$

Let us now study the field  $\hat{\delta}(\mathbf{k})$  in the Fourier space defining the *power density spectrum*, which quantifies the contribution of the square amplitude for different Fourier modes (Coles & Lucchin 2002):

$$\langle \hat{\delta}(\mathbf{k}) \hat{\delta}(\mathbf{k}') \rangle \equiv (2\pi)^3 P(k) \delta_D^{(3)}(\mathbf{k} + \mathbf{k}') \xrightarrow{\mathbf{k}' = -\mathbf{k}} \langle |\hat{\delta}(\mathbf{k})|^2 \rangle \propto P(k), \quad (1.45)$$

where  $\delta_D^{(3)}(\mathbf{k}) = \frac{1}{(2\pi)^3} \int e^{i\mathbf{k}\cdot\mathbf{x}} d^3\mathbf{x}$  is the 3D Dirac Delta, the properties of reality ( $\hat{\delta}(-\mathbf{k}) = \hat{\delta}^*(\mathbf{k})$ ) and complex conjugate ( $\hat{\delta}(\mathbf{k}) \hat{\delta}^*(\mathbf{k}) = |\hat{\delta}(\mathbf{k})|^2$ ) have been applied, and the infinite volume of the Universe  $V_\infty = \int d^3\mathbf{x}$  has been used to normalize.  $P(k)$  is a measure of the power of  $k$ -scale fluctuations, where  $k$  is the wave-number of plane waves having wavelength  $\lambda = 2\pi/k$ , and tell us with what density a given wave at a given scale contributes to the field reconstruction of the total density contrast  $\hat{\delta}(\mathbf{k})$ . Actually,  $P(k)$  is a *power density*, since the real *power of fluctuations* is given by  $P(k) d^3k$  that tells us with what power that wave contributes to the reconstruction of  $\hat{\delta}(\mathbf{k})$ . By computing the FT<sup>-1</sup> of  $P(k)$ , we obtain its counterpart in real space, the *two-point correlation function* (2PCF):

$$\xi(r) = \xi(\mathbf{r}) = \frac{1}{(2\pi)^3} \int P(k) e^{i\mathbf{k}\cdot\mathbf{r}} d^3\mathbf{k}. \quad (1.46)$$

It is a double average, over all directions and all positions, and measure how  $\delta(\mathbf{x})$  correlates with itself considering all points at distance  $\mathbf{r}$ . Due to the CP we have also that  $\xi(r) = \xi(\mathbf{r}) = \langle \delta(\mathbf{x}) \delta(\mathbf{x}') \rangle = \xi(|\mathbf{x} - \mathbf{x}'|)$  where  $r$  is the comoving distance between  $\mathbf{x}$  and  $\mathbf{x}'$ . The power spectrum (in Fourier space) or the correlation function (in real space) are formally equivalent, as both describe the same property in two different spaces.

In the present scenario, since the only quantity that defines the field is the variance  $\sigma^2$ , assuming the EH, through the Parseval theorem we can show that the variance  $\sigma^2(\mathbf{k})$  of the point density contrast field  $\hat{\delta}(\mathbf{k})$  in 3D Fourier space can be written in cartesian coordinates as:

$$\sigma^2(\mathbf{k}) = \frac{1}{(2\pi)^3} \int P(k) d^3\mathbf{k}. \quad (1.47)$$

It is the sum of all contributions over all  $\mathbf{k}$ , it is an integrated information over the whole Fourier space of  $P(k)$ . From the physical point of view it is the total power of the density

<sup>19</sup>It is an operator that transforms a function into another function through integration.

<sup>20</sup>States that, for various types of functions, it is possible to reconstruct a function from its Fourier transform. This theorem suggests that if we have complete information about the frequency and phase of a wave, we can accurately reconstruct the original wave.

contrast field.

To compute  $\sigma^2$ , it would be necessary to evaluate the density in each point of the space, which is practically unfeasible to reconstruct the entire density field. A practical and convenient method involves representing the fluctuation field by "filtering" on some resolution scale  $R$ , rather than using a punctual variance. Using this approach, we can recover the density fluctuation from a discrete distribution of observable tracers. The density fluctuation from a discrete distribution of tracers can be expressed as:

$$\delta_M = \frac{M - \langle M \rangle}{\langle M \rangle}, \quad (1.48)$$

where  $\langle M \rangle$  is the mean mass present inside a spherical volume of radius  $R$ .

The mass variance, denoted by  $\sigma_M^2$ , is a measure of the convolution of the point density with a window function  $W(\mathbf{x}, R)$  of radius  $R$ :

$$\delta_M(\mathbf{x}) = \frac{\delta M}{M} = \delta(\mathbf{x}) \otimes W(\mathbf{x}, R), \quad (1.49)$$

Utilizing the convolution theorem and considering the limit as  $V_u \rightarrow \infty$ , the mass variance can be expressed as:

$$\sigma_M^2 = \frac{1}{(2\pi)^3} \int P(k) \hat{W}^2(\mathbf{k}, R) d^3\mathbf{k}. \quad (1.50)$$

where  $\hat{W}(\mathbf{k}, R)$  is the FT of the window function and is a function of  $R$  (and thus of  $M$ ). This quantity is related to the typical amplitude of a density fluctuation on a scale  $R$ . Furthermore, the mass variance varies with the radius over which it is filtered:

- $\sigma_M^2 \rightarrow \sigma^2$  for  $R \rightarrow 0$ , because the window function is not filtering;
- $\sigma_M^2 \equiv \delta^2 \rightarrow 0$  for  $R \rightarrow \infty$ , because the window function is filtering the entire Universe recovering the mean density.

Since the normalization of the power spectrum  $A_s$  is not determined by inflation theory, an alternative approach to parameterize it is setting the value of the mass variance computed with a filtering scale of  $R = 8h^{-1}\text{Mpc}$  at the present time  $z = 0$ . It can be shown that it is:

$$\sigma_8^2 = \frac{1}{(2\pi)^2} \int_0^\infty k^2 P(k) |\hat{W}^2(\mathbf{k}, R = 8h^{-1}\text{Mpc})| dk. \quad (1.51)$$

The square root of  $\sigma_8^2$  in spherical coordinates represents the mass fluctuation spheres with a radius of  $8h^{-1}\text{Mpc}$  and serves as a free parameter crucial for predicting the characteristics of the low-redshift Universe.

Now that we have the theoretical tools, we can discuss the behaviors of the primordial power spectra  $P(k, t = t_i)$  for  $\delta_\Phi$  and  $\delta_\rho$ . As mentioned earlier, upon exiting inflation, they are scale-free. To reproduce this property in the shape of the power spectrum for  $\delta_\rho$ , which is our observable in the CMB (Hinshaw et al. 2013), a widely used parameterization following various versions of inflationary theory is expressed as a power-law  $P_{i,\rho}(k) = A_s k^{n_s}$ , where  $A_s$  is the amplitude of fluctuations, and  $n_s$  is the spectral index. This assumption is made because the power-law is the simplest functional form that allows scale-free behavior, and if  $A_s$  is not constrained by inflationary models and must be constrained with observations, on the contrary  $n_s$  is (Longair 2008; Ryden 2016). Indeed, knowing that during inflation metric fluctuations are produced by a stochastic process,  $P_{i,\Phi}(k)$  must be flat<sup>21</sup>, and this,

<sup>21</sup>It is also called *white noise* because the signal amplitude is the same at all scales  $\mathbf{k}$

given the relationship between metric and density fluctuations, implies that  $n_s \simeq 1$  and  $P_{i,\Phi}(k) = A_\Phi k^{n_s-1}$ .  $P_{i,\rho}(k) = A_s k^{n_s}$  with  $n_s \simeq 1$  is called the *Harrison-Zel'dovich power spectrum*, and this result is consistent with current CMB observations (Planck Collaboration et al. 2020a).

It is important to note that, although the Zel'dovich power spectrum is scale-free and thus exhibits self-similar scales with a fixed slope of 1, this positive slope favors higher power for perturbations on small scales (high  $\mathbf{k}$ ) compared to those on large scales (low  $\mathbf{k}$ )<sup>22</sup> (Coles & Lucchin 2002). Since the cosmological horizon  $R_H(t)$  is an increasing function of time, the first scales to enter it are the small ones, so they are those scales that experience the stagnation effect first (see Sect. 1.5.2). At equivalence this effect ends, which makes this cosmic moment extremely important because it is the moment after which perturbations can grow freely.

The primordial density fluctuations in the density field are present at the time  $t_i = t_{f,\text{infl}}$  with an amplitude  $\delta_i = \delta(\mathbf{x}, t_i)$ . To understand how they evolve for  $t > t_i$ , we need to examine on which scales, from a physical perspective, the total action is approximable by gravitational interaction alone; otherwise, we will not have perturbation growth. Thus, we introduce a function called the *growth factor* that depends only on time and not on scales, aiming at reproducing the scale-free property of the Zel'dovich power spectrum. At time  $t > t_i$ , we will have:

$$P(k, t) = \delta_i^2 \delta_+^2(t) \propto P_i \delta_+^2(t), \quad (1.52)$$

where the dependence on cosmology ( $\propto z, \propto a$ ) is encapsulated in the growth factor. We will provide an overview on the analytical description of the growth of perturbations in linear regime, which is a reliable approximation for describing a remarkable part of the evolution of cosmic structures. Subsequently, we will explore the nonlinear regime and the methodologies employed to describe it.

## 1.5.2 Linear evolution

Through the study of the growth factor, parameter that quantifies the growth rate of these perturbations, we can infer the expansion rate of the entire Universe. As the expansion intensifies, gravitational collapse becomes increasingly inhibited. The purpose of the *Perturbative Theory* is to elucidate the rate at which initial density perturbations must grow to replicate the observed inhomogeneities today. This model is applicable to non-relativistic matter and on scales that do not surpass the cosmological horizon.  $R_H$  separates the Universe in two different regions (Weinberg 2008):

- **Scales  $r > R_H$**  : Gravity is the sole force at play, and the growth of perturbations needs to be addressed with relativistic theory. On these scales, we can neglect radiative processes so density fluctuations can grow indefinitely. To derive the rate of their growth, density fluctuations can be treated as small closed universes evolving in a background mono-component flat Universe. From the second Friedmann equation we obtain the following relations:

$$H_B^2 = \frac{8\pi}{3} G \rho_B, \quad H_P^2 = \frac{8\pi}{3} G \rho_P - \frac{c^2}{a^2}, \quad (1.53)$$

where the subscripts B and P refer to the background and the perturbed Universe, respectively. Since the perturbed universe is entirely contained within the background

---

<sup>22</sup>This means that density perturbations are more inhomogeneous on small scales than they are on large scales

universe, their respective scale factors are initially the same. We can enforce the equivalence of their Hubble parameters, leading to:

$$\delta = \frac{\rho_P - \rho_B}{\rho_B} = \frac{3c^2}{8\pi G} \frac{1}{\rho_B a^2} \propto \rho_B^{-1} a^{-2}. \quad (1.54)$$

From Sect. 1.3.2 we know the evolution of the background perturbation follows that of the dominant component at a particular epoch. Thus, we can categorize the behavior of the density perturbation into two regimes based on the matter-radiation equivalence time. We denote  $z_{\text{eq}}$  as the redshift of equivalence, representing the epoch when the density of matter and radiation fluids achieved equality. Consequently, for  $z > z_{\text{eq}}$ , radiation dominates, and  $\rho_b \propto a^{-4}$ . Conversely, for  $z < z_{\text{eq}}$ , matter dominates, leading to  $\rho_b \propto a^{-3}$ . The other components follow the behavior of the dominant component.

$$\begin{aligned} \rho_B \propto a^{-4} &\rightarrow \delta = \delta_r \propto a^2 \propto t && \text{for } z > z_{\text{eq}}, \\ \rho_B \propto a^{-3} &\rightarrow \delta = \delta_m \propto a \propto t^{2/3} && \text{for } z < z_{\text{eq}}. \end{aligned} \quad (1.55)$$

So, as mentioned, density perturbations on scales larger than the cosmological horizon are bound to undergo continuous growth.

- **Scales  $r < R_H$** : Microphysics, such hydrodynamical and dynamical processes, becomes significant, and different components exhibit distinct behaviors. On these scales, the *Jeans theory* offers a dependable description of these phenomena in the linear regime. It summarizes that the density fluctuations are the original responsible for the formation and evolution of virialized large-scale structures, that arise as consequences of gravitational instabilities. The investigation will be thoroughly covered in the next subsection. Specifically, we will explore the dynamics and evolution of these perturbations by applying the Jeans theory to a collisional and self-gravitating fluid within an expanding background.

### Jeans theory

Assuming a background with homogeneity and isotropy, composed of a fluid with matter density  $\rho(\mathbf{x}, t)$  in an expanding universe, the fundamental fluid equations in the Newtonian approximation are given by:

$$\frac{\partial \rho}{\partial t} + \nabla \cdot (\rho \mathbf{v}) = 0, \quad [\text{Continuity Equation}] \quad (1.56)$$

$$\frac{\partial \mathbf{v}}{\partial t} + (\mathbf{v} \cdot \nabla) \mathbf{v} = -\frac{1}{\rho} \nabla p - \nabla \Phi, \quad [\text{Euler Equation}] \quad (1.57)$$

$$\nabla^2 \Phi = 4\pi G \rho, \quad [\text{Poisson Equation}] \quad (1.58)$$

$$p = p(S, \rho) = p(\rho), \quad [\text{Equation of State}] \quad (1.59)$$

$$\frac{dS}{dt} = 0. \quad [\text{Adiabatic Condition}] \quad (1.60)$$

Here,  $\mathbf{v}$  is the velocity vector,  $\Phi$  is the gravitational potential,  $S$  is entropy, and  $p$  is pressure. The latter, Eq. (1.60), excludes dissipative terms like viscosity or thermal conduction and is supported by observational evidence, as CMB experiments have indicated that primordial fluctuations are in line with being adiabatic. In particular, adiabatic perturbations influence all particle species in a way that preserves the relative ratios in their number densities. Consequently,  $p$  can be expressed in terms of  $\rho$  only, thus we can consider only three variables, namely  $\rho$ ,  $\mathbf{v}$ , and  $\Phi$  (Jeans 1902; Weinberg 1972).

Now we introduce small perturbations, namely  $\delta\rho \ll 1$ ,  $\delta\mathbf{v} \ll 1$ , and  $\delta\phi \ll 1$ , so that the linear regime is valid. Consequently, we have the following perturbed quantities:

$$\rho = \rho_B + \delta\rho, \quad (1.61)$$

$$\phi = \Phi_B + \delta\Phi, \quad (1.62)$$

$$\mathbf{v} = \mathbf{v}_B + \delta\mathbf{v} = H\mathbf{x} + \mathbf{v}_{\text{pec}}, \quad (1.63)$$

where ‘‘B’’ refers to background quantities,  $\mathbf{x}$  is the position and  $H$  is the Hubble parameter. Notably, the velocity perturbation in Eq. (1.63),  $\delta\mathbf{v}$ , corresponds to the peculiar velocity,  $\mathbf{v}_{\text{pec}}$ . We remark that Eq. (1.63) reduces to the Hubble-Lemaître Law for an unperturbed fluid, for which  $\mathbf{v}_{\text{pec}} = 0$ .

From Eq. (1.42), considering small perturbations ( $\delta \ll 1$ ), we linearize the set of fundamental imperturbated equations to obtain a hydrodynamic system for the linearized density fluctuations. Neglecting squared terms and other mixed terms and looking for general solutions in the form of plane-parallel waves, solutions are found in terms of Fourier modes, with the generic form expressed as:

$$f(r, t) = f_k(t) e^{i\mathbf{k}r}, \quad (1.64)$$

where the general expression  $f(r, t)$  represents  $\delta\rho$ ,  $\delta\phi$ , or  $\delta\mathbf{v}$ ,  $r$  is the comoving spatial coordinate,  $k = |\mathbf{k}|$  is the absolute value of the wavevector  $\mathbf{k}$ , and  $f_k(t)$  is the amplitude of the Fourier mode also accounting for the expansion of the universe.

Solutions for the density contrast in Fourier space is given by the differential equation named *dispersion relation*:

$$\ddot{\delta}_{\mathbf{k}} + 2H(t)\dot{\delta}_{\mathbf{k}} + (k^2c_s^2 - 4\pi G\rho_B)\delta_{\mathbf{k}} = 0, \quad (1.65)$$

where  $\delta_{\mathbf{k}} \equiv \delta\mathbf{k}$  defined in Eq. (1.43), and  $c_s = \sqrt{\partial p/\partial\rho}$  is the sound speed. In addition,  $2(\dot{a}/a)\dot{\delta}_{\mathbf{k}}$  is the term that accounts for the expansion of the Universe and depends on the cosmological model via the Hubble parameter  $H(t) = \dot{a}/a$  and its  $z$ -dependence in Eq. (1.34), while the term  $k^2c_s^2\delta_{\mathbf{k}}$  accounts for the characteristic velocity field of the fluid under investigation. This equation describes how the field of fluctuations evolves over time in an expanding Universe and we can recognise the equation governing the motion of a damped harmonic oscillator (Jeans 1902).

The solutions of Eq. (1.65) can be discriminated depending on the wavelength  $\lambda = 2\pi/k$  relative to the fundamental scale defined as *Jeans length*:

$$\lambda_J \propto c_s \left( \frac{\pi}{G\rho_B} \right)^{1/2}, \quad (1.66)$$

expressed in physical units. Now we can study the behavior of plane waves in relation to  $\lambda_J$ :

- For  $\lambda < \lambda_J$ , the perturbation propagates through the fluid as a sound wave with constant amplitude and phase velocity  $c_{ph} = \omega/k$ , where  $\omega(k) = \sqrt{k^2c_s^2 - 4\pi G\rho_B}$ . All fluid components oscillate, signifying that perturbations are carried as waves without exhibiting growth or dissipate. This implies that when the wavelength associated with a perturbation is in this range, the perturbation can not lead to gravitational instability and to the consequent collapse of the structure.
- For  $\lambda_J < \lambda < \lambda_H$ , the dispersion relation has growing and decaying mode solutions  $\delta(\mathbf{x}, t) = A(\mathbf{x})\delta_+(t) + B(\mathbf{x})\delta_-(t)$ , where  $A$  and  $B$  are functions of comoving coordinates. The terms  $\delta_+$  and  $\delta_-$  correspond to time-dependent growing and decaying modes, respectively. The growing solution is of interest since the decaying solution does not lead

to gravitational instability. For a generic universe, the growing solution has an integral form:

$$\delta_+(z) = H(z) \int_z^\infty \frac{dz' (1+z')}{H^3(z')}. \quad (1.67)$$

Although it lacks an analytical solution, a parametric solution to approximate its trend is given by:

$$f \equiv \frac{d \log \delta_+}{d \log a} \simeq \Omega_m^\gamma + \frac{\Omega_\Lambda}{70} \left( 1 + \frac{1}{2} \Omega_m \right), \quad (1.68)$$

known as the *linear growth rate*. The logarithmic derivative of the growth factor determines the perturbation's evolution over time, providing information about the Universe's expansion history. Therefore, this factor determines the amplitude of peculiar velocity flows and redshift distortions (Peebles 1980). The exponent  $\gamma$  is predicted to be approximately 0.545 according to GR (Coles & Lucchin 2002). This linear growth rate serves as a powerful method to search for deviations from GR on cosmological scales (see Moresco & Marulli 2017b, for further details).

In the subsequent discussion, we will provide a brief overview of the behaviors of fluctuations both before and after the epoch of matter-radiation equivalence. We consider a cosmological background dominated by two distinct components: the radiation component before equivalence and the matter component in the post-equivalence epoch. From Eq. (1.68), it can be demonstrated that the growth outside and within the horizon is slower for  $\Omega < 1$  compared to a flat Universe, while for  $\Omega > 1$ , it is faster. The following solutions are applicable when  $\Omega = 1$  and  $\lambda_J < \lambda < \lambda_H$ .

- **Before Equivalence ( $t < t_{eq}$ ):**

- *Radiation Density Fluctuations*: they do not undergo growth and propagate as waves. Quickly canceled due to a Jeans scale larger than the cosmic horizon. They have a very high speed of sound  $c_s = 0.58c$  and this implies a very high radiative pressure.
- *Baryonic Fluctuations*: they are still coupled to radiation by Compton scattering. They propagate as waves and are eventually dissipated.
- *DM Fluctuations*: DM decoupled from the cosmological fluid. Due to the dominance of the radiation component,  $\lambda_{DM}$  fluctuations remain frozen (*stagnation effect*) because they can grow at most by a factor of 5/2.

- **After Equivalence ( $t > t_{eq}$ ):**

- *Radiation Density Fluctuations*: Continue to oscillate without substantial growth. Primarily due to their high sound speed.
- *Baryonic Matter Fluctuations*: Baryon-photon fluid oscillates in potential wells created by already collapsed DM halos. After its decoupling at  $z_{dec} \approx 1000$ , baryonic matter is free to collapse into DM halos. This effect is called *baryon catch-up* and the perturbations grow as:  $\delta_b = \delta_{DM}(1 - a_{dec}/a)$ .
- *Dark Matter Fluctuations*: their scales are still larger than the Jeans scale and grow as  $\delta_{DM} \propto a$ . Density perturbations entering the horizon after  $t_{eq}$  continue to undergo growth. Only for  $t > t_{dec}$ , as the energy contribution of  $\Lambda$  increases,  $\delta_{DM}$  can have trends that deviate from  $\propto a(t)$  due to the geometry of the Universe.

## Linear effects on the Power Spectrum

Density perturbations entering the cosmological horizon before the radiation-matter equivalence,  $t_h < t < t_{\text{eq}}$ , experience damping due to an effect known as stagnation or the *Mészáros effect* (see Meszaros 1974). This effect arises from the fact that the Hubble drag term during the radiation-dominated era is larger than during the matter-dominated era. By comparing the free-fall time ( $\tau_{\text{ff}} \propto 1/\sqrt{G\rho_m}$ ), which represents the characteristic time for a perturbation to collapse under its gravitational force, and the Hubble time, we find:

$$\frac{\tau_H}{\tau_{\text{ff}}} \begin{cases} \propto \left(\frac{\rho_m}{\rho_{\text{rad}}}\right)^{1/2} \gg 1 & \text{for } t < t_{\text{eq}} \\ \sim 1 & \text{for } t > t_{\text{eq}} \end{cases}. \quad (1.69)$$

Since for  $t < t_{\text{eq}}$  the free-fall time is larger than the expansion time, density perturbations once entered the horizon cannot grow, affecting the primordial shape of the perturbation power spectrum.

As the cosmological horizon expands over time (see definition in Eq. (1.37)), larger perturbations will enter the cosmological horizon at later times, experiencing less stagnation (or zero stagnation if they do not enter the horizon before  $t_{\text{eq}}$ ). However, perturbations on scales larger than the horizon, with  $\lambda > \lambda_H$  (where  $\lambda_H \equiv R_H$ ), continue to grow at the same rate seen in Eq. (1.55), independently of the scale or wavenumber. Consequently, the power spectrum at the equivalence moment has a peak at  $k_{H,\text{eq}}$ , the wavenumber associated with the cosmological horizon at the equivalence time. This value depends mainly on  $\Omega_m h^2$  and  $\Omega_r h^2$ , corresponding to the matter and radiation densities and the Hubble parameter.

Technically, the shape of the power spectrum  $P(k)$  at the equivalence time can be reproduced by defining a transfer function,  $T(k)$ . This function represents the fraction of the primordial power spectrum  $P(k, t_i)$  unaffected by microphysical effects inside the horizon. For an initial cosmological time  $t_i$ , the transfer function is defined as follows:

$$P(k, t_{\text{eq}}) = P(k, t_i) T^2(k). \quad (1.70)$$

The shape of the observed power spectrum  $P(k)$  provides powerful constraints for cosmology, depending on the amount and nature of the matter in the Universe. Additionally, the nature of DM plays a significant role. In the early Universe, a diverse set of particles constantly interacted, depending on temperature, so particles are considered "coupled," maintaining thermodynamic equilibrium. Photons, following a blackbody distribution, share their temperature and distribution with any species X directly or indirectly coupled to them, resulting in X being in "equilibrium" with the rest of the Universe. As the Universe expands, temperature drops as  $T \approx 1/a$  and particle interactions become rare, taking more time than the age of the Universe to occur. From this point, corresponding to the scale factor  $a_{\text{dec}}$ , the species X is considered "decoupled" (Padmanabhan 1993). The rest mass of particles in relation to the Universe's temperature is crucial in this framework. The distinction between the relativistic regime ( $k_B T \gtrsim m_X c^2$ ) and the non-relativistic one ( $k_B T < m_X c^2$ ) is essential, and the transition between them is denoted by  $a_{\text{NR}}$  (Coles & Lucchin 2002).

The concept of *free-streaming* refers to the diffusion process where non-collisional DM particles flow from overdense to underdense regions, canceling perturbations. The effectiveness depends on the free-streaming distance covered in a given time interval, denoted by:

$$\lambda_{\text{FS}} = \int_0^t \frac{a(t)}{v(t)} dt, \quad (1.71)$$

where  $v(t)$  is the velocity as function of time. Similarly, a free-streaming mass is defined as  $M_{\text{FS}} = \frac{4\pi}{3}\rho_{\text{DM}}\lambda_{\text{FS}}$ . If a DM perturbation has a size smaller than  $\lambda_{\text{FS}}$  or a mass lower than  $M_{\text{FS}}$ , it cannot survive, as particles, on average, travel distances greater than its size.

As we mentioned in Sec. 1.4, two types of DM particles are defined based on their nature at their decoupling from radiation: HDM particles, still relativistic at decoupling, and CDM particles, non-relativistic before decoupling. From their definition, CDM particles are expected to be more massive than HDM particles. For a matter component consisting entirely of HDM particles, the matter power spectrum falls sharply to zero to the right of the peak, as shown in Figure 1.3. In CDM models, all perturbations, including the smallest ones, survive the dissipative process and eventually collapse, leading to a bottom-up scenario of structure formation (Bullock & Boylan-Kolchin 2017). On the other hand, HDM particles decouple while still relativistic, resulting in a matter power spectrum that sharply falls off to zero beyond the peak. Since relativistic particles have a free-streaming distance comparable to the cosmological horizon, the HDM model predicts the formation of structures with  $M \geq 10^{15-16} M_{\odot}$ . This leads to a top-down scenario where galaxy clusters form first, followed by fragmentation into galaxies (Longair 2008). This difference in the observational forecast of the two models is an excellent way to "falsify"<sup>23</sup> the theory of structure formation through comparison with current observations. Modern observations support a scenario where the Universe's main matter component is primarily cold, that implies a hierarchical structure formation model (Tegmark et al. 2004). For the CDM scenario, the transfer function is given by:

$$T(k) = \begin{cases} 1 & \text{for } k < k_{H,\text{eq}} \\ \propto k^{-2} & \text{for } k > k_{H,\text{eq}} \end{cases}. \quad (1.72)$$

This function acts as a filter that smoothens larger wavenumbers and predicts a scale of  $R_{H,\text{eq}} \simeq 16(\Omega_{0,m}h^2)^{-1}\text{Mpc}$ . From the mapping of perturbations on small scales (large  $\mathbf{k}$ ), it is possible to discriminate on which scales there is a suppression of the observed power spectrum  $P_{\text{obs}}(k)k^3$  compared to that predicted by the CDM component alone  $P_{\text{CDM}}(k)k^3$ . This allows us to understand what fraction of all dark matter is warm. Currently, this is the most effective method for constraining the mass of neutrinos.

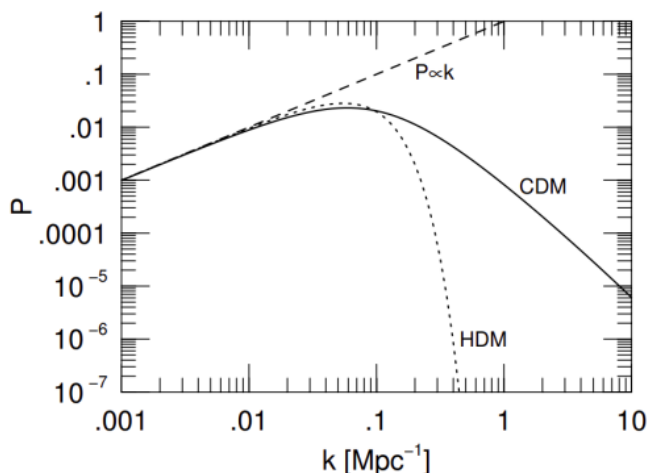


**Figure 1.3:** The power spectrum at the equivalence  $t = t_{\text{eq}}$  for a matter component entirely formed by CDM (solid line) or HDM (dotted line). It is also represented the primordial Zel'dovich power spectrum (dashed line), having a spectral index  $n_s = 1$ . Credits to Ryden (2016).

<sup>23</sup>Here falsify is meant in the sense of confirming or rejecting a model, both results being a scientific progress.

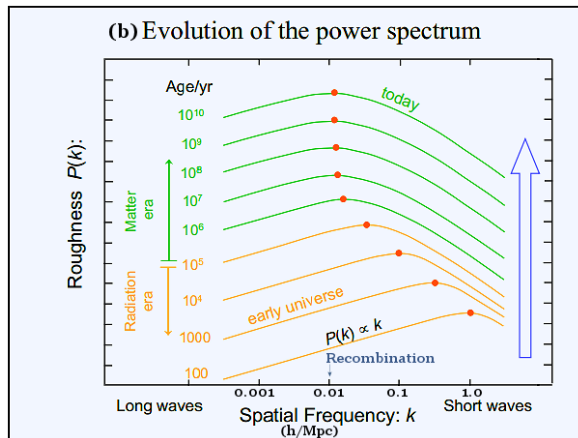


**Figure 1.4:** Evolution of the power spectrum. Evolution of the power spectrum. It shows that in the primordial universe the curve  $P(k)$  is a straight line extended to a high value of  $\mathbf{k}$  (shorter  $\lambda$ ) and then evolves by shifting the maximum to a lower value of  $\mathbf{k}$  (longer  $\lambda$ ). Credits to: <https://universe-review.ca/R05-04-powerspectrum.htm>

Therefore, after studying the trends, we can state that at  $t = t_{eq}$  the fluctuations must be smaller than those observed in the CMB ( $\simeq 10^{-5}$ ) and, therefore, even more so in the linear regime. This implies that after equivalence,  $P(k)$  will shift upward parallel to itself in a self-similar growth, continuing to grow with a factor  $\propto a \propto t^{2/3}$  as calculated in Eq. (1.55) and shown in Figure 1.4. This happens until the fluctuations reach a value  $\delta \rightarrow 1$ . From this point onwards, they enter the non-linear regime, and the linear approximation discussed in this subsection is no longer valid. Also, in Figure 1.4, it can be observed that small scales reach the non-linear regime first. In other words, the first structures to initiate collapse will be those of small mass ( $R \rightarrow M$ ) (Coles & Lucchin 2002).

### 1.5.3 Nonlinear evolution

When  $\delta \sim 1$  the linear regime breaks down and the weakly-nonlinear regime takes effect. Describing with the small-perturbations approximation the formation of structures formed due to gravitational instabilities over cosmological history, is no longer applicable. This because, in this first nonlinear stage, the distribution function of fluctuations  $P(\delta)$  starts to deviate from its Gaussian shape.

The transition from the linear to nonlinear regime in density perturbations is explained by the *Zel'dovich approximation* (Zel'dovich 1970). Specifically, in an expanding Universe, this approximation connects the comoving coordinates  $\mathbf{r} = \mathbf{x}/a(t)$ , where  $a(t)$  is the expansion factor at time  $t$ , to the Lagrangian coordinates  $\mathbf{q}$  as  $t \rightarrow 0$  through the relation:

$$\mathbf{r}(\mathbf{q}, t) = \mathbf{q} + \delta_+(t)\mathbf{s}(\mathbf{q}). \quad (1.73)$$

The term  $\delta_+(t)\mathbf{s}(\mathbf{q})$  describes the perturbation evolution, with  $\mathbf{s}(\mathbf{q})$  called *initial displacement field* that is determined by the initial density perturbations. Here  $\delta_+(t)$  is the linear density fluctuation growth rate<sup>24</sup> in the expanding universe. The ansatz is that initial density perturbations are described by the gradient of a potential vector field (i.e., an initial force),  $\mathbf{s}(\mathbf{q})$  is a potential vector field  $\Psi$ , and so can be expressed as:

$$\mathbf{s}(\mathbf{q}) \equiv \Psi(\mathbf{q}) = -\nabla_{\mathbf{q}}\Phi(\mathbf{q}). \quad (1.74)$$

<sup>24</sup>Often indicated with the notation  $D(z)$ .

In this way particles do not experience additional interactions at later times, implying they can cross each other without deviating from their motion. The linear Poisson equation relates the density contrast value to the gravitational potential through the equation:

$$\delta = -\delta_+ \nabla^2 \Phi. \quad (1.75)$$

Consequently, the divergence of the linear Zel'dovich displacement field can be linked to the density contrast (Falck et al. 2012):

$$\nabla \cdot \Psi = -\delta. \quad (1.76)$$

This relation forms the basis for the reconstruction of the density field.

Then, when  $\delta \sim 1$  and the strongly-nonlinear regime occurs, it is essential to consider that the evolution of the baryonic component differs from that of DM. Baryons are influenced by hydrodynamical effects, such as star formation, SNe explosions, and feedback from active galactic nuclei (AGN). All these phenomena complicate the description of the entire scenario with a comprehensive theoretical framework.

While some approximate analytical models have been proposed like the *Spherical evolution* to describe this phase, N-body simulations are generally relied upon to accurately reproduce the growth of nonlinear perturbations.

### Spherical approximation

While numerical simulations are crucial for a detailed study of the nonlinear growth of cosmic structures, we can explore the evolution of perturbations in the nonlinear regime by making certain simplifying. Specifically, the analytical model presented here, known as the *spherical evolution model* (Gunn & Gott 1972), is sufficiently accurate to depict the isolated formation of spherical collapsed overdensities (i.e., dark matter halos) and underdensities (i.e., cosmic voids). Assuming an initially spherical perturbation, whether positive or negative, we can represent it as a closed or open universe, respectively, evolving in a mono-component background Universe, represented by the subscript B in the following equations. The initial time considered is  $t_i > t_{\text{eq}}$ , where  $t_{\text{eq}}$  is the matter-radiation equivalence time. Consequently, we study the evolution of perturbations in the matter-dominated cosmic epoch. Assuming the validity of the CP, each perturbation can be treated as an independent Friedmann Universe until it evolves adiabatically and the only interaction to consider is gravity. In this model, a spherical top-hat perturbation is considered and modeled as a set of concentric shells. As stated in Sheth & van de Weygaert (2004), the evolution of the perturbation depends solely on the total energy embedded in the shell and its peculiar velocity, independently of the radial distribution of the density field inside it.

- **Overdensities:** Let us consider the evolution of an initially overdense shell. For a matter perturbation in an expanding universe, the growing and decaying modes of perturbation scale as  $\delta_+ \propto t^{2/3}$  and  $\delta_- \propto t^{-1}$ , respectively. Hence, the density contrast can be expressed as a combination of these two modes:

$$\delta_i = \delta_+(t_i) \left(\frac{t}{t_i}\right)^{2/3} + \delta_-(t_i) \left(\frac{t}{t_i}\right)^{-1}. \quad (1.77)$$

Assuming a null initial velocity for the perturbations and considering  $t = t_i$ , we can find:

$$\delta_i = \frac{5}{3} \delta_+(t_i). \quad (1.78)$$

Hence 3/5 of the initial perturbation is represented by the growing mode, while the remaining 2/5 decays with time. Considering the density parameter of the perturbation universe,  $\Omega_P$ , described in terms of a closed universe, we find that for a closed Universe it is necessary that  $(1 + \delta_i) > \Omega(t_i)^{-1}$ . For mono-component Universes with  $w = 0$ , we find the threshold for  $\delta(t_i)$  leading to collapse:

$$\delta(t_i) = \frac{3}{5}\delta_i > \frac{1 - \Omega_{0,B}}{(1+z)\Omega_{0,B}}. \quad (1.79)$$

From this equation we can see that for closed or flat background universes the collapse is achieved for any positive value of the initial density contrast, while for open universes the expansion can inhibit the collapse. The expected behavior for an overdense perturbation growing in our Universe involves initial expansion, slower than the Hubble flow, gradual halting until reaching a maximum radius  $r_{\max}$ . After the turn around, the perturbation reverses its motion and decouples from the Hubble flow towards its final collapse. At the turn around ( $t = t_{\max}$ ), the density contrast is:

$$\delta(t_{\max}) \simeq \frac{\rho_P(t_{\max})}{\rho_B(t_{\max})} - 1 = \left(\frac{3\pi}{4}\right)^2 - 1 \simeq 4.6. \quad (1.80)$$

The relation suggests that at the turn around, the collapsing region is already in the nonlinear regime and is nearly 5 times denser than the background universe. The same quantity obtained using linear theory would be:

$$\delta(t_{\max}) = \delta(t_i) \left(\frac{t_{\max}}{t_i}\right)^{2/3} \simeq 1.06. \quad (1.81)$$

After the turn around, the physical scale of the perturbation decreases until  $t = 2t_{\max}$ , time at which the full collapse would be reached, forming a singularity. However, in reality, the matter in the collapsing region eventually virializes. The virialization is reached at  $t_{\text{vir}} = 3t_{\max}$ , at which the size of the perturbation becomes stable, within a virialization radius  $R_{\text{vir}}$ .

Assuming the absence of any mass or energy loss since the turn around, the total energy of the system satisfies the *virial theorem*<sup>25</sup>. From this, considering the potential energy of a self-gravitating sphere of mass  $M$ , the total energy  $E(t_{\text{vir}}) = E(t_{\max})$ , and assuming no mass or energy loss since the turn around, it follows that  $\rho_P(t_{\text{vir}}) = 8\rho_P(t_{\max})$ . Therefore, the density contrast at  $t_{\text{coll}} = 2t_{\max}$  and  $t_{\text{vir}} = 3t_{\max}$  is given by:

$$\begin{aligned} \delta(t_{\text{coll}}) &= \frac{8\rho_P(t_{\max})}{\rho_b(t_{\max})} \left(\frac{t_{\text{coll}}}{t_{\max}}\right)^2 \simeq 180 \\ \delta(t_{\text{vir}}) &= \frac{8\rho_P(t_{\max})}{\rho_b(t_{\max})} \left(\frac{t_{\text{vir}}}{t_{\max}}\right)^2 \simeq 400 \end{aligned}, \quad (1.82)$$

while the same quantities extrapolated from linear theory are:

$$\begin{aligned} \delta(t_{\text{coll}}) &= 1.06 \left(\frac{t_{\text{coll}}}{t_{\max}}\right)^{2/3} \simeq 1.69 \\ \delta(t_{\text{vir}}) &= 1.06 \left(\frac{t_{\text{vir}}}{t_{\max}}\right)^{2/3} \simeq 2.2 \end{aligned}. \quad (1.83)$$

---

<sup>25</sup> $2\mathcal{T} + \mathcal{V} = 0$ , where  $\mathcal{T}$  is the kinetic energy (or internal thermal energy) associated with the motions of particles and  $\mathcal{V}$  is the gravitational potential energy.

Eqs. (1.82), computed for a mono-component model, strongly depend on the cosmological model for the background universe, particularly its matter density parameter, whereas their linearly extrapolated counterparts have weaker dependence (Jenkins et al. 2001; Kitayama & Suto 1996).

- **Underdensities:** The evolution of an underdense spherical region, commonly referred to as a *void*, differs from its overdense counterpart. In this scenario, the net radial acceleration is outward with respect to the sphere's center, directly proportional to the mean density contrast  $\Delta(r, t)$  of the void. The inner shells, being more underdense, experience a stronger outward acceleration than the outer shells. Consider an inverse top-hat spherically symmetric underdense perturbation as concentric shells with radii  $r_i$ . The mass  $M$  within the perturbation radius  $r$  determines the acceleration for each shell in the Newtonian regime:

$$\frac{d^2r}{dt^2} = -\frac{4\pi G}{3}\rho_B(1 + \Delta)r, \quad (1.84)$$

where  $\rho_B$  represents the density of the background universe. At the initial time the mass is given by  $M = \frac{4\pi}{3}\rho_B r_i^3 (1 + \Delta_i)$  and the average value of  $\delta_i$  within  $r_i$  is given by  $\Delta_i = \frac{3}{r_i^3} \int_0^{r_i} \delta_i(r) r^2 dr$ . Eq. (1.84) can be analytically solved for a mono-component Universe, and it is possible to derive the linear initial density deficit:

$$\Delta_i^L(\theta) = -\left(\frac{3}{4}\right)^{2/3} \frac{3}{5} (\sinh \theta - \theta)^{2/3}, \quad (1.85)$$

where  $d\theta$  is the dimensionless conformal time  $d\theta = \frac{r_i}{r} \sqrt{\left|\frac{5}{3}\Delta_i(t)\right|} H_i(t) dt$ .

As matter moves out of the voids, the density asymptotically decreases to  $\delta = -1$ . The phenomenon of *shell-crossing*<sup>26</sup> leads to the accumulation of matter around voids, forming sheets and filaments. The evolution of an underdensity profile results in the formation of a high-density ridge. Starting from the shell-crossing event, the development of the void can be characterized by an outward-moving shell that follows a self-similar pattern (Suto et al. 1984). At the shell-crossing event, the void has a precisely determined excess Hubble expansion rate:

$$H_{sc} = \frac{4}{3} H(t_{sc}), \quad (1.86)$$

where  $H(t_{sc})$  is the Hubble parameter of the background Universe. From this we can see that the low-density environment expands faster than the Hubble flow (Sheth & van de Weygaert 2004). Substituting  $\theta_{sc}$  in Eq. (1.85) we can find that at the shell-crossing event the void has expanded by a factor of  $(1 + \delta_v^{NL})^{-1/3} = 1.697$  in comoving radius<sup>27</sup>, with  $1 + \delta_v^{NL} \simeq 0.205$ . From this we can observe that voids are only nearly nonlinear objects since  $|\Delta_{sc}| \approx 0.795 < 1$ .

In conclusion, during the evolution of spherical voids, expansion occurs, in contrast to the collapse observed for overdensities. Void borders become denser, and the central regions reach lower density contrasts. Icke (1984) demonstrated that voids tend to assume a spherical form, unlike collapsing objects, which tend to evolve into filamentary or sheet-like structures. Moreover, since the expansion of a void can be considered as

<sup>26</sup>As the density diminishes towards the center of a void, the material near the center exhibits a more rapid outward motion compared to the matter near the external boundaries. Shells that were initially in close proximity to the center will eventually overtake the shells located further outward, ultimately surpassing them.

<sup>27</sup>Note that these values are independent of the size of the void.

the time reversal of the collapse of an overdensity, any eventual initial asphericity tends to be mitigated. The latter deduction is fundamental in this Thesis, because of the assumption of sphericity of 2D voids.

## ***N*-body simulations**

As we mentioned above, Cosmology is marked by the non-replicability of the study object due to the unique nature of the Universe. We have shown that it is still possible to do science through the formulation of analytical models based on reasonable assumptions and verifying them through the statistical study of certain properties. In the case of the formation of cosmic structures, the evolution of density perturbations can be approximated as the dynamical evolution of a system of particles, which act as tracers for the total mass distribution. However, especially in the nonlinear regime, the number of particles required to reproduce the complex physics of interactions leading to virialized structures becomes enormous and, therefore, the analytical study becomes impractical. A crucial approach to address this challenge and testing cosmological models involves the use of *N*-body simulations. By definition, an *N*-body simulation is a simulation which can solve the problem of predicting the individual motions of a group of *N* objects interacting with each other.

The primary factor crucial for simulating the development of density perturbations is the gravitational interaction, exerting its dominance on large scales and impacting DM, the dominant matter component of the Universe. Simulations exclusively incorporating gravitational forces are termed *N*-body simulations, while simulations that additionally evolve the baryonic component including other microphysical interactions are referred to as hydrodynamic simulations. After the initial conditions for the matter density field are established based on prediction of inflation theories, we choose the theoretical physical evolution model by setting the cosmological parameters. Finally, the simulation is executed to guide the evolution of the initial system and, subsequently, the resulting outcome can be assessed in comparison to observations.

Thanks to advancements in both technology and computational techniques, we can now make reliable predictions across a vast array of phenomena using simulations that incorporate billions of particles. Despite the remarkable successes in this field of research, significant limitations persist in creating cosmological simulations. Once the number of particles is determined by computational capacity, the spatial resolution of the simulation is entirely dictated by the covered volume. Small volumes enable the study of galaxy formation models that capture physical processes with high resolution in the analyzed portion of the universe. On the other hand, large volumes facilitate a more detailed examination of the LSS, allowing for statistical treatment of the universe's properties. Simulations characterized by both high resolution and large volume remain challenging to achieve at present.

The framework all the numerical simulations are based on is the Newtonian approximation in which gravity is driven by the mass continuity equations, Euler equation conservation of momentum and the Poisson equation. *N*-body codes numerically solve the following system of differential equations by discretizing the problem into *N* particles:

$$\begin{cases} \mathbf{F}_i = GM_i \sum_{i \neq j} \frac{M_j}{r_{ij}^2} \hat{\mathbf{r}}_{ij} \\ \ddot{\mathbf{x}}_i = \frac{d^2 \mathbf{x}_i}{dt^2} = \frac{d\mathbf{v}_i}{dt} = \frac{\mathbf{F}_i}{M_i} , \\ \dot{\mathbf{x}}_i = \frac{d\mathbf{x}_i}{dt} = \mathbf{v}_i \end{cases} \quad (1.87)$$

where, for each  $i$ -th particle,  $\mathbf{F}_i$  is the gravitational force,  $M_i$  is the mass,  $\mathbf{x}_i$  is the comoving coordinates of the position, and  $\mathbf{v}_i$  the velocity components. Then  $r_{ij}$  is the comoving distance between the  $i$ -th and  $j$ -th particles, and  $\hat{r}_{ij}$  is the related versor. Given this system of equations, the Euler equation of motion can be re-written as:

$$\frac{d\mathbf{x}_i}{dt} + 2\frac{\dot{a}}{a}\mathbf{v}_i = -\frac{1}{a^2}\nabla\Phi = -\frac{G}{a^3}\sum_{i,j\neq i}m_j\frac{\mathbf{x}_i - \mathbf{x}_j}{|\mathbf{x}_i - \mathbf{x}_j|^3} = \frac{\mathbf{F}_i}{a^3}. \quad (1.88)$$

Applying the Second Friedman Equation reported in Eq. (1.21), the Poisson Equation of the system becomes:

$$\nabla^2\Phi = 4\pi G\bar{\rho}(t)a^2\delta = \frac{3}{2}H_0^2\Omega_0\frac{\delta}{a}, \quad (1.89)$$

where  $\delta$  is the local density contrast,  $\bar{\rho}(t)$  the average non-relativistic matter density, and  $\Omega_0$  the non-relativistic matter density parameter.

An  $N$ -body simulation involves integrating the dynamical equations over discretized time steps,  $\delta t$ . The choice of  $\delta t$  depends on various criteria, tailored to different approaches, and falls into three main categories: total energy conservation, convergence of final positions and velocities, and reproducibility of the initial conditions (Bagla & Padmanabhan 1997). During each time interval, the total gravitational force of the system,  $F_i$ , is computed. Subsequently, the motion equation undergoes numerical integration, yielding new velocities,  $v_i(t \pm \delta t)$  and, at least, new positions,  $x_i(t \pm \delta t)$ . The time is then updated to  $t = t + \delta t$ , and the process is iteratively repeated in this order.

In  $N$ -body codes there are various approaches and their differences are based on the way to compute the force  $F_i$  acting on the  $i$ -th particle:

- *Particle-Particle* (PP): The force acting on the  $i$ -th particle is calculated by summing up the contributions of all other particles in the simulation. This method is highly accurate, providing the exact solution for the forces. However, it is computationally expensive, scaling as the number of particles squared  $N^2$ . Additionally, if two particles approach too closely, the force diverges to infinity, necessitating the introduction of an arbitrary force softening parameter.
- *Particle Mesh* (PM): Quantities that can be considered as field quantities are treated as such. Potential, gravitational force, and density are calculated by interpolating these quantities on a grid. Values at each point are computed as a weighted sum using a kernel function, which can vary. While this method may be the fastest, its resolution is limited by the smoothing scale of the grid (see Hockney & Eastwood 1981, for more details).
- *Hierarchical Tree* (HT): These methods utilize barycentric codes and graph theory. A hierarchical tree is constructed, decomposing each region into sub-regions until it contains at most one particle. At each level, a region is characterized by the total mass of the hosted particles and the position of their center of mass. Distant regions from the particle under investigation are treated as a single particle with the mentioned characteristics. This approach reduces the number of operations needed to calculate the force acting on each particle. It is widely used due to its efficient scaling ( $N \log N$ ) and ease of linearization, but it requires a substantial amount of memory to store all levels of the hierarchical tree (see Barnes & Hut 1986, for more details).



## Chapter 2

# $\Lambda$ CDM tensions and modified gravity

Over the past decades, the  $\Lambda$ CDM model has garnered significant acclaim for its success in explaining various cosmological observations, including the accelerated expansion of the Universe (Perlmutter et al. 1999; Riess et al. 1998), abundances of light nuclei (see e.g. Cyburt et al. 2016), the CMB anisotropies (Planck Collaboration et al. 2020b), and LSS statistics (Bernardeau et al. 2002). Despite its achievements, this model is currently under intense scrutiny due to both theoretical and observational challenges.

Addressing theoretical concerns, as described in Sect. 1.4, the  $\Lambda$ CDM model lacks a physical description for the nature of CDM. Additionally, cosmological models based on GR theory face challenges in reconciling with theory of the *Standard Model*<sup>1</sup> and imply the cosmological singularity of BB at the “beginning” of the Universe. Moreover, as mentioned in Sect. 1.3.1 and Sect. 1.4, even the cosmological constant  $\Lambda$  presents some criticisms. There are, in fact, two historical problems against its validity:

- *coincidence*: it revolves around the statistical improbability of living in the precise era transitioning from matter domination to late-time acceleration, where  $\Omega_\Lambda \approx \Omega_m$ . The vastly different evolution histories of these components makes this coincidence unlikely.
- *fine-tuning*: this problem pertains to the significant mismatch, about 120 orders of magnitude, between theoretical expectations  $|\Lambda_{\text{th}}| \lesssim 10^{-26} \text{ kg m}^{-3} \simeq 10^{-47} \text{ GeV}^4$  (Weinberg 1989) and observational values  $\Lambda_{\text{obs}} \simeq 10^{95} \text{ kg m}^{-3} \simeq 10^{74} \text{ GeV}^4$  of the cosmological constant (Planck Collaboration et al. 2016b).

Regarding observational concerns, the increasing precision of modern cosmological and astrophysical measurements has led to statistically significant tensions in the values of cosmological parameter values obtained from different probes. These discrepancies become particularly pronounced when considering probes covering different redshift ranges: those related to local measurements (late or low-redshift probes) and those related to the measurement of CMB anisotropies (early or high-redshift probes). Among the most puzzling tensions today we can mention (see Di Valentino et al. 2021a,b,c, for a detailed review):

---

<sup>1</sup>The Standard Model of Particle Physics is a specific physical theory developed within the framework of Quantum Field Theory, which, in turn, is the extension of quantum mechanics to Special Relativity. It describes the elementary components of matter and their interactions, although it considers only three out of the four fundamental forces observed in nature: electromagnetic interaction, weak interaction (unified in the so-called electroweak interaction), and strong interaction. Any model in particle physics that merges, at high energies, these three forces into a single one is called Grand Unified Theory (GUT).

- *Hubble parameter tension:* local direct measurements of  $H_0$  using the distance ladder approach (Freedman et al. 2019) are in about  $4.4\sigma$  tension with CMB indirect measurements assuming the  $\Lambda$ CDM model (Planck Collaboration et al. 2020a).
- *Curvature tension:* Planck data show a preference at  $3.4\sigma$  for a closed Universe (Planck Collaboration et al. 2020a; Di Valentino et al. 2020), in disagreement with the concordance flat  $\Lambda$ CDM scenario. This tension is related to the contribution to the strangely higher gravitational lensing effect in the CMB power spectra, which are strongly degenerate with  $\Omega_\kappa$ .
- *Growth of structures tension:* direct measurements of the growth rate from weak lensing and clustering (Hildebrandt et al. 2020) suggest a lower growth rate compared to what is inferred from Planck data, with a significance level of approximately  $2 - 3\sigma$ . This tension is commonly assessed using the parameter  $S_8$ , defined  $\sigma_8 = \sqrt{\Omega_m/0.3}$ , and can also be determined from galaxies' redshift-space distortions through its relationship with  $f\sigma_8(z=0)$ , where  $f$  is defined in Eq. (1.68).
- *Universe age tension:* the age of the Universe obtained from local measurements using very old-dated objects appears marginally larger than the corresponding age obtained using CMB Planck data in the context of the  $\Lambda$ CDM cosmology (Planck Collaboration et al. 2020a).

The presence of these tensions within the  $\Lambda$ CDM model could imply a deviation from the assumed standard scenario and may hint at the existence of undiscovered physics. For this reason, in recent years, many alternatives to the standard cosmological model have been formulated to simultaneously seek theoretical justifications and accommodation of observational data. Although not all models in the literature can be categorized sharply into one or the other, they can be broadly divided into two main categories of models commonly used to describe accelerating cosmologies: *dark energy models* and *modified gravity models* (see Yoo & Watanabe 2012; Joyce et al. 2016, for reviews).

As introduced in Sect. 1.3.1, dark energy (DE) models typically alter the stress-energy content of the Universe on the RHS of Einstein's field equation (Eq. (1.27)) by incorporating a component characterized by an equation of state parameter  $w \simeq -1$ , which could exhibit temporal variations. Different DE models have been proposed, from scenarios that interpret the DE as a dynamical field instead of a constant component, to models including interaction between DM and DE. Conversely, modified gravity (MG) models are based on variations of the LHS of the equation to alter the Einstein-Hilbert action, thus modifying GR itself.

Here, in Sect. 2.1, we will focus on the family of MG models, specifically on one popular subclass of them in Sect. 2.1.3. Additionally, in Sect. 2.1.4 we will discuss the degeneracies between the effects of some of these models and those incorporating massive neutrinos. Neutrinos constitute another elusive component of the  $\Lambda$ CDM cosmology. Despite the assumption in the standard model that neutrinos are massless, evidence from solar neutrino oscillations indicates that they possess mass (Fukuda et al. 1998; Ahmed et al. 2004). Numerous studies have highlighted that the presence of massive neutrinos leaves imprints on the LSS of the observable Universe that are strongly degenerate with DE and MG models (i.e. Baldi et al. 2014; Lorenz et al. 2017; Giocoli et al. 2018a), and may also help alleviate tensions associated with the  $\Lambda$ CDM cosmology (Lambiase et al. 2019; Sakstein & Trodden 2020).

## 2.1 Modified gravity theories

The main objective of these models is to explain the recent acceleration of the Universe by exploiting potential modifications of gravity. With respect to the  $\Lambda$ CDM scenario, the viability of a MG model depends on two main factors:

- It must exhibit a nearly identical expansion history to that of the  $\Lambda$ CDM model on large scales because it agrees with observational data, while, it must incorporate what is known as a *screening mechanism* in small and overdense regions (Brax & Valageas 2013) to restore the well-tested<sup>2</sup> predictions of GR on small scales.
- It must diverges from  $\Lambda$ CDM model in terms of how gravitational instability dynamically evolves density perturbations.

There are many different ways to modify the effects of gravity and reproduce a variety of effects on observables. To understand how to classify the different approaches, it is essential to introduce the *Lovelock's theorem* (Lovelock 1971, 1972). This theorem asserts that the only possible second-order Euler-Lagrange expression obtainable in a four-dimensional space from a scalar density of the form  $\mathcal{L} = \mathcal{L}(g_{\mu\nu})$  is:

$$E^{\mu\nu} = \alpha\sqrt{-g} \left[ R^{\mu\nu} - \frac{1}{2}g^{\mu\nu}R \right] + \lambda\sqrt{-g}g^{\mu\nu}, \quad (2.1)$$

where  $\alpha$  and  $\lambda$  are constants. This implies that if we attempt to formulate any gravitational theory within a four-dimensional space using an action principle based solely on the metric tensor and its derivatives, then the only possible field equations that are second-order or lower are either Einstein's equations or equations involving a cosmological constant.

From the Lovelock's theorem descends that to construct metric theories of gravity with field equations differing from those of GR, we must undertake one (or more) of the following actions (Clifton et al. 2012):

- consider other fields (scalar, vector, tensor) beyond the metric tensor. This implies increasing the degrees of freedom (dof);
- accept higher than second derivatives of the metric in the field equations;
- work in a space with dimensionality different from four;
- give up locality (more common) or give up tensor field equations of rank  $(2, 0)$ , symmetry of field equations under index exchange, or field equations without divergence (less common).

These different approaches determine the four major families into which the currently existing MG models can be divided, as shown in Figure 2.1.

### 2.1.1 Higher derivative theories of gravity

One approach to extend GR involves allowing the field equations to exceed second order. This generalization may be deemed advantageous as it results in the graviton<sup>3</sup> propagator

<sup>2</sup>GR has been validated within the Solar System by numerous experiments (Bertotti et al. 2003; Will 2005; Hinterbichler & Khoury 2010)

<sup>3</sup>In theories of quantum gravity, the graviton is a hypothetical elementary particle that mediates the force of gravitational interaction and represents the quantum of gravity. Given that the gravitational force appears to travel at the speed of light and has a very great range, if it exists, it is predicted to be massless.

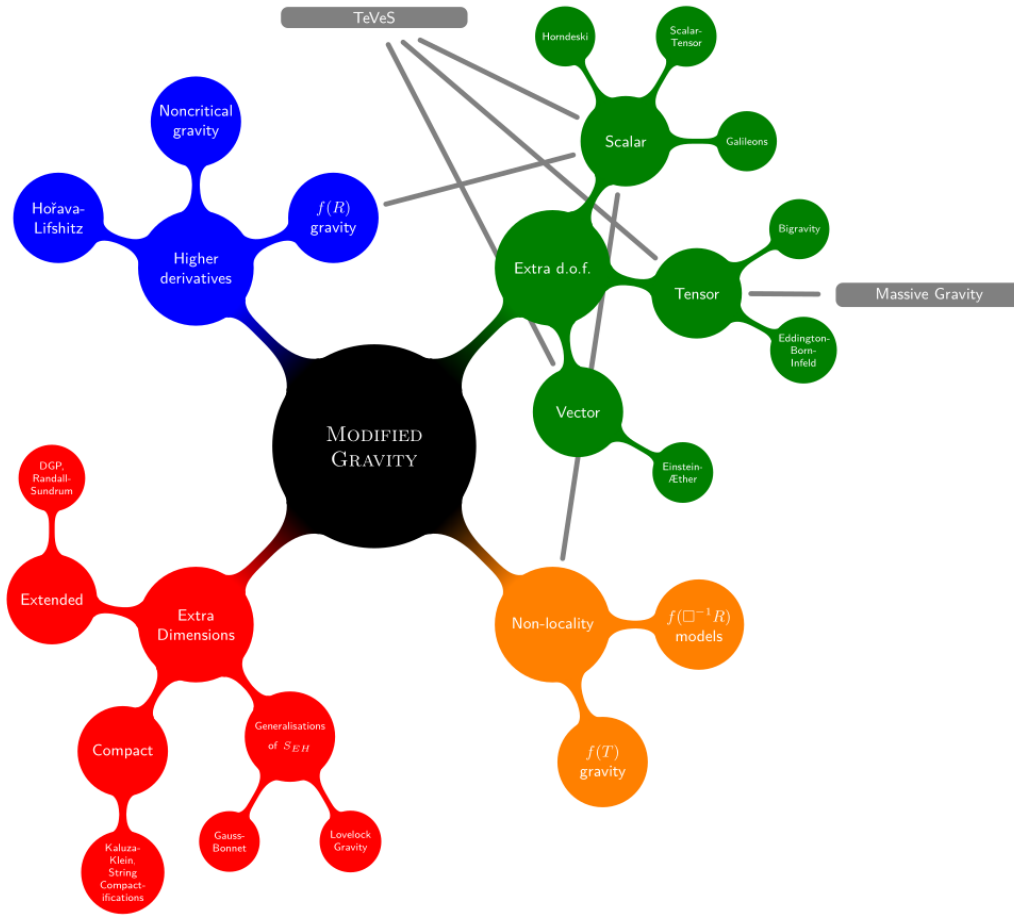


**Figure 2.1:** A summary of the four major families in MG, with related main theories. They are classified according to the way in which they avoid the Lovelock’s restrictions: Extra fields theories with relative subclasses that distinguish between scalar, tensor and vector fields (green bubbles); Higher derivative theories with relative subclasses including the  $f(R)$  gravity (blue bubbles); Extra dimensional theories that ramificate in extended, compact and generalization of Einstein’s action (red bubbles); Non-locality theories (orange bubbles). Gray lines indicate a connection between the theories, for example  $f(R)$  gravity is a higher derivatives theory but also considers a scalar field. Credits to [Guarnizo Trilleras \(2016\)](#).

decaying more rapidly in the ultraviolet. However, modifying gravity in this manner also comes with several drawbacks. In particular, it can introduce instabilities into the theory, such as ghost-like dof (see [Woodard 2007](#), for a comprehensive review).

Such theories can exhibit intriguing phenomenology and, in many cases, can be demonstrated to be less prone to instabilities than others. For instance, if the higher derivatives only affect what would otherwise be non-dynamical modes, they may simply render them dynamical instead of automatically generating a ghost. This is exemplified in  $f(R)$  gravity (that we will see in Sect. 2.1.3), where the higher-order derivatives act on conformal mode that does not propagate in GR.

### 2.1.2 Scalar-tensor theories of gravity

The so-called scalar-tensor theories represent a well-established and extensively studied set of alternative theories of gravity found in the literature. They serve as the primary method for modeling deviations from GR and are especially intriguing due to their relatively simple

field equations, which enable exact analytic solutions to be derived in various physically relevant scenarios. These theories naturally emerge from the dimensional reduction of higher-dimensional theories.

The bases of the scalar-tensor theories lie in expressing the Einstein-Hilbert action, denoted as  $S$ , in the following form:

$$S = \int d^4x \sqrt{-g} \left( \frac{M_{\text{P}}^2 R}{2} - \frac{1}{2} \dot{\phi}^2 - V(\phi) \right) + S_m [A^2(\phi) g_{\mu\nu}, \psi] , \quad (2.2)$$

where  $M_{\text{P}}^2 = 1/(8\pi G)$  is the reduced Planck mass and  $S_m$  is the action of the matter field  $\psi$ . In this formulation, both the tensor field and the scalar field of GR mediate the gravitational interaction. One of the most representative of these theories is the Brans-Dicke theory (Brans & Dicke 1961).

It is feasible to select  $V(\phi)$  and  $A(\phi)$  in general scalar-tensor theories in a way that both avoid Solar System limitations and have an intriguing phenomenology for the scalar field. The key lies in leveraging the scalar field's reaction to the effective potential, which is influenced by external matter sources. This enables us to construct scenarios in which the field exhibits varying behavior based on the density of the surrounding matter. The so-called *Chameleon field* (Khouri & Weltman 2004a,b) is a well-known illustration of this situation, where the effective mass of the scalar field:

$$m_{\text{eff}}^2(\phi) = \frac{d^2 V_{\text{eff}}}{d\phi^2} = \frac{d^2 V}{d\phi^2} + \frac{d^2 A}{d\phi^2} \bar{\rho} \quad (2.3)$$

is designed to get larger in high-density areas and smaller in low-density areas, as Figure 2.2 illustrates.

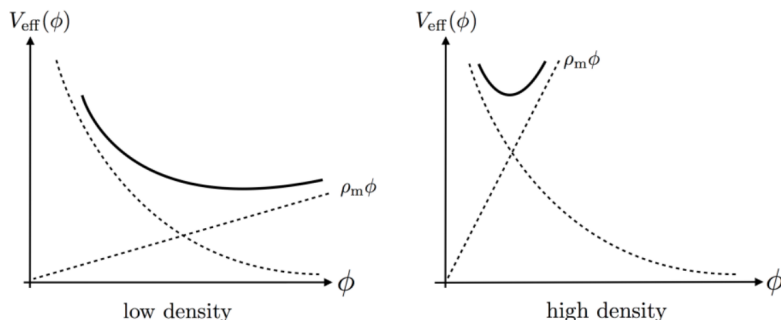


**Figure 2.2:** Chameleon effective potential in regions of low and high density. *Left:* In broad regions at low density, the potential's curvature is shallow, which causes the scalar field to become light and mediate a long-range fifth force. *Right:* the extra fifth force around matter overdensities is suppressed as a result of the scalar field gaining a significant mass on small scales with high density. Credits to Elder et al. (2016).

### 2.1.3 $f(R)$ gravity

Fourth-order theories of gravity have a long history, dating back to as early as 1918 (Weyl 1918). These theories go beyond the simple linear form that gives Einstein's equations and expand the Einstein-Hilbert action by adding more scalar curvature invariants or by generalizing the action to be a function of the Ricci scalar. In this context, we focus on the latter option, which, according to Lovelock's theorem, results in fourth-order field equations unless a constant term is added to the gravitational Lagrangian. Such theories, commonly known as  $f(R)$  theories of gravity, have been extensively investigated, and several reviews

dedicated to them are available (e.g., see [Nojiri & Odintsov 2007](#); [Nojiri et al. 2009](#); [Nojiri & Odintsov 2011](#)). The interest in  $f(R)$  theories was sparked from the 1960s, by findings suggesting that the quantization of matter fields in an unquantized space–time can give rise to such theories ([Utiyama & DeWitt 1962](#)), and that they could lead to a period of early accelerating expansion in the Universe’s history ([Starobinsky 1980, 2007](#); [Nojiri & Odintsov 2008b](#)). More recently, they have garnered considerable attention as a potential explanation for the observed late-time accelerating expansion of the Universe ([Hu & Sawicki 2007](#); [Nojiri & Odintsov 2008a](#)). We will now examine some details about this class of higher-derivative models that also theorizes a scalar field, which consists of higher-curvature corrections to the Einstein-Hilbert action:

$$S = \frac{M_{\text{P}}^2}{2} \int d^4x \sqrt{-g} (R + f(R)) + S_m [g_{\mu\nu}, \psi], \quad (2.4)$$

where  $f(R)$  is a function of the Ricci scalar, selected to assume importance in the regime of low curvature, where  $R \rightarrow 0$ . In this class of MG models, GR can be recovered by forcing  $f$  to be proportional to the cosmological constant  $f = -2\Lambda^{\text{GR}}$  and more general cosmic acceleration can be obtained by following [Carroll et al. \(2004\)](#).

A well-studied  $f(R)$  model is that proposed by [Hu & Sawicki \(2007\)](#) that is consistent with both the observed large-scale expansion of the Universe and local tests of gravity. It is defined as:

$$f(R) = -m^2 \frac{c_1 \left(\frac{R}{m^2}\right)^n}{c_2 \left(\frac{R}{m^2}\right)^n + 1}, \quad (2.5)$$

where  $m^2 \equiv H_0^2 \Omega_{\text{m}}$  defines the mass scale  $m$ , while  $c_1, c_2$  and  $n$  are non-negative free parameters. Considering the present vacuum density parameter  $\Omega_{\Lambda}$  and matter density parameter  $\Omega_{\text{m}}$ , the background expansion history is consistent with the one predicted by the  $\Lambda$ CDM model under the condition  $c_1/c_2 = 6\Omega_{\Lambda}/\Omega_{\text{m}}$ . Additionally, forcing  $c_2 (R/m^2)^n \gg 1$  the scalar field  $f_R \equiv df(R)/dR$  can be approximated by:

$$f_R \approx -n \frac{c_1}{c_2^2} \left(\frac{m^2}{R}\right)^{n+1}, \quad (2.6)$$

and restricting our analysis to the case  $n = 1$ , only the parameter  $c_2$  can be used to indicate the scalar field, and the model at the present-day can be represented by the parameter  $f_{R0}$ :

$$f_{R0} \equiv -\frac{1}{c_2} \frac{6\Omega_{\Lambda}}{\Omega_{\text{m}}} \left(\frac{m^2}{R_0}\right)^2, \quad (2.7)$$

where  $R_0$  denotes the current background value of the Ricci scalar. At this point, by modifying the action defined in Eq. (2.2) with regard to the metric  $g_{\mu\nu}$ , we may obtain the modified Einstein equations for this  $f(R)$  model and, from its trace, we obtain the motion equation for this scalar field:

$$\nabla^2 \delta f_R = \frac{a^2}{3} [\delta R (f_R) - 8\pi G \delta \rho], \quad (2.8)$$

where  $a$  is the scale factor of the metric. By extracting the time-time component from this equation, assuming small perturbations  $\delta f_R, \delta R, \delta \rho$  on a homogeneous background and the quasi-static field approximation (slow variation for  $f_R$ ), we obtain:

$$\nabla^2 \psi = \frac{16\pi G}{3} a^2 \rho - \frac{a^2}{6} \delta R (f_R). \quad (2.9)$$

---

<sup>3</sup> $\delta f_R \equiv f_R - \bar{f}_R, \delta R \equiv R - \bar{R}$  and  $\delta \rho \equiv \rho - \bar{\rho}$ , where the barred values represent the background quantities.

This is the equivalent of the Poisson equation for scalar metric perturbations  $2\psi = \delta g_{00}/g_{00}$ .

From the combination of Eqs. (2.8) and (2.9) it is possible to derive the exact solution for the extreme cases and to study on what scales and how the gravity of the  $f(R)$  model diverges from GR:

- For  $|f_{R0}| \gg |\psi|$  the interaction range of an additional fifth force is determined by the Compton wavelength of the scalar field  $\mu^{-1} = (3 \, df_R/dR)^{1/2}$ :
  - for  $k \gg \mu$  fifth force enhances the gravity field up to a factor of 4/3
  - for  $k \ll \mu$  standard GR gravity is restored
- For  $|f_{R0}| \ll |\psi|$  Eq. (2.9) can be roughly represented by the conventional Poisson equation, resulting in the GR recovery in high spacetime curvature regions due to the effects of the Chameleon-screening mechanism. The screening condition for an ideal spherical source of mass  $M$  causing the small fluctuation of the scalar field in the homogeneous background is  $|f_R| \leq 2/3 \Psi_N(r)$ , where  $\Psi_N = GM/r$  is the Newtonian potential of the overdensity. According to this approximation, the radius  $r = r_N$  for which  $\Psi_N(r) = 3/2 |f_R|$  represents the boundary between the screened and unscreened regimes:
  - for  $r \ll r_N \Rightarrow f_{R0} \ll \Psi_N$  on small scales the fifth force is always screened
  - for  $r \gg r_N \Rightarrow f_{R0} \gg \Psi_N$  on large scales there is no screening mechanism active

Now we can evaluate appropriate estimates for the free parameter  $f_{R0}$ . When  $f_{R0} \ll \Psi_N$ , the scenario that arises is not of significant cosmological interest, as it becomes indistinguishable from General Relativity even on large scales. Conversely, if  $f_{R0} \gg \Psi_N$ , we would encounter the improbable scenario where gravity is consistently amplified. Hence, we should set the parameter  $f_{R0}$  to be approximately within the same order of magnitude as the Newtonian potential  $\Psi_N$ , which typically falls within the range  $10^{-5} \leq \Psi_N \leq 10^{-6}$ . This interval is then the one in which we expect to find  $f_{R0}$  and that, although a bit extreme, a value of  $10^{-4}$  can be considered acceptable, especially in the presence of massive neutrinos, as we will see in Sect. 2.1.4. As depicted in Figure 2.3, the higher the absolute value of  $f_{R0}$ , the further the  $f(R)$  models deviate from the  $\Lambda$ CDM model. This deviation is reflected in a higher normalization of the power spectrum of the  $f(R)$  model at small physical scales, i.e., for large values of  $k$  in Fourier space.

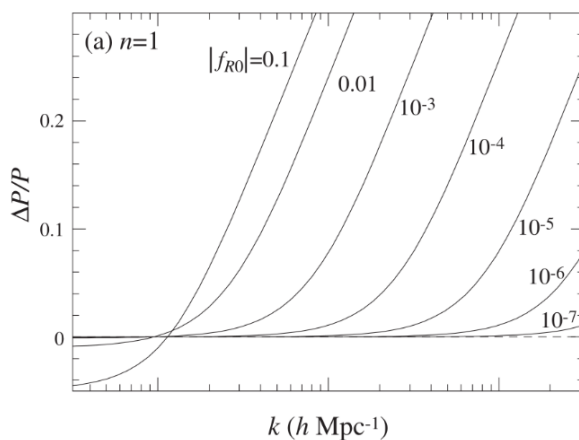


**Figure 2.3:** Deviations of power spectra of the  $f(R)$  models with  $n = 1$  as a function of the absolute value of the  $f_{R0}$  parameter, with respect to that of  $\Lambda$ CDM (reference dotted line). Credits to [Hu & Sawicki \(2007\)](#).

### 2.1.4 Massive neutrinos

As introduced in Sect. 1.5.1 and 1.5.2, neutrinos are massive particles participating in the overall matter composition of the cosmos, influencing the formation and development of cosmic structures. Neutrinos decouple from the cosmological fluid in the early Universe, due to their small masses, when their thermal energy decreases to a level below their mass. Nowadays precision cosmology allows to put strong constraints on the total sum of masses of the different types of neutrinos in the Standard Model of Particle Physics,  $M_\nu \equiv \sum m_\nu$ . In fact, a number of astronomical observations limit the total neutrino mass to be  $M_\nu \lesssim 0.1 - 0.3 \text{eV}$  (see e.g. Seljak et al. 2006; Yèche et al. 2017; Poulin et al. 2018), and the neutrino contribution to the total amount of energy in the Universe at late cosmological epochs can be computed as (Mangano et al. 2005):

$$\Omega_\nu \approx \frac{M_\nu}{93.14 h^2 \text{eV}}. \quad (2.10)$$

As we have seen in Sect. 1.4, neutrinos can be considered as a HDM component and this is due to their weak interaction cross-section. Indeed, unlike CDM particles, neutrinos have the ability to freely move through high-density matter perturbations due to their high thermal velocity. According to Eq. (1.71) we can derive their typical free-streaming length as:

$$\lambda_{\text{FS}}(z, M_\nu) = a(z) \frac{2\pi}{k_{\text{FS}}} = 7.7(1+z) \frac{H_0}{H(z)} \left( \frac{1 \text{eV}}{M_\nu} \right) h^{-1} \text{Mpc}, \quad (2.11)$$

where  $k_{\text{FS}}$  refers to the free-streaming wavenumber associated with it, which, during the non-relativistic transition of neutrinos at  $z_{\text{nr}}$ , attains its minimum value (Lesgourgues et al. 2013):

$$k_{\text{FS}}(z_{\text{nr}}) \simeq 0.0178 \left( \Omega_{\text{m}} \frac{M_\nu}{1 \text{eV}} \right)^{1/2} h^{-1} \text{Mpc}. \quad (2.12)$$

This is the scale that discriminates neutrino modes behavior between large and small scales:

- for  $k < k_{\text{FS}}$  on large scales they evolve as CDM perturbations since neutrino velocities can be neglected,
- for  $k \gg k_{\text{FS}}$  the free-streaming causes the slowdown of neutrino perturbation expansion and this has the effect of suppressing clustering below their free-streaming thermal scale.

The physical features of neutrinos also influence the matter power spectrum shape (Saito et al. 2008; Wagner et al. 2012), the halo mass function (Marulli et al. 2011; Villaescusa-Navarro et al. 2013), the clustering properties of CDM halos and redshift-space distortions (Marulli et al. 2011; Zennaro et al. 2018; ?).

Furthermore, it has been shown that the observable effects predicted by MG theories exhibit significant degeneracy with the signatures caused by the existence of massive neutrinos. In fact, as we said in Sect. 2.1.3, the typical extent of the fifth force in  $f(R)$  models is determined by the Compton wavelength  $\mu^{-1}$ , and it can span several tens of Mpc (Cataneo et al. 2015), contingent upon the value of the parameter  $f_{R0}$ . This range is comparable to the scale of neutrino free-streaming, which can be approximated using Eq. (2.11). Neutrino free-streaming can therefore counteract the accelerated growth of cosmic structures, resulting in a balancing effect on the cosmological fluctuations predicted by MG models. This presents a significant challenge for cosmology, as it necessitates robust methodologies and diverse cosmological techniques to tightly constrain at the same time massive neutrinos and MG, particularly in untangling their joint impacts.

In Chapter 3 we will formally introduce cosmic voids and evaluate their contribution in this context. Due to their unique characteristics of being underdense and having exceptional spatial extension, which are comparable to the ranges covered by the fifth force in  $f(R)$  models and by neutrino free-streaming, voids are highly responsive to both of these components. Their statistics, in fact, plays the role of key probes in unraveling the presented degenerate scenarios (Contarini et al. 2021).



## Chapter 3

# Cosmic voids and gravitational lensing

In this chapter, we will now address the central subject of this Thesis: cosmic voids. Voids are extended and underdense regions that emerge between the filaments and the walls of the cosmic web and constitute the predominant volume of the LSS of the Universe (Cautun et al. 2014). In Sect. 1.5.1 we highlighted how voids originate from the evolution of underdensities in the primordial matter density field, expanding at a rate that is inversely proportional to the density they contain (see Sect. 1.5.3). These expanding volumes result in a fall in density, which is caused by the redistribution of the mass over the expanding volume and by mass loss to surrounding overdensities. A ridge forms around the void as a consequence of the accumulation on the edge of matter from the inner part (Suto et al. 1984). Therefore we can assert that cosmic voids represent the negative counterpart in the density field of the extensively studied galaxy clusters.

Recent years have seen an increase in interest in this topic due to the scientific breakthroughs made possible by recent and ongoing redshift surveys<sup>1</sup>, which have achieved deeper redshifts and covered wider sky areas than in the past. The development of these observational surveys, together with the improvement of both numerical simulations and theoretical models have increased the use of voids as a cosmological probe (see Pisani et al. 2019, and references therein).

This field of studies has great potential because void features and statistics provide us with the opportunity to disentangle model degeneracies by combining orthogonal probes. In fact, unlike galaxy clusters, cosmic voids have some important benefits in physical analysis:

- a) they only experience a mildly nonlinear evolution, alleviating every issue brought up by the completely nonlinear regime of structure evolution (Sheth & van de Weygaert 2004);
- b) there is a tendency towards sphericity as their evolution proceeds (Icke 1984);
- c) baryonic physics has almost no influence on their life history (Schuster et al. 2023);
- d) they are extremely sensitive to diffuse components like DE and massive neutrinos thanks to their very large sizes (Massara et al. 2015; Sánchez et al. 2017; Massara & Sheth 2018; Kreisch et al. 2019; Cautun et al. 2018; Contarini et al. 2021);

---

<sup>1</sup>For example Sloan Digital Sky Survey (SDSS-III Eisenstein et al. 2011) with Baryon Oscillation Spectroscopic Survey (BOSS Dawson et al. (2013), eBOSS Dawson et al. (2016)) and *Euclid* mission (Laureijs et al. 2011; Amendola et al. 2018; Euclid Collaboration: Blanchard et al. 2020; Euclid Collaboration et al. 2022).

- e) they are weakly affected by screening mechanisms in MG because of their low-density interiors and shallow gravitational potentials (Martino & Sheth 2009; Baker et al. 2018; Cautun et al. 2018; Contarini et al. 2021).

All of these features enable us to model quite easily a cosmic void. For example, the first two characteristics allow us, using a spherical expansion model, to forecast the statistical distribution of voids based on their size (Sheth & van de Weygaert 2004) and this is crucial for constraining cosmological parameters. Additionally, in this Thesis work, we are primarily interested in the last two characteristics because they make voids perfect laboratories to detect the gravitational effects produced by the fifth force, helping therefore to discriminate between the competing MG models (Barreira et al. 2015; Baker et al. 2018).

On the other hand, voids' biggest drawback has to do with how they are defined and identified. Indeed, not only do we lack a universal definition for the void radius and center, but we are also unable to trivially identify these objects. This is due to the fact that cosmic voids are structures that do not emit light, but are instead defined by the distribution of luminous tracers. Consequently, we have to use some ad-hoc techniques to recover the void shape and position from the matter tracers.

In this context, one of the most effective tools for detecting and analyzing the properties of voids is gravitational lensing, which involves studying the deflection of light from background sources. This deflection is influenced by gravitational effects, allowing its intensity to be correlated with fluctuations in the density field encountered along the path of light from the source to the observer (Serenio & Umetsu 2011). This connection of lensing with the gravitational potential makes it an excellent method for investigating MG models within voids (Umetsu 2020). Besides its promising application to study MG models, this type of statistic has already been shown to be highly sensitive to the growth rate of large-scale structure and the expansion history of the Universe (Bartelmann 2010; Troxel & Ishak 2015).

In this chapter, we will discuss the definition of cosmic voids in Sect. 3.1 and their main statistical properties in Sect. 3.2. Here, we will briefly introduce the theoretical framework of the void size function and the current understanding of the primary characteristics associated with the density profiles of cosmic voids. Then, we will provide an overview of the theoretical foundations of gravitational lensing in Sect. 3.3, with particular attention to the weak regime and its applications to voids and MG models.

### 3.1 Definition and void finding

One of the primary problems with the cosmological use of cosmic void statistics is that, despite their increasing use in recent literature, for several statistics there is not yet a model developed from first principles, so neither is there a universal definition of the associated void. In fact, the definition one gives is closely related to the type of analysis one wants to perform, that is, from the type of study one wants to apply to the voids. For example, there is no standard range of values to categorize voids based on their size, shape, and internal density. This lack of paradigm in their definition makes the identification of voids non-trivial. Indeed, it is essential to reconstruct the shape of voids and determine the position of their centers based on the distribution of luminous tracers, which predominantly reside along their boundaries. Over the years, many different definitions have been given and the scientific community has put forward various algorithms for identifying cosmic voids using the position of 3D tracers, but the use of one rather than another method obviously depends on the type of study and its intended purpose. We can categorize these methods into three main classes based on the detection criteria, as outlined by Lavaux & Wandelt (2010):

- *Geometrical criterion.* Geometry-based algorithms aim at identify cosmic voids by searching for local density minima within a reconstructed continuous density field by partitioning the volume into cells, which can have different geometric shapes. Density is evaluated in each of these cells. According to this class of criteria, cosmic voids are characterized as underdense regions that take on the shape of either spherical cells or polyhedra (Platen et al. 2007; Neyrinck 2008; Sutter et al. 2015). Nowadays, the most popular algorithm exploiting this method is the *Void IDentification and Examination toolkit* (VIDE, Sutter et al. 2015). VIDE is based on an enhanced version of the *ZOnes Bordering On Voidness* (ZOBOV, Neyrinck 2008) algorithm, a parameter-free method that does not rely on any assumption regarding the shape of the void. Specifically tailored to detect regions of low density, it is built upon the original *VOronoi BOund Zones* (VOBOZ, Neyrinck et al. 2005) method, designed for the detection of overdensities. The VIDE void finding procedure is based on the so-called *Voronoi tessellation* performed on the tracer catalog. This procedure permits the volume to be divided into so-called *Voronoi cells*, which are always containing a single particle. Moreover, every point inside every single cell is closer to the particle inside it than it is to any other particle. The algorithm determines the density mean value of each cell by calculating the inverse of the Voronoi cell volume, assuming that each particle has the same mass.
- *Density criterion.* Voids are identified as areas devoid of tracers or, similarly, regions where the local density is below a specified mean density threshold (Elyiv et al. 2013). Depending on the density of the surrounding environment, the tracers are categorized as either wall tracers or field tracers; the former group includes tracers in high density areas, such as the walls, while the latter group includes tracers in low density areas, such as the cosmic voids. Thus, the so-called wall tracers cannot exist inside of voids. One notable application of this approach is evident within the context of the *VIMOS Public Extragalactic Redshift Survey*<sup>2</sup> (VIPERS) where, based on the identification of empty spheres, Micheletti et al. (2014) created an algorithm for void detection. Thus, voids discovered in this manner are identified as areas free of galaxies with absolute magnitudes brighter than a given threshold (B-band brighter than  $M_B = -19.8$  in that case).
- *Dynamical criterion.* These void finders detect cosmic voids as regions that are being emptied of matter, characterized by a radial velocity field pointing outward from the void centers. Instead of using tracers to rebuild the density distribution, methods based on dynamic criteria use them as test particles to sample the velocity field (Forero–Romero et al. 2009; Elyiv et al. 2015). Rather than being underdense zones, voids are recognized in these algorithms as areas where tracers are evacuating from. One benefit of dynamic void identification is that it is possible to partially mitigate the issues caused by shot noise like the sparsity of tracers. It also makes it possible to recreate continuous velocity and density fields as a function of time. The two instances of this kind of method are proposed by Elyiv et al. (2015). By randomizing the Eulerian positions, the two algorithms, the *Uncorrelating Void Finder* and the *Lagrangian Zel’dovich Void Finder*, can recreate the Lagrangian positions of galaxies. The two dynamical void finders work by taking into account a volume of the universe that is probed by “particles” such as galaxies or DM halos. Utilizing these as test particles, the objective is to reconstruct their Lagrangian locations by following their orbits back in time to a homogeneous and isotropic initial distribution.

---

<sup>2</sup>It was an ESO programme with the purpose of studying the LSS distribution of galaxies at  $z = 0.5 - 1.2$ , over total sky area of 24 squares degree (Guzzo et al. 2014).

### 3.1.1 2D voids

On the described three main criteria are based not only the 3D void finders but also the 2D void finders, with the difference that in the second case the 3D density (or tracers) distribution is projected along the line of sight. This kind of finder is suitable especially for weak lensing (WL) investigations around voids (see [Sánchez et al. 2017](#); [Cautun et al. 2018](#); [Fang et al. 2019](#); [Davies et al. 2021a,b](#)), which we will introduce in the last section of this chapter.

Indeed, 2D WL voids have been demonstrated to correspond to deeper line-of-sight projected underdensities compared to 3D voids. Consequently, they exhibit a larger tangential shear signal ([Davies et al. 2018](#)). This potentially makes 2D voids better than 3D voids for WL cosmological analyses. This has been exemplified by [Davies et al. \(2019a\)](#) in the context of modified gravity models, which can be considerably better constrained with 2D WL voids than with 3D voids identified via galaxy positions, as we will see in Sect. 3.3.6. The overall signal-to-noise ratio ( $S/N$ ) of void lensing profiles relies on the number of voids and the magnitude of their lensing profile. The method of void identification impacts the count of 2D voids, with variations depending on the approach used. However, the key distinction lies in the amplitude of the lensing profile: 2D void lensing profiles, because of the identification method itself, generally exhibit an amplitude approximately ten times larger than that of the WL signal derived from 3D voids. This substantial difference in amplitude is the primary factor contributing to the higher  $S/N$  observed for 2D voids with respect to 3D voids ([Cautun et al. 2018](#); [Davies et al. 2018](#)).

[Davies et al. \(2018\)](#) focused on a specific category of 2D voids known as *VOids from LEns-ing* (VOLEs), where voids are delineated as circular regions devoid of WL peaks. However, as with 3D voids, the definition and subsequent identification of 2D voids lacks of universality. There exist indeed multiple techniques for detecting 2D underdense regions, which are based on different approaches for defining voids ([Colberg et al. 2008](#); [Cautun et al. 2018](#)). This variability can introduce relevant differences in void observables across the multiple void-finding methodologies. Nevertheless, this variability can also be leveraged by selecting the void-finding algorithm that aligns best with the intended objective. In our case, we aim at optimizing the amplitude of void lensing profiles (or equivalently, the  $S/R$  of void lensing profiles), while mitigating the influence of observational uncertainties on the resulting void statistics. To achieve this goal, we have developed a new 2D void finder algorithm, implementing some of the features of the 2D void finder that, according to [Cautun et al. \(2018\)](#) and [Davies et al. \(2021b\)](#), is ideal for WL analyses. Now, we will briefly present the conclusions reached in these two papers, which specifically investigated 2D void statistics employing a variety of void-finding algorithms, focusing on the limitations and advantages associated with each void finder.

The study of [Cautun et al. \(2018\)](#) makes use of several void finders with the goal of determining which ones are best suited for probing chameleon-type modified gravity models. Broadly, they split the void finders into two categories: the ones that identify 3D underdensities (i.e., “standard” voids) and the ones that identify 2D underdensities in the plane of the sky. The underdensities identified by the latter methods are not formally called voids, since voids are 3D objects, but nonetheless, it is possible to think of them as 2D voids that are very elongated along the line of sight. Specifically, these definitions of 2D voids and corresponding finders are among the most commonly used in the literature to analyze simulations:

- *2D spherical voids* (SVF 2D): 2D spherical voids are obtained by finding the void centers in a rectangular grid constructed over the projected distribution of mock galaxies along one of the axes of the simulations, and counting the number of galaxies in each grid cell. The centers of empty grid cells are considered as prospective void centers, and

circles are grown from those centers until the integrated number density of galaxies at the circle radius is equal to 40 per cent of the mean density. Following this procedure, if the overlap between two voids exceeds 80 per cent of the sum of their radii, only the larger void is retained in the catalog. Similar to its 3D counterpart, the SVF 2D void finder relies on three parameters: the density threshold used to define a void, the method for removing overlapping voids, and the extent of the projected redshift range. For the first criteria they found that choosing the value 0.4 results in the strongest detection of WL by 2D underdensities.

- *Tunnels*: The tunnels correspond to elongated line-of-sight regions that intersect one or more voids without passing through overdense regions (Davies et al. 2018). Using galaxies as tracers of the matter distribution, the tunnels are identified as circles in the plane-of-the-sky that are devoid of galaxies. The typical size of tunnels depends on the number density of tracer galaxies (or the extent of the density field) and the depth of the line-of-sight used for their identification. Higher tracer density or a larger line-of-sight depth results in smaller tunnels. In the distant observer approximation, tunnels are represented as line-of-sight cylinders devoid of galaxies.

To identify tunnels, the galaxy catalogue is projected along one of the simulation axes, yielding a 2D distribution of galaxies. The largest circles devoid of galaxies are identified by constructing a *Delaunay tessellation* with galaxies as its vertices (see Zhao et al. 2016, for a detailed review). For realistic surveys, the tunnels resemble conical frustums. In practical terms, the angular opening of the tunnels is very small, so they can be approximated as having planar top and bottom circular bases. Only tunnels larger than 0.4 times the mean projected galaxy separation are considered, as the focus is on detecting the modified gravity signature of underdense regions. Finally, the tunnel catalog depends on two free parameters: the minimum accepted radius, and the length of line-of-sight projection. The former is determined by analyzing the enclosed projected matter density within tunnels, while the latter should be chosen based on the specifics of the observational survey being matched.

- *Troughs*: The troughs are akin to tunnels in that they represent elongated regions of low galaxy density along the line of sight (Gruen et al. 2015). Unlike tunnels, however, all troughs share the same radius and are defined by randomly positioned circles on the celestial plane containing very few galaxies. These troughs are identified utilizing the same projected mock galaxy data sets as the tunnels, assuming a distant observer approximation. Typically, a radius is chosen to standardize the entire trough catalog, and in Cautun et al. (2018), a radius of  $2 h^{-1}$  Mpc was selected, similar to the typical radius of tunnels. Furthermore, troughs of this size encompass a comparable number of galaxies to the 5 arcsec troughs examined by Gruen et al. (2015); Barreira et al. (2017). The identification process for troughs begins by randomly placing circles with a radius of  $2 h^{-1}$  Mpc on the simulated sky plane. Troughs are defined by circles containing two or fewer galaxies within them. This selection method is consistent with that utilized by (Gruen et al. 2015), striking a balance between selecting highly underdense regions and covering a substantial portion of the available simulation area.

In Figure 3.1 we show a visual comparison of the most typical 2D underdensities described above. They generally have much smaller radii than their 3D counterparts. The analysis of Cautun et al. (2018) demonstrates that the 2D voids, initially identified as regions of lower density in the projected galaxy distribution, also correspond to underdense regions in the projected matter density field. While most underdense areas in the matter field are classified as 2D voids, there is considerable variation in both the center and size of these voids across the

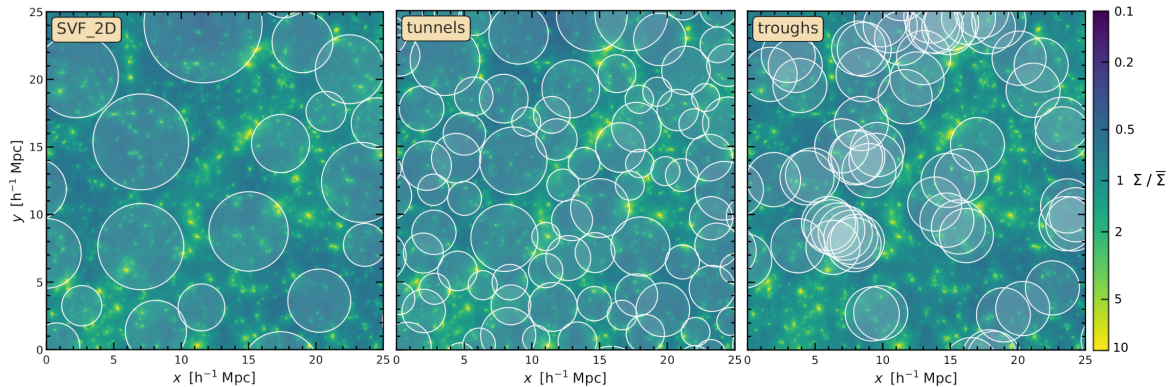


**Figure 3.1:** Plots of 2D voids (left), tunnels (center), and troughs (right) that are represented with white circles. 2D voids in a smaller region of size  $25 \times 25 (h^{-1}\text{Mpc})^2$  in the  $xy$  plane of the whole simulation box. In the background, an image displays the projected density of the box along the line of sight  $z$ -direction in the distant observer approximation. On the right, the colorbar shows the scale of surface mass density contrast values. Credits to: [Cautun et al. \(2018\)](#).

three types. SVF 2D voids and tunnels exhibit relatively little overlap, with tunnels typically being smaller and covering a greater portion of the sky compared to SVF 2D voids. Troughs, on the other hand, are highly clustered within underdense regions and exhibit significant overlap.

A very important conclusion that will be used as the basis of this work is that the authors, when studying the void matter density profiles, found that voids in  $f(R)$  gravity scenarios exhibit deeper density profiles. This is indeed expected because of the influence of a fifth force, which effectively evacuates underdense regions more rapidly. Moreover, they compared the stacked tangential shear of lensing signal (see Sect. 3.3.4 and Sect. 3.3.6) by voids identified in  $f(R)$  and GR scenarios, revealing that the former generally predicts a stronger void lensing effect. The tangential shear profiles of voids are found to depend on the method used for void identification. In Figure 3.2 we report the void WL  $S/N$  predictions computed by [Cautun et al. \(2018\)](#) for surveys featuring the characteristics of *Euclid* ([Laureijs et al. 2011](#); [Amendola et al. 2018](#)) and the LSST ([LSST Dark Energy Science Collaboration 2012](#)). Here it is shown that 2D voids, particularly tunnels and 2D SVF, exhibit both stronger lensing signals and more pronounced model differences compared to 3D voids, which in contrast do not have a WL signal with sufficient power to differentiate between  $f(R)$  models.

These aspects are very important in constructing an optimal 2D void finder for the intended purpose. In this work, given the available maps and the specific purpose, we chose several of the listed features mediated among various 2D WL finders, looking for the best and most stable configuration that we will present in the chapter 4.

## 3.2 Statistical properties of voids

As we mentioned above, with the advent of the era of large galaxy surveys, we have become able to acquire vast numbers of galaxies distributed over huge volumes. On one hand, sampling larger Universe volumes allows us to gather a statistically relevant sample of cosmic voids and to identify the largest (and so rarest) underdensities; on the other hand, the higher galaxy number density enables us to resolve also the smallest voids, increasing dramatically the total number of voids to analyze. Both of these achievements are crucial for the effective statistical analysis of the properties of cosmic voids.

We underline how the extensive spatial distribution of cosmic voids, combined with their

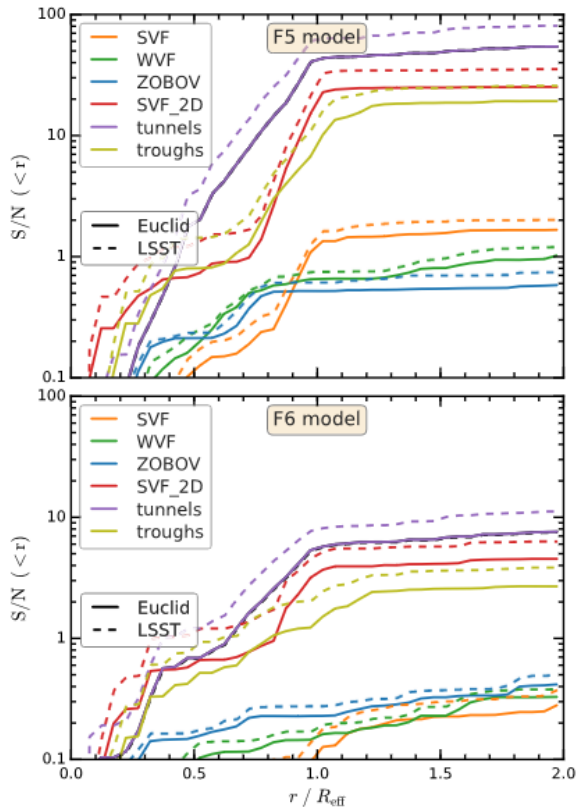


**Figure 3.2:** Differences between  $f(R)$  and GR models in the cumulative tangential shear  $S/N$  as a function of the rescaled void radius. These discrepancies are computed for the scenario F5 (i.e with  $f_{R0} = -10^{-5}$ , top panel) and F6 (i.e with  $f_{R0} = -10^{-5}$ , bottom panel). Each color represents one of the six void types examined in this study. Predictions for lensing on *Euclid*-like and LSST-like surveys are illustrated with solid and dashed lined respectively. In both  $f(R)$  gravity models and for both surveys, tunnels (purple curve) show  $S/N$  greater than all other void definitions, both 2D and 3D. Credits to: [Cautun et al. \(2018\)](#).

distinct underdense characteristics, renders these objects the perfect setting for testing various cosmological models. The most studied cosmological contribution of void statistics comes from number counts and density profiles. In particular, concerning the first statistics, we show that the application of the so-called excursion set formalism enables the prediction of void counts as a function of their radius.

### 3.2.1 Size function

For cosmic voids, just like with what happens to clusters, a zero-order statistics can be defined through object counts, and it can be used to constrain the cosmological parameters. Though, while number counts for overdensities are determined as a function of mass, yielding the halo mass function, void counts are determined as a function of radius since they are poor of matter. In this context, it is defined *void size function* (VSF) the comoving number density of voids as a function of their effective radius.

The VSF has been modeled for the first time in [Sheth & van de Weygaert \(2004\)](#) where the authors introduced the Sheth-van de Weygaert model (SvdW), with the same excursion-set approach used to model the mass function of DM halos ([Press & Schechter 1974](#); [Bond et al. 1991](#)). In the following, we will briefly describe the excursion-set formalism, to serve as a basis for the theoretical model of the void size function.

## Excursion-set formalism

The excursion-set formalism is an analytical framework for examining the LSS of the Universe. Using this method, we may forecast the numerical density of cosmic objects by connecting the linear perturbation theory of cosmology to its nonlinear equivalent at late times (Bond et al. 1991). The excursion set formalism relies on understanding the statistical characteristics of the linear density field. In combination with the spherical collapse approximation, this approach offers insights into many aspects of halo formation and can be used to predict DM halos abundances and clustering (see Zentner 2007; Jennings et al. 2013).

Recalling the formalism introduced in Sect. 1.5.1, smoothing Eq. (3.1) on a scale  $R$  through a filter function in Fourier space  $W(\mathbf{k}, R)$ , we obtain the smoothed linear density perturbation field in real space as:

$$\delta(\mathbf{x}, R) = \frac{1}{(2\pi)^3} \int \hat{\delta}(\mathbf{k}, R) W(\mathbf{k}, R) e^{i\mathbf{k}\cdot\mathbf{x}} d^3\mathbf{k}, \quad (3.1)$$

where  $\mathbf{x}$  is the punctual comoving position and  $\hat{\delta}(\mathbf{k})$  is the Fourier transform of the point density contrast field in that position. The smoothing scale  $R$  is related to the corresponding variance of the linear density field, calculated based on the size of the region under consideration:

$$\sigma^2(R) \equiv S(R) = \frac{1}{(2\pi)^2} \int k^2 P(k) |W(\mathbf{k}, R)|^2 dk, \quad (3.2)$$

where  $P(k)$  is the matter power spectrum in linear theory. We can describe a trajectory  $\delta(x, S)$  as a sequence of overdensities resulting from successive increases in the smoothing scale by increments of  $\Delta S$ . The random walk is carried out by  $\delta(x, S)$  when a top-hat filter in  $k$ -space is applied. With an assumed Gaussian distribution for the linear density field, the excursion-set formalism enables us to assign probabilities to random walks that meet specific criteria for the smoothing scale at which they cross different density thresholds.

The spherical evolution model combined with the excursion-set gives a fair explanation of the statistics of DM halos for the collapse of perturbations. A collapse takes place when the linear density fluctuation hits a barrier or critical value  $\delta_c^L$ , which is calculated in linear theory<sup>3</sup>, as it was covered in Sect. 1.5.3. Using the excursion-set formalism we can determine the fraction of trajectories that cross for the first time this barrier, taking into consideration the *cloud-in-cloud* process as well. This process happens when the trajectories repeatedly cross the  $\delta_c^L$  threshold during the creation of a structure, and physically speaking, this happens when one collapsing halo envelops another halo. In this context, it is required to take into account as halo only those items that do not include larger objects; that is, to take into account just the minimum feasible value of  $\sigma(M)$  measured at each of the threshold crossings.

We can expand the model to forecast the development of underdense regions within the initial density field, which are inherently linked to voids in the evolved density field observed today. A crucial assumption underlying the connection between the excursion set and the abundance of nonlinear objects is that each collapse happens independently. This concept is applicable to collapsing objects because the comoving volume they occupy decreases. Unlike overdense regions, which contract, voids expand. We will observe that this poses a challenge when aligning the predictions of the excursion set with void statistics. Nevertheless, we will begin with the basic spherical evolution model outlined in Sheth & van de Weygaert (2004) where the critical density threshold is established as the shell-crossing density,  $\delta_v^L = -2.71$ . We can utilize the excursion-set formalism to calculate the fraction of random walks that cross

---

<sup>3</sup>This value lies in the range  $\delta_c^L = [1.06, 1.686]$ , between the density contrast of turn-around point and the complete halo collapse, respectively.

the barrier  $\delta_c^L$ . Similar to the cloud-in-cloud process, the concept of the *void-in-void* process acknowledges that a void of a certain size could exist within another underdense region on a larger scale. Therefore, we establish the first crossing distribution by linking the random walks with the smoothing scale at which they initially pierce the barrier  $\delta_v^L$ . Another scenario, known as the *void-in-cloud* process, arises when a void of a particular size is encompassed within an overdense region on a larger scale. Eventually, this larger region will collapse into a halo, eliminating the void. The scenario where a large underdense region encompasses a small overdense one, termed *cloud-in-void*, is inconsequential for the formation of collapsed structures. This is because the clouds condensing in a large-scale void are not torn apart as their parent void expands around them (van de Weygaert 2014). The disparity between the void-in-cloud and cloud-in-void processes results in an asymmetry between the populations of halos and voids: both evolve from the same symmetric Gaussian initial conditions, but overdensities and underdensities are anticipated to evolve toward distributions with distinct characteristics. In order to account for this asymmetry, Sheth & van de Weygaert (2004) proposed that the excursion-set method applied to voids requires a second barrier, the threshold for collapse of overdense regions,  $\delta_c^L$ . Hence, in computing the first crossing distribution, we must ascertain the maximum scale at which a trajectory breaches the threshold  $\delta_v^L$ , provided it has not surpassed  $\delta_c$  at any larger scale. In Figure 3.3 we present an overview of the four processes involved in the formation of halos and voids as described by the excursion-set formalism.

### Theoretical model formulation

As mentioned above, in a double barrier problem, the distribution of fluctuations that evolve into voids is derived as the conditional first crossing distribution of the matter density contrast filtered at decreasing Lagrangian radius. A fluctuation can be considered a void with a radius  $R_v$  only if the density contrast, filtered at this scale, surpasses the negative linear threshold for void formation,  $\delta_v^L$ , without exceeding the critical collapse threshold for an overdensity  $\delta_c^L$  at any larger scale. This model is based on the assumption of sphericity for voids, in analogy with the derivation for spherical fluctuations in Lagrangian space of the multiplicity function in Sheth & van de Weygaert (2004). The density field initially evolved linearly at the relevant epoch, whereas the observed voids exist in Eulerian space, meaning they are part of the completely nonlinearly evolved density field.

The excursion-set theory, when applied to underdense regions, forecasts the fraction of the Universe occupied by cosmic voids, which is determined by the multiplicity function  $f_{\ln \sigma}$ :

$$f_{\ln \sigma} = 2 \sum_{j=1}^{\infty} j\pi x^2 \sin(j\pi\mathcal{D}) \exp\left[-\frac{j\pi x^2}{2}\right] \quad (3.3)$$

with

$$x \equiv \frac{\mathcal{D}}{|\delta_v^L|} \sigma \quad ; \quad \mathcal{D} \equiv \frac{|\delta_v^L|}{\delta_c^L + |\delta_v^L|}, \quad (3.4)$$

where  $\sigma$  is the square root of the mass variance filtered on a radius  $R$ . At this point, from Eq. (3.3), it is feasible to derive the distribution of void number density as a function of their size within linear theory as:

$$\frac{dn^L}{d \ln r^L} = \frac{f_{\ln \sigma}(\sigma) d \ln \sigma^{-1}}{V(r^L) d \ln r^L}, \quad (3.5)$$

where  $V(r^L) = \frac{4}{3}\pi (r^L)^3$  is the volume of the spherical perturbation of radius  $r^L$ .

Now, in order to move from the linear to the nonlinear theory, it is possible to assume the conservation of the total number of voids. In addition, as we anticipated in Sect. 1.5.3, when

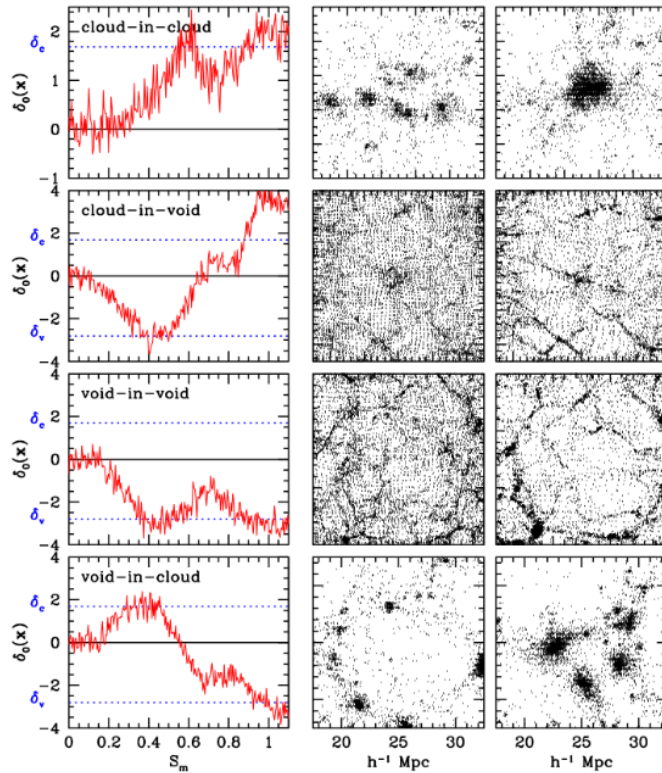


**Figure 3.3:** Four modes of the excursion-set formalism for a two-barrier problem. Each row corresponds to one of the four fundamental modes of hierarchical clustering: the cloud-in-cloud process, the cloud-in-void process, the void-in-void process, and the void-in-cloud process (from top to bottom). Each mode is illustrated using three frames. The panels on the left display random walks representing the local density perturbation  $\delta_0(\mathbf{x})$  plotted against the (mass) resolution scale  $S_m$ . In each graph, the dashed horizontal lines indicate the collapse barrier  $\delta_c$  and the shell-crossing void barrier  $\delta_v$  (the superscript  $L$  is not specified here). The two frames on the right illustrate the evolution of the associated particle distribution, first at an earlier time (second column) and then at a later time (third column). Credits to: [Sheth & van de Weygaert \(2004\)](#).

underdensities approach shell-crossing, they will have expanded according to  $a \propto (\delta_v^L)^{-3}$ . This necessitates to correct the linear radius, and so the void abundance becomes:

$$\left. \frac{dn}{d \ln r} \right|_{\text{SvdW}} = \frac{dn}{d \ln (ar^L)}, \quad (3.6)$$

with the relation linking the linear and nonlinear radii is:

$$\frac{r}{r^L} = \left( \frac{\bar{\rho}}{\rho_v} \right)^{1/3} \quad (3.7)$$

where  $\bar{\rho}$  represents the mean density of the Universe, while  $\rho_v$  denotes the average density within the void under consideration.

As highlighted in [Jennings et al. \(2013\)](#), considering the inherent tendency of voids to expand and intersect, the assumption of conservation of the number of voids may not be valid, especially for large voids. Given that only void-in-cloud process is accounted in the parameter  $\mathcal{D}$  of the SvdW model but not the void-in-void side effect, this renders the model unphysical. In this regard, to falsify the model, it is useful to calculate the fraction of the

entire volume of the Universe occupied by voids as:

$$\mathcal{F}(R) = \int_R^\infty V(r) \frac{dn}{d \ln r} \frac{dr}{r} > 1. \quad (3.8)$$

From this, we can observe that the prediction of the SvdW model is incorrect since it predicts a volume occupied by voids greater than the total volume of the Universe.

To address the challenges related to the total void volume in the SvdW model, [Jennings et al. \(2013\)](#) introduced the volume conserving (Vdn) model. Unlike the SvdW model, the Vdn model no longer relies on conserving the total number of voids, instead, it assumes that the total volume of voids remains constant during the transition from the linear to the nonlinear regime. Particularly, they define the volume fraction in linear theory,  $\mathcal{F}_L$ , as:

$$\mathcal{F}_L(R) = \int_{R^L}^\infty V(r^L) \frac{dn}{d \ln r^L} \frac{dr^L}{r^L}. \quad (3.9)$$

They demonstrate that this fraction is conserved by defining the nonlinear abundance as

$$V(r)dn = V(r^L) dn^L|_{r^L(r)}, \quad (3.10)$$

obtaining the abundance of voids expressed in the form:

$$\left. \frac{dn}{d \ln r} \right|_{\text{Vdn}} = \left. \frac{V(r^L)}{V(r)} \frac{dn}{d \ln r^L} \frac{d \ln r^L}{d \ln r} \right|_{r^L(r)}. \quad (3.11)$$

A comparison of the volume fractions of the Universe occupied by the voids expected to form in the two different investigated models is presented in [Figure 3.4](#). The Vdn model conserves the entire fraction from the linear theory, whereas for the SvdW model the fraction unphysically exceeds unity. Conversely, [Figure 3.5](#) displays the calculated VSF along with the corresponding void abundance as determined by simulations. The Vdn model and void counts correspond very well, whereas the SvdW model, which consistently overestimates abundances, does not.

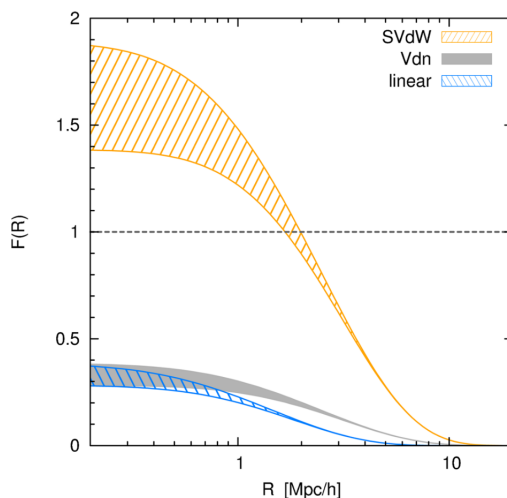


**Figure 3.4:** The cumulative volume fraction occupied by voids with radii larger than  $R$  is compared across different theoretical models: linear theory (blue striped region,  $R = r^L$ ), SvdW model (orange striped region,  $R = r$ ), and Vdn model (grey shaded region,  $R = r$ ). These regions correspond to an expected range of  $1.06 \leq \delta_c^L \leq 1.686$ , with  $\delta_v^L = -2.7$  maintained throughout. In the case of the SvdW model, the fraction unphysically exceeds unity at  $R \sim 2 h^{-1} \text{Mpc}$ , while the Vdn model conserves the total fraction from linear theory,  $\mathcal{F}(0) \sim 0.3$ . Credits to: [Jennings et al. \(2013\)](#).

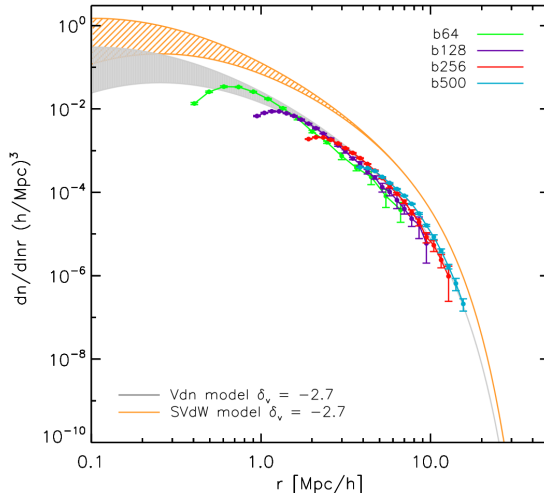


**Figure 3.5:** The void abundance in simulations is compared to model predictions. Voids are characterized by a radius equivalent to the radius of a sphere with a density  $\rho_v = 0.2\bar{\rho}_m$  in the DM distribution of  $\Lambda$ CDM cosmology simulations. Simulations are conducted with box sizes of  $64 h^{-1}\text{Mpc}$  (green),  $128 h^{-1}\text{Mpc}$  (purple),  $256 h^{-1}\text{Mpc}$  (red), and  $500 h^{-1}\text{Mpc}$  (cyan). The error bars represent the dispersion around the mean from eight different realizations of this cosmology in each box size. The range in predictions covers the parameter interval  $\delta_c = [1.06, 1.686]$ , with  $\delta_v = -2.7$ . It is evident how the data are consistent with simulations for the Vdn model (grey shaded), but not for the SvW model (orange hatched). Credits to: [Jennings et al. \(2013\)](#).

### 3.2.2 Density profile

The void density profile represents another significant statistical measure extensively examined in recent literature ([Sutter et al. 2014](#); [Hamaus et al. 2014](#); [Voivodic et al. 2020](#)). It is defined as the average relative deviation of mass density  $\rho_v(r)$  or number density  $u_v(r)$  from the mean density of the Universe,  $\bar{\rho}$ , around the center of a void:

$$u_v(r) \equiv \frac{n_{vg}(r)}{\langle n_g \rangle} - 1 = \frac{\rho_v(r)}{\bar{\rho}} - 1, \quad (3.12)$$

where  $n_{vg}(r)$  is the galaxy (or, more generally, the matter tracer) number density in a sphere of radius  $r$  centered on a void and  $\langle n_g \rangle$  the average density of galaxies and  $\rho_v$  and  $\bar{\rho}$  are their corresponding mass density, respectively. With the use of tracer particles, one can estimate the density within a radial shell, which has a thickness of  $2\delta r$  and is located at a distance  $r$  from the center of a void, as

$$\rho_v(r) = \frac{3}{4\pi} \sum_i \frac{m_i(\mathbf{r}_i) \Theta(r_i)}{(r + \delta r)^3 - (r - \delta r)^3}, \quad (3.13)$$

where  $m_i$  is the mass of particle  $i$ ,  $\mathbf{r}_i$  its coordinate vector of length  $r_i$ , and  $\Theta$  define the radial bin combining two Heaviside step functions  $\theta$ , like  $\Theta(r_i) \equiv \theta[r_i - (r - \delta r)] \theta[-r_i + (r + \delta r)]$ .

Various functional shapes have been suggested for void density profile in literature. These can be categorized into two primary groups: empirical models, which seek an appropriate form to match the void density profile ([Paz et al. 2013](#); [Nadathur et al. 2015](#); [Hamaus et al. 2014](#); [Voivodic et al. 2020](#)), and theoretically driven models ([Finelli et al. 2015](#)). In particular, the most widely used belongs to the first category and is the so-called Hamaus-Sutter-Wandelt (HSW) profile presented in [Hamaus et al. \(2014\)](#). It follows a simple parametric form:

$$\frac{\rho_v(r)}{\bar{\rho}} - 1 = \delta_c \frac{1 - (r/r_s)^\alpha}{1 + (r/r_v)^\beta}, \quad (3.14)$$

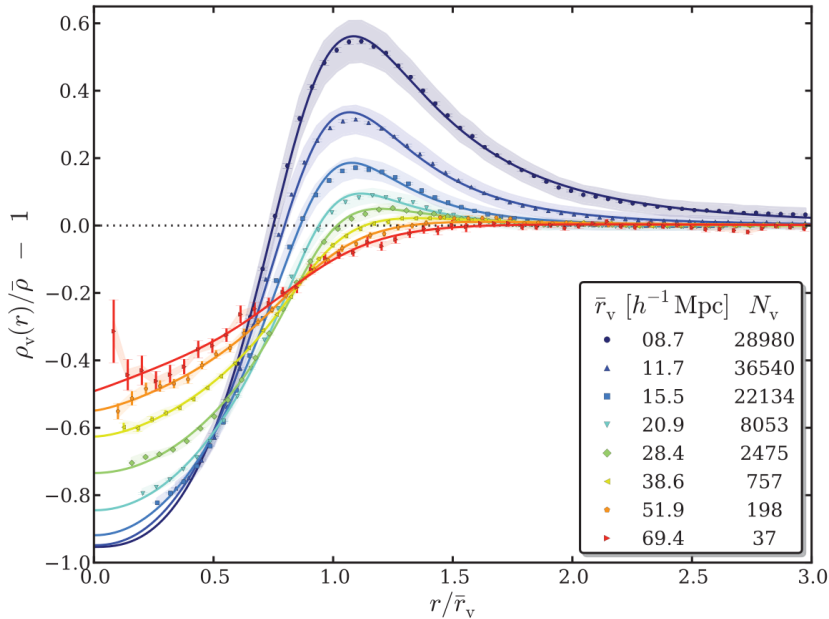


**Figure 3.6:** Stacked density profiles of voids at  $z = 0$  are presented in eight consecutive bins based on void radius, with mean values and counts of voids reported in the inset. Shaded regions represent the standard deviation  $\sigma$  within each stack (scaled down by 20 for clarity), while error bars depict standard errors on the mean profile  $\sigma/\sqrt{N_v}$ . Solid lines show the best-fit solutions of the Eq. (6.13). Credits: [Hamaus et al. \(2014\)](#).

where  $\delta_c$  is the central density contrast,  $r_s$  a scale radius at which  $\rho_v = \bar{\rho}$ , called *effective radius*, and  $\alpha$  and  $\beta$  determine the inner and outer slope, respectively, of the density maximum resulting from the overdense shell surrounding the void, called *compensation wall*.

In Figure 3.6 we show the best fits of this model to the stacked density profiles of cosmic voids identified with VIDE (see Sect. 3.1) in a  $N$ -body simulation. [Hamaus et al. \(2014\)](#) voids are significantly underdense in their interiors, particularly the smaller ones. All profiles exhibit compensation walls of increased density, with a peak slightly beyond their effective radius, which shifts outward for larger voids. The height of these compensation walls diminishes with void size, resulting in a less steep inner profile slope and a broader wall. This pattern distinguishes voids as either overcompensated or undercompensated, depending on whether the total mass inside their compensation wall exceeds or falls short of the mass absent in the center. Ultimately, at sufficiently large distances from the void center, all profiles converge toward the mean background density.

Another approach to compute density profiles involves calculating the cross-correlation between the centers of voids and tracer particles, utilizing the two-point correlation function,  $\xi_{v,g}(r)$ . This estimator quantifies the probability of encountering a tracer at a comoving distance  $r$  from a void center (refer to Sect. 1.5.1 for details). This can be represented as the integrated profile of void density contrast, calculated within a sphere of radius  $r$  and volume  $V$  centered on voids:

$$\xi_{v,g}(r) = \frac{1}{3r^2} \frac{d}{dr} [r^3 \Delta(r)] , \quad (3.15)$$

where

$$\Delta(r) = \frac{3}{r^3} \int_0^r u_v(r') r'^2 dr' , \quad (3.16)$$

with  $u_v$  being the quantity defined in Eq. (6.13). The two methodologies presented for estimating void density profiles are equivalent and lead to the same result.

### 3.3 Weak gravitational lensing

One of the most promising studies that can be used to investigate MG models in voids is related to the phenomenon of gravitational lensing. We understand from GR that the trajectory of light rays traveling from a source to an observer is affected by both the gravitational field of local structures and the geometry of the Universe (Schneider et al. 1992). Lensing refers to the deflection of photons emitted by distant galaxies as they travel towards the observer, caused by matter fluctuations along the line of sight (Sereno & Umetsu 2011). As a result, images of background sources exhibit gravitational lensing signatures due to the presence of cosmic structures, enabling the investigation of the mass and density distribution of cosmic objects present along the line of sight (Blandford & Narayan 1992; Umetsu 2020). Additionally, tomographic studies of the observed lensing signal, conducted across large survey areas and in redshift bins, offer insights into the redshift evolution of the LSS of the Universe and provide robust constraints on cosmological parameters. Indeed, such tomographic studies, also known as *cosmic shear* analyses, represent primary cosmological probes in both current (see, e.g., Giblin et al. 2021; Amon et al. 2022) and future (LSST Dark Energy Science Collaboration 2012; Laureijs et al. 2011) surveys.

In this section, we introduce the fundamental concepts of gravitational lensing, with a focus on WL regime. The analysis of the WL from voids concerns, therefore, the small distortions of background light sources caused by underdense regions. Unlike its strong counterpart, which is observable when a lens and a lensed source are precisely aligned along the line of sight, WL is more prevalent and thus better suited for statistical investigations.

#### 3.3.1 Lens equation

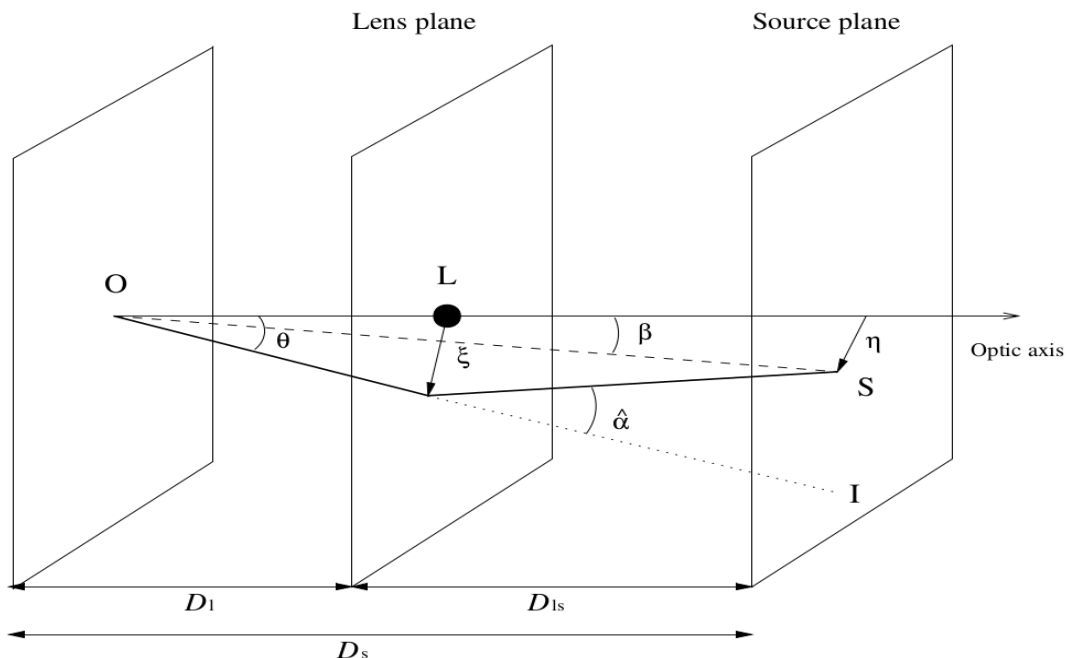


**Figure 3.7:** Scheme representing the lens system described in Sect. 3.3.1. Credits to Umetsu (2020).

Let us consider the system depicted in Fig. 3.7 to introduce the lens equation, which describes the bending of light ray trajectories due to intervening matter along the line of sight. We

use the *thin lens* approximation, in which the surface density of the lens matter perfectly describes its distribution. Given that the physical size of the lens is typically much smaller than the distances between the observer, lens, and source, this estimate is accurate.

The line that passes across the sites of the lens and the observer is what we refer to as the *optical axis*. The observer, lens, and source planes—referred to as O, L, and S, respectively—are all perpendicular to the optical axis. We consider in particular a distant source behind the lens at a position  $\eta = \beta D_s$  on S, where  $D_s$  is the angular diameter distance between the observer and the source and  $\beta$  is the angle subtended by  $\eta$ . The observer measures an angle  $\theta$  between the optical axis and the source position on L, namely  $\xi = \theta D_l$ , where  $D_l$  is the observer-lens angular diameter distance. This is because the lens deflects the trajectory of a light ray generated by the source by a bending angle  $\hat{\alpha}$ .

If  $\beta$ ,  $\theta$ , and  $\hat{\alpha}$  are small, we derive the formula that connects the true position of the source S, to its observed position I:

$$\theta D_s = \beta D_s + \hat{\alpha} D_{ls}, \quad (3.17)$$

where  $D_{ls}$  is the angular diameter distance between lens and source. Defining the reduced deflection angle,  $\alpha = \hat{\alpha} D_{ls} / D_s$ , we obtain the lens equation, expressed as:

$$\beta = \theta - \alpha(\theta). \quad (3.18)$$

The lens equation is valid only in the local Universe and we can note that it may have more than one solution  $\theta$  for a source position  $\beta$  (Hattori et al. 1999; Kneib & Natarajan 2011).

### 3.3.2 Convergence and shear

Consider a lens in terms of an extended distribution of matter to understand how the lens equation, Eq. (3.18), describes the deflection of the light ray path in relation to gravity. Under the Born approximation<sup>4</sup> and neglecting lens-lens coupling, the deflection angle can be expressed as the gradient of a 2D lensing potential. This potential is obtained by projecting the 3D Newtonian potential<sup>5</sup>,  $\Phi$ , onto the lens plane and simply rescaling it. We can describe the lens effective 2D gravitational potential,  $\hat{\Psi}$ :

$$\hat{\Psi}(\theta) \equiv \frac{D_{ls}}{D_l D_s} \frac{2}{c^2} \int_0^{z_s} \Phi(\theta D_l, z) dz, \quad (3.19)$$

where  $\theta$  is the observed angular position of the lensed image, the angular diameter distances are in comoving units,  $c$  is the speed of light,  $z$  is the redshift and  $z_s$  is the source redshift. Eq. (3.19), therefore, behaves as the Poisson equation projected and weighted by a geometric factor based on the distances to the lens, source, and observer. It suggests that the reduced deflection angle is equal to the gradient of  $\hat{\Psi}$ , that is to say

$$\nabla \hat{\Psi}(\theta) = \alpha(\theta). \quad (3.20)$$

Now, expressing the *convergence*,  $\kappa$ , as

$$\kappa(\theta) = \frac{\Sigma(\theta)}{\Sigma_{\text{cr}}}, \quad (3.21)$$

<sup>4</sup>It is the perturbation method used for scattering by an extended body or field. It involves using the incident field as the driving field at each point in the scatterer rather than the total field. This method is accurate if the dispersed field is modest in comparison to the incident field on the scatterer (see Bartelmann & Schneider 2001, for a detailed review).

<sup>5</sup>It denotes the 3D gravitational potential given by the Poisson equation  $\nabla^2 \Phi = 4\pi G a^2 \delta\rho_m$ , where  $\delta\rho_m = \rho_m - \bar{\rho}_m$  with  $\rho_m$  and  $\bar{\rho}_m$  the local and the background matter density respectively;  $a$  is the scale factor; and  $G$  is the gravitational constant.

where  $\Sigma$  is the surface mass density, while  $\Sigma_{\text{cr}}$  is the critical surface mass density, which is defined as

$$\Sigma_{\text{cr}} \equiv \frac{c^2}{4\pi G} \frac{D_s}{D_l D_{ls}}, \quad (3.22)$$

we can obtain that the Laplacian of  $\hat{\Psi}$  is

$$\nabla^2 \hat{\Psi}(\boldsymbol{\theta}) = 2\kappa(\boldsymbol{\theta}). \quad (3.23)$$

$\Sigma_{\text{cr}}$ , in Eq. (3.22), barely depends on the source redshift (Umetsu 2020) if the source redshift is significantly larger than the lens redshift, which lessens the importance of precisely defining the source redshift distribution (Okabe et al. 2010).

From Eq. (3.18), mapping the  $\boldsymbol{\beta}$  points on the source plane onto the  $\boldsymbol{\theta}$  points on the lens plane, we obtain the following Jacobian matrix,  $\mathbf{A}$ :

$$\mathbf{A} = \frac{\partial \boldsymbol{\beta}}{\partial \boldsymbol{\theta}} = \left( \delta_{ij} - \frac{\partial \alpha_i(\boldsymbol{\theta})}{\partial \theta_j} \right) = (\delta_{ij} - \Psi_{ij}), \quad (3.24)$$

where  $\delta_{ij}$  is the Kronecker delta, while  $\theta_i$  and  $\theta_j$  are the  $i$ -th and  $j$ -th components of  $\boldsymbol{\theta}$ , respectively.  $\Psi$  is defined as:

$$\Psi_{ij} \equiv \frac{\partial^2 \hat{\Psi}(\boldsymbol{\theta})}{\partial \theta_i \partial \theta_j}, \quad (3.25)$$

and from this we can write

$$\mathbf{A} = A_{ij} = \begin{pmatrix} 1 - \Psi_{11} & -\Psi_{12} \\ -\Psi_{12} & 1 - \Psi_{22} \end{pmatrix}. \quad (3.26)$$

This is called *deformation matrix*, it is a  $2 \times 2$  matrix and a tensor of rank 2 which describes the first-order mapping between the plane of the lens (LP) and the plane of the source (SP). It can be written as the sum of its isotropic  $A_{\text{iso}}$  and anisotropic  $A_{\text{aniso}}$  components:

$$\mathbf{A} = A_{\text{iso}} + A_{\text{aniso}}, \quad (3.27)$$

with

$$A_{\text{iso}} = \left( \frac{1}{2} \text{tr} A \cdot I \right)_{ij} = (1 - \kappa) \delta_{ij}, \quad (3.28)$$

where  $\text{tr} A$  is the trace of  $A$  and  $I$  is the identity matrix. The  $A_{\text{iso}}$  transformation preserves the directions of the vectors to which it is applied, and it tells us that convergence is a quantity that describes a transformation that at first order is isotropic. Images are rescaled by a constant factor in all directions as a result of the convergence, which causes isotropic modifications of the original shape.

We now focus on the anisotropic component of  $A$ , which can be obtained as follows:

$$A_{\text{aniso}} = (A - A_{\text{iso}})_{ij} = \begin{pmatrix} -\frac{1}{2}(\Psi_{11} - \Psi_{22}) & -\Psi_{12} \\ -\Psi_{12} & \frac{1}{2}(\Psi_{11} - \Psi_{22}) \end{pmatrix}. \quad (3.29)$$

$A_{\text{aniso}}$  is therefore an antisymmetric matrix that has null trace, and is the opposite matrix of what is called the *shear matrix*. It describes an anisotropic transformation that has a privileged direction, defined by the largest eigenvalue. The gradient of the gravitational force, or the gravitational tidal field projection, can be measured and this allows to model the distortions seen in background sources. In particular, the differential deflection of light

bundles causes the shape distortion of extended sources. We can define the *shear* pseudovector  $\gamma = (\gamma_1, \gamma_2)$  on the LP, where the  $\gamma_1$  and  $\gamma_2$  components are expressed as follows:

$$\gamma_1 = \frac{1}{2}(\Psi_{11} - \Psi_{22}), \quad (3.30)$$

$$\gamma_2 = \Psi_{12} = \Psi_{21}. \quad (3.31)$$

Given that the eigenvalues of the shear matrix are  $\pm\sqrt{\gamma_1^2 + \gamma_2^2} = \pm\gamma$ , it is feasible to rotate the coordinates by an angle  $\phi$  in a way that maintains the following expression:

$$\begin{pmatrix} \gamma_1 & \gamma_2 \\ \gamma_2 & -\gamma_1 \end{pmatrix} = \gamma \begin{pmatrix} \cos 2\phi & \sin 2\phi \\ \sin 2\phi & -\cos 2\phi \end{pmatrix}. \quad (3.32)$$

From Eqs. (3.29) and (3.28), the  $A$  matrix can be parametrized in terms of convergence,  $\kappa$ , and shear,  $\gamma = \gamma_1 + i\gamma_2$ , so we express the deformation matrix as follows:

$$\mathbf{A} = \begin{pmatrix} 1 - \kappa - \gamma_1 & -\gamma_2 \\ -\gamma_2 & 1 - \kappa + \gamma_1 \end{pmatrix} = (1 - \kappa) \begin{pmatrix} 1 & 0 \\ 0 & 1 \end{pmatrix} - \gamma \begin{pmatrix} \cos 2\phi & \sin 2\phi \\ \sin 2\phi & -\cos 2\phi \end{pmatrix}. \quad (3.33)$$

The eigenvalues of  $\mathbf{A}$  are  $\lambda_{\pm} = 1 - \kappa \pm \gamma$ , with  $\lambda_+ \geq \lambda_-$ . We observe from Eq. (3.33) that the image distortions are minimal in the regime where  $|\kappa| \ll 1$  and  $|\gamma| \ll 1$ . The *weak lensing* (WL) regime is the name we give to this limiting case.

In addition, as a consequence of Liouville's theorem<sup>6</sup>, lensing conserves the surface brightness of background sources. Consequently, lensed images are magnified; this process is measured by the magnification factor,  $\mu$ , which can be written as:

$$\mu = \frac{\delta\Omega^I}{\delta\Omega^S} = \frac{1}{\det A} = \frac{1}{(1 - \kappa)^2 - \gamma^2}, \quad (3.34)$$

where  $\det A$  is the determinant of  $A$  and  $\delta\Omega^I$  and  $\delta\Omega^S$  are the lensed and unlensed image solid angles, respectively.

### 3.3.3 Weak-lensing signal from observed ellipticity

As it was previously mentioned, WL occurs more frequently than strong lensing. This is simply due to statistical reasons, as the occurrence of strong lensing necessitates the (unlikely) alignment of the source and lens along the line of sight (Hattori et al. 1999). On the other hand, the WL phenomenon results in less pronounced effects and can only be detected statistically over a large number of galaxies. It is extensively used in cosmology to map the LSS of the Universe (Kilbinger 2015b) and plays a critical role in the estimation of galaxy cluster masses and density of vast regions (Umetsu 2020), which is an important requirement for carrying out cosmological analyses based on these statistical features (Allen et al. 2011).

Nevertheless, detecting the subtle image distortions caused by weak lensing (WL) is challenging due to shape measurement noise, the isotropic smearing component of the point spread function (PSF), and the impact of instrumental PSF anisotropy. A method to accurately extract the lensing signal from noisy images of source galaxies was first proposed by Kaiser et al. (1995). Over the following few decades, this method has been improved and extended (see, e.g., Kuijken 1999; Bridle et al. 2002; Heymans et al. 2006; Refregier et al. 2012; Mandelbaum et al. 2018). This method is based on the quadrupole moments,  $Q_{ij}$  with

<sup>6</sup>This theorem states that in an ensemble of many identical states with distinct initial circumstances, the density of states remains constant along all trajectories in phase space.

$i, j = 1, 2$ , of the source brightness distribution,  $I(\boldsymbol{\theta})$ , which are expressed as (Kaiser et al. 1995):

$$Q_{ij} = \frac{\int d^2\theta q_I[I(\boldsymbol{\theta})] \Delta\theta_i \Delta\theta_j}{\int d^2\theta q_I[I(\boldsymbol{\theta})]}, \quad (3.35)$$

where  $q_I[I(\boldsymbol{\theta})]$  is a weight depending on the brightness (Bartelmann & Schneider 2001), and  $\Delta\theta_i = \theta_i - \bar{\theta}_i$  is the offset from the centroid of the image. We can express the complex ellipticity,  $e = e_1 + ie_2$ , as

$$e = \frac{Q_{11} - Q_{22} + 2iQ_{12}}{Q_{11} + Q_{22}}. \quad (3.36)$$

It allows us to calculate  $e_s$ , the intrinsic source ellipticity, as

$$e_s = \frac{e - 2g + e^*g^2}{1 + |g|^2 - 2\Re(e^*g)}, \quad (3.37)$$

where the complex conjugate of  $e$  is  $e^*$ , and the reduced shear is  $g = \gamma/(1 - \kappa)$ .  $\mathbb{E}(e_s)$ , the  $e_s$  expectation value, is null since  $e$  is invariant under  $\pi$  rotations. Eq. (3.37) in this scenario becomes (Schneider & Seitz 1995)

$$\sum_n w_n \frac{e_n - \delta_g}{1 - \Re(e_n^* \delta_g)} = 0, \quad (3.38)$$

where  $e_n$  and  $w_n$  are the image ellipticity and the statistical weight of the  $n$ -th object, respectively.  $\delta_g$  is the complex distortion and it is expressed as:

$$\delta_g = \frac{2g}{1 + |g|^2}. \quad (3.39)$$

In the weak lensing regime, that is  $|\kappa|, |\gamma| \ll 1$ , Eq. (3.37) reduces to  $e_s \simeq e - 2g$ . Consequently, the observed decreased shear in the WL regime can be represented as follows, assuming randomly oriented sources:

$$\langle g \rangle \simeq \frac{\langle e \rangle}{2}, \quad (3.40)$$

where the average of the source ensemble's observed ellipticities is denoted by  $\langle e \rangle$ . With  $N$  being the number of sources and  $\sigma$  being the source ellipticity dispersion, which is dominated by the intrinsic shape noise, the statistical uncertainty on  $\langle g \rangle$  reduces as  $\propto \sigma/\sqrt{N}$ . The observed decreased shear,  $g^{\text{ob}}$ , is typically stated as a function of the real reduced shear,  $g^{\text{tr}}$  (Heymans et al. 2006; Massey et al. 2007; Mandelbaum et al. 2014), in order to account for biases produced by observational and instrumental effects

$$g_i^{\text{ob}} = (1 + m_i) g_i^{\text{tr}} + c_i \quad (i = 1, 2), \quad (3.41)$$

where estimates for  $m_i$  and  $c_i$  are derived from simulation and observational samples of galaxies.

### 3.3.4 Tangential and cross shear

From Eq. (3.40), we deduce that observed ellipticities can be used to infer shear in the WL regime. We also note that the shear components  $\gamma_1$  and  $\gamma_2$ , introduced in Sect. 3.3.2, rely on the chosen coordinate frame. In order to identify coordinate-independent shear components with respect to a specified reference point, we define the polar coordinate frame  $(\vartheta, \varphi)$  centered

on  $\boldsymbol{\theta}_c$ , such that  $\boldsymbol{\theta} = (\vartheta \cos \varphi, \vartheta \sin \varphi) + \boldsymbol{\theta}_c$ . We can express the convergence averaged within and along a circle of radius  $\vartheta$  and center  $\boldsymbol{\theta}_c$ ,  $\bar{\kappa}(\vartheta)$  and  $\kappa(\vartheta)$ , as:

$$\bar{\kappa}(\vartheta) = \frac{2}{\vartheta^2} \int_0^\vartheta d\vartheta' \vartheta' \kappa(\vartheta') = \frac{\bar{\Sigma}(\vartheta)}{\Sigma_{\text{cr}}}, \quad (3.42)$$

$$\kappa(\vartheta) = \oint \frac{d\varphi}{2\pi} \kappa(\vartheta, \varphi) = \frac{\Sigma(\vartheta)}{\Sigma_{\text{cr}}}, \quad (3.43)$$

where  $\bar{\Sigma}(\vartheta)$  is the surface mass density averaged within a circle with radius  $\vartheta$ ,  $\Sigma(\vartheta)$  is the surface mass density averaged along a circle with radius  $\vartheta$ , and  $\Sigma_{\text{cr}}$  the surface critical density, as defined in Eq. (3.22).

Next, we present the cross shear component, denoted as  $\gamma_\times$ , which is a 45° rotation, and the tangential shear,  $\gamma_+$  or  $\gamma_t$ . Their expressions are the following:

$$\gamma_+(\boldsymbol{\theta}) = -\gamma_1(\boldsymbol{\theta}) \cos(2\varphi) - \gamma_2(\boldsymbol{\theta}) \sin(2\varphi), \quad (3.44)$$

$$\gamma_\times(\boldsymbol{\theta}) = +\gamma_1(\boldsymbol{\theta}) \sin(2\varphi) - \gamma_2(\boldsymbol{\theta}) \cos(2\varphi). \quad (3.45)$$

From these equations, we find (Kaiser 1995):

$$\gamma_+(\vartheta) = \oint \frac{d\varphi}{2\pi} \gamma_+(\vartheta, \varphi) = \bar{\kappa}(\vartheta) - \kappa(\vartheta) = \frac{\Delta\Sigma(\vartheta)}{\Sigma_{\text{cr}}}, \quad (3.46)$$

$$\gamma_\times(\vartheta) = \oint \frac{d\varphi}{2\pi} \gamma_\times(\vartheta, \varphi) = 0, \quad (3.47)$$

where  $\Delta\Sigma(\vartheta)$ , the excess surface mass density (ESMD), is written as follows (Miralda-Escude & Babul 1995):

$$\Delta\Sigma(\vartheta) = \bar{\Sigma}(\vartheta) - \Sigma(\vartheta). \quad (3.48)$$

We see that  $\gamma_\times$ , which is predicted to be consistent with zero, offers a helpful null test for WL measurements based on Eq. (3.47). Using a circle with radius  $\vartheta$  and center  $\boldsymbol{\theta}_c$ ,  $g_+(\vartheta)$ , we can calculate the average reduced tangential shear as follows:

$$g_+(\vartheta) = \oint \frac{d\varphi}{2\pi} g_+(\vartheta, \varphi) = \oint \frac{d\varphi}{2\pi} \frac{\gamma_+(\vartheta, \varphi)}{1 - \kappa(\vartheta, \varphi)}. \quad (3.49)$$

Given an almost circular symmetry in the projected mass distribution, the reduced tangential shear can be stated as follows:

$$g_+(\vartheta) \simeq \frac{\gamma_+(\vartheta)}{1 - \kappa(\vartheta)}. \quad (3.50)$$

This formalism is essential to represent the WL signal generated by galaxy clusters and voids, where the object center is considered to be  $\boldsymbol{\theta}_c$ .

### 3.3.5 Weak lensing from multiple lenses

As we have seen, being the projection of a 3D potential, Eq. (3.23) can be interpreted as a 2D Poisson equation. By substituting the 3D Poisson equation and Eq. (3.19) into it, the convergence can be expressed in terms of the matter overdensity (Davies et al. 2021b):

$$\kappa(\boldsymbol{\theta}, z) = \frac{3H_0^2\Omega_m}{2c^2} \int_0^{z_s} \frac{D_{\text{ls}}D_l}{D_s} \frac{\delta(D_l\boldsymbol{\theta}, z)}{a(z)} dz. \quad (3.51)$$

This shows that the observed WL convergence is equivalent to the projected density along the line of sight, weighted by  $D_{\text{ls}}D_l/D_s$ , which is the lensing efficiency factor.

Eq. (3.51) describes the WL effect of a single lens. However, light encounters gravitational lensing from the full mass distribution along its path as it moves from the source to the observer. On cosmological scales, light rays traverse numerous overdense or underdense extended regions at various locations. As a result, the thin lens approximation is not applicable. The transverse deflection caused by an infinitely thin lens plane still follows the equations mentioned earlier. However, the path of the rays must be fully integrated along their trajectory. For a given source plane at comoving distance  $\chi_s$ , the source plane position of a ray, initially observed at position  $\boldsymbol{\theta}$ , is thus represented by the continuous Volterra integral equation in implicit form (Jain & Seljak 1997):

$$\boldsymbol{\beta}(\boldsymbol{\theta}, \chi_s) = \boldsymbol{\theta} - \frac{2}{c^2} \int_0^{\chi_s} d\chi \frac{\chi_s - \chi}{\chi_s \chi} \nabla_{\boldsymbol{\beta}} \phi(\boldsymbol{\beta}(\boldsymbol{\theta}, \chi), \chi). \quad (3.52)$$

To first order, we can assess the gravitational potential along an unaffected trajectory, allowing us to use the so-called *Born approximation* (Bartelmann & Schneider 2001; Seitz & Schneider 1995) that is common in many diffusion problems of physics:

$$\boldsymbol{\beta}(\boldsymbol{\theta}, \chi_s) = \boldsymbol{\theta} - \frac{2}{c^2} \int_0^{\chi_s} d\chi \frac{\chi_s - \chi}{\chi_s \chi} \nabla_{\boldsymbol{\theta}} \phi(\boldsymbol{\theta}, \chi). \quad (3.53)$$

A noteworthy feature of the Born approximation is its ability to simplify the relationship between  $\boldsymbol{\beta}$  and  $\boldsymbol{\alpha}$  to an effective thin lens, mirroring Eq. (3.18). This allows for the definition of an effective convergence, which represents the divergence of the effective (curl-free) deflection field:  $2\kappa_{\text{eff}} = \nabla \cdot \boldsymbol{\alpha}_{\text{eff}}$ . When the approximation is invalid, the relationship between  $\boldsymbol{\beta}$  and  $\boldsymbol{\alpha}$  cannot be simplified to an effective potential alone, potentially leading to the generation of a curl component. This implies that the magnification tensor loses its symmetry, necessitating the inclusion of a rotation term  $\omega$  and the emergence of so-called B-modes in the shear field. In this broader context, the magnification tensor needs to be reformulated (Gouin et al. 2019).

$$A_{ij}(\boldsymbol{\theta}) = \begin{pmatrix} 1 - \kappa - \gamma_1 & -\gamma_2 - \omega \\ -\gamma_2 + \omega & 1 - \kappa + \gamma_1 \end{pmatrix}. \quad (3.54)$$

Now, we introduce the *lensing kernel*  $W(z)$ , a weight function of the multiple lenses that has the form:

$$W(z) = \frac{3H_0^2 \Omega_{m0}}{2c} \frac{1+z}{H(z)} D_1(z) \int_z^{z_s} \frac{dn}{dz_s} dz_s \frac{D_{1s}(z_s, z)}{D_s(z_s)}, \quad (3.55)$$

where  $\Omega_m$  is the fractional total matter density at present,  $D$  is the angular diameter distance in comoving units,  $H(z)$  is the Hubble parameter, and  $H_0$  is its present-day value, while the redshift distribution of sources is represented by  $dn/dz_s$  (Kilbinger 2015b). From this the calculation for a single lens can be extended to several lenses as:

$$\kappa(\boldsymbol{\theta}) = \int_0^{z_s} W(z) \delta\rho(D_1(z)\boldsymbol{\theta}, z) dz = \int_0^{z_s} \frac{dn(z)}{dz_s} \kappa(\boldsymbol{\theta}, z) dz. \quad (3.56)$$

As can be seen from this equation the WL convergence represents the projected mass density contrast weighted by a geometric factor, therefore positive and negative  $\kappa$  values correspond to overdense and underdense regions along the line of sight (Davies et al. 2019b).

Lastly, computed the projected field convergence, if lenses are axially symmetric, we can connect the radial tangential shear profile of an object,  $\gamma_t(r_p)$ , to its radial convergence profile,  $\kappa(r_p)$ , using (see Umetsu 2020; Seitz & Schneider 1995, for a detailed description):

$$\gamma_t(r_p) = \bar{\kappa}(< r_p) - \kappa(r_p), \quad (3.57)$$

where  $r_p$  is the 2D projected radius of the considered object on the sky plane and

$$\bar{\kappa}(< r_p) = \frac{1}{\pi r_p^2} \int_0^{r_p} 2\pi r'_p \kappa(r'_p) dr'_p \quad (3.58)$$

is the average enclosed convergence within radius  $r_p$ <sup>7</sup>. Since the tangential shear is the quantity directly measured by observations, it is fundamental in the studies of WL voids and Eq. (3.57) is of key importance in this work. Like the convergence, the tangential shear  $\gamma_t$  is positive when primarily overdense regions are encountered along the line of sight, and negative instead when underdense regions are predominant (Boschetti et al. 2023).

### Multiple-lenses approximation

The discrete version of the ray propagation Eq. (3.52) for a fiducial source plane corresponding to the distance of the plane  $j + 1$  reads (Gouin et al. 2019)

$$\boldsymbol{\beta}^{j+1} = \boldsymbol{\theta} - \sum_{i=1}^j \frac{D_{i;j+1}}{D_{j+1}} \boldsymbol{\alpha}^i(\boldsymbol{\beta}^i), \quad (3.59)$$

where  $\boldsymbol{\alpha}^i$  is the deflection field in the lens plane  $i$ ,  $D_{j+1}$  is the angular diameter distance between the observer and the plane  $j + 1$ , and  $D_{i;j+1}$  is the angular diameter distance between planes  $i$  and  $j + 1$ . In Figure 3.8 we show the trajectories of light rays, which originate from undisturbed positions in a regular grid  $\boldsymbol{\theta} \equiv \boldsymbol{\beta}$ , and undergo successive deflections as they traverse from one plane to the next.

The actual execution of the summation described in Eq. (3.59) is computationally intensive and memory-intensive because computing the source plane positions  $\boldsymbol{\beta}^{j+1}$  necessitates storing all previously computed positions up to  $j$ . For this reason, Hilbert et al. (2009) proposed a different method where Eq. (3.59) can be reformulated as a recursion over just three consecutive planes<sup>8</sup>:

$$\boldsymbol{\beta}^{j+1} = \left(1 - \frac{D_j}{D_{j+1}} \frac{D_{j-1;j+1}}{D_{j-1;j}}\right) \boldsymbol{\beta}^{j-1} + \frac{D_j}{D_{j+1}} \frac{D_{j-1;j+1}}{D_{j-1;j}} \boldsymbol{\beta}^j - \frac{D_{j;j+1}}{D_j} \boldsymbol{\alpha}^j(\boldsymbol{\beta}^j). \quad (3.60)$$

Furthermore, apart from the comprehensive propagation of light rays, the source plane positions and related parameters (convergence  $\kappa$ , shear  $\gamma$ , and rotation  $\omega$ ) will be also determined utilizing the Born approximation. This involves employing the discrete version of Eq. (3.53):

$$\boldsymbol{\beta}^{j+1} = \boldsymbol{\theta} - \sum_{i=1}^j \frac{D_{i;j+1}}{D_{j+1}} \boldsymbol{\alpha}^i(\boldsymbol{\theta}). \quad (3.61)$$

### 3.3.6 Weak-lensing in 2D voids

It is interesting to note that in an underdense line of sight or in a void, the deflection angle with respect to the geodesic of the photon is in the opposite direction (outward) compared to that of overdense regions of matter (inward). This is because lensing is a gravitational effect, and as we have seen, it is the matter overdensity that curves the spacetime around it, thereby determining the trajectory that light and other matter must follow. Voids are

<sup>7</sup>Notice that here and throughout this Thesis we use  $r_p$  rather than  $\theta$  to represent the 2D distance from the void center.

<sup>8</sup>This recursion requires the introduction of an artificial  $\beta^0 \equiv \beta^1 = \theta$  slice in the initial setup.

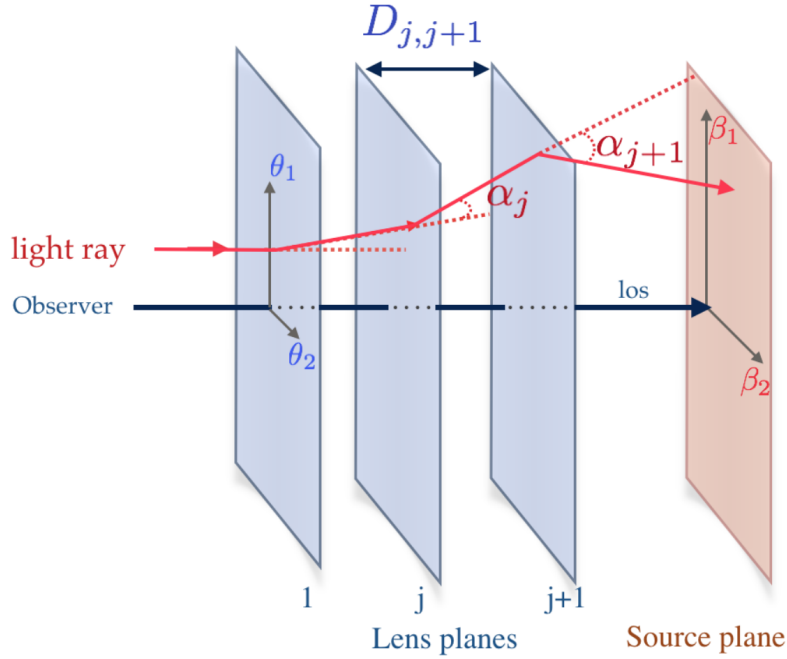


**Figure 3.8:** A diagram illustrating the path of a light ray passing through a light cone segmented into multiple discrete lens planes. The trajectory of the ray (depicted by the red line) is altered upon encountering each thin lens plane, resulting in a deflection. The deflection field is established for each plane and varies based on the angular position within that plane  $\alpha^j$  ( $\beta^j$ ). Credits to: [Gouin et al. \(2019\)](#)

large, underdense regions of the Universe defined by networks of clusters surrounding them, so the deflection effect will be oriented towards these clusters. Additionally, the measured magnitudes of astronomical objects also depend on the environment and the type of inhomogeneity along the line of sight, as well as the internal characteristics of the source. This results in a (de-)magnification in underdense areas (see also [Clarkson et al. 2012](#); [Bolejko & Ferreira 2012](#)). The reversed behavior of various features in voids, such as the reversal of signs regarding shear radial profiles and convergence values, is referred to as anti-lensing ([Bolejko et al. 2013](#)).

The application of WL analyses to cosmic voids helps to alleviate the issue related to the scarcity of luminous tracers necessary to identify 3D voids, as WL is sensitive to total matter and thus allows us to detect voids within this domain. In the scientific literature, the detection of WL around 2D voids is typically approached in two distinct manners:

- *Tunnels WL*: by measuring the tangential shear  $\gamma_t$  or the convergence  $\kappa$ , which characterize the distortion of the shapes of background galaxies caused by the underdense structures extending from the observer to the source. In this way one measures the projected profile of ultra-large structures, with sizes typically hundreds of Mpc ([Higuchi et al. 2013](#); [Gruen et al. 2015](#); [Davies et al. 2021b](#); [Shimasue et al. 2024](#));
- *Void lensing (VL)*: by measuring the ESMD,  $\Delta\Sigma$ , which represents the projection of the total matter contained within a thin lens situated somewhere between the observer and the source. In this way one measures the projected profiles of voids with radii  $\leq 50h^{-1}$  Mpc, where the thin lens approximation remains valid, as demonstrated in [Boschetti et al. \(2023\)](#).

The differences between the two approaches are fundamental. In tunnel WL we have less 3D

information and we focus on measuring the weak lensing signature of ultra-large underdense structures that intersect the line-of-sight, resulting in regions of underdensity. As mentioned in Sect. 3.1, these structures are known as *troughs* or *tunnel voids*, and their relation to a generic definition of voids with predictable void abundance is current object of research. We have also already presented, in Sect. 3.1.1, the importance of tangential shear analysis in choosing the definition of our 2D voids and in particular for what purpose this choice is made. In fact, as demonstrated in Cautun et al. (2018), the tangential shear by tunnels has the largest constraining power for  $f(R)$  gravity.

On the contrary in the second approach, 3D information is partially recovered and the objective is to extract dynamic and morphological information about the conventional definition of voids. As pointed out again in Cautun et al. (2018), VL does not maximize the tangential shear signal and it is therefore more difficult to discriminate between different gravity models. Therefore, in this work we followed the former approach.

### 3.3.7 Weak lensing in $f(R)$ gravity

As already specified, the main way to connect the WL signal measured from voids to gravity theory is through the lensing potential in Eq.(3.19). Here, in fact,  $\Phi$  is the gravitational potential that determines photon geodesics by coupling to photons (not matter). To analyze correctly a MG scenario, it is essential to differentiate between various types of potentials, since in some models the fifth force exclusively impacts massive matter particles, while in others it directly influences photon geodesics. Moreover, WL is valuable for testing gravity as it detects the sum of newtonian potentials, which are typically unequal in MG scenarios. Essentially, by observing the distortion in the shapes of distant galaxies as their light traverses voids, we directly probe the cleanest (less affected by baryonic complications), simplest (with fewer nonlinearities), and most sensitive environment for testing MG (Boschetti et al. 2023). However, this implies that secondary effects and corrections must be considered in the MG models, which greatly complicate the description of this potential making degenerate the constraints derivable from simulated observables (Baker et al. 2018). In this work, we consider the  $f(R)$  models, where the difference between them and GR is not attributable to effects on the lensing potential but only to the distribution of matter on LSS.

In the newtonian gauge<sup>9</sup>, the perturbed metric can be written as:

$$ds^2 = (1 + 2\Psi)dt^2 - a^2(t)(1 - 2\Phi)dx_i dx_j, \quad (3.62)$$

where  $\Phi$  and  $\Psi$  are the Einstein-frame metric gravitational potentials. In standard GR model we can read the two potentials as:

$$\Phi = \Psi = \Psi_N, \quad (3.63)$$

where the Newton potential  $\Psi_N$  can be written in terms of the Poisson equation. In the  $f(R)$  modified gravity models the two modified Poisson equations for the metric potentials result from the variation of the Einstein equations:

$$\begin{aligned} \frac{\nabla^2\Phi}{a^2} &= -\frac{c^2\nabla^2}{2a^2}\delta f_R + 4\pi G\delta\rho, \\ \frac{\nabla^2\Psi}{a^2} &= \frac{c^2\nabla^2}{2a^2}\delta f_R + 4\pi G\delta\rho, \end{aligned}$$

which, in terms of the Newton potential, are:

$$\Phi = \Psi_N - \frac{c^2}{2}\delta f_R, \quad \Psi = \Psi_N + \frac{c^2}{2}\delta f_R. \quad (3.64)$$

---

<sup>9</sup>Newtonian gauge is a perturbed form of the FLRW line element.

At this point we can introduce the lensing potential  $\Phi_1$  as:

$$\Phi_1 = \frac{\Phi + \Psi}{2}. \quad (3.65)$$

This indicates that the two additional terms in MG models cancel out, leaving the lensing potential in  $f(R)$  gravity unchanged from its ordinary GR form (Hu & Sawicki 2007; Giocoli et al. 2018a). From this, we can redefine the convergence  $\kappa$  in Eq. (3.56) in the conventional way as:

$$\kappa(\boldsymbol{\theta}) = \int_0^\infty dw \frac{w}{c^2} g(w) \nabla^2 \Phi_1(w, w\boldsymbol{\theta}), \quad (3.66)$$

where  $w$  represents the comoving radial distance and  $g(w)$  the survey weight function.

Considering the successful measurements of the WL signal from cosmic voids identified in real galaxy surveys (e.g., Gruen et al. 2015; Sánchez et al. 2017), we can conclude that the WL phenomenon represents a promising method for assessing the matter distribution within and surrounding voids, and constitutes a tool potentially important for investigating modifications of gravity (Barreira et al. 2015; Cai et al. 2015). In the next chapter we will focus on the development of an efficient pipeline to carry on this kind of studies.

# Chapter 4

## 2D void finder

As we outlined in Sect. 3.1, the first and fundamental step necessary for voids cosmological studies is their identification. In particular, in Sect. 3.1.1, we introduced the importance of 2D voids for WL analyses and the main identification methods, emphasizing their merits and shortcomings related to galaxy shape noise and optimization of  $S/N$ . In this Thesis work we develop a finding algorithm for 2D voids in WL maps, which is based on density and geometrical criteria and is targeted for measuring voids' tangential shear profiles. To do this, we take into consideration the conclusions of Cautun et al. (2018) and Davies et al. (2021b), overcoming the problems of identifying centers discussed in the second work. We started from the algorithm of a pre-existing peak finder called `pyTwinPeaks` – already successfully applied for WL studies of galaxy clusters (Giocoli et al. 2018b) – extending it to include a new code for the identification of tunnel voids.

Our 2D void finder is written in Python language and implemented with Python libraries for cosmological calculations. It allows us to reconstruct the most underdense regions in the projected convergence field of a chosen redshift range, providing information about center, size and shape of projected voids, without exploiting the 3D positions of galaxies (or, more generally, mass tracers). The 2D void finder can be divided in four main steps: detection of underdense regions (Sect. 4.1), identification of void centers (Sect. 4.2), assignment of void radii (Sect. 4.3) and cleaning of the sample (Sect. 4.4). These steps are schematized in Figure 4.1 and will be presented in detail in the following sections. The code will be made public and released to the scientific community in the near future.

Before delving into the technical description of the algorithm steps, we briefly overview the preparation of the input data. In fact, the finder requires in input a FITS<sup>1</sup> file containing the WL convergence field projected on a plane and weighted for the lensing kernel. Such a file must be prepared so that it has a header including the field of view (FOV) data of the map in degrees, the number of pixels on one side of the map<sup>2</sup> and the redshift of the sources. Before moving to the void identification pipeline, the finder executes a preliminary routine adding Gaussian shape noise – which depends on the intrinsic ellipticity distribution of the background galaxies – to the convergence map in order to reproduce the galaxy shape noise. Then we apply an additional Gaussian filter to smooth and mitigate the impact of galaxy shape noise on the measured void statistics, discerning between voids produced by physical signals in the WL maps and spurious voids resulting from noise. This procedure is the same used in Davies et al. (2021b) and it has been shown to maximize the  $S/N$  obtained from the tangential shear of the 2D voids. At the end of this procedure the algorithm derives the  $S/N$

---

<sup>1</sup>It is the acronym of Flexible Image Transport System, a format defined in Hanisch et al. (2001).

<sup>2</sup>Here we make use square maps, but for future applications to real data the maps may have more complex geometries.

value of the smoothed  $\kappa$  map (SNR map hereafter) by dividing the smoothed convergence map by the noise associated with the filter used. This preliminary pipeline is included in the algorithm and can be tuned by the user. For example, it is possible not to add the galaxy shape noise and not to smooth the maps. Moreover, by changing the input parameters like the filter size or the ellipticity distribution of background galaxies, it is possible to study various characteristics of the LSS in WL maps, also switching between the identification of overdense and underdense regions. The algorithm presented in this Thesis work represents therefore a versatile 2D void finder, which is designed to be adaptable for specific case studies.

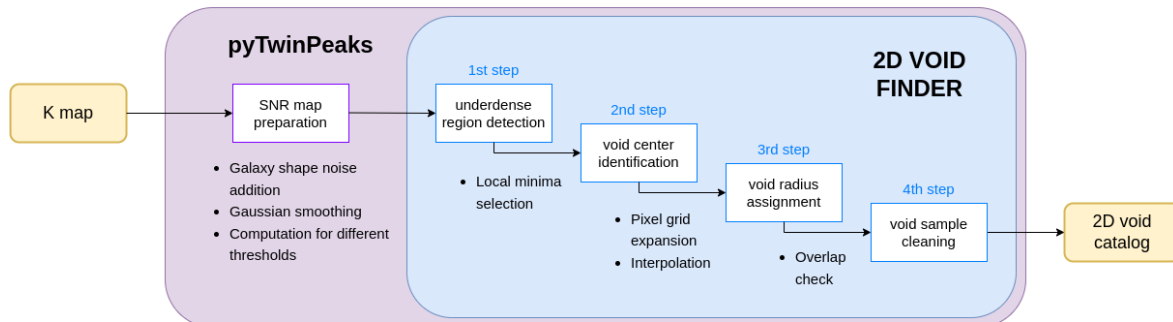


**Figure 4.1:** Diagram showing the four main steps of the 2D void finder algorithm that allows the identification of voids from a WL convergence map.

## 4.1 Connected regions detection

Once the preliminary routine has been completed according to the chosen guidelines, the finder algorithm proceeds with the detection of connected regions of pixels, which is the pillar on which we based the search for WL voids. The pipeline provides a preliminary assignment of pixel regions of interest. This step is crucial to evaluate all the threshold of  $S/N$  desired in signal-to-noise (SNR) map and to determine the compromise between the calculation time and the accuracy of the detection process. The idea behind this part of the method is to exemplify the subsequent identification of the real 2D voids by analyzing the information stratification of the underdense (or overdense in the case of peaks) regions in the SNR map at different thresholds and simultaneously extract their topological features. The main goal is to identify the 2D underdensities with the deepest and cleanest tangential shear signal. Therefore, it is of key importance the selection of the  $S/N$  values to test: restricting the analysis to physically significant thresholds in our maps implies a robust assignment of void centers and radii.

### 4.1.1 Peaks/Valleys reconstruction

The algorithm is designed to work indiscriminately on the search for overdensity or underdensity zones, performing the same procedures within the same conditional code structure. The object of the search, in fact, depends exclusively on an input variable chosen by the user that discriminates between the two possibilities. In the general setting of our 2D void finder, our choice falls on valleys. The valleys reconstruction phase operates in the following way:

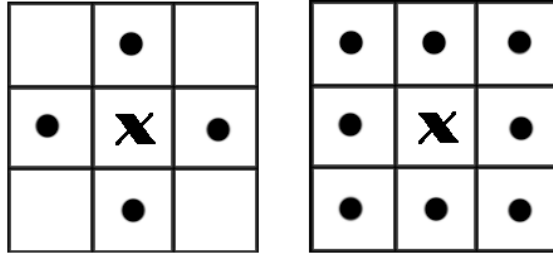


**Figure 4.2:** Two types of connectivity between adjacent pixels through which the connected region is determined. The one on the right is chosen for the finding algorithm. Credits to: [https://blog.csdn.net/pursuit\\_zhangyu/article/details/94209489](https://blog.csdn.net/pursuit_zhangyu/article/details/94209489)

1. It creates a mask to be applied on the SNR map to obtain all pixels in the map that have  $S/N$  below the selected threshold.
2. It reconstructs the valleys by performing connected component analysis, that is, the pixels that survived the application of the mask. Starting with a pixel, the type of expansion (i.e. *connectivity*) used to define the pixels belonging to the connected region can follow two different patterns, as shown in Figure 4.2. In the first case, only the pixels with side adjacent to the central one are considered connected; in the second case, pixels that are adjacent by their corners to the reference pixel are also regarded as connected. To expedite this process, the latter form of connectivity was selected because it estimates the SNR value of a larger number of pixels simultaneously.
3. It constructs a total map as a sum of layers in which each layer contains a separate connected region of pixels with  $S/N < (S/N)_{\text{th}}$ . We present in Figure 4.3 two examples of reconstructed map, showing in gray scale the masked pixels and with different colors separate connected regions. If the chosen threshold is very high ( $S/N \lesssim 0$ ) many of the pixels will satisfy the condition and will not be masked, resulting in a few very large connected regions, i.e., an almost homogeneous field. The maximum counts of connected regions occur for intermediate values of threshold ( $S/N \lesssim -2$ ) but, as can be seen in the left image of Figure 4.3, the regions have very jagged and elongated shapes. When the threshold is very low ( $S/N \lesssim -4$ ), like in the right image of Figure 4.3, very few pixels will satisfy the condition while most of them will be masked, resulting in a few very small but fairly circular connected regions, i.e., the areas that are the projection of the most underdense lines of sight in the whole FOV.
4. From each connected region the code extracts 16 topological features, among which the most relevant are: perimeter of the region, area, eccentricity, the coordinates  $(x, y)$  of the centroid weighted by the value of the SNR<sup>3</sup>, coordinates of the pixel with the minimum  $S/N$  value, etc. Since the extracted coordinates are in units of pixels<sup>4</sup>, they are converted to arcminutes through the relation:

$$x_{\text{arcmin}} = \left( x_{\text{pix}} - \frac{n_{\text{pix}}}{2} \right) \cdot l_{\text{arcmin}}, \quad (4.1)$$

<sup>3</sup>A centroid is a type centering based on the weighted average that relates to a geometric property, such as area, rather than a physical property like weight or mass. As such, centroids pertain to the inherent characteristics of abstract shapes rather than tangible objects. They serve as coordinates that define the “center” of a shape. In this case it is obtained through the weighted average of the coordinates of the pixels belonging to the area of the connected region, where the weight of each pixel depends on its  $S/N$  value.

<sup>4</sup>The algorithm by default centers the map in  $(0, 0)$  so each axis will range from  $-n_{\text{pix}}/2$  to  $n_{\text{pix}}/2$ .

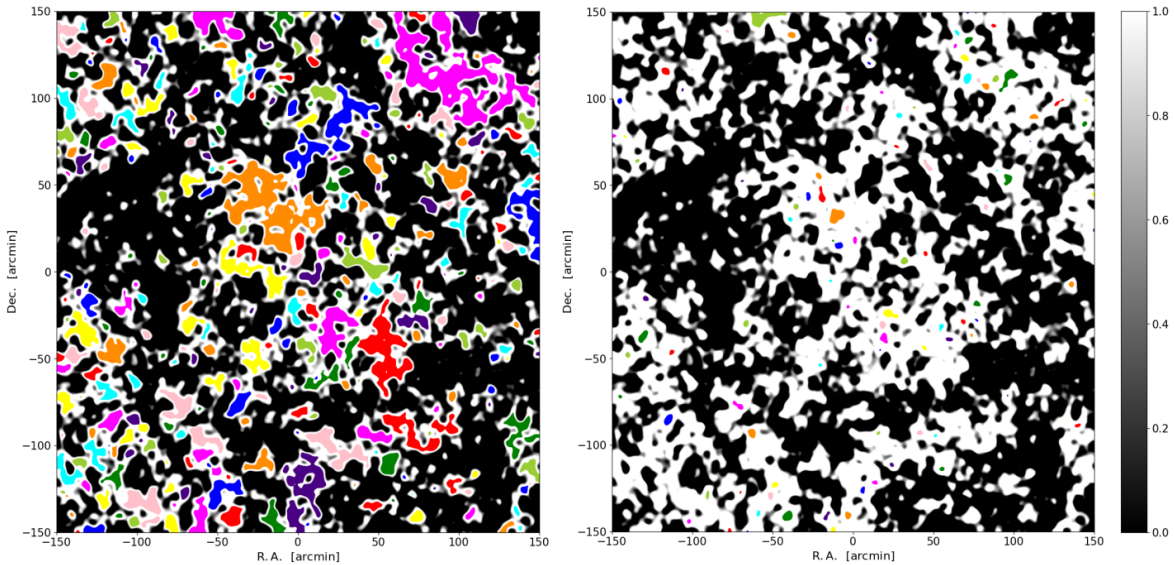


**Figure 4.3:** Explanatory comparison of two maps (R.A.-Dec. coordinates) of connected regions obtained using different thresholds. The normalized gray scale distinguishes overdense and underdense regions, in darker and lighter colors respectively. On the left we show the connected regions with  $S/N \leq -2$  and on the left those with  $S/N \leq -4$ . Distinct connected regions are represented with different colors.

where  $x_{\text{pix}}$  is the coordinate in the SNR map in units of pixels,  $n_{\text{pix}}$  is the number of pixels per side of the map, and  $l_{\text{arcmin}} = \text{FOV}_{\text{arcmin}} n_{\text{pix}}$  is the measure in arcminutes of the side of a pixel.

At this point, once the connected regions that are underdense with respect to a certain threshold in the SNR map have been reconstructed, we take care of the overlapping cases. In fact, we want to include the possibility of merging two or more local underdensities when these result very close to each other. For this purpose, a preliminary radius is temporarily assumed for each connected region, deduced from the extracted area  $A$  through the approximation of that region as circular, i.e.:

$$R_{\text{pr}} = \sqrt{A/\pi}. \quad (4.2)$$

We note that, despite the connected regions are mutually exclusive by construction, when converting these regions into circles, their areas may indeed overlap. Therefore we impose that regions whose distance is less than half the sum of the preliminary radii,

$$D_{\text{pr}} < \frac{(R_{\text{pr},1} + R_{\text{pr},2})}{2}, \quad (4.3)$$

will undergo merging and become a single region of greater area. The way distance is calculated represents a substantial difference between peaks and valleys:

- for peaks, the distance is calculated between the pixel coordinates of the weighted centroids of the respective regions,
- for valleys, the distance is calculated between the coordinates of the pixels with the minimum  $S/N$  value of the respective regions.

This choice is the result of the requirement to maintain internal consistency with the second step of the algorithm that we will see in Sect. 4.2.1 and is aimed at stabilizing the final outcome.

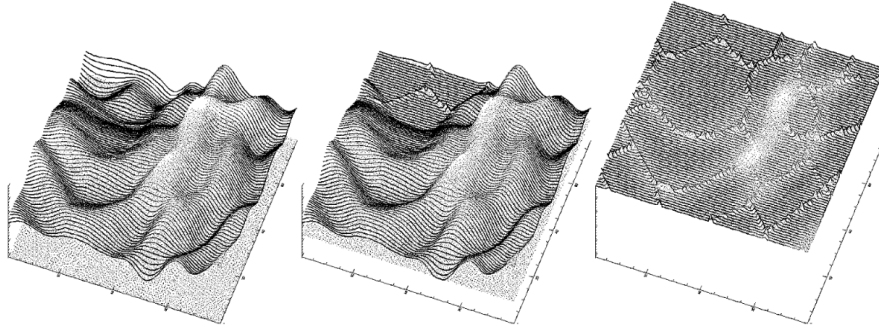


**Figure 4.4:** Graphical representation of the watershed technique in three frames. In the left-hand frame, the surface to be segmented is shown. Basins surrounding the local minima of the surface begin to flood as the water level rises (indicated by the dotted plane initially positioned below the surface). When two basins converge near a ridge of the density surface, a dam is constructed (as shown in the central frame). Eventually, the entire surface becomes flooded, resulting in a network of dams that defines a segmented volume and outlines the corresponding cosmic web (shown in the right-hand frame). Credits to: [Platen et al. \(2007\)](#).

For a given range of thresholds selected by the user, the algorithm repeats the steps just described and produces a catalog of underdense regions. This is done to create a mapping of the  $S/N$  field. The number of values to test inside the threshold range can also be changed, determining the number of layers used to trace regions with the same limit in  $S/N$ . A large number of test thresholds would improve the accuracy of the finding procedure, but at the same time it would increase the computation time.

The key result, which serves as input for the next step, is the catalog of the properties of each region connected to each threshold. In particular, in the case of void analysis, we need to consider the area and the coordinates in arcminutes of the pixel with the minimum  $S/N$ . Among the catalogs of various thresholds, it becomes particularly important to select the one that has a good compromise between a very low threshold and a relevant number of minima, thus connected regions. This is because we aim at having a statistically significant number of underdensities, but at the same time a deep (and so uncontaminated) tangential shear signal. Such a catalog contains the positions of local minima identified in the map and will be used to discriminate the absolute minima.

## 4.2 Center identification

Once the catalog of the positions of the minima and the areas of each region, for each threshold, is obtained, the algorithm uses this information to identify the absolute minima over the entire WL convergence map. In this process, absolute minima are distinguished from local minima, which are merely spurious fluctuations caused by noise. This step is the heart of the algorithm as well as the most delicate, as it defines the final catalog of the centers of our 2D voids, thereby significantly affecting the resulting statistics.

The process of 2D void center identification is based on a revisited version of a procedure often used in 3D void finders such as VIDE (see Sect.3.1), called *watershed* ([Platen et al. 2007](#)). This term was chosen to recall the analogy to a landscape being inundated by rising water levels. Imagine a surface resembling a landscape (shown in the first panel of Figure 4.4). Initially, the surface is submerged at each minimum point. As the water level increases, more and more of the landscape becomes submerged by the expanding basins. Eventually, these basins converge at the ridges, corresponding to saddle points in the density (or SNR) field.

The second panel in Figure 4.4 illustrates this intermediate stage, where the ridges delineate the basin boundaries, enforced by high dams. The final outcome, as shown in the third image in Figure 4.4, is a partitioning of the landscape into individual cells, separated by the ridge dams. This procedure establishes a hierarchy of voids by identifying various basins and ridges. Through this substructure partitioning, a parent void encompasses multiple subvoids. Each void originates from a parent and may contain several child subvoids, organized into different levels.

Our application of this technique consists of a similar procedure, adapted for the 2D configuration. To identify the absolute minima, the code checks the persistence of the relative minima on the results obtained with different thresholds. Starting from the lowest threshold, the code checks if a minimum is also contained in the 2D void<sup>5</sup> at the next higher threshold. The procedure is also repeated for the subsequent thresholds, up to the limit set by the user. If a minimum identified at the lowest threshold is also present at the subsequent thresholds, then it is considered an absolute minimum. The result of this procedure can be visually represented through a plot like the one in Figure 4.5, in order to help the users choose the most suitable threshold range for their case. The final void catalog will be composed of underdensities having as center a persistent minimum identified at the initial threshold (i.e. lowest in the cycle), and as size the preliminary radius computed from the area of the region identified with the final threshold (i.e. highest in the cycle).

The selection of the initial threshold of this cycle determines the limit for the identification of void centers and so the “depth”<sup>6</sup> of the center of the final 2D voids, which consequently falls back on the amplitude of the tangential shear signal we will extract from these voids. This choice must be balanced to achieve a statistically significant number of underdensities and relevant amplitude of the final WL signal. The selection of the final threshold in the cycle is important as well. In fact, if this threshold is too low (close to the initial threshold) the absolute minima will coincide with the local one, and the final voids will result very small and fragmented. If instead the final threshold is too high (close to the average value of the map  $S/N = 0$ ) the radius of the underdensities will be expanded to the point that many voids will merge and the final catalog will be composed of few objects. It is therefore necessary to choose wisely a stop threshold that has a good trade-off between the preservation of good void statistics and not excessive merging.

#### 4.2.1 Weighted centroids vs absolute minima

Let us now focus on the method selected for the identification of the void centers in the procedure just described. We will explain now how the choice of using SNR map minima rather than weighted centroids (see Sect. 4.1) as the center of the 2D voids solves an important topological problem.

Albeit the centroid methodology relies on the weighting of the  $S/N$  values, in some cases the center assigned with this technique may fall outside the connected region. In fact, especially at high  $S/N$  values, the connected regions may show very elongated shapes. Imagine, for example, the extreme case of an underdense region shaped as a half moon: the centroid of this region would lie near the geometrical center, i.e. in an overdense zone. This would negatively affect the final tangential shear profile, leading to a contamination of the average signal extracted from the map.

Using the centroid in our center identification procedure would therefore cause a continuous shifting with respect to the SNR map minima. This would also impact the final

---

<sup>5</sup>These voids are considered to be circular and centered on the  $S/N$  minima, with a preliminary radius assigned with Eq. 4.2.

<sup>6</sup>By this term we mean the degree of underdensity of a void.

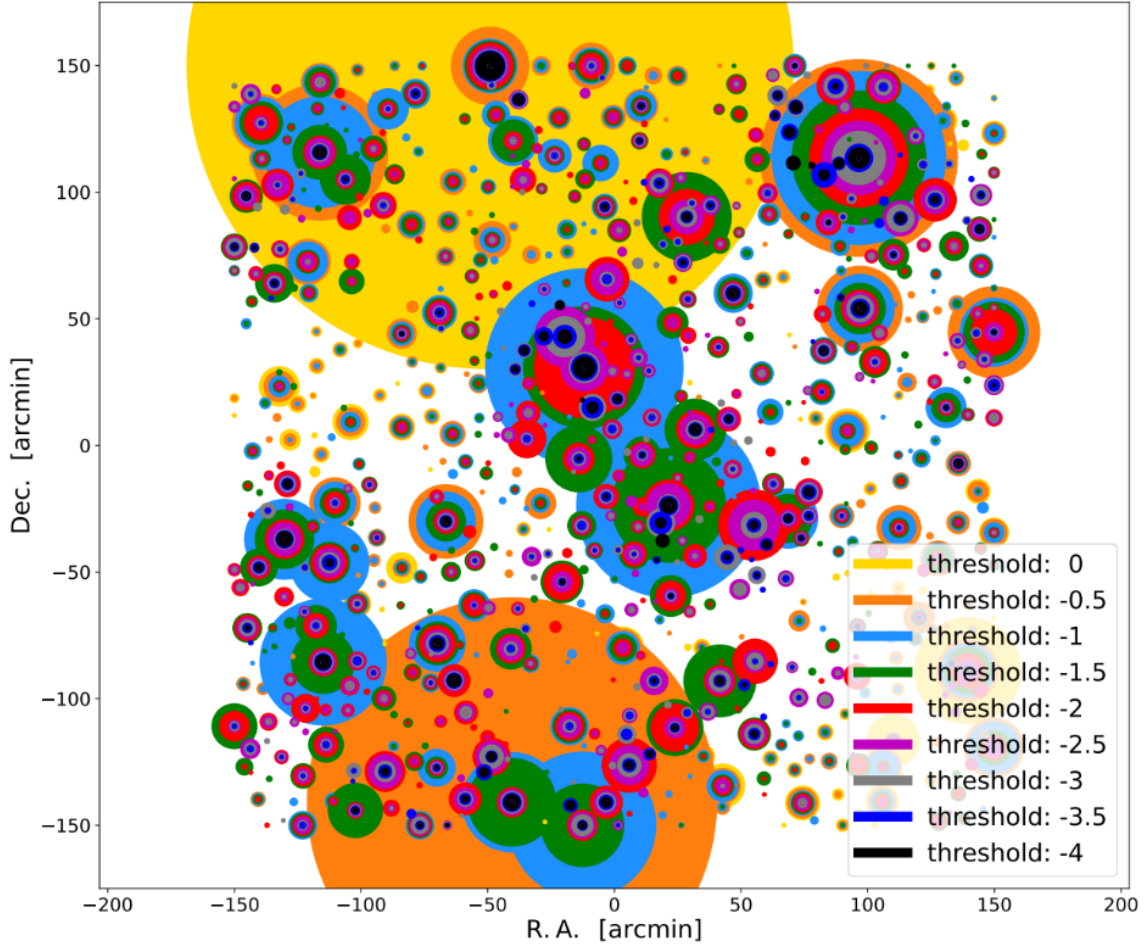


**Figure 4.5:** Graphical representation of all local minima and corresponding preliminary radii of each threshold produced by the same map shown in Figure 4.3. Each void of a given threshold is represented with the colored area of the same color, this color varies depending on the threshold as shown in legend. We note that, near the map boundaries, the circular expansion of the void radii at very high threshold is fictitious, as these underdensities are not really extending outside the map.

number of 2D voids, since on the position of the void centers depends the overlap criterion used to merge the underdensities. We note that the choice of using the centroids is useful in the case the underdense regions are regular and isotropic. As pointed out by [Davies et al. \(2021b\)](#), this technique has the advantage of minimizing the impact of the noise fluctuations characterizing the connected regions at very low  $S/N$  values. On the other hand, they also show that finders using as void centers the minima in the convergence map maximize the amplitude of the tangential shear extracted from these voids. The authors, however, underline that in their analysis the underdensities centered on the absolute minima are also those that are more prone to be generated by spurious fluctuations.

With our procedure, we address the latter problem and create a catalog of 2D voids characterized by the positive aspects of both the centering methodologies. In fact, we use as void centers the absolute minima in the  $S/N$  field, which leads to the optimal signal in the shear profiles, but we face the problem of the noise contamination by analyzing the same underdensities at different thresholds, to check for the persistence of a given center in higher  $S/N$  regions. We validated the goodness of our technique by verifying that it leads to the void tangential shear profiles that show, at the same time, the deepest signal and the smallest associated uncertainties (computed from the scatter between the different profiles of voids in the catalog).

### 4.3 Final radius assignment

The next step of the 2D void finder algorithm developed in this Thesis work is the assignment of the final value of the radius to the voids identified through the previous steps. We want our 2D voids to correspond to circles enclosing the exact  $S/N$  value selected by the user, also adapting the procedure to the characteristics of the convergence map (e.g. spatial resolution, edge limits).

The procedure we apply to accomplish this task can be summarized in the following four points:

1. *Conversion to Pixels*: The algorithm starts by converting from arcminutes to pixels the coordinates of the centers of the previously identified 2D voids, through the inverse formula of Eq.(4.4). This is done in order to make our pipeline work with the information stored in the minimum unity of the SNR map, i.e. to make it suited to any spatial resolution of the map.
2. *Grid initialization*: For all voids in the catalog, the code initializes a grid of size  $3 \times 3$  pixels, with the central pixel corresponding to the void center, i.e. the point with minimum  $S/N$  value. These pixels are selected by applying a circular mask<sup>7</sup> around the void center. Since we assume that the individual  $S/N$  values are associated with the center of the pixels, we make the circular mask have a radius equal to

$$r_{\text{mask}} = \frac{l_{\text{grid}}}{2} - \frac{l_{\text{pix}}}{2}, \quad (4.4)$$

where  $l_{\text{grid}}$  is the side of the grid and  $l_{\text{pix}}$  is the side of a pixel, both in units of pixels. The usage of the mask is performed to speed up the computational time and works by selecting all those pixels within it: any pixel contained in or even crossed by the circle defining the mask is considered part of the selected region.

---

<sup>7</sup>The choice of a circular mask is motivated by the initial assumption to model 3D voids as spheres, or equivalently circles in 2D.

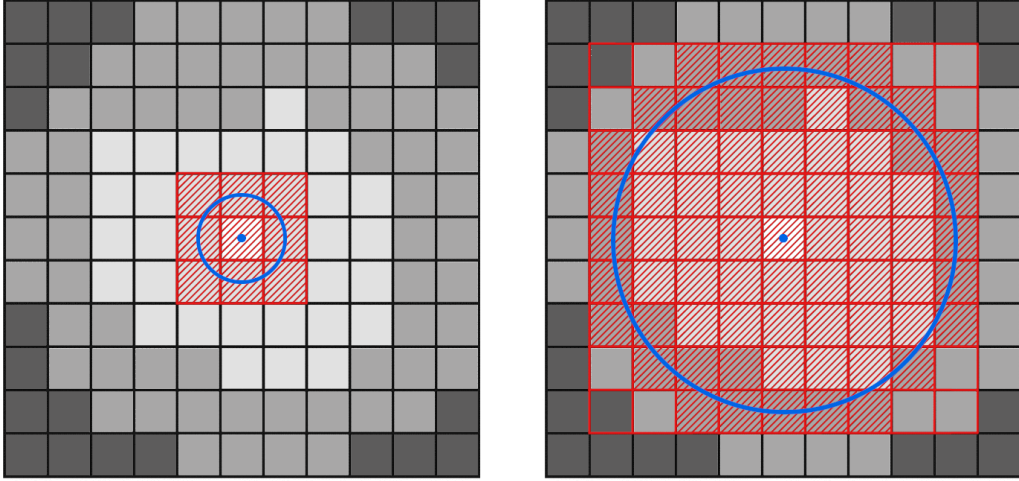


**Figure 4.6:** Representation of two steps of the pixel grid expansion on the underlying SNR map of convergence. The left image shows the first step of the procedure (with a  $3 \times 3$  grid) while the right panel shows the fourth step (three rows of pixels added to the initial grid). The blue circle represents the mask and the red hatched squares are the pixels included by the mask and considered to compute the average  $S/N$  value.

3. *Grid Expansion:* At this point the average  $S/N$  of all pixels belonging to the circular mask is calculated. This value must be lower than the stop threshold set by the user (i.e. the one chosen to determine the final void radius), so we proceed by expanding the grid. We add to the previous grid a new row of pixel to each side, so the corresponding circular mask will have a radius increased by one pixel. Then, we compute the new averaged  $S/N$  value and we repeat the procedure until this value surpasses the stop threshold. We illustrate this process in Figure 4.6.
4. *Radius interpolation:* The algorithm considers the radii of the circles computed before and after surpassing the stop threshold, and performs the interpolation between these values to find the radius corresponding exactly to the selected threshold. This is done because the expansion of the grid in pixels (and consequently the radius of the circular mask) is discrete and determined by the pixel size. Finally, the radii of each void is converted back in arcminutes via Eq.(4.4).

Regarding the treatment of those voids whose centers are near the edges of the SNR map, one possible strategy is to remove these objects from the final catalog. However, to avoid lowering the statistics of voids, we treat them by masking those cells of the grid that fall beyond the boundaries. In particular, a value *Not a Number* (NaN) is assigned to each pixel outside the map but belonging to the grid. In this way, we formally extend the original map adding pixels with values that do not impact the procedure of  $S/N$  value averaging.

## 4.4 Void cleaning

The very last step of the finder algorithm concerns the cleaning of the final sample of voids. We note that the first steps of this algorithm were already oriented to maximize the signal and reduce the impact of the noise. Now that we have assigned a final radius to each underdensity the only remaining prescription to follow is the removal of the overlapping voids. Indeed, we cannot consider independent the WL signals extracted from two or more underdensities that

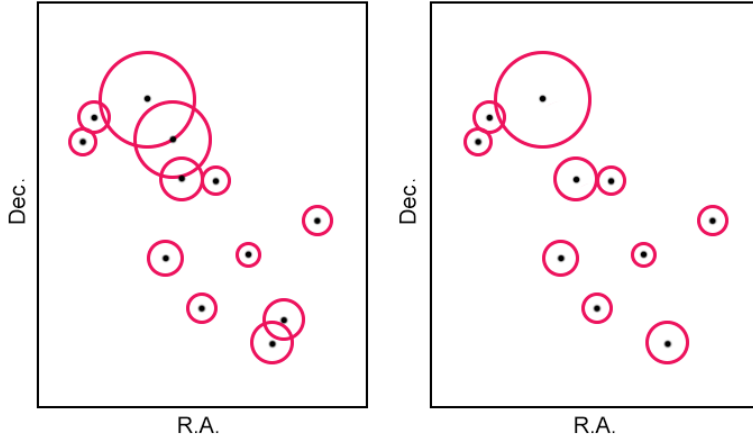


**Figure 4.7:** Representation of 2D voids extracted from a SNR map, before and after the cleaning procedure. The red circles represent the extent of our voids centered on the absolute minima (black dots). After the cleaning (right panel), the voids that have greater degree of overlapping are removed. We highlight that, in a complex configuration as the one displayed in the upper left corner, only one is removed.

are overlapping. Since a first overlap check was already performed during the previous steps this procedure is expected to have a small impact on the final catalog of voids.

This final cleaning relies solely on the positions and the sizes of the voids, and can be divided in three main steps:

1. We sort the identified 2D voids in descending order according to the size. Then, for each void, we compute the distance from its center to that of all other voids.
2. Starting from the first void in the list (the largest), we check if the distances from the other centers meet one of these two conditions:
  - The distance between the centers is less than or equal to 75% of the sum of the two radii:  $D_{\text{centres}} \leq 75\% \cdot (r_1 + r_2)$ . Here  $r_1$  represents the radius of the considered void and  $r_2$  the radius of one of the other voids in the list.
  - A void is completely contained in another void, i.e. void-in-void scenario.
3. In case that at least one of these conditions is met the void smaller in size is removed, updating accordingly the list of voids.

The procedure is then repeated from the first step, moving to the following void in the list. This kind of approach imposes the preservation of the largest underdensities that, in principle, are those with the stronger signal. Moreover, the choice of using an updated list of voids ordered according to their size allows us to avoid unnecessary removal of underdensities. In fact, as also represented in Figure 4.7, in case of three overlapping voids in a row, with sizes progressively smaller, only the central one is removed, keeping the largest and smallest of the three, which finally result non overlapping.

The final output of this finding algorithm is an ASCII<sup>8</sup> file composed of three columns. Each row contains the information relative to one void: the  $X$  and  $Y$  positions of the void center, and the void radius, all of them in units of arcminutes. Additional information,

<sup>8</sup>ASCII means “American Standard Code for Information Interchange” and represents the most common character encoding format for text data in computers.

e.g. perimeter, area, eccentricity of the connected regions and other characteristics of the underdensities found at different thresholds, is stored in separate files.



## Chapter 5

# Simulated Weak-lensing maps

As we have seen in Sect. 1.5.3, employing  $N$ -body simulations is a key strategy for predicting the gravitational interactions among cosmic objects. These simulations allow us to reproduce the evolution of density perturbations and to model the formation of cosmic structures, even in the non-linear regime, thereby testing different cosmological scenarios. In this chapter, we first present the simulations used in this Thesis work (Sect. 5.1) and then the technique used to extract DM halo catalogs (Sect. 5.2). Eventually, we briefly describe the ray-tracing process used to create light-cones, which are then employed to build WL convergence maps (Sect. 5.3). These maps will be the inputs for the 2D void finder we developed (see Chapter 4) and will be used to predict the amplitude of the WL signal from cosmic voids in different cosmological models.

### 5.1 DUSTGRAIN-*pathfinder* simulations

In our analysis, we utilize projected matter distributions and halo catalogs extracted from a suite of cosmological DM-only  $N$ -body simulations known as DUSTGRAIN. The DUSTGRAIN (Dark Universe Simulations to Test GRAvity In the presence of Neutrinos) is an ongoing project aimed at generating extensive and detailed mocks useful for analyses of galaxy clustering, weak lensing, and redshift-space distortions within cosmological models characterized by deviations from standard GR and featuring a significant fraction of cosmic matter density in the form of massive neutrinos. Specifically, we focus on MG theories of the  $f(R)$  class, as outlined in Sect. 2.1.3, with our analysis constrained to Eq. (2.8), thereby leaving the model with only one free parameter:  $f_{R0}$ . These simulations are tailored to investigate the degeneracies between  $f(R)$  gravity models and massive neutrinos. They have been recently employed in various studies aimed at devising methods to disentangle these cosmic degeneracies, exploiting for example the WL phenomenon (Giocoli et al. 2018a; Peel et al. 2018), clustering statistics (García-Farieta et al. 2020), the abundance of massive halos (Hagstotz et al. 2019a) and cosmic voids (Contarini et al. 2021), analysis of the large-scale velocity field (Hagstotz et al. 2019b), and exploration of machine learning techniques (Merten et al. 2019).

As currently widely acknowledged (Baldi et al. 2014; He 2013; Motohashi et al. 2013; Wright et al. 2017), MG theories like  $f(R)$  gravity – in the form proposed by Hu & Sawicki (2007) – are highly degenerate with the influences of massive neutrinos on structure formation. This presents significant challenges for ongoing and future large-scale galaxy surveys in developing robust methodologies to distinguish between these two phenomena. Specifically, conventional statistical analyses such as the matter auto-power spectrum, lensing convergence power spectrum, and halo mass function may exhibit minimal distinctions from their standard

$\Lambda$ CDM predictions for certain combinations of the  $f(R)$  gravity parameter  $f_{R0}$  and the total neutrino mass  $M_\nu \equiv \sum m_{\nu,i}$  (see Baldi et al. 2014; Peel et al. 2018), establishing a “maximum degeneracy” relationship between the two models. To properly explore the parameter space in which this kind of “maximum degeneracy” relation is expected, a suite of smaller-scale and lower-resolution  $N$ -body simulations, called the DUSTGRAIN-*pathfinder* was run, to (at least coarsely) sample the  $\{f(R), M_\nu\}$  parameter space. At now, the *pathfinder* runs already offer a substantial amount of valuable simulated data and novel informational content, warranting a thorough analysis.

Technically, the DUSTGRAIN-*pathfinder* runs are cosmological collisionless simulations following the evolution of an ensemble of  $2 \cdot 768^3$  particles of DM particles within a periodic cosmological box of  $750 h^{-1}$ Mpc on a side, under the effect of a gravitational interaction determined by Eq. 2.4. The reference standard cosmology  $\Lambda$ CDM simulation is characterized by GR and  $M_\nu = 0$ eV, CDM particles with mass  $M_{\text{cdm}}^p = 8.1 \times 10^{10} h^{-1} M_\odot$ , and gravitational softening  $\varepsilon_g = 25 h^{-1}$ kpc, approximately corresponding to 1/40 of the mean particle separation (MPS). The cosmological parameters assumed in these simulations are consistent with the Planck2015 constraints (see Planck Collaboration et al. 2016b), i.e.  $\Omega_m = \Omega_{\text{cdm}} + \Omega_b + \Omega_\nu = 0.31345$ ,  $\Omega_\Lambda = 0.68655$ ,  $H_0 = 67.31 \text{ km s}^{-1} \text{ Mpc}^{-1}$ ,  $A_s = 2.199 \times 10^{-9}$ ,  $n_s = 0.9658$ , which give for the  $\Lambda$ CDM at  $z = 0$  a root-mean-square of the linear density fluctuation smoothed on a scale of  $8 h^{-1}$  Mpc equal to  $\sigma_8 = 0.842$ . The remaining simulations aim at explore the  $\{f(R), M_\nu\}$  parameter space. The parameter  $|f_{R0}|$  varies within the range  $[10^{-6}, 10^{-4}]$ , while  $M_\nu$  ranges from  $[0, 0.3]$  eV, giving in total 20 different combinations of these parameters.

The DUSTGRAIN simulations have been run with MG-Gadget, an updated version of GADGET2 (Springel 2005) that incorporates  $f(R)$  gravity models and presented by Puchwein et al. (2013). This code incorporates the MG additional force and the *Chameleon* screening mechanism (see Sect. 2.1.3). This mechanism is distinctive to  $f(R)$  gravity and is responsible for solving the nonlinear Poisson-like equation for the  $f_R$  scalar degree of freedom

$$\nabla^2 f_R = \frac{1}{3} (\delta R - 8\pi G \delta \rho), \quad (5.1)$$

through an iterative scheme known as *Newton-Gauss-Seidel*, applied to the native gravitational tree of GADGET, which is exploited as an adaptive mesh. The MG-Gadget code has been extensively tested (see e.g. the MG code comparison project described in Winther et al. 2015) and utilized for diverse purposes, including extensive collisionless cosmological simulations on large scales (Baldi & Villaescusa-Navarro 2018; Arnold et al. 2019) and hydrodynamical simulations (e.g. Roncarelli et al. 2018).

In this work, we used the simulation results produced in (Giocoli et al. 2018a) where, following the approach already adopted in Baldi et al. (2014), they have combined the MG-Gadget solver with the particle-based implementation of massive neutrinos developed by Viel et al. (2010). This is in order to incorporate massive neutrinos into the simulations as an additional particle family, each with its own distinct initial transfer function and velocity distribution. Consequently, both CDM and neutrino particles contribute to the density source term for the evolution of scalar perturbations on the RHS of the Poisson equation (Eq. 5.1).

Initial conditions have been generated following the approach of Zennaro et al. (2018) and Villaescusa-Navarro et al. (2018). This method involves creating two fully correlated random realizations of the linear matter power spectrum for standard CDM particles and massive neutrinos, based on their individual transfer functions, which are calculated by the Boltzmann solver code CAMB (Lewis et al. 2000) at the starting redshift of the simulation  $z_i = 99$ . Additionally, the scale-dependent growth rate  $D_+(z_i, k)$  for the neutrino component is computed to determine neutrino gravitational velocities accurately. Thermal neutrino

**Table 5.1:** Summary of the main numerical and cosmological parameters of the subset of the DUSTGRAIN-*pathfinder* simulations considered in this Thesis. Here,  $f_{R0}$  represents the MG parameter,  $M_\nu$  the neutrino mass in eV,  $m_{\text{cdm}}^p$  CDM particle mass, and  $\Omega_{\text{cdm}}$  and  $\Omega_\nu$  the CDM and neutrino density parameters, respectively.

Simulation	Gravity	$f_{R0}$	$M_\nu$ [eV]	$\Omega_{\text{cdm}}$	$\Omega_\nu$	$m_{\text{cdm}}^p$ [ $h^{-1} M_\odot$ ]
$\Lambda$ CDM	GR	-	0	0.31345	0	$8.1 \times 10^{10}$
$fR4$	$f(R)$	$-1 \times 10^{-4}$	0	0.31345	0	$8.1 \times 10^{10}$
$fR5$	$f(R)$	$-1 \times 10^{-5}$	0	0.31345	0	$8.1 \times 10^{10}$
$fR6$	$f(R)$	$-1 \times 10^{-6}$	0	0.31345	0	$8.1 \times 10^{10}$
$\Lambda$ CDM <sub>0.15</sub>	GR	-	0.15	0.30987	0.00358	$8.01 \times 10^{10}$

velocities are then added on top of the latter by random sampling the neutrino momentum distribution at the starting redshift  $z_i$  for the specific neutrino mass under consideration.

In this Thesis, we restrict the analysis to a subset of the DUSTGRAIN-*pathfinder* that includes a standard  $\Lambda$ CDM simulation as a reference model, 3 pure  $f(R)$  runs (i.e. with  $M_\nu = 0$  eV) and a  $\Lambda$ CDM model with massive neutrinos of mass  $M_\nu = 0.15$  eV, for a total of 5 simulations. We summarize their main parameters in Table 5.1. We note that the value of  $\Omega_m$  (that includes neutrinos) remains constant to facilitate the comparison of the density power spectrum between cosmologies with and without neutrinos. This ensures that the peak positions of the power spectra are identical and that the spectra match the long-wavelength limit. For a more detailed overview of the DUSTGRAIN-*pathfinder* simulations, refer to Giocoli et al. (2018a) and Hagstotz et al. (2019a). During the evolution of these simulations, a sequence of comoving snapshots has been stored, each representing the specified comoving volume of  $750^3 h^{-3} \text{Mpc}^3$  at a particular cosmological epoch. For all simulations, 34 snapshots were stored for a range of redshifts that enable the construction of lensing light-cones up to  $z_s = 4$ , as described below.

## 5.2 The halo catalogs

For all simulations, we identified collapsed CDM structures in each comoving snapshot using a *Friends-of-Friends* (FoF) algorithm (FoF, Davis et al. 1985) applied to the CDM particles. We utilized a linking length  $\lambda = 0.16 \times d$ , where  $d$  represents the MPS, and retained only structures with more than 32 CDM particles.

Subsequently, we applied the SUBFIND algorithm (Springel et al. 2001) on top of the FoF catalogues to identify gravitationally bound structures. This allows us to associate standard quantities such as the virial mass,  $M_{200}$ , and the virial radius,  $R_{200}$ , to the main halo of each FoF group. The computation of these quantities involved growing spheres of radius  $R$  around the most-bound particle of each main halo, enclosing a total mass  $M$ , until the condition

$$M_{200} = \frac{4}{3}\pi R_{200}^3 \times 200 \times \rho_{\text{crit}} \quad (5.2)$$

is fulfilled for  $R = R_{200}$  and  $M = M_{200}$ , where  $\rho_{\text{crit}} \equiv 3H^2/8\pi G$  is the critical density of the Universe. This mass threshold corresponds to  $M_{\text{min}} \simeq 2.59 \times 10^{12} h^{-1} M_\odot$  for the  $\Lambda$ CDM case, while for the simulations containing also massive neutrinos we decided to follow the approach of not linking them to the collapsed halos (Giocoli et al. 2018a). The selection criteria have been carefully chosen to ensure a complete and sufficiently dense sample of DM halos, essential for identifying a statistically significant number of cosmic voids. The impact of this assumption has been examined by conducting the analysis with various low-mass

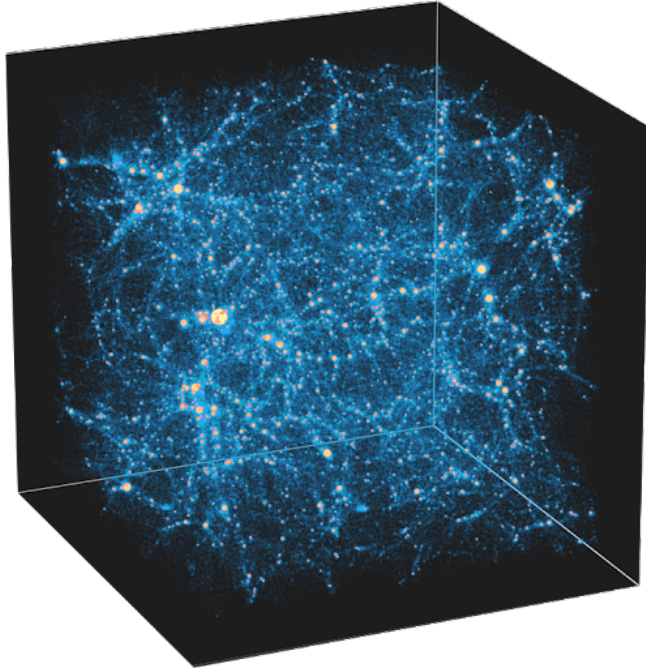


**Figure 5.1:** Graphical representation of the DUSTGRAIN-*pathfinder*  $\Lambda$ CDM snapshot at  $z = 0$ . The comoving box measures  $750 h^{-1}$  Mpc on each side. We can note that the DM halos (yellow circles, with their size indicative of the halo mass) result correctly placed in the densest regions of the simulation, i.e. in the intersection points of the filaments DM particles (blue points).

selections. An example of the resulting catalog of DM particles and associated halos is shown in Figure 5.1.

At the end, the DM halo catalogs extracted from the DUSTGRAIN-*pathfinder*  $\Lambda$ CDM simulations are characterised by a MPS, of  $8.7 h^{-1}$ Mpc for  $z = 0$  and  $12.4 h^{-1}$ Mpc for  $z = 2$ . This MPS value is comparable to the expected one for the *Euclid* wide spectroscopic survey (Laureijs et al. 2011; Amendola et al. 2018). This survey is indeed the reference point of our analysis and is expected to cover approximately  $15\,000 \text{ deg}^2$  of the sky, sampling over 50 million  $\text{H}\alpha$  galaxies.

### 5.3 Weak-lensing past light-cones

There are different methods available for extracting lensing light-cones from large cosmological  $N$ -body simulations. In recent literature we can find two main methodologies, also used to investigate MG scenarios. The first involves post-processing reconstructions that rely on slicing a series of comoving particle snapshots, as done, for instance, by Shirasaki et al. (2017). The second entails simpler and quicker algorithms, which efficiently store only the projected matter density within a designated FOV. This implies bypassing the need for the flat-sky approximation, which depends on the size of the comoving box, but leads to the creation of only one light-cone realization. Notable examples of such algorithms can be found in the works of Barreira et al. (2017) and Arnold et al. (2019). For our current analysis of the DUSTGRAIN-*pathfinder*, we opt for the former mentioned method. Specifically, we utilize the post-processing approach, constructing past light-cones for each  $N$ -body simulation through the MAPSIM routine (see Giocoli et al. 2014, for a detailed description).

In this method, particles from different snapshots are associated to distinct lens planes based on their comoving distances from the observer and whether they fall within a specified

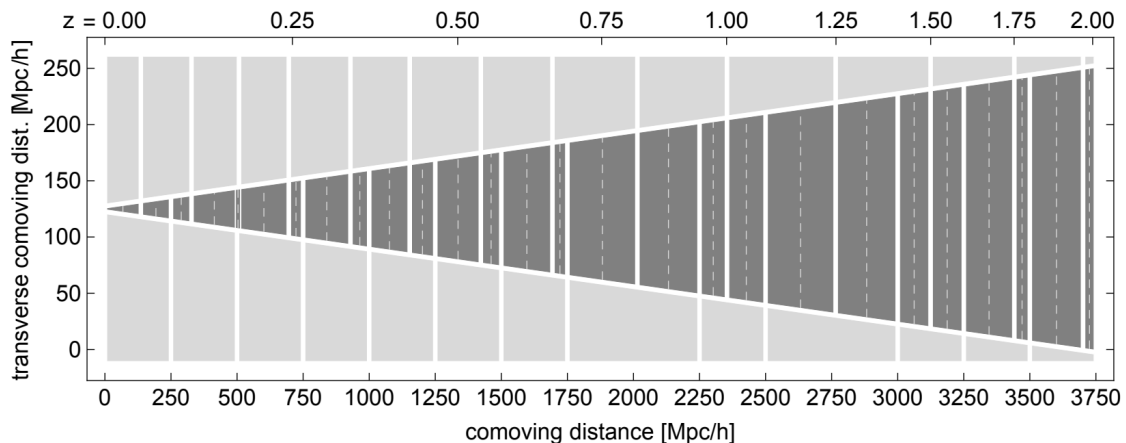


**Figure 5.2:** Example of light-cone construction with MAPSIM from  $z = 0$  to  $z = 2$  for a  $\Lambda$ CDM simulation with box size  $250 h^{-1}$  Mpc. The dark shaded region represents the light cone, expanding until its transverse comoving size matches that of the simulation box. Within each segment of the light cone, the mass distribution is projected onto a lensing plane positioned at the center of the segment (dashed line). The areas located above the light cone represent the simulation snapshots utilized to construct each segment. Conversely, the regions below the light cone represent groups of segments that have undergone the same randomization process. Credits to: [Tessore et al. \(2015\)](#)

aperture of the FOV. We use the particles stored in 21 different snapshots to construct continuous past-light-cones from  $z = 0$  to  $z = 4$ , with a square sky coverage of  $5 \text{ deg}$  by side, so we have sky maps of  $25 \text{ deg}^2$ . Due to the high time resolution of the stored snapshots, we can construct 27 lens planes to represent the distribution of projected matter density. In the MAPSIM algorithm, the observer is positioned at the apex of a pyramid, with its square base located at the comoving distance corresponding to  $z = 4$ . For each cosmological model we construct 256 different realizations of light-cone by randomising the various comoving cosmological boxes through combinations of the following procedures:

- changing the sign of the cartesian coordinates;
- redefining the position of the observer;
- modifying the order of the axes in the coordinate system.

By construction, these variations maintain the clustering characteristics of the particle distribution in each simulation snapshot ([Roncarelli et al. 2007](#)). Furthermore, improvements made to MAPSIM ([Giocoli et al. 2017](#); [Castro et al. 2018](#)) allow us to save the respective halo and sub-halo catalogs linked to a particular randomization of the past light-cone. Such randomization is performed for each simulation box at different redshifts, belonging to the range  $z_{\text{obs}} < z < z_s$ . After randomization, our light cones occupy approximately  $V_{\text{box}}/3$ .

Figure 5.2 shows the schematic construction of a light-cone for a  $\Lambda$ CDM simulation. It is evident that for lower redshifts a significant portion of the simulation box volume remains unutilized. Employing randomization techniques such as rotation and translation of the box provides a means to exploit also this volume, allowing the extraction of multiple light-cones from a single simulation ([Jain et al. 2000](#)). In this approach, each light-cone ends up encompassing a random portion of the simulation box.

### 5.3.1 Multiplane rays-tracing

The MAPSIM pipeline enables the construction of lensing planes from various simulation snapshots, saving for each plane  $l$ , on each pixel, with coordinate indices  $(i, j)$ , the particle surface mass density  $\Sigma$ :

$$\Sigma_l(i, j) = \frac{\sum_k m_k}{A_l}, \quad (5.3)$$

where  $\sum_k m_k$  is the sum over all particle masses associated with the pixel and  $A_l$  is the comoving pixel area of the  $l$ -lens plane. Since gravitational lensing is sensitive to the projected matter density distribution along the line-of-sight, we project all particles between two defined comoving distances from the observer onto each lens plane; we consistently account for this component in the simulations involving massive neutrinos.

Recalling the theoretical concepts expressed in Sect. 3.3.5, we create the convergence map by weighting the lens planes by the lensing kernel (see Eq. 3.55) and assuming the Born approximation (see Eq. 3.53 and Bartelmann & Schneider 2001 for a detailed description), as usually done in the literature (Petri et al. 2016, 2017; Giocoli et al. 2017, 2018b; Castro et al. 2018). In fact, according to Giocoli et al. (2016) and Castro et al. (2018), the Born approximation provides an accurate estimate of the probability distribution function (PDF) and the convergence power spectrum, even at small scales. Furthermore, in Schäfer et al. (2012) it has been demonstrated through the analytical solution of a perturbative expansion that the Born approximation is a enough accurate for WL down to extremely small scales ( $l \geq 10^4$ ). For the sake of clarity, we show in Figure 5.3 the shape of the lensing kernel function  $D_{\text{lens}} = (D_{l,s} \cdot D_l)/D_s$ . The simulations employed in our analysis are characterized by a discretized form of this function, which depends on the number of planes that are actually located between  $z = 0$  (observer position) and  $z = 1$  (source plane position).

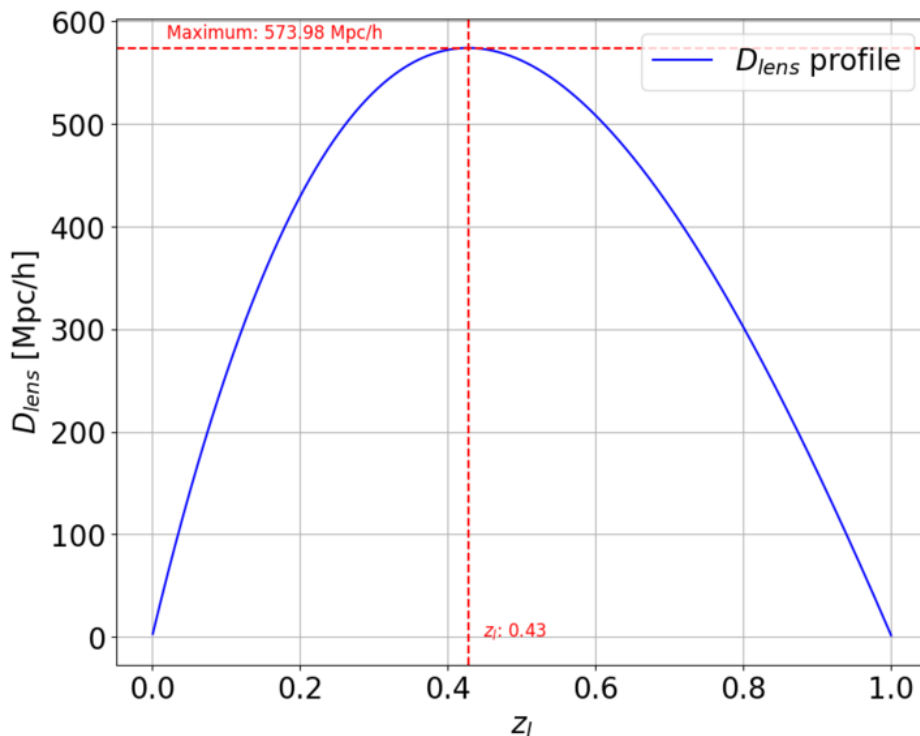


**Figure 5.3:** Lensing kernel as a function of the redshift of the lens, considering a source positioned at  $z = 1$ . We indicate with red dashed lines the maximum value of this function, reached in this case at  $z_l = 0.43$ .

At the end, from the particle surface mass density  $\Sigma_l$ , we can derive the convergence map  $\kappa$  at a specified source redshift  $z_s$  as follows:

$$\kappa = \sum_l \frac{\Sigma_l}{\Sigma_{\text{crit},l,s}}, \quad (5.4)$$

where  $l$  varies over the different lens planes with the lens redshift  $z_l$  smaller than  $z_s$  and  $\Sigma_{\text{crit},l,s}$  represents the critical surface density at the lens plane  $z_l$  for sources at redshift  $z_s$  as defined in Eq. (3.22). Figure 5.4 shows an example of the WL convergence map for  $z_s = 1$  within a past light-cone ranging from  $z = 0$  to  $z = 1$ . Each convergence map is constructed with a square aperture of 300 *arcmin* on each side and is resolved with  $2048 \times 2048$  pixels, providing an angular resolution of approximately 9 *arcmin* per pixel. The origin of each map coordinate system (R.A., Dec.) is positioned at the center such that each side spans from  $-150$  to  $+150$  *arcmin*.

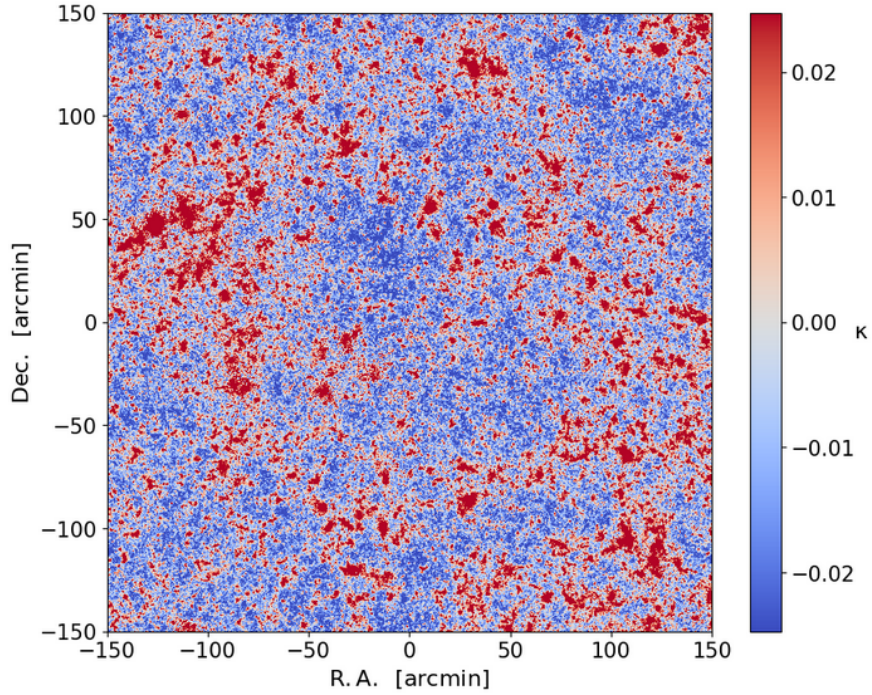


**Figure 5.4:** Example of WL convergence map for  $z_s = 1$  within the FOV of  $5 \times 5 \text{ deg}^2$  aperture. This map represents the basis of our past light-cone pyramid. The color scale of the underlying map corresponds to the convergence value associated with each pixel.



# Chapter 6

## Results

As we discussed in chapter 2 MG models constitute a compelling alternative to the standard  $\Lambda$ CDM cosmological framework, and among them  $f(R)$  models represent one of the most studied (see Sect. 2.1.3). On large cosmological scales MG models lead to an enhancement in the evolution of density perturbations. This effect, however, can in principle be counterbalanced by the presence of massive neutrinos, as they prevent the growth of cosmic structures thanks to their free-streaming effect (see Sect. 2.1.4). In fact, the range of the fifth force in  $f(R)$  models falls within the same order of magnitude as the free-streaming scale of neutrinos. This distinctive feature makes MG models particularly interesting for cosmological studies, yet their constraints from observations remain challenging. This Thesis aims to leverage the lensing of cosmic voids as a novel method to detect deviations caused by MG from scenarios characterized by GR. The choice of this probe is due to a twofold reason. First, WL is sensitive to the total gravitational potential, making it an effective tool for probing the underlying theories of gravity and the mass of neutrinos, which influence the total matter distribution in the Universe. Second, cosmic voids provide a unique environment to disentangle the effects of these scenarios: MG effects are expected to be unaffected by screening mechanisms because of void underdense interiors, while massive neutrinos effects are expected to be mitigated given that the void spatial scales are comparable with the free-streaming length.

In this chapter we focus therefore on the study of alternative cosmological scenarios by using the WL signal extracted from 2D voids. We will show in particular how 2D voids extracted with the methodology presented in Chapter 4 are ideal to maximize the tangential shear signal from underdensities, as we have seen in Sects. 3.1.1 and 3.3.6, and so to highlight the differences between various cosmological scenarios (see Sect. 3.3.7). We will carry on our analysis using 2D voids identified in the SNR maps extracted from mock light-cones in  $N$ -body simulations (see Sect. 5, in particular 5.3), with a keen eye on the future applications of this methodology to real data. This chapter is organized as follows.

In Sect. 6.1, we showcase the void catalogs extracted from the simulations through the application of the 2D finder algorithm we developed in this work. Subsequently, we analyze the VSF (Sect. 6.1.1) and tangential shear profiles (Sect. 6.1.2) measured from the 2D void catalogs. In Sect. 6.2, we compare these statistics for the different cosmological models considered, focusing also on a possible dependency of the WL on the 2D void size. In Sect. ??, we test the usage of a popular 3D void density profile parametrization to fit our tangential shear profiles. Here, we also present a new parametric formula designed to fit directly the shear profiles of 2D voids. Finally, in Sect. 6.4, we carry out the Bayesian analysis of our data modelling the tangential shear profiles in different cosmologies through the new parametric form.

## 6.1 Void catalogs from WL maps

To generate the catalog of voids for which to extract the tangential shear profiles, we applied the 2D void finder algorithm we developed (Chapter 4) to the WL convergence maps  $\kappa(\boldsymbol{\theta})$  produced from the DUSTGRAIN-*pathfinder* simulations through the multiplane ray-tracing (Chapter 5). The convergence maps used in our analysis are 256 for each cosmological model (five models in total, see Table 5.1). Each map is made of  $2048 \times 2048$  pixels, covering a squared area of  $25 \text{ deg}^2$  (5 deg per side).

The setting of the free parameters of the 2D void finder employed for this analysis is the result of numerous tests, which were aimed at finding the best configuration to extract a deep and clean (i.e. showing a low level of scatter) average shear profile. The technical settings applied to our algorithm are as follows:

- On each pixel of the map  $\kappa(\boldsymbol{\theta})$  we added galaxy shape noise  $n(\boldsymbol{\theta})$  modeled as a Gaussian random field with a top-hat filter with a size that corresponds to the pixel area  $A_{\text{pix}}$  in arcminutes. According to Lin & Kilbinger (2015); van Waerbeke (2000) its variance is given by

$$\sigma_{\text{pix}}^2 = \frac{\sigma_{\epsilon}^2}{2} \frac{1}{n_{\text{gal}} A_{\text{pix}}}, \quad (6.1)$$

where  $\sigma_{\epsilon}^2 = \langle \epsilon_1^2 \rangle + \langle \epsilon_2^2 \rangle$  is the variance of the intrinsic ellipticity distribution of the source galaxies and  $n_{\text{gal}}$  is the source galaxy number density. We assumed a *Euclid*-like setup (Amendola et al. 2018), so  $\sigma_{\epsilon}^2 = 0.3$  and  $n_{\text{gal}} = 30 \text{ arcmin}^{-1}$  at  $z_s = 1$ . In this way, we obtained a noised convergence map  $\kappa_n(\boldsymbol{\theta}) = \kappa(\boldsymbol{\theta}) + n(\boldsymbol{\theta})$ .

- We suppress the noise by smoothing via a filter represented by a Gaussian window function

$$W(\boldsymbol{\theta}) = \frac{1}{\pi \theta_G} \exp\left(-\frac{\theta^2}{\theta_G^2}\right), \quad (6.2)$$

with the choice of  $\theta_G = 2.5 \text{ arcmin}$ . In this way we obtained a noised and smoothed convergence map  $\kappa_{2.5}(\boldsymbol{\theta}) \equiv (\kappa_n * W)(\boldsymbol{\theta}) = \int d\boldsymbol{\theta}' \kappa_n(\boldsymbol{\theta} - \boldsymbol{\theta}') W(\boldsymbol{\theta}')$ .

- We assumed that intrinsic ellipticities are uncorrelated between source galaxies. In this way, the noise after the smoothing can be described as a Gaussian random field (Bond & Efstathiou 1987). According to van Waerbeke (2000), its variance is related to the number of galaxies contained in the filter as:

$$\sigma_{\text{noise}}^2 = \frac{\sigma_{\epsilon}^2}{2} \frac{1}{2\pi n_{\text{gal}} \theta_G^2}. \quad (6.3)$$

In this way, we can relate the two variances of the Gaussian fields  $\sigma_{\text{noise}}^2 = 2 \cdot \sigma_{\text{pix}}^2$  and derive the lensing  $S/N$  ratio (SNR)<sup>1</sup> of the map as  $\kappa_{2.5}(\boldsymbol{\theta})/\sigma_{\text{noise}}$ .

- To identify the connected pixel regions resulting from the projection of underdense lines of sight, we analyzed 11 threshold levels from  $\text{SNR} = -5$  to  $\text{SNR} = 0$  with a step of 0.5. Moreover, to discriminate absolute minima from local minima, we used a start threshold of  $\text{SNR} = -4$  and a stop threshold of  $\text{SNR} = -3$ .
- Finally, as the stop threshold for the expansion of the pixel grid in the ray assignment, we used the value  $\langle \text{SNR} \rangle = -2.5$ .

---

<sup>1</sup>Thus, the physical meaning of this ratio is that  $S$  represents the number of photon counts on the sky area analyzed, while  $N$  denotes the lensing background noise from sources in the background.

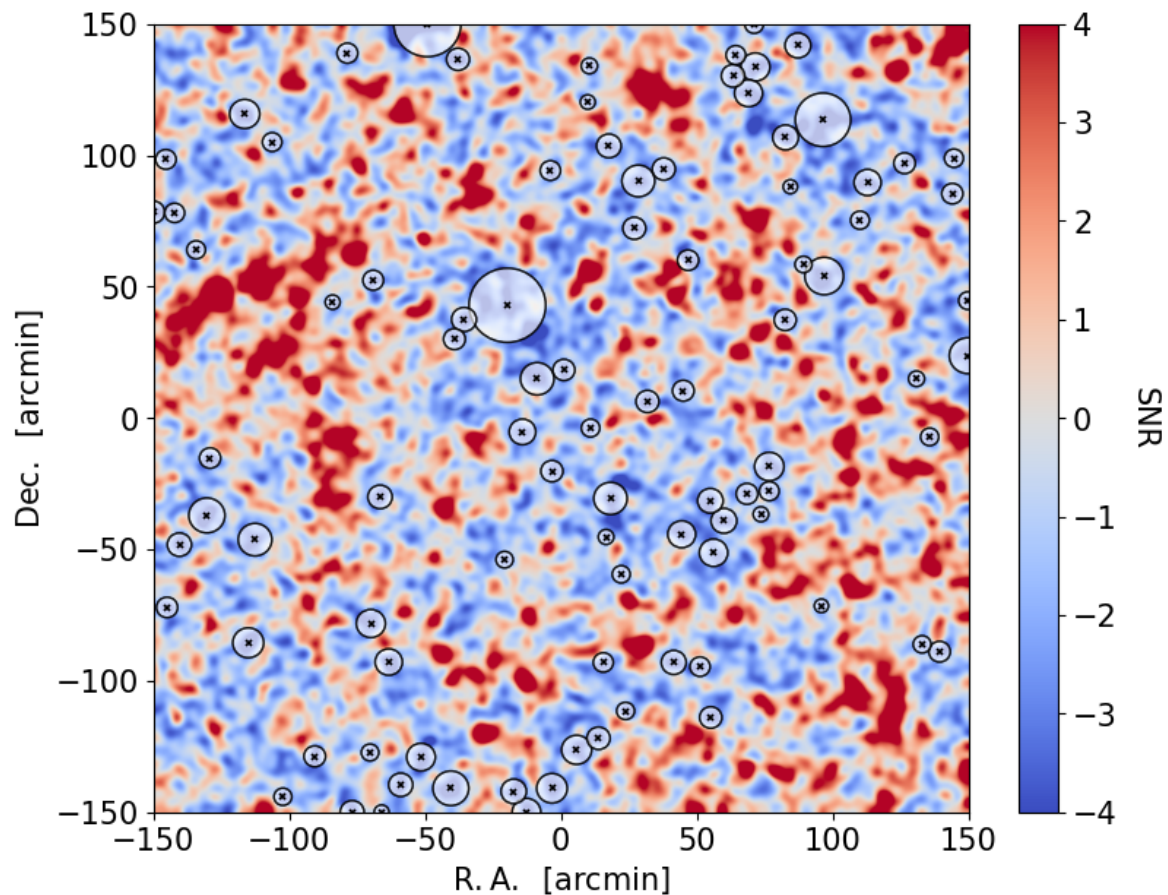


**Figure 6.1:** Example of SNR map of the WL convergence (R.A., Dec.) extracted from the  $\Lambda$ CDM DUSTGRAIN-*pathfinder* simulations. Colors from blue to red represent areas with increasing SNR, as indicated by the colorbar on the right. The 2D voids identified by our algorithm are shown as lighter areas delimited by black circles. The corresponding centers (absolute minima) are marked with black crosses.

Our 2D voids in the final catalog are thus highly underdense voids that represent the projection of underdense areas along the line of sight, i.e., tunnel voids. They are designed to optimize the detectable tangential shear signal (Cautun et al. 2018; Davies et al. 2021b) which is expected to be negative when analyzing of underdense regions. Since the lensing signal is influenced by all the matter along the line of sight, we expect that the signal we detect cannot be trivially interpreted as the projection of isolated 3D voids. For example, we anticipate that the feature of the compensation wall, present in the density profiles of 3D voids, will not be detectable in the lensing signal, as it is smoothed out by the overlay of various underdensities and flattened due to projection effects.

In Figure 6.1 shows as example a SNR map from one of the 256 convergence maps produced for the  $\Lambda$ CDM scenario, where the positions of the voids is also marked. We can note that these voids correspond very well with the negative regions of SNR. All negative regions on the map that are not associated with 2D voids are either considered part of a larger, spatially nearby void, or are considered to be caused by SNR fluctuations. We also emphasize how the chosen criterion for assigning the void radius is particularly effective in identifying voids as entirely negative regions surrounded by positive areas, i.e. the void sizes result correctly expanded until they reach a WL positive signal.

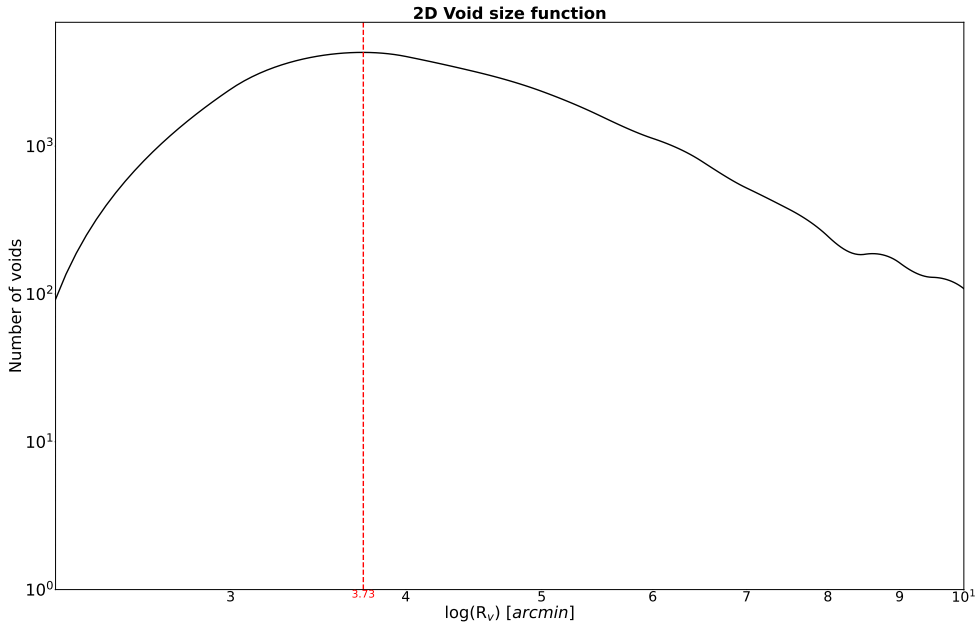


**Figure 6.2:** Total counts of 2D voids as function of their size for the  $\Lambda$ CDM scenario. We restricted the analysis to the radii included in the range  $[2, 10]$  arcmin. As a reference, we indicate with a vertical dashed line the position of the maximum value of the distribution. As explained in the text, the data error bars are not represented in this case.

### 6.1.1 $\Lambda$ CDM 2D void size functions

Compared to 3D voids identified in galaxy surveys, generally covering scales of tens of megaparsecs (see e.g. Contarini et al. 2022a), 2D voids extracted in this work from SNR maps are characterized by relatively small sizes. Their angular extension span from 1 to 15 arcmin. To convert this quantity in spatial scales we need to consider the effective lens plane of our system. As we showed in Figure 5.3, the peak of the lensing kernel function (see Sect. 5.3.1) of our mock light-cones is at the redshift  $z_l = 0.43$ . At this distance, our voids would result having radii between  $0.3356$  and  $5.0336 h^{-1}$  Mpc. This substantial shrinking of the size is not unexpected. In fact, these are formally tunnel voids (see Sect. 3.1.1), which emerge when photons from distant sources encounter on their path mainly underdense regions, especially at redshifts around the maximum of the lensing kernel function. These underdensities can be thought as a series of 3D voids that partially intercept the observer’s line of sight. Here, there is also an effect due to the loss of void signal in cases where there is a highly overdense region outside of a void. The resulting projection on the plane of the sky is therefore expected not to conserve the original size of 3D voids, but to cover only those areas where the signal is dominated by a negative convergence.

We now focus on studying the abundance of the 2D voids extracted from WL convergence maps as a function of their projected radius  $R_v$  in arcminutes. The whole sample of voids is derived from the 256 maps built for the  $\Lambda$ CDM scenario and is composed of  $\approx 22$  thousands voids. We restrict our analysis to the range  $[2, 10]$  arcmin to avoid the statistically rarest objects, which are characterized by large uncertainties. Then we measure the number of voids as a function of their size in 200 equi-spaced radial bins. The result represents the so-called void size function (Section 3.2.1) and is shown in Figure 6.2. The error associated to void

number counts is can be considered Poissonian-like. However, for the peculiar nature of 2D voids, this approximation may turn out to be inaccurate. For this reason, we avoided for the moment to represent the error bars in this plot, relying on an interpretation of the results based only on the trend of our data.

The shape of the void size function is consistent with the one measured for 3D voids (Hamaus et al. 2016b; Ronconi & Marulli 2017; Contarini et al. 2022b,a), i.e. it shows how small voids are more abundant with respect to the larger ones. More complex is the interpretation of the reduction in number counts at very small scales. This is mainly a spatial resolution effect, given by the pixel size and by the smoothing applied to the SNR maps. It imposes a lower limit to the size of voids that can be reliably identified. Moreover, the void-in-cloud effect may have an impact (see Sect. 3.2.1). This phenomenon occurs indeed when voids are encompassed within larger overdense structures and causes a lowering in the abundance of very small voids. The number of voids and the distribution of their sizes will serve as a basis for the study of void tangential shear profiles.

### 6.1.2 $\Lambda$ CDM tangential shear profile from void

As already highlighted throughout the first part of the Thesis, the void statistics on which we will focus is the tangential shear profile. The analysis of the WL signal from cosmic voids represent an emerging probe that still lacks a dedicated and in-depth study. This kind of analysis is expected to be promising especially to test MG models, also in the more complex configuration in which massive neutrinos are taken into account. In this work, we extract the tangential shear profile from 2D voids adopting the following procedure:

1. For each SNR map we apply a regular grid centered on each void of the sample. The grid is designed to cover a region up to ten times the void radius, therefore is characterized by a side length of  $20R_v$  ( $\pm 10R_v$  around the center). Such extension is then converted in pixel units. This kind of approach makes use of boundary conditions, to deal with lack of SNR values beyond the edges of the map. This grid is used to extract the values of smoothed convergence,  $\kappa_{2.5}(\boldsymbol{\theta}) = \kappa_{2.5}(r_p)^2$ , in the corresponding region of the map.
2. Around the void center, we build up 64 circular concentric shells from  $r_{\min} = 0$  to  $r_{\max} = 10R_v$ , to divide the profile in different linear bins.
3. We compute the average of the convergence values stored in the pixels included in each shell. In this way, for each shell, a differential value of the convergence,  $\kappa(r_p)$ , is associated to the midpoint of the bin, i.e., at the intermediate value  $r_p$  between the inner and outer radius of the shell.
4. We also compute the average of the convergence stored in the pixels included in the area  $r \leq r_p$ . This is equivalent to compute, for each of the 64 bins, the integral quantity  $\bar{\kappa}(< r_p)$  via Eq. (3.58), i.e. the convergence enclosed inside a circle of radius  $r_p$ .
5. We perform the *stacking* of void profiles, i.e. we rescale the spatial extension of each profile by the corresponding radius of the void,  $R_v$ . This implies having void profiles spanning from 0 to 10  $r_p/R_v$ . Representing void profiles in unit of the void radius is useful to compare profiles of voids with different sizes, uniforming their behavior as seen in Sect. 3.2.2. Finally, the tangential shear  $\gamma_t(r_p)$  is computed for each bin by subtracting the value of the differential convergence to the integral convergence, i.e. applying Eq. (3.57).

---

<sup>2</sup>Hereafter we will omit the subscript 2.5, as we will always refer to the convergence noised and smoothed with  $\Theta_G$ .

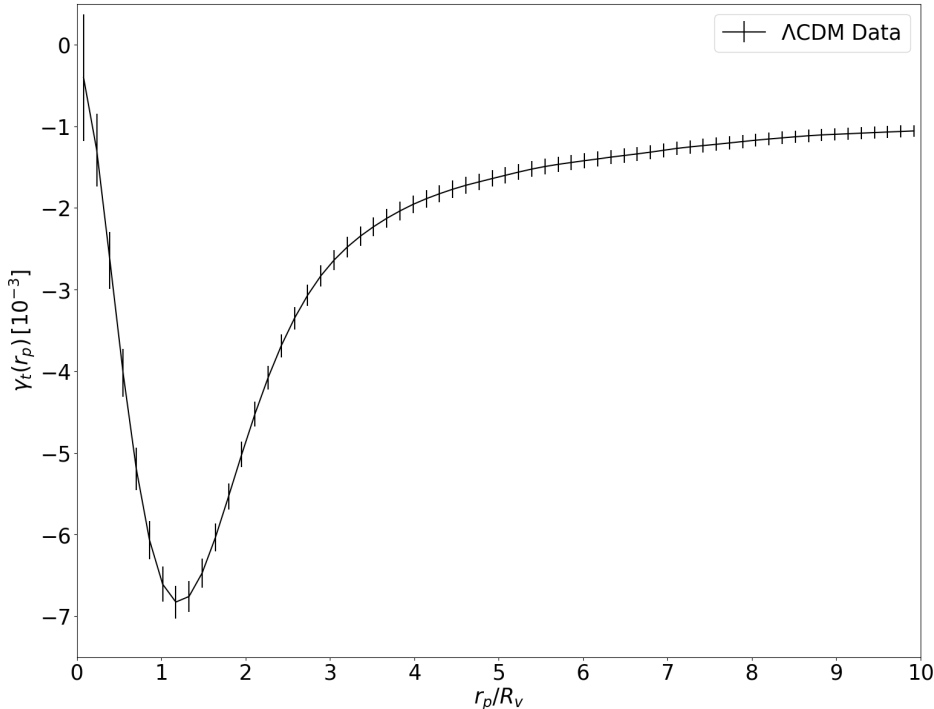


**Figure 6.3:** Stacked tangential shear profile measured using the 2D voids extracted for the  $\Lambda$ CDM simulations. The error bars represent the sum of observational and statistical uncertainties.

The uncertainty to associate to the tangential shear is evaluated as the sum in quadrature of the statistical error  $\sigma_{\text{stat}}$  and the observational error  $\sigma_{\text{obs}}$ :

$$\sigma_{\text{tot}} = \sqrt{\sigma_{\text{stat}}^2 + \sigma_{\text{obs}}^2}. \quad (6.4)$$

The first represents the scatter between all the  $\gamma_t(r_p)$  profiles and mainly depends on the number of voids,  $N$ :

$$\sigma_{\text{stat}} = \frac{\sigma_{\text{measure}}}{\sqrt{N}}, \quad (6.5)$$

where  $\sigma_{\text{measure}}$  is the standard deviation of the value distribution of  $\gamma_t(r_p)$  measured at a given  $r_p$  (i.e. radius bin). The second is instead inserted to mimic the error expected with real data. The observational error is added to every radius bin and is mostly driven by the uncertainty on the intrinsic ellipticity distribution of the source galaxies,  $\sigma_\epsilon$ :

$$\sigma_{\text{obs}} = \sqrt{\frac{\sigma_\epsilon^2}{3600 n_{\text{gal}} A_{\text{shell}}}}. \quad (6.6)$$

Here  $A_{\text{shell}} = (r_{>,\text{shell}}^2 - r_{<,\text{shell}}^2)$  with  $r_{>,\text{shell}}$  and  $r_{<,\text{shell}}$  that are the inner and outer radii of the shell considered for the computation of the convergence. This formula stems from the type of pre-processing described above. All the following analysis will follow this strategy for the computation of the tangential shear errors.

In Figure 6.3 we report the stacked tangential shear profile measured around voids identified in the  $\Lambda$ CDM SNR maps. Firstly, we note that the tangential shear profile obtained is statistically negative, as expected for a signal generated by underdensities. Furthermore, this signal is of the same order of magnitude ( $10^{-3}$ ) as found in the literature for tunnel voids, such as in [Davies et al. \(2019a\)](#). With respect to the findings of these authors, however,

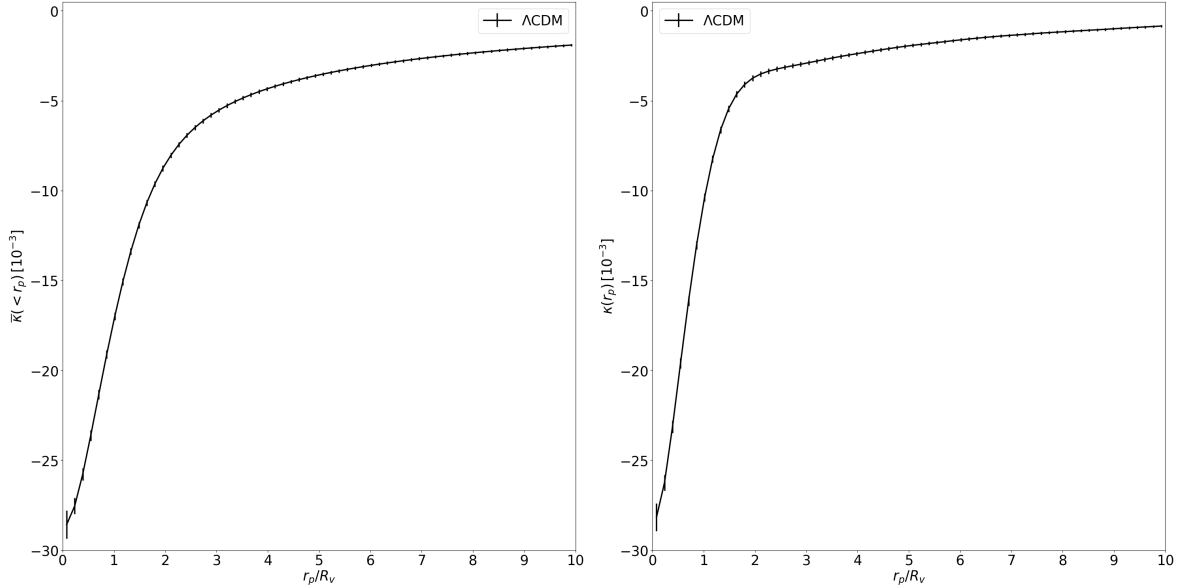


**Figure 6.4:** Left and right panels show the integrated,  $\bar{\kappa}(< r_p)$ , and differential,  $\bar{\kappa}(r_p)$ , convergence profiles extracted from the stacking of 2D voids, for the  $\Lambda$ CDM scenario, in the left and right plot respectively. Both are represented with error bars including observational and statistical uncertainties.

we detect a WL signal that is negative up to larger scales, i.e. approximately ten times the radius assigned to our voids. We also note that the minimum value of  $\gamma_t(r_p)$  is not measured in the most internal parts of voids, but on scales slightly larger than  $r_p/R_v = 1$ . The largest amplitude in the signal is reached indeed when the difference between  $\kappa(r_p)$  and  $\bar{\kappa}(< r_p)$  is maximum. To better understand this feature, let us analyze the behavior of the tangential shear at the lower and upper extremes of the profile:

- For  $r_p/R_v \rightarrow 0$ :  $\gamma_t(r_p) \rightarrow 0$  because both  $\kappa(r_p)$  and  $\bar{\kappa}(< r_p)$  tend towards the same value in a homogeneous density field (the center of the void) as it can be seen in Figure 6.4. This rise in the profile is due to the compensation of opposite deflections of the path of photons coming from background sources and passing nearby the center of a projected void. Such compensation indeed depends on the symmetry of the voids, i.e. the large-scale distribution of matter surrounding them.
- For  $r_p/R_v \rightarrow 10$ :  $\gamma_t(r_p)$  tends towards 0 as expected, i.e. close to the deflection due to the average convergence of the Universe. However, the rise in the profile is very slow, especially for  $\bar{\kappa}(< r_p)$  since it is an integrated quantity and thus, less sensitive to overdensities outside the void compared to  $\kappa(r_p)$ . In fact, as it can be seen in Figure 6.4, at large radii, the integrated and differential profiles do not tend towards the same value but  $\bar{\kappa}(< r_p)$  is more negative than  $\kappa(r_p)$ , leading to a lowering of the  $\gamma_t(r_p)$  profile.

### Void size dependency

Now we focus on studying the dependency of the tangential shear profile on the void size. This analysis allows us to examine how the tangential shear properties vary with void radii and provides valuable insights into the matter distribution around voids at different scales. Moreover, we expect the stacking procedure to be more effective when analyzing void with similar sizes, which are expected to be auto-similar (see Sect. 3.2.2).

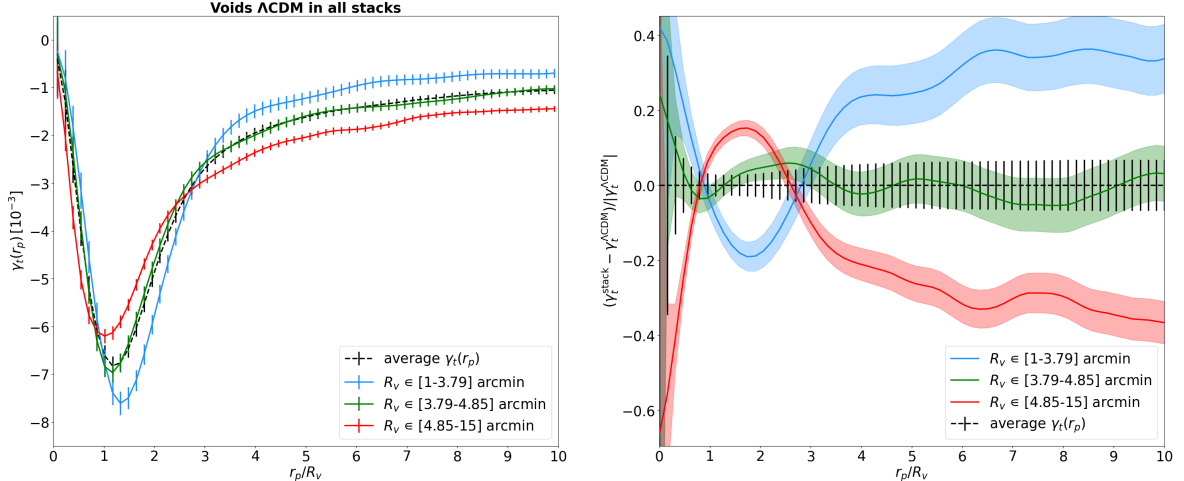


**Figure 6.5:** On the left, the tangential shear profiles measured from samples of voids with different sizes: small (in light-blue), medium (green) and large (red). We report with a black dashed line our reference profile, i.e. the one computed using the whole void sample. On the right, the residuals between the profiles of each radius selection and our reference stacked void profile. The data here represented are extracted from the standard  $\Lambda$ CDM subset of the DUSTGRAIN-*pathfinder* simulations.

We divide our sample of voids according to their size, selecting the following three intervals of radius to include the same number voids in each of them:

- *small voids* with radii  $R_v$  included in the range  $[1, 3.97]$  arcmin;
- *medium voids* with radii  $R_v$  included in the range  $[3.97, 4.85]$  arcmin;
- *large voids* with radii  $R_v$  included in the range  $[4.85, 15]$  arcmin.

Then we extract the tangential shear profiles from these equi-populated void samples. The result is represented in Figure 6.5. From the left plot of this figure we can identify a trend between the three bins. In particular, we note that the signal of small voids is deeper and rises more rapidly towards the mean shear signal of the universe, while for the subsample of large voids, we observe a less profound signal and a slower rise. This behavior is similar to the one expected for the density profiles of 3D voids (Nadathur et al. 2015; Hamaus et al. 2014; Voivodic et al. 2020). In fact, small voids usually show deeper interiors and high compensation walls. This usually happens because large voids are characterized by internal substructures and are more irregular in shape, as they have been subject to merger events. In our case, another effect plays an important role: as we saw from the analysis of the void size function, small voids are much more numerous with respect to the large ones. Therefore, if we divide the sample into equi-populated bins, the bin containing the large voids will cover a broader range of radii. This means that the stacked signal for large voids is more affected by the distinct behavior of different void shear profiles, resulting in an average smoothed trend.

To facilitate the comparison between different void subsamples, we show in right panel of Figure 6.5 for the three cases the residuals computed with respect to the tangential shear profile of the complete sample of voids,  $\gamma_t^{\text{total}}(r_p)$ , which represents our reference in this case and it is also reported in Figure 6.3. In particular, we use the formula:

$$\Delta\gamma = \frac{\gamma_t^{\text{profile}}(r_p) - \gamma_t^{\text{total}}(r_p)}{|\gamma_t^{\text{total}}(r_p)|}. \quad (6.7)$$

This approach is utilized to compute all the tangential shear profile residuals that will be shown hereafter, considering different cases for  $\gamma_t^{\text{profile}}(r_p)$  and fixing a specific reference model.

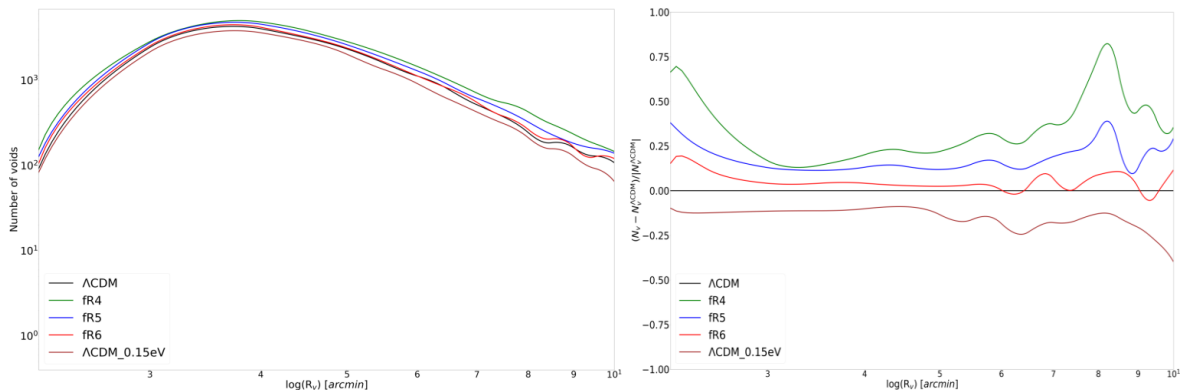


**Figure 6.6:** *Right:* size functions of 2D voids measured in simulations featuring different cosmological models:  $\Lambda$ CDM (black),  $fR4$  (green),  $fR5$  (blue),  $fR6$  (red) and  $\Lambda$ CDM<sub>0.15eV</sub> (brown). *Left:* the corresponding residuals computed with respect to the  $\Lambda$ CDM model. Also in this case, error bars are not represented (see Sect. 6.1.1).

We finally observe that the subsample of voids of intermediate size is the most similar to the average shear profile computed with the totality of the void sample.

## 6.2 Comparison with alternative gravity scenarios

We now present the results for alternative cosmological scenarios ( $fR4$ ,  $fR5$ ,  $fR6$  and  $\Lambda$ CDM<sub>0.15eV</sub>, see Table 5.1), compared to the  $\Lambda$ CDM. We start by analyzing the void size function, i.e. the total number counts of 2D voids as a function of their radius, extracted from the 256 SNR map realizations, for each cosmological model. We show the results in Figure 6.6. On the right we present the five void size functions in the range [2, 10] arcmin and on the left the corresponding residuals computed with respect to the  $\Lambda$ CDM case.

We note that all the size distributions are characterized by a similar shape and the main difference is in their amplitude, i.e. there is a difference in the number of voids at each radius bin. The trend observed for different cosmological scenarios is the one expected: regarding MG models, scenarios with higher values of the parameter  $|f_{R0}|$  are those that produce the greater increase in the number of void counts, while in the presence of massive neutrinos, the abundance of voids results suppressed. Higher values of  $|f_{R0}|$  implies indeed a stronger action of the fifth force, which in turn favors the evolution of LSS, including cosmic voids. On the other side, larger is the neutrino mass, more suppressed is the growth of cosmic structures and so the formation of voids. To conclude, the models  $fR6$  and  $\Lambda$ CDM<sub>0.15eV</sub> are those expected to be the most similar to the  $\Lambda$ CDM case, although showing opposite trends.

Now we focus on the differences of the stacked tangential shear profiles in alternative cosmologies. We start by considering voids of different sizes all together in a unique bin of radius. We show the stacked shear profiles in the left panel of Figure 6.7, highlighting the differences with respect to the  $\Lambda$ CDM case through the residuals shown in the right panel of the same figure (the residual computation is done as in Eq. 6.7). The observed trends are in agreement with theoretical expectations since we detect deeper tangential shear signals for MG models with stronger fifth-force intensities and a shallower signal in the presence of massive neutrinos. This is explained by the fact that cosmic voids experience a depletion of their internal density profiles when their evolution is enhanced, conversely they are less underdense when their growth is hampered.

We note, however, that there is a pivot point at  $r_p/R_v \simeq 4$  where all models results almost

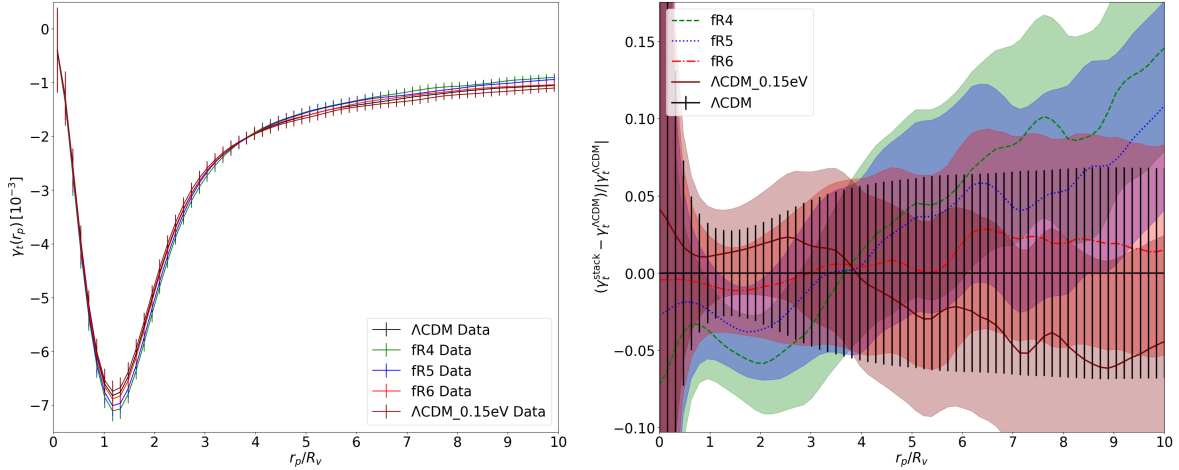


**Figure 6.7:** Stacked tangential shear profiles for different cosmological models (left panel) and corresponding residual with respect to the profile measured in the  $\Lambda$ CDM scenario (right panel). Both the plots utilize the following color scheme:  $\Lambda$ CDM (black),  $fR4$  (green),  $fR5$  (blue),  $fR6$  (red) and  $\Lambda$ CDM<sub>0.15eV</sub> (brown). The error bars represent the total uncertainty derived from statistical and observational errors (see Eqs. 6.4, 6.5, 6.6). For the sake of clarity, on the residual plot the uncertainties associated to the profiles in alternative cosmologies are represented as shaded colored regions.

degenerate. Over this scale, there is an inversion in the trends of the profiles. This point indicates the transition between the regions dominated by the effects of the underdensities and overdensities. Going toward the outskirts of 2D voids the tangential shear profiles start in fact to deviate from the  $\Lambda$ CDM, following the effects expected by the presence of overdensities, i.e. an increase of signal for MG models and a decrease for the scenario with massive neutrinos. The fact that this transition scale is at a distance equal to four times the radius of our voids obviously depends on the chosen definition of 2D void radius. Moreover, we must consider that the tangential shear is also based on the measure of integrated convergence,  $\kappa(< r_p)$ , so it is subject to the influence of the internal underdensity within the profile even at large distances from the center. For this reason, we should not be surprised that the transition scale is found at relatively far distance from the center of our 2D voids.

Finally, it is possible to appreciate how, given the large error bars associated with the profiles, it is statistically impossible to completely discriminate between these five cosmological models. This is due to the fact that in our analysis we aim at building our data sample with the characteristics of real surveys like *Euclid*. Therefore, although our mock light cones cover a relatively limited Universe volume, our tangential shear profiles have been treated to include a significant observational error, which dramatically increases the uncertainty on the extracted data. For illustrative purposes only, we report in Figure 6.8 the same plot represented in the right panel of Figure 6.7 but for tangential shear profiles characterized by statistical errors only. We can therefore conclude that the observational error is the aspect that will need to be addressed most in future surveys if the aim is to apply this kind of approach to constrain  $f(R)$  models.

As an additional test, we show the stacked profiles of voids in different cosmologies by dividing our sample of voids based on their radius. We then use the three equi-populated bins already introduced in Figure 6.5 and present the results in Figures 6.9, 6.10, 6.11, for small-size, medium-size, and large-size voids, respectively. We note that the main trend of the profiles is the same even for voids characterized by different sizes and that, even using these sub-samples, the statistical discrimination between the different alternative cosmological scenarios here analyzed is not possible due to the large uncertainties.

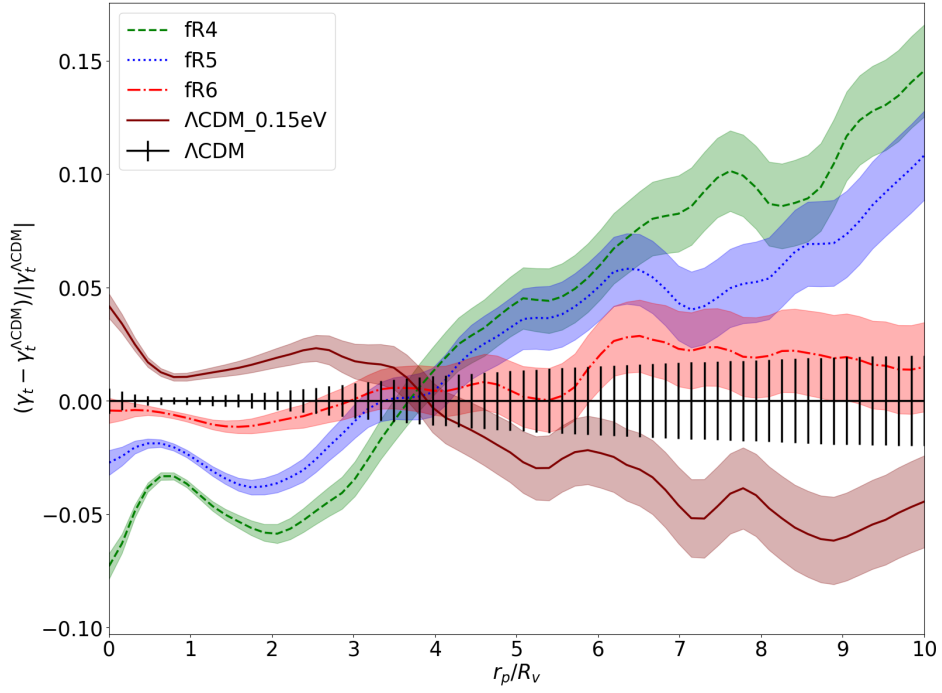


**Figure 6.8:** Same as the right panel of Figure 6.7 but for the unrealistic case in which we associate to the tangential shear profiles characterized only the statistical errors.

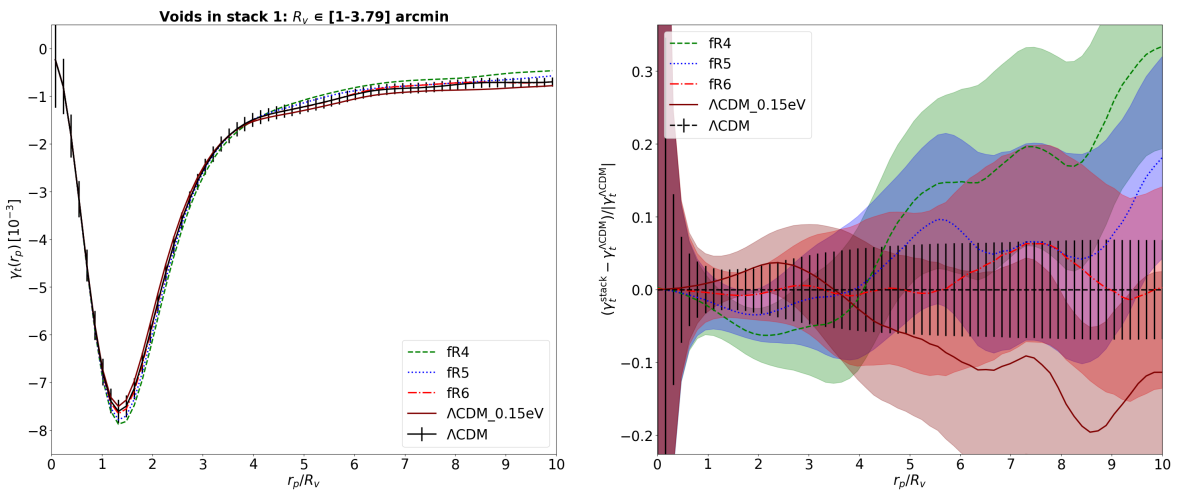


**Figure 6.9:** Same as Figure 6.7 but for small-size voids, i.e. with radius in the range [1, 3.79] arcmin.

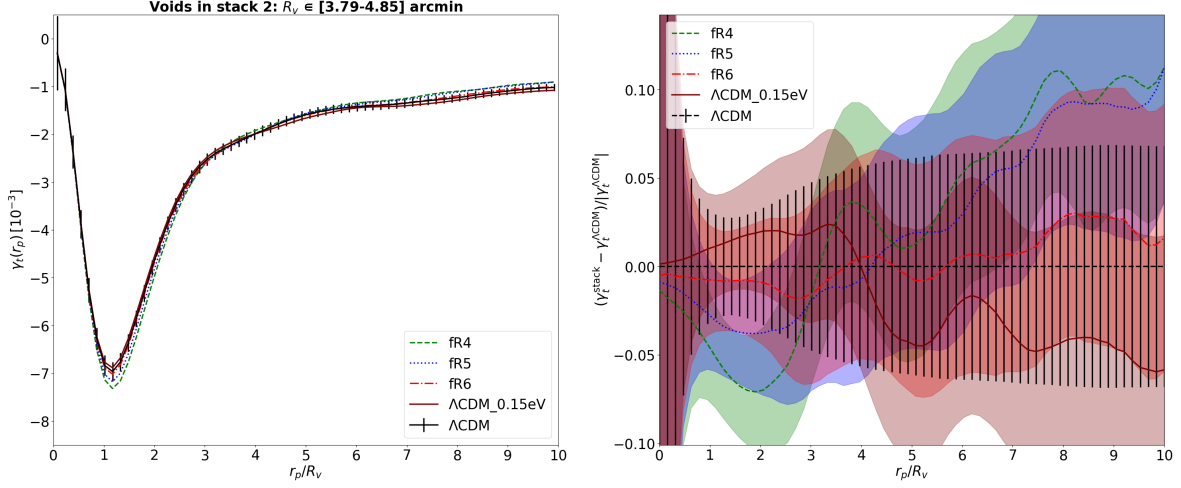


**Figure 6.10:** Same as Figure 6.7 but for medium-size voids, i.e. with radius in the range  $[3.79, 4.85]$  arcmin.

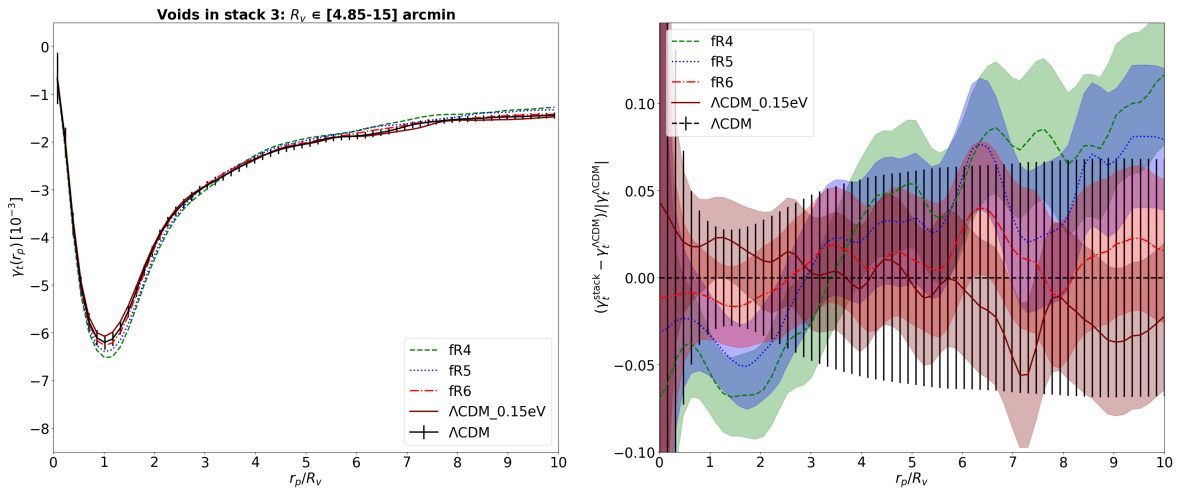


**Figure 6.11:** Same as Figure 6.7 but for large-size voids, i.e. with radius in the range  $[4.85, 15]$  arcmin.

## 6.3 Modeling the tangential shear profiles

In the final part of this Thesis work, we aim at modeling the tangential shear profile using a parametric formula. Indeed, although a theoretical model based on first principles has never been formulated for the WL signal from voids, we can resort to fitting our data with an empirical function and study the behavior and limits of its free parameters in different configurations. Albeit this approach does not directly constrain the parameters of the cosmological model, it still represents a first step towards understanding the physics governing the WL phenomenon in voids.

### 6.3.1 Integration of 3D void density profiles

The first method we follow is to start from a known parametric formula from the literature to represent the density profile of 3D voids. Following the approach of [Fang et al. \(2019\)](#) and [Boschetti et al. \(2023\)](#), we can integrate the functional form of the density profile along the line of sight to obtain the surface mass density,  $\Sigma(r_p)$ , from which we can then derive the tangential shear profile,  $\gamma(r_p)$ . Below, we report the details of this procedure, as it is very technical and it will be necessary a non-trivial implementation. This requires a convenient definition of the coordinate system:

$$r_z = \sqrt{r^2 - r_p^2}; \quad r = \sqrt{r_z^2 + r_p^2}; \quad \frac{dr}{dr_z} = \frac{1}{2} \cdot \frac{2 \cdot r_z}{r} = \frac{r_z}{\sqrt{r_z^2 + r_p^2}}, \quad (6.8)$$

where  $r$  is the radius of the 3D void, while  $r_z$  is its projection along the line of sight. From this we can compute:

$$\Sigma(r_p) = 2 \int_{r_p}^1 \frac{r \cdot \rho(r)}{\sqrt{r^2 - r_p^2}} dr = 2 \int_0^{10} \rho \left( \sqrt{r_z^2 + r_p^2} \right) dr_z. \quad (6.9)$$

We integrate therefore up to a distance of ten times the void radius, adding a factor 2 to exploit the symmetry around the void center. Then, we perform another integration, but this time over the projected radius to obtain  $\bar{\Sigma}(< r_p)$  (see Eq. 3.58):

$$\bar{\Sigma}(< r_p) = \frac{1}{\pi r_p^2} \int_0^{r_p} 2\pi r'_p \cdot \Sigma(r'_p) dr'_p = \frac{2}{r_p^2} \int_0^{r_p} r'_p \cdot \Sigma(r'_p) dr'_p. \quad (6.10)$$

Finally, subtracting  $\Sigma(r_p)$  from  $\bar{\Sigma}(< r_p)$  yields the excess surface mass density through Eq. (3.48):

$$\Delta\Sigma(r_p) = [\bar{\Sigma}(< r_p) - \Sigma(r_p)] \cdot R_v. \quad (6.11)$$

Let us underline that here we also added the multiplication by  $R_v$ , since it is necessary to take into account the dependency on the void radius and recover the correct physical units. Now, the excess surface mass density is proportional to the tangential component of the shear through the critical surface mass density,  $\Sigma_{\text{crit}}$  (Eq. 3.22):

$$\gamma_t(r_p) = \kappa(< r_p) - \kappa(r_p) = \frac{\Delta\Sigma(r_p)}{\Sigma_{\text{cr}}}. \quad (6.12)$$

Now we can apply this pipeline to fit our tangential shear profiles, assuming a functional form for  $\rho(r)$ . In addition to allowing the variation of the coefficients of the function defining  $\rho(r)$ , we also consider  $\Sigma_{\text{crit}}$  as a free parameter. Although this quantity could, in principle, be derived by knowing the cosmological parameters of the simulation, in our case, we are not able

to model the lens system with a single lens plane. Dealing with tunnel voids, the contribution of the signal is indeed defined by multiple lenses, which cannot be characterized by a unique redshift value. In practice, we will use  $\Sigma_{\text{crit}}$  as a normalization factor for fitting our data. As data vector, we consider for the moment the stacked tangential shear profile measured in the  $\Lambda$ CDM mock light cones. We postpone the description of the fitting employed technique to Sect. 6.4.

The first functional form we consider to represent the density profile of 3D voids is the one proposed by [Hamaus et al. \(2014\)](#) and already introduced in Sect. 3.2.2, i.e. the HSW function in Eq. 6.13:

$$\frac{\rho_v(r)}{\bar{\rho}} - 1 = \delta_c \frac{1 - (r/r_s)^\alpha}{1 + (r/r_v)^\beta}. \quad (6.13)$$

As already seen, it is characterized by four free parameters ( $\delta_c, \alpha, \beta, r_s$ ), so it is expected to fit properly voids of different sizes and internal densities. Nevertheless, the no combination of free parameters lead to an optimal fit of our data. This can be seen in the left panel of Figure 6.12, where we report the best fit of the data with the HSW model. Even considering a confidence level at  $3\sigma$  the overall shape of the model does not reproduce the one of the tangential shear profiles. The reduced  $\chi^2$  shows indeed a value very far for the unity, i.e.  $\tilde{\chi}_{\text{HSW}}^2 = 17.53$ .

The second functional form we consider is the hyperbolic tangent (HT) profile presented in [Voivodic et al. \(2020\)](#). Although less popular, this parametric form has the property of using only two free parameters, representing simpler shapes of 3D voids. It is expressed as:

$$\rho_v(r/R_v) = 1 + |\delta_c| \bar{\rho}_m \left\{ \frac{1}{2} \left[ 1 + \tanh \left( \frac{y - y_0}{s(R_v)} \right) \right] - 1 \right\}. \quad (6.14)$$

In this parameterization,  $\delta_c$  is the density contrast at the void center,  $y = \ln(r/R_v)$  and  $y_0 = \ln(r_0/r_v)$ . The radius  $r_0$  is determined by requiring that the integral of the profile up to  $R_v$  is  $\Delta_v = 0.2$ . This allows us to express  $r_0(s)$  (in units of  $h^{-1}$  Mpc) as a second-order polynomial function:  $r_0(s) = 0.37s^2 + 0.25s + 0.89$ , where  $s$  represents the gradient of the profile. The parameter  $s$  works similarly to the concentration parameter in the NFW profile, governing the rate at which density increases as we move away from the center of the void.  $\delta_c$  and  $s$  are therefore the only free parameters of the HT profile.

We represent in the right panel of Figure 6.12 the result of the fit of the tangential shear profile assuming the HT function to model the density profile. Also in this case the integration of the 3D void density profile does not lead to a good representation of our tangential shear profiles. In fact also with this model the reduced  $\chi^2$  is far for the unity, i.e.  $\tilde{\chi}_{\text{HT}}^2 = 28.83$ .

The motivation of this inconsistency must be sought of the very nature of our voids. In our case, we are trying to model the WL signal generated by tunnel voids, which is the result of projecting numerous underdensities along the line of sight. Following the approach described in this section, we are instead imposing the modeling of the tangential shear through the projection of the typical density profile of isolated 3D voids. This assumption cannot be valid for our tunnel voids, which instead derive from the projection of a complex distribution of underdensities with different sizes and positions. Therefore, we emphasize that in the analyses of [Fang et al. \(2019\)](#) and [Boschetti et al. \(2023\)](#) the usage of the 3D density profiles was effective for the following reason. Both the authors make use of a tomographic approach, considering only the WL signal generated by the matter distribution present in relatively thin redshift slices. In this way, they exploit a lens plane that follows the simplified condition of having only one, or in any case a few, 3D voids along the line of sight.

As explained in Sect. 3.3.6, this kind of approach has the advantage of being able to relate to the physical properties of 3D voids. On the other hand, with respect to the usage of

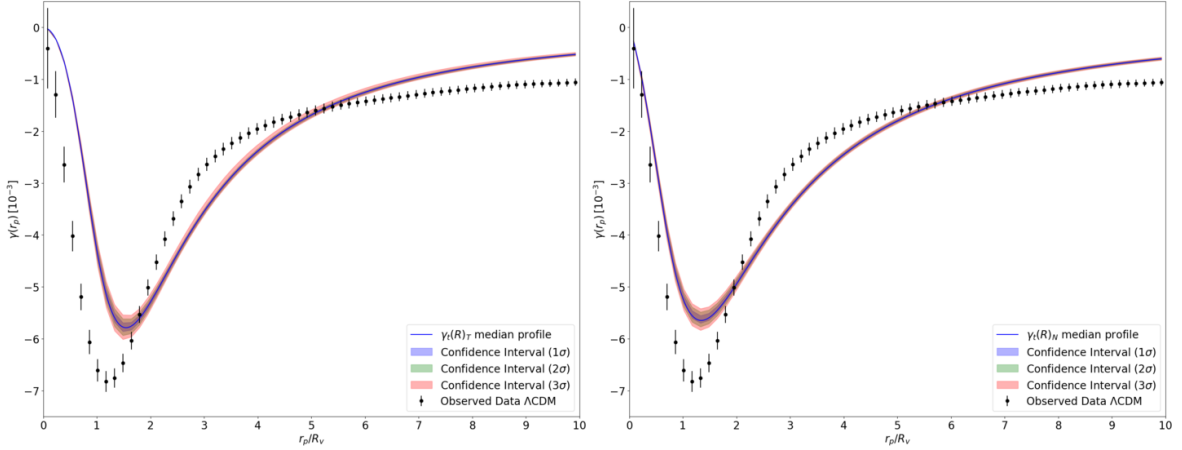


**Figure 6.12:** Best fits of the stacked tangential shear profiles measured in the  $\Lambda$ CDM mock light cones adopting two different void density profile functions: HSW (right panel) and HT (left panel). The data are represented with black markers, while the best fit model with a blue solid line. As indicated in the caption, different colored areas show the intervals covered for different confidence levels:  $1\sigma$  (blue),  $2\sigma$  (green) and  $3\sigma$  (red).

tunnel voids, it leads to the extraction of a weaker WL signal, with an amplitude about ten times smaller, and thus less exploitable for studying the effects of MG models. Our strategy will therefore be to seek a new parameterization of the tangential shear profile that is suitable for describing the signal generated by tunnel voids. Thus, instead of relying on the expected behavior for density profiles of 3D voids, we will focus on trying to directly reproduce the shape and the amplitude of the observed tangential shear profiles.

### 6.3.2 A new parametric formula

In this section we present and validate a new parametric function suitable for the modeling of the shear profiles extracted from our void catalogs. Our goal is to accurately reproduce the shape and amplitude of our shear profiles, employing the smallest possible number of free parameters. Moreover, we want this new functional form to be flexible enough to represent the shear profiles both for different void sizes and for the five cosmological models analyzed in this Thesis work. An example demonstrating the degree of “flexibility” we expect to reach with this function is shown in Figure 6.13. Here, we display the stacked tangential shear profiles extracted from our sample of voids, distinguished by average void size and cosmological model.

The functional form found that best met these requirements is the following:

$$\gamma_t(r_p) = a \left( \frac{1 - r_p^b}{1 + r_p^c} - \frac{\exp(d \cdot r_p)}{1 + \exp(e \cdot r_p - (d + e))} \right). \quad (6.15)$$

The coefficients  $a$ ,  $b$ ,  $c$ ,  $d$ ,  $e$  represent the five free parameters of our model. These parameters are not intended to have a physical meaning but rather to regulate the shape and amplitude of the profile across different scales. To understand their role, we illustrate in Figure 6.14 the effect that varying singularly each parameter produces on the shear profile. Below we report a brief description of the main effects of the each parameter.

*a:* *Amplitude or normalization.* It modifies the amplitude of the function, i.e. its normalization, and it is related to the overall depth of the tunnel void. It can be reabsorbed using the correct  $\Sigma_{rmcrit}$ .

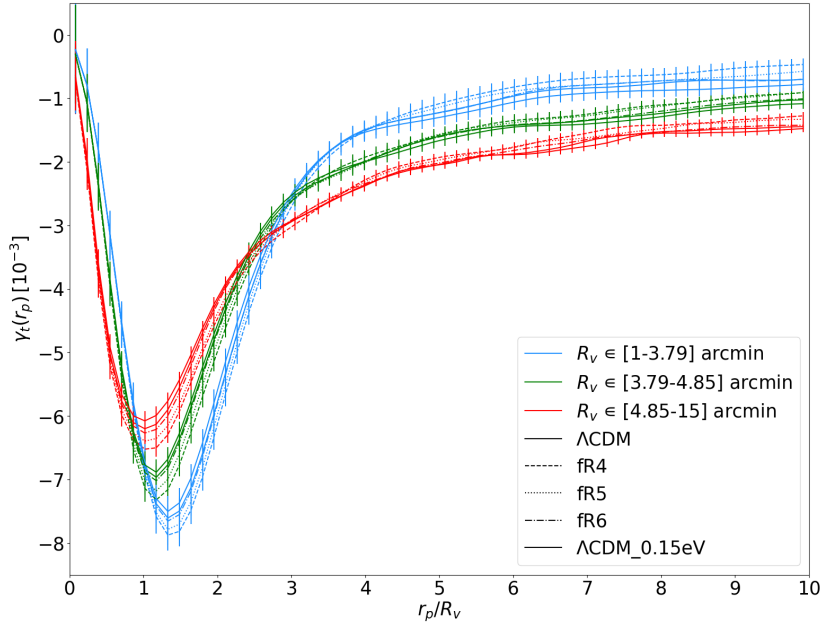


**Figure 6.13:** Stacked tangential shear profiles of all the analyzed cosmologies, divided in subsamples of different sizes of voids. The split of the void sample is the one presented in Sect. 6.1.2 and is used to distinguish voids of small (blue), medium (green) and large (red) sizes. As reported in the legend, the results for different cosmologies are instead reported using different line styles.

- b: Position of the minimum.* It plays a role in determining the position of the absolute minimum of the profile, also influencing the amplitude of the profile at large distances from the void center.
- c: Exponential growth.* It regulates the exponential rise after the minimum, so the slope of the outer part of the profile.
- d: Depth of the minimum.* It determines the minimum value of the profile and it is related to the central density contrast of the tunnel void.
- e: Starting point of the exponential term.* It influences the scale at which the exponential part of the function begins to become dominant.

Finally, in Figure 6.15 we present one of the most important results of this work, namely the application of the new function for fitting the stacked tangential shear profile extracted from the  $\Lambda\text{CDM}$  simulations. It is easy to notice how there is an excellent match with the data, across all scales. Since in this case we are restricted to the data extracted from the  $\Lambda\text{CDM}$  scenario only, we fall into the regime of overfitting. This leads to a reduced  $\chi^2$  much smaller than one,  $\tilde{\chi}^2 = 0.035$ . However, given the enormous variation in the trend of the profiles reported in Figure 6.13, it is crucial that our parametric formula retains the five degrees of freedom assigned to it. In the next section, we will analyze the correlation between the coefficients of this function and their variation based on the void sizes and the different considered cosmological models.

## 6.4 Bayesian statistical analysis

In this final section, we will use the Bayesian statistics to place constraints on the free parameters of the new functional form proposed in Sect. 6.3.2 and to study their variation

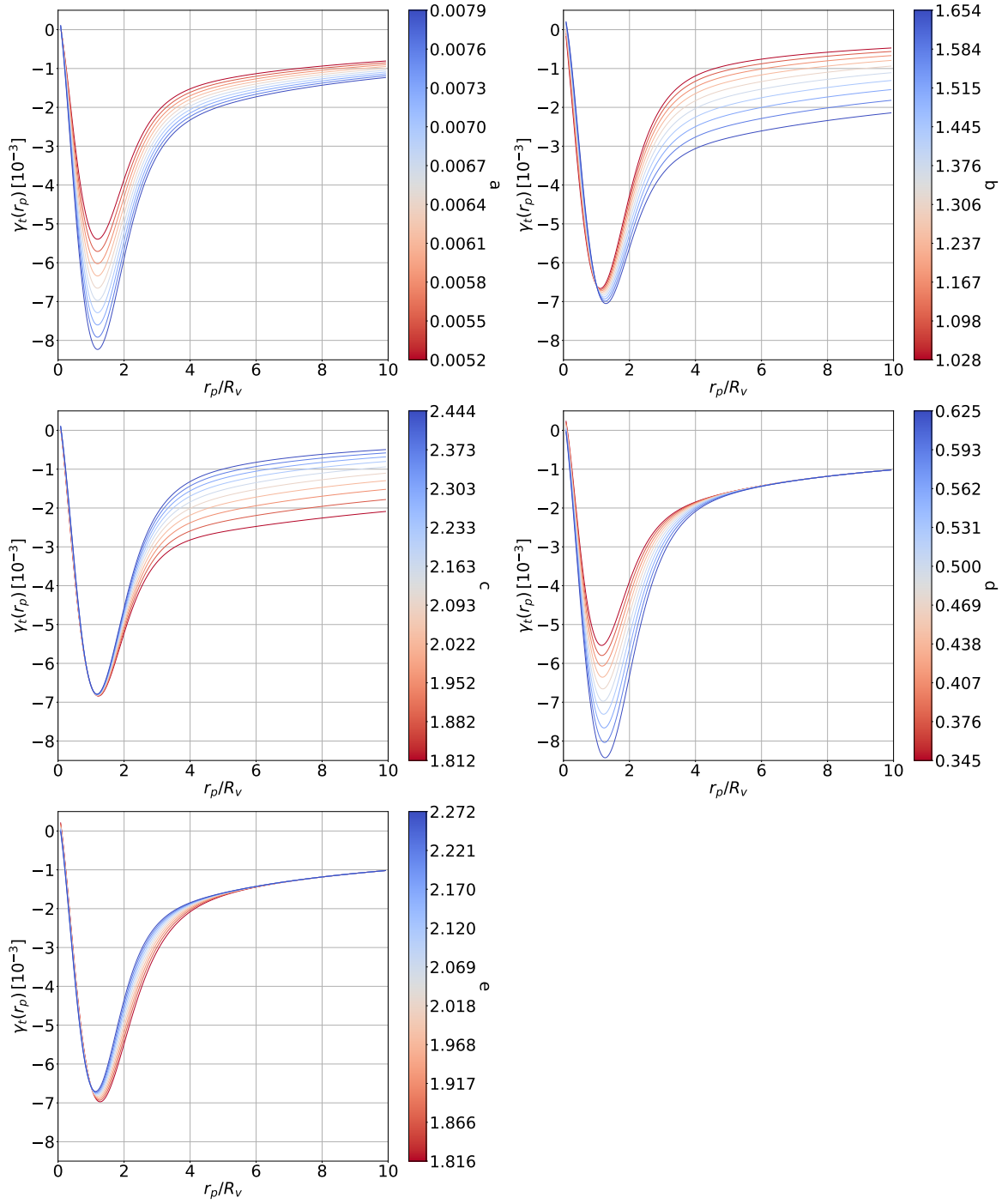


**Figure 6.14:** Effects of varying individually the coefficients of the function reported in Eq. 6.15. For each parameter, ten curves are represented, colored according to the value of the selected parameter. The colorbar located on the right of each subplot shows the association of the color used with the parameter value. The different panels refer to the parameter  $a$  (top left),  $b$  (top right),  $c$  (central left),  $d$  (central right) and  $e$  (bottom left).

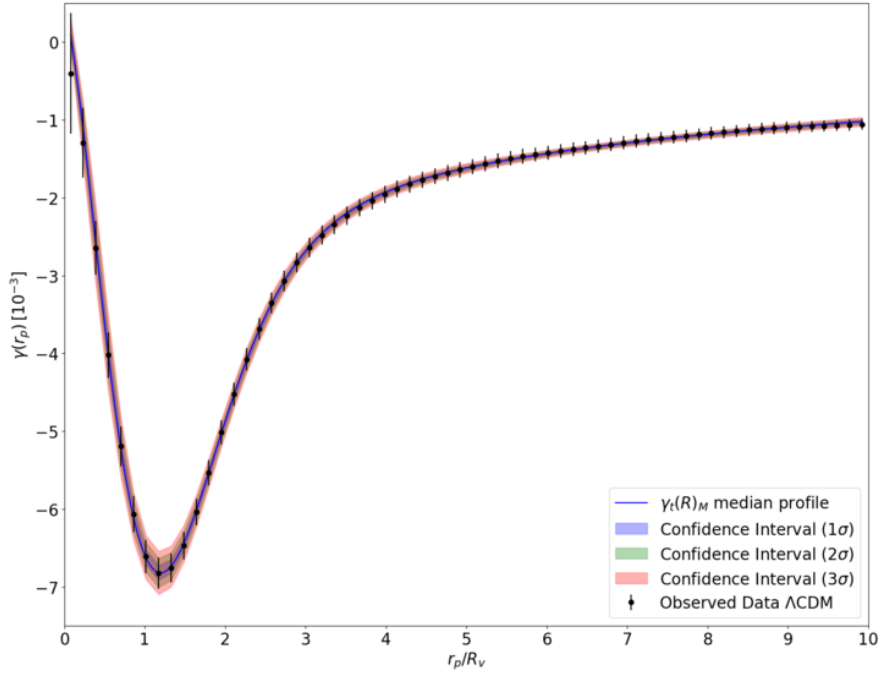


**Figure 6.15:** As Figure 6.12 but employing the fitting formula reported in Eq. 6.15.

based on the characteristics of the void sample. First, let us recall the theorem that lies at the heart of any modern statistical treatment, i.e., the *Bayes' theorem*:

$$p(\boldsymbol{\theta}|\mathbf{x}) = \frac{p(\mathbf{x}|\boldsymbol{\theta})p(\boldsymbol{\theta})}{p(\mathbf{x})}, \quad (6.16)$$

where  $\boldsymbol{\theta} = (\theta_1, \theta_2, \dots, \theta_N)$  denotes the set of model parameters and  $\mathbf{x}$  represents the data set. Let us break down the elements present in Eq. (6.16):

- $p(\boldsymbol{\theta})$  is the prior probability distribution, expressing what is known relative to the parameters before considering the data;
- $p(\mathbf{x}|\boldsymbol{\theta})$  is the likelihood function, representing the probability of obtaining the observed data given the set of parameters  $\boldsymbol{\theta}$ ;
- $p(\boldsymbol{\theta}|\mathbf{x})$  is the posterior distribution, reflecting updated knowledge after incorporating observed data;
- $p(\mathbf{x})$  is the evidence function, ensuring the normalization of the posterior.

Bayesian statistics has gained importance in cosmology and astrophysics due to the advent of large data catalogs and powerful computing resources. The utilization of Bayesian methods is closely related to the employment of numerical sampling techniques like *Markov Chain Monte Carlo* (MCMC). MCMC are powerful statistical tools that allow us to efficiently sample a posterior distribution without needing to know its exact form. By generating a chain of samples, MCMC explores the parameter space, with the frequency of samples in different regions of the space being proportional to the posterior probability of those regions.

This is the technique utilized to achieve the results presented in Sect. 6.3.1 and 6.3.2. In fact, to perform the best fit of different models with our simulated data we used *Cobaya*<sup>3</sup> (Torrado & Lewis 2021). This is a Bayesian analysis code that allows the efficient exploration of

<sup>3</sup><https://cobaya.readthedocs.io/en/latest/>

the posterior distribution using different MCMC samplers and offers functionalities for maximizing and importance-reweighting Monte Carlo samples with new priors and likelihoods. The code is Python-based and utilizes hybrid OpenMP/MPI parallelization to optimize the computational time. In our analysis, we impose the likelihood to be Gaussian and we set our parameter priors to follow a uniform distribution. `Cobaya` also enables us to require the reaching of a certain level of convergence for the chains. We set the value of the Gelman-Rubin diagnostics (Lewis 2013) to  $R - 1 = 0.001$ , which is generally reached when the chains are fully converged.

We present first the result of the posterior sampling related to Figure 6.15. We show in Figure 6.16 the constraints obtained on the five coefficients of the function (6.15) through the fit of the  $\Lambda$ CDM shear profile. The best fit of our model in this case is obtained by extracting the median values of the individual parameter distributions, which in this case are virtually Gaussian<sup>4</sup>. We also note how the orientation and extent of the confidence contours determine the degree of correlation between the various parameters. For example, the strong anti-correlation between the coefficients  $a$  and  $d$  is evident, as also expected from the trends reported in Fig. 6.14.

Now we focus on the confidence contours associated to the fit of the tangential shear profiles split according to the void size. We show in Figure 6.17 the constraints of the three equi-populated sub-samples of voids: small-size ( $R_v \in [1, 3.97]$  arcmin), medium-size ( $R_v \in ]3.97, 4.85]$  arcmin) and large-size ( $R_v \in ]4.85, 15]$  arcmin). In this plot we can identify, for each parameter, a distinct behavior in the constraints, with medium-size voids always in the middle. However, it is interesting to note that the extent of the contours does not always show the same trend. Voids of different sizes seem to constrain these coefficients more or less effectively. For example, the parameter  $a$  is better constrained by small voids, while  $b$  is better constrained by the large ones. As can also be seen in Figures 6.14  $a$  is related to the depth of the minima and so that is why it is best determined by small voids. The degeneracy between various pairs of parameters also varies with the void radius.

We now come to the final analysis of this work. We want to focus on the discriminating power of the void tangential shear profiles, and to do this, we will examine the confidence contours obtained for the parameters of the function (6.15). Let us underline that, in this analysis, we make no distinctions based on the size of the voids and perform the stacking of all the voids extracted for a given cosmology. We tested the effects of splitting the sample in different size bins but did not find any significant difference with respect to the case of considering the total sample of voids.

We report in Figure 6.18 the confidence contours obtained from fitting the shear profiles extracted in simulations featuring the five cosmological models considered in this work:  $\Lambda$ CDM,  $fR4$ ,  $fR5$ ,  $fR6$ ,  $\Lambda$ CDM<sub>0.15eV</sub>. As expected by the analysis of the results shown in Figure 6.7, the uncertainties associated to our tangential shear profiles are too large to discriminate the cosmological scenarios here analyzed. In fact, the parameter constraints computed for the different cosmologies are statistically compatible with each other, i.e. their contours at the 68% confidence level are always overlapping with the standard  $\Lambda$ CDM case. Nevertheless, we note how the confidence contours follow the expected trend, i.e. are ordered according to the level of enhancement/damping of the growth of LSS.  $fR4$  and  $\Lambda$ CDM<sub>0.15eV</sub> show indeed the most extreme behaviors. The parameters that appear to be the most sensitive to the variation of the cosmological model are  $a$ ,  $d$  and  $e$ . In fact, the coefficient  $a$  and  $d$  are responsible for the normalization and the depth of the shear profile and are naturally related to the evolution of the void density profiles. On the other hand  $e$  has an impact on the

---

<sup>4</sup>Thanks to the symmetry of the projected 1D distributions, the peak of the posterior coincides with the mean and median of the distribution.

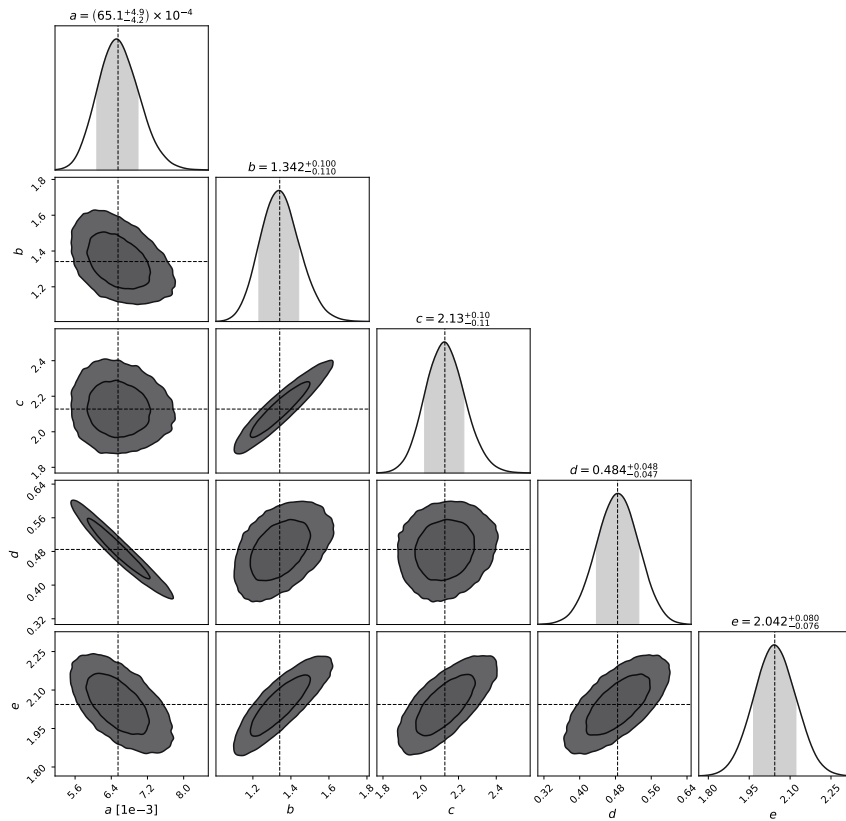


**Figure 6.16:** Corner plot for the five parameters of the function (6.15), used to model the void tangential shear profiles extracted from the  $\Lambda$ CDM simulations. The confidence contours correspond to the 68% and 95% confidence levels. The horizontal and vertical lines indicate the best fit parameters. There are also reported, with the relative uncertainty, over the panels containing the 1D projected posterior distributions.

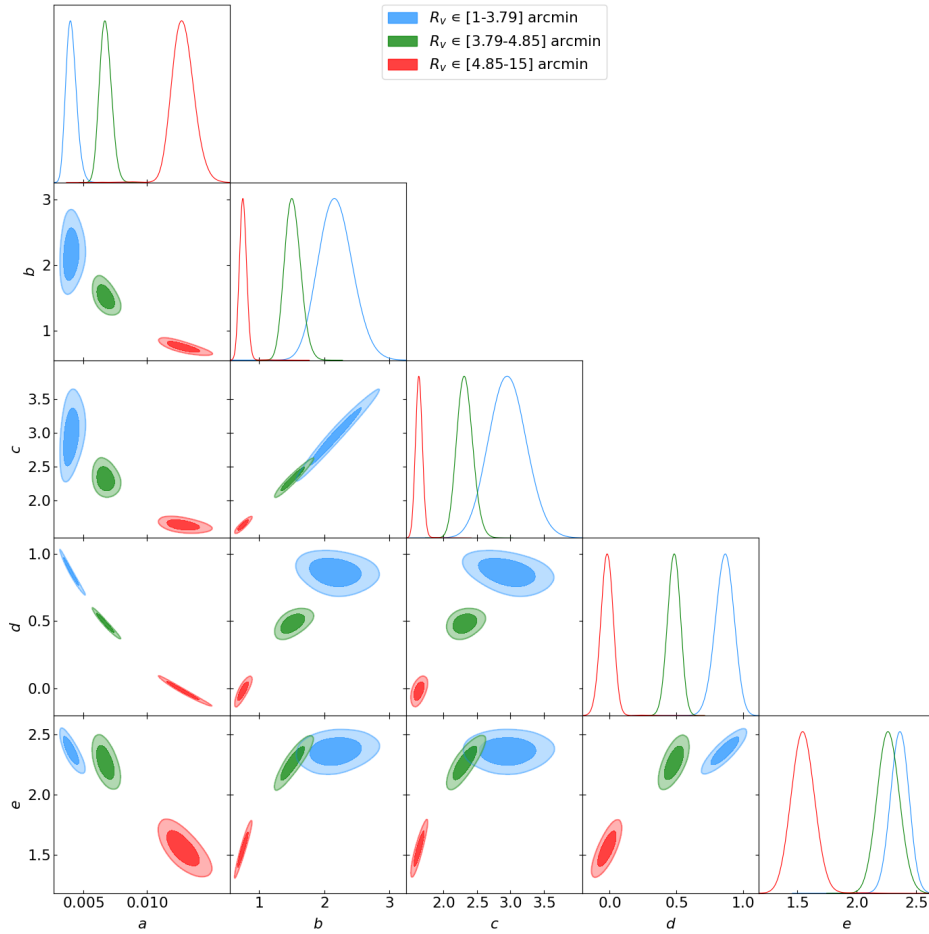


**Figure 6.17:** 68% and 95% confidence levels for the five parameters of the function (6.15), used to model the tangential shear profiles extracted from  $\Lambda$ CDM simulations. Different colors are for samples of voids with different sizes: small (blue), medium (green), and large (red) radii.

transition scale where the exponential rise starts to become dominant. Apparently, this peculiar behavior of the shear profile is also an important feature to consider when investigating different cosmological models.

As a final consideration, we would like to emphasize that, in the set-up assumed to prepare the data analyzed in this work, the differences between the tangential shear profiles for models alternative to the standard  $\Lambda$ CDM were found not to be statistically significant. However the usage of larger simulations or the inclusion of smaller observational errors could easily lead us to a condition where we can effectively use this type of statistics to investigate scenarios featuring MG and the presence of massive neutrinos.

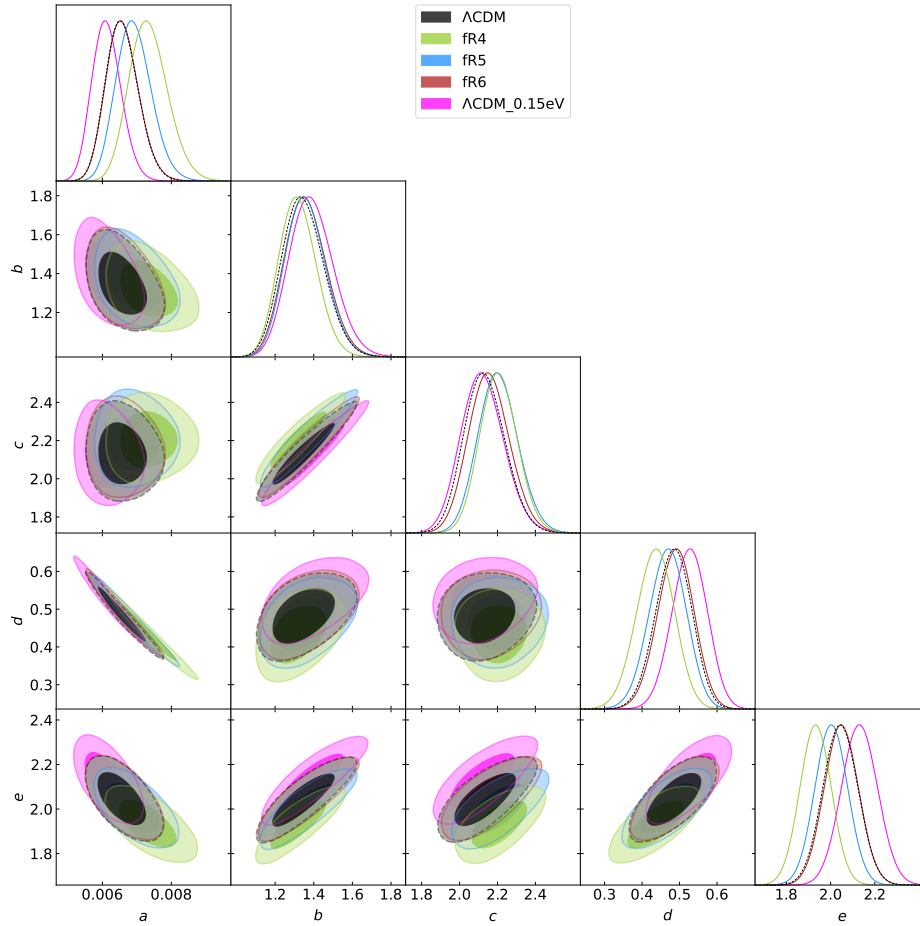


**Figure 6.18:** 68% and 95% confidence levels for the five parameters of the function (6.15), used to model the void tangential shear profiles extracted from simulations featuring different cosmological scenarios:  $\Lambda\text{CDM}$  (black),  $fR4$  (green),  $fR5$  (blue),  $fR6$  (red),  $\Lambda\text{CDM}_{0.15\text{eV}}$  (pink).

# Chapter 7

## Conclusions

In this Thesis work, we investigated the usage of cosmic voids as cosmological probe. Voids are the most underdense regions of the Universe and, with their tremendous size of tens of megaparsecs, they represent perfect laboratories to test gravity models on large scale. In particular, we studied the effects of gravitational lensing produced by cosmic voids. This involves analyzing the deflection of photons along the line of sight caused by these underdensities and quantifying the small distortions of background light sources through a quantity called tangential shear.

The primary goal of this work was to build a pipeline to identify cosmic voids in WL maps and measure the stacked tangential shear profile generated by these voids. Then, we aimed at exploiting this pipeline to study the void tangential shear profile extracted from cosmological simulations that implements modified gravity (MG) models. The final step of this project regarded the modeling of the shear profiles through a parametric formula, to study the impact of MG models on our data. We summarize below the path we followed to achieve the objectives just discussed.

Firstly, in Chapter 1 we presented the theoretical foundations of the currently accepted standard  $\Lambda$ CDM model, highlighting both its strengths and weaknesses in predicting the observational properties of the large-scale structure of the Universe. Subsequently, in Chapter 2, we described the main alternatives to the  $\Lambda$ CDM scenario. We introduced the family of MG models, with particular emphasis on the subclass known as  $f(R)$  models (Hu & Sawicki 2007). Furthermore, we highlighted the possible degeneracies between scenarios featuring MG models and those incorporating massive neutrinos, which are considered another elusive component of our Universe. Then, in Chapter 3 we provided a detailed introduction to of cosmic voids and their main statistics, i.e. number counts and density profiles. Then we presented the theory of weak gravitational lensing (WL) and we focused on the importance of 2D voids for WL analyses (Davies et al. 2018, 2021b).

In Chapter 4 we developed an original finding algorithm for 2D voids in WL maps, which is based on density and geometrical criteria and is targeted for measuring and maximizing the tangential shear signal from voids. To do this, we took into account the findings of Cautun et al. (2018) and Davies et al. (2021b) and we implemented our own approach into an existing peak finding algorithm called `pyTwinPeaks` (see Giocoli et al. 2018b). We extended this code by introducing a new pipeline for identifying tunnel voids. At the end, our 2D void finder enables a fast and computationally efficient reconstruction of the regions with the lowest signal in the convergence field, providing us with details regarding the center, size, and geometry of projected voids, all without relying on the 3D position of galaxies. Our finder is stable, optimized for efficiency over time, and is generalized for a wide range of settings.

In Chapter 5 we presented the data used for our analysis. We employed a set of  $N$ -

body cosmological simulations known as *DUSTGRAIN-pathfinder* (Giocoli et al. 2018a; Peel et al. 2018) to explore five cosmological scenarios: standard  $\Lambda$ CDM, as a reference model, three  $f(R)$  models with different strength for the fifth-force, and a  $\Lambda$ CDM model featuring massive neutrinos of mass  $M_\nu = 0.15$  eV. After identifying collapsed structures in the matter distribution (i.e. DM halos), we constructed 256 different realizations of light-cones by randomizing the various comoving cosmological boxes, for each cosmological model. Then we computed convergence maps using a ray-tracing process, assuming the observer at  $z = 0$  and the source plane at  $z = 1$ . Each map has size of  $300 \times 300$  arcmin and includes a realistic galaxy shape noise tailored on the expectation for the ESA mission *Euclid*.

Finally, in Chapter 6, we presented the results of our analysis. We showed the effectiveness of the 2D void finder in identifying negative regions in the convergence maps: voids centers are identified as the minima in the SNR field and their sizes correctly expand until they reach a positive WL signal zone. We analyzed the size distribution of our samples of voids, noting how the average void radius is consistently smaller than the typical one for 3D voids. This is due to the fact that our 2D voids are classified as tunnel voids, i.e. derive from the projection of a long series of 3D voids that partially intercept the observer’s line of sight. Studying this result for different cosmologies we found that the trend is the one expected: MG models with higher values of the parameter  $|f_{R0}|$  are those compared to the  $\Lambda$ CDM model that produce the greater increase in the number of void counts, while in the presence of massive neutrinos, the abundance of voids results suppressed. Higher values of  $|f_{R0}|$  imply indeed a stronger action of the fifth force, which in turn favors the evolution of LSS, including cosmic voids. On the other side, larger is the neutrino mass, more suppressed is the growth of cosmic structures and so the formation of voids.

Then, we delved into the tangential shear analysis. For each void, we measured the value of the tangential shear within shells extending from the center of the void up to ten times the void radius. Thereafter we calculated the stacked tangential shear signal by rescaling each profile according to the corresponding void size and averaging the values of the tangential shear. The uncertainty we associated to the profiles aims at reproducing real survey conditions like those of *Euclid*. In our approach, the uncertainty associated to the tangential shear is evaluated as the sum in quadrature of the statistical error (Eq. 6.5) and the observational error (Eq. 6.6).

We found that the stacked tangential shear profile we obtained is statistically negative, as expected for the signal generated by underdensities. Furthermore, the amplitude of this signal is of the same order of magnitude as found in the literature for tunnel voids, such as in Davies et al. (2019a). We also analyzed the behavior of the observed tangential shear profile according to the size of voids using three equi-populated sub-samples. We showed that smaller voids exhibit a deeper signal, characterized by a steep rise towards zero, whereas larger voids display a less profound signal with a less steeper rise. This behavior reflects the density profile features of 3D voids reported in previous studies (Hamaus et al. 2014; Voivodic et al. 2020). Specifically, smaller voids tend to have deeper interiors and higher compensation walls, while larger voids often feature internal substructures and irregular shapes due to merger events.

Then we focused on the comparison of the tangential shear profiles measured in the five cosmologies analyzed. As expected, we found a stronger tangential shear signal in MG models characterized by more intense fifth-force effects and a weaker signal in the presence of massive neutrinos. This result can be easily understood considering that the WL signal is naturally related to the depth of void density profiles. In fact, when their growth is accelerated, cosmic voids undergo a depletion of their internal density profiles. Conversely, when their growth is damped, voids evolve more slowly and appear shallower. This behavior characterizes almost equally 2D voids of all sizes. However, given the relatively large uncertainties associated to our

data, it was found not to be possible to distinguish statistically the considered cosmological scenarios using the void tangential shear profile. We demonstrated therefore that the best strategy to follow to improve the constraining power of this analysis is to try to mitigate the observational errors.

Finally, the last goal of the Thesis: modeling the void tangential shear profiles. First, we tried to use two well-known functional forms, generally used to reproduce density profiles of 3D voids, i.e. the Hamaus-Sutter-Wandelt (HSW, [Hamaus et al. 2014](#)) and the hyperbolic tangent profile (HT, [Voivodic et al. 2020](#)). We integrated these density profiles along the line of sight to derive the corresponding tangential shear signal and fit our data varying the free the coefficients of the HSW or HT profile. We demonstrated that both the parametric functions are inappropriate to reproduce the signal measured with our 2D voids. The observed discrepancy is due to the fact that our underdensities are the results of the projection of numerous underdense regions along the line of sight and not a single 3D void. For this reason, we empirically developed a new parametric formula to represent the tangential shear profile, which is suitable by construction for describing the signal generated by tunnel voids. We also required this new functional form to be flexible enough to accurately fit the shear profiles for various void sizes and across the five cosmological models here examined.

The final parametric formula has been presented in Eq. (6.15). Its coefficients,  $a$ ,  $b$ ,  $c$ ,  $d$ ,  $e$  represent the five free parameters of our model. For now, we interpreted them only mathematically as: normalization, position of the minimum, exponential growth, depth of the minimum, starting point of the exponential term. We verified that it accurately reproduces both the shape and amplitude of all our stacked shear profiles. This represents one of the most important results of this work, providing a useful tool to analyze the behavior of the WL signal in tunnel voids.

In the end, we performed a Bayesian analysis to constrain the free coefficients of the newly introduced parametric formula. We firstly considered the  $\Lambda$ CDM tangential shear profiles and we sampled the posterior distribution of our parameters through MCMC techniques. We analyzed the resulting confidence contours to understand the correlation between the parameters. Then we divided our sample in three equi-populated radius bins. We found that the extent and the orientation of the confidence contours change with the void radius, i.e. the degeneracy between these parameters depends on the void average size.

Finally we focused on the cosmological dependency of the parameters by analyzing the deviation of the confidence contours computed with data extracted from different cosmological models. We showed that the trend of the contours follows the degree of enhancement or damping of the growth of LSS. Specifically,  $fR4$  and  $\Lambda$ CDM<sub>0.15eV</sub> exhibit the most extreme behaviors in this regard. The parameters that appeared to be the most sensitive to variations in the cosmological model are  $a$ ,  $d$ , and  $e$ . Indeed, the coefficients  $a$  and  $d$  primarily control the normalization and depth of the shear profile, reflecting the evolution of the void density profiles. Conversely, the parameter  $e$  influences the transition scale at which the exponential rise begins to dominate.

We also verified that the constraining power derived from the analysis of the tangential shear profiles is not sufficient to statistically distinguish the alternative cosmological models analyzed from the standard  $\Lambda$ CDM. This was already expected from the simple comparison of the uncertainties associated with our data. This result, however, is important to design the characteristics of the optimal survey to exploit WL from voids as a cosmological probe. For example, a larger sky area would certainly help to reduce the statistical error, while a larger number of background sources would lead to a smaller observational error.

## 7.1 Future perspectives

The results presented in this Thesis work demonstrate the viability of analyzing the WL signal from 2D voids as cosmological probe. Given our encouraging findings, we plan to further expand this project in different ways. In the future, we will proceed as follows:

- We will release the 2D void finder algorithm developed in this work. We plan to reorganize the library `pyTwinPeaks` to work consistently with both underdensities and overdensities and make it publicly available.
- We will test pipeline using simulations with larger volumes to enhance void statistics and gain a better understanding of the behavior of larger underdensities. This will also allow us to infer the sky area required to have a statistical error small enough to distinguish between particular cosmological models.
- We intend to broaden our analysis to the investigation of simulations with different cosmological parameters and possibly other alternatives to the standard  $\Lambda$ CDM scenario.
- We aim at applying our pipeline in the context of a tomographic analysis, i.e. extracting the effects of the lensing signal at different redshifts. This test will be useful to determine the optimal redshift for conducting this kind of studies.
- Finally, we plan explore the feasibility of our analysis on real data catalogs. An ambitious goal would be to constrain  $f(R)$  models, but for this we will first need to effectively parameterize the variations of the tangential shear profiles as a function of the cosmology. This would require the usage of a very large number of simulations featuring different cosmologies. We will also consider the possibility of using standard cosmological probes in addition to WL from voids, to take full advantage of the complementarity of constraints derived from under- and overdensities.
- Our long-term efforts will go into the theoretical modeling of the tangential shear profile for cosmic voids. Its derivation from the first principles has not been developed yet and it would in fact allow the constraining of the parameters of the cosmological model and their evolution in time.

As a final consideration, we want to emphasize the fact that this Thesis work is based on the use of a cosmological probe that is still almost unexplored, and that the results obtained constitute an important step forward in this field. We indeed plan to publish our findings in a scientific paper and continue to develop the methodology presented to achieve an effective exploitation of the WL from cosmic voids.

# Bibliography

- Abdalla, E., Abellán, G. F., Aboubrahim, A., et al. 2022, [Journal of High Energy Astrophysics](#), **34**, 49
- Ahmed, S. N., Anthony, A. E., Beier, E. W., et al. 2004, [Phys. Rev. Lett.](#), **92**, 92
- Albrecht, A., Bernstein, G., Cahn, R., et al. 2006, [arXiv e-prints](#), astro
- Allen, S. W., Evrard, A. E., & Mantz, A. B. 2011, [Annu. Rev. Astron. Astrophys.](#), **49**, 409
- Amendola, L., Appleby, S., Avgoustidis, A., et al. 2018, [Living Reviews in Relativity](#), **21**, 2
- Amon, A., Gruen, D., Troxel, M. A., et al. 2022, [Phys. Rev. D](#), **105**, 023514
- Arnold, C., Fosalba, P., Springel, V., Puchwein, E., & Blot, L. 2019, [Mon. Not. R. Astron. Soc.](#), **483**, 790
- Bacon, R., Mary, D., Garel, T., et al. 2021, [Astron. Astrophys.](#), **647**, A107
- Bagla, J. S. & Padmanabhan, T. 1997, [Pramana](#), **49**, 161
- Baker, T., Clampitt, J., Jain, B., & Trodden, M. 2018, [Phys. Rev. D](#), **98**, 023511
- Baldi, M. 2012, [Monthly Notices of the Royal Astronomical Society](#), **422**, 422
- Baldi, M. 2020, [Mem. Soc. Astron. It.](#), **91**, 197
- Baldi, M. & Villaescusa-Navarro, F. 2018, [Mon. Not. R. Astron. Soc.](#), **473**, 3226
- Baldi, M., Villaescusa-Navarro, F., Viel, M., et al. 2014, [Mon. Not. R. Astron. Soc.](#), **440**, 75
- Barnes, J. & Hut, P. 1986, [Nature](#), **324**, 446
- Barreira, A., Bose, S., Li, B., & Llinares, C. 2017, [Journal of Cosmology and Astroparticle Physics](#), **2017**, 2017
- Barreira, A., Cautun, M., Li, B., Baugh, C. M., & Pascoli, S. 2015, [J. Cosm. Astro-Particle Phys.](#), **2015**, 028
- Bartelmann, M. 2010, [Classical and Quantum Gravity](#), **27**, 233001
- Bartelmann, M. & Schneider, P. 2001, [Phys. Rept.](#), **340**, 291
- Becker-Szendy, R., Bratton, C. B., Casper, D., et al. 1992, [Phys. Rev. D](#), **46**, 46
- Bennett, C. L., Banday, A. J., Górski, K. M., et al. 1996, [The Astrophysical Journal](#), **464**, 464
- Bernardeau, F., Colombi, S., Gaztañaga, E., & Scoccimarro, R. 2002, [Phys. Rept.](#), **367**, 1
- Bertotti, B., Iess, L., & Tortora, P. 2003, [Nature](#), **425**, 374
- Bianchi, E. & Rovelli, C. 2010, [arXiv e-prints](#), [arXiv:1002.3966](#)
- Blandford, R. D. & Narayan, R. 1992, [Annu. Rev. Astron. Astrophys.](#), **30**, 311
- Bloomfield, J., Flanagan, É. É., Park, M., & Watson, S. 2013, [J. Cosm. Astro-Particle Phys.](#), **2013**, 010
- Bolejko, K., Clarkson, C., Maartens, R., et al. 2013, [Phys. Rev. Lett.](#), **110**, 021302
- Bolejko, K. & Ferreira, P. G. 2012, [J. Cosm. Astro-Particle Phys.](#), **2012**, 003
- Bond, J. R., Cole, S., Efstathiou, G., & Kaiser, N. 1991, [Astrophys. J.](#), **379**, 440
- Bond, J. R. & Efstathiou, G. 1987, [Mon. Not. R. Astron. Soc.](#), **226**, 655
- Bonici, M., Carbone, C., Davini, S., et al. 2023, [Astron. Astrophys.](#), **670**, A47
- Bos, E. G. P., van de Weygaert, R., Dolag, K., & Pettorino, V. 2012, [Mon. Not. R. Astron. Soc.](#), **426**, 440
- Boschetti, R., Vielzeuf, P., Cousinou, M.-C., Escoffier, S., & Jullo, E. 2023, [arXiv e-prints](#), [arXiv:2311.14586](#)
- Brans, C. & Dicke, R. H. 1961, [Physical Review](#), **124**, 925
- Brax, P. & Valageas, P. 2013, [Phys. Rev. D](#), **88**, 023527
- Brax, P. & Valageas, P. 2014, [Phys. Rev. D](#), **90**, 023507

- Bridle, S. L., Kneib, J. P., Bardeau, S., & Gull, S. F. 2002, in *The Shapes of Galaxies and their Dark Halos*, ed. P. Natarajan, 38–46
- Bull, P., Akrami, Y., Adamek, J., et al. 2016, *Physics of the Dark Universe*, 12, 12
- Bullock, J. S. & Boylan-Kolchin, M. 2017, *Annu. Rev. Astron. Astrophys.*, 55, 343
- Burgess, C. P. 2013, *arXiv e-prints*, arXiv:1309.4133
- Cai, Y.-C., Padilla, N., & Li, B. 2015, *Monthly Notices of the Royal Astronomical Society*, 451, 451
- Camacho, H., Andrade-Oliveira, F., Troja, A., et al. 2022, *Mon. Not. R. Astron. Soc.*, 516, 5799
- Carroll, S. M. 2001, *Living Reviews in Relativity*, 4, 1
- Carroll, S. M., Duvvuri, V., Trodden, M., & Turner, M. S. 2004, *Phys. Rev. D*, 70, 70
- Castorina, E., Sefusatti, E., Sheth, R. K., Villaescusa-Navarro, F., & Viel, M. 2014, *J. Cosm. Astro-Particle Phys.*, 2014, 049
- Castro, T., Quartin, M., Giocoli, C., Borgani, S., & Dolag, K. 2018, *Mon. Not. R. Astron. Soc.*, 478, 1305
- Cataneo, M., Rapetti, D., Schmidt, F., et al. 2015, *Phys. Rev. D*, 92, 92
- Cautun, M., Cai, Y.-C., & Frenk, C. S. 2016, *Mon. Not. R. Astron. Soc.*, 457, 2540
- Cautun, M., Paillas, E., Cai, Y.-C., et al. 2018, *Mon. Not. R. Astron. Soc.*, 476, 3195
- Cautun, M., van de Weygaert, R., Jones, B. J. T., & Frenk, C. S. 2014, *Mon. Not. R. Astron. Soc.*, 441, 2923
- Chang, C., Pujol, A., Mawdsley, B., et al. 2018, *Monthly Notices of the Royal Astronomical Society*, 475, 475
- Chiang, C.-T., LoVerde, M., & Villaescusa-Navarro, F. 2019, *Phys. Rev. Lett.*, 122, 122
- Clarkson, C., Ellis, G. F. R., Faltenbacher, A., et al. 2012, *Mon. Not. R. Astron. Soc.*, 426, 1121
- Clifton, T., Ferreira, P. G., Padilla, A., & Skordis, C. 2012, *Phys. Rept.*, 513, 1
- Colberg, J. M., Pearce, F., Foster, C., et al. 2008, *Monthly Notices of the Royal Astronomical Society*, 387, 387
- Coles, P. & Lucchin, F. 2002, *Cosmology: The Origin and Evolution of Cosmic Structure*, Second Edition
- Contarini, S., Marulli, F., Moscardini, L., et al. 2021, *Mon. Not. R. Astron. Soc.*, 504, 5021
- Contarini, S., Pisani, A., Hamaus, N., et al. 2022a, *arXiv e-prints*, arXiv:2212.03873
- Contarini, S., Pisani, A., Hamaus, N., et al. 2024, *Astron. Astrophys.*, 682, A20
- Contarini, S., Verza, G., Pisani, A., et al. 2022b, *Astron. Astrophys.*, 667, A162
- Cyburt, R. H., Fields, B. D., Olive, K. A., & Yeh, T.-H. 2016, *Reviews of Modern Physics*, 88, 015004
- Davies, C. T., Cautun, M., Giblin, B., et al. 2021a, *Mon. Not. R. Astron. Soc.*, 507, 2267
- Davies, C. T., Cautun, M., & Li, B. 2018, *Mon. Not. R. Astron. Soc.*, 480, L101
- Davies, C. T., Cautun, M., & Li, B. 2019a, *Mon. Not. R. Astron. Soc.*, 490, 4907
- Davies, C. T., Cautun, M., & Li, B. 2019b, *Mon. Not. R. Astron. Soc.*, 488, 5833
- Davies, C. T., Paillas, E., Cautun, M., & Li, B. 2021b, *Mon. Not. R. Astron. Soc.*, 500, 2417
- Davis, M., Efstathiou, G., Frenk, C. S., & White, S. D. M. 1985, *Astrophys. J.*, 292, 371
- Dawson, K. S., Kneib, J.-P., Percival, W. J., et al. 2016, *Astron. J.*, 151, 44
- Dawson, K. S., Schlegel, D. J., Ahn, C. P., et al. 2013, *Astron. J.*, 145, 10
- de Bernardis, P., Ade, P. A. R., Bock, J. J., et al. 2000, *Nature*, 404, 955
- de Jong, J. T. A., Kuijken, K., Applegate, D., et al. 2013a, *The Messenger*, 154, 44
- de Jong, J. T. A., Verdoes Kleijn, G. A., Erben, T., et al. 2017, *Astron. Astrophys.*, 604, A134
- de Jong, J. T. A., Verdoes Kleijn, G. A., Kuijken, K. H., & Valentijn, E. A. 2013b, *Experimental Astronomy*, 35, 25

- Dhawan, S., Jha, S. W., & Leibundgut, B. 2018, *Astron. Astrophys.*, **609**, A72
- Di Valentino, E., Anchordoqui, L. A., Akarsu, Ö., et al. 2021a, *Astroparticle Physics*, **131**, 102605
- Di Valentino, E., Anchordoqui, L. A., Akarsu, Ö., et al. 2021b, *Astroparticle Physics*, **131**, 102604
- Di Valentino, E., Anchordoqui, L. A., Akarsu, Ö., et al. 2021c, *Astroparticle Physics*, **131**, 102604
- Di Valentino, E., Melchiorri, A., & Silk, J. 2020, *Nature Astronomy*, **4**, 196
- Di Valentino, E., Mena, O., Pan, S., et al. 2021d, *arXiv e-prints*, [arXiv:2103.01183](https://arxiv.org/abs/2103.01183)
- Dolgov, A. D. & Kawasaki, M. 2003, *Physics Letters B*, **573**, 1
- Einstein, A. 1915, *Sitzungsberichte der Königlich Preussischen Akademie der Wissenschaften*, **778**
- Einstein, A. 1917, *Sitzungsber. Preuss. Akad. Wiss. Berlin (Math. Phys.)*
- Eisenstein, D. J., Weinberg, D. H., Agol, E., et al. 2011, *Astron. J.*, **142**, 72
- Elder, B., Houry, J., Haslinger, P., et al. 2016, *Phys. Rev. D*, **94**, 94
- Elyiv, A., Marulli, F., Pollina, G., et al. 2015, *Monthly Notices of the Royal Astronomical Society*, **448**, 448
- Elyiv, A. A., Karachentsev, I. D., Karachentseva, V. E., Melnyk, O. V., & Makarov, D. I. 2013, *Astrophysical Bulletin*, **68**, 68
- Energy Survey, D., Kilo-Degree Survey Collaboration, :, et al. 2023, *arXiv e-prints*, [arXiv:2305.17173](https://arxiv.org/abs/2305.17173)
- Etherington, I. 1933, *The London, Edinburgh, and Dublin Philosophical Magazine and Journal of Science*, **15**, 15
- Euclid Collaboration, Scaramella, R., Amiaux, J., et al. 2022, *Astron. Astrophys.*, **662**, A112
- Euclid Collaboration: Blanchard, A., Camera, S., Carbone, C., et al. 2020, *Astron. Astrophys.*, **642**, A191
- Falck, B., Neyrinck, M., Aragon-Calvo, M., Lavaux, G., & Szalay, A. 2012, *Astrophysical Journal*, **745**, 745
- Fang, Y., Hamaus, N., Jain, B., et al. 2019, *Mon. Not. R. Astron. Soc.*, **490**, 3573
- Finelli, F., García-Bellido, J., Kovács, A., Paci, F., & Szapudi, I. 2015, *Monthly Notices of the Royal Astronomical Society*, **455**, 455
- Fixsen, D. J., Cheng, E. S., Gales, J. M., et al. 1996, *Astrophys. J.*, **473**, 576
- Forero-Romero, J. E., Hoffman, Y., Gottlöber, S., Klypin, A., & Yepes, G. 2009, *Monthly Notices of the Royal Astronomical Society*, **396**, 396
- Freedman, W. L., Madore, B. F., Hatt, D., et al. 2019, *Astrophys. J.*, **882**, 34
- Friedmann, A. 1922, *Zeitschrift für Physik*, **10**, 377
- Frusciante, N. & Perenon, L. 2020, *Phys. Rept.*, **857**, 1
- Fukuda, Y., Hayakawa, T., Ichihara, E., et al. 1998, *Phys. Rev. Lett.*, **81**, 81
- García-Farieta, J., Marulli, F., Moscardini, L., Veropalumbo, A., & Casas-Miranda, R. 2020, *Monthly Notices of the Royal Astronomical Society*
- Giblin, B., Heymans, C., Asgari, M., et al. 2021, *Astron. Astrophys.*, **645**, A105
- Giocoli, C., Baldi, M., & Moscardini, L. 2018a, *Mon. Not. R. Astron. Soc.*, **481**, 2813
- Giocoli, C., Di Meo, S., Meneghetti, M., et al. 2017, *Mon. Not. R. Astron. Soc.*, **470**, 3574
- Giocoli, C., Jullo, E., Metcalf, R. B., et al. 2016, *Mon. Not. R. Astron. Soc.*, **461**, 209
- Giocoli, C., Marulli, F., Moscardini, L., et al. 2021, *Astron. Astrophys.*, **653**, A19
- Giocoli, C., Meneghetti, M., Metcalf, R. B., Etori, S., & Moscardini, L. 2014, *Mon. Not. R. Astron. Soc.*, **440**, 1899
- Giocoli, C., Moscardini, L., Baldi, M., Meneghetti, M., & Metcalf, R. B. 2018b, *Mon. Not. R. Astron. Soc.*, **478**, 5436
- Giocoli, C., Tormen, G., & van den Bosch, F. C. 2008, *Mon. Not. R. Astron. Soc.*, **386**, 2135
- Gorski, K. M. 1994, *The Astrophysical Journal*, **430**, 430
- Gouin, C., Gavazzi, R., Pichon, C., et al. 2019, *Astron. Astrophys.*, **626**, A72

- Greg, A., W, A., Ansari, R., et al. 2012
- Gruen, D., Friedrich, O., Amara, A., et al. 2015, [Monthly Notices of the Royal Astronomical Society](#), 455, 455
- Guarnizo Trilleras, A. 2016, A Model-Independent Approach to Dark Energy Cosmologies: Current and Future Constraints, PhD thesis
- Gunn, J. E. & Gott, J. Richard, I. 1972, [Astrophys. J.](#), 176, 1
- Guth, A. H. 1981, [Phys. Rev. D](#), 23, 347
- Guzzo, L., Scodreggio, M., Garilli, B., et al. 2014, [Astron. Astrophys.](#), 566, A108
- Hagstotz, S., Costanzi, M., Baldi, M., & Weller, J. 2019a, [Mon. Not. R. Astron. Soc.](#), 486, 3927
- Hagstotz, S., Gronke, M., Mota, D. F., & Baldi, M. 2019b, [Astron. Astrophys.](#), 629, A46
- Hamaus, N., Aubert, M., Pisani, A., et al. 2022, [Astron. Astrophys.](#), 658, A20
- Hamaus, N., Pisani, A., Choi, J.-A., et al. 2020, [J. Cosm. Astro-Particle Phys.](#), 2020, 023
- Hamaus, N., Pisani, A., Sutter, P. M., et al. 2016a, [Phys. Rev. Lett.](#), 117, 091302
- Hamaus, N., Sutter, P. M., & Wandelt, B. D. 2014, [Phys. Rev. Lett.](#), 112, 251302
- Hamaus, N., Sutter, P. M., & Wandelt, B. D. 2016b, in *The Zeldovich Universe: Genesis and Growth of the Cosmic Web*, ed. R. van de Weygaert, S. Shandarin, E. Saar, & J. Einasto, Vol. 308, 538–541
- Hanisch, R. J., Farris, A., Greisen, E. W., et al. 2001, [Astron. Astrophys.](#), 376, 359
- Hattori, M., Kneib, J., & Makino, N. 1999, [Progress of Theoretical Physics Supplement](#), 133, 1
- He, J.-h. 2013, [Phys. Rev. D](#), 88, 103523
- Heavens, A., Fantaye, Y., Sellentin, E., et al. 2017, [Phys. Rev. Lett.](#), 119, 119
- Heymans, C., Van Waerbeke, L., Bacon, D., et al. 2006, [Mon. Not. R. Astron. Soc.](#), 368, 1323
- Higuchi, Y., Oguri, M., & Hamana, T. 2013, [Monthly Notices of the Royal Astronomical Society](#), 432, 432
- Hilbert, S., Hartlap, J., White, S. D. M., & Schneider, P. 2009, [Astron. Astrophys.](#), 499, 31
- Hildebrandt, H., Köhlinger, F., van den Busch, J. L., et al. 2020, [Astron. Astrophys.](#), 633, A69
- Hinshaw, G., Larson, D., Komatsu, E., et al. 2013, [Astrophys. J. Suppl.](#), 208, 19
- Hinterbichler, K. & Khoury, J. 2010, [Phys. Rev. Lett.](#), 104, 231301
- Hockney, R. W. & Eastwood, J. W. 1981, *Computer Simulation Using Particles*
- Hogg, D. W. 1999, [arXiv e-prints](#), astro
- Hu, W. & Sawicki, I. 2007, [Phys. Rev. D](#), 76, 064004
- Hubble, E. 1929, [Proceedings of the National Academy of Science](#), 15, 168
- Icke, V. 1984, [Mon. Not. R. Astron. Soc.](#), 206, 1P
- Iocco, F., Mangano, G., Miele, G., Pisanti, O., & Serpico, P. D. 2009, [Phys. Rept.](#), 472, 1
- Ishak, M. 2019, [Living Reviews in Relativity](#), 22, 1
- Jain, B. & Seljak, U. 1997, [Astrophys. J.](#), 484, 560
- Jain, B., Seljak, U., & White, S. 2000, [Astrophys. J.](#), 530, 547
- Jeans, J. H. 1902, [Philosophical Transactions of the Royal Society of London Series A](#), 199, 1
- Jeffrey, N., Gatti, M., Chang, C., et al. 2021, [Mon. Not. R. Astron. Soc.](#), 505, 4626
- Jenkins, A., Frenk, C. S., White, S. D. M., et al. 2001, [Mon. Not. R. Astron. Soc.](#), 321, 372
- Jennings, E., Li, Y., & Hu, W. 2013, [Monthly Notices of the Royal Astronomical Society](#), 434, 434
- Joyce, A., Jain, B., Khoury, J., & Trodden, M. 2015, [Phys. Rept.](#), 568, 1
- Joyce, A., Lombriser, L., & Schmidt, F. 2016, [Annual Review of Nuclear and Particle Science](#), 66, 95
- Kaiser, N. 1995, [Astrophys. J. Lett.](#), 439, L1
- Kaiser, N., Squires, G., & Broadhurst, T. 1995, [Astrophys. J.](#), 449, 460
- Khoury, J. & Weltman, A. 2004a, [Phys. Rev. D](#), 69, 044026

- Khoury, J. & Weltman, A. 2004b, *Phys. Rev. Lett.*, **93**, 171104
- Kilbinger, M. 2015a, *Reports on Progress in Physics*, **78**, 086901
- Kilbinger, M. 2015b, *Reports on Progress in Physics*, **78**, 086901
- Kitayama, T. & Suto, Y. 1996, *Astrophys. J.*, **469**, 480
- Kneib, J.-P. & Natarajan, P. 2011, *Astron. Astrophys. Rev.*, **19**, 47
- Kreisch, C. D., Pisani, A., Carbone, C., et al. 2019, *Mon. Not. R. Astron. Soc.*, **488**, 4413
- Kreisch, C. D., Pisani, A., Villaescusa-Navarro, F., et al. 2022, *Astrophys. J.*, **935**, 100
- Kuijken, K. 1999, *Astron. Astrophys.*, **352**, 355
- Lahav, O. & Liddle, A. R. 2019, *arXiv e-prints*, [arXiv:1912.03687](https://arxiv.org/abs/1912.03687)
- Lambiase, G., Mohanty, S., Narang, A., & Parashari, P. 2019, *The European Physical Journal C*, **79**, 79
- Langlois, D. 2005, in NATO Advanced Study Institute (ASI) Series B, Vol. 188, Particle Physics and Cosmology: the Interface, **235**
- Langlois, D. 2019, *International Journal of Modern Physics D*, **28**, 1942006
- Laureijs, R., Amiaux, J., Arduini, S., et al. 2011, *arXiv e-prints*, [arXiv:1110.3193](https://arxiv.org/abs/1110.3193)
- Lavaux, G. & Wandelt, B. D. 2010, *Monthly Notices of the Royal Astronomical Society*, **403**, 403
- Lavaux, G. & Wandelt, B. D. 2012, *Astrophys. J.*, **754**, 109
- Lazeyras, T., Villaescusa-Navarro, F., & Viel, M. 2021, *J. Cosm. Astro-Particle Phys.*, **2021**, 022
- Le Verrier, U. J. 1859, *Annales de l'Observatoire de Paris*, **5**, 1
- Lee, J. & Park, D. 2009, *The Astrophysical Journal*, **696**, 696
- Lemaître, G. 1927, *Annales de la Société Scientifique de Bruxelles*, **47**, 49
- Lesci, G. F., Marulli, F., Moscardini, L., et al. 2022, *Astron. Astrophys.*, **659**, A88
- Lesgourgues, J., Mangano, G., Miele, G., & Pastor, S. 2013, *Neutrino Cosmology* (Cambridge University Press)
- Lewis, A. 2013, *Phys. Rev. D*, **87**, 103529
- Lewis, A., Challinor, A., & Lasenby, A. 2000, *Astrophys. J.*, **538**, 473
- Li, P. 2023, *The Astrophysical Journal Letters*, **950**, 950
- Li, Z., Wu, P., & Yu, H. 2011, *The Astrophysical Journal Letters*, **729**, 729
- Lin, C.-A. & Kilbinger, M. 2015, *Astron. Astrophys.*, **576**, A24
- Linde, A. D. 1983, *Physics Letters B*, **129**, 177
- Longair, M. S. 2008, *Galaxy Formation*
- Lorenz, C. S., Calabrese, E., & Alonso, D. 2017, *Phys. Rev. D*, **96**, 043510
- Lovelock, D. 1971, *Journal of Mathematical Physics*, **12**, 498
- Lovelock, D. 1972, *Journal of Mathematical Physics*, **13**, 874
- LSST Dark Energy Science Collaboration. 2012, *arXiv e-prints*, [arXiv:1211.0310](https://arxiv.org/abs/1211.0310)
- Mandelbaum, R., Lanusse, F., Leauthaud, A., et al. 2018, *Mon. Not. R. Astron. Soc.*, **481**, 3170
- Mandelbaum, R., Rowe, B., Bosch, J., et al. 2014, *The Astrophysical Journal Supplement Series*, **212**, 212
- Mangano, G., Miele, G., Pastor, S., et al. 2005, *Nuclear Physics B*, **729**, 221
- Martin, J. 2012, *Comptes Rendus Physique*, **13**, 566
- Martino, M. C. & Sheth, R. K. 2009, *arXiv e-prints*, [arXiv:0911.1829](https://arxiv.org/abs/0911.1829)
- Marulli, F., Carbone, C., Viel, M., Moscardini, L., & Cimatti, A. 2011, *Monthly Notices of the Royal Astronomical Society*, **418**, 418
- Massara, E. & Sheth, R. K. 2018, *arXiv e-prints*, [arXiv:1811.03132](https://arxiv.org/abs/1811.03132)
- Massara, E., Villaescusa-Navarro, F., Viel, M., & Sutter, P. M. 2015, *J. Cosm. Astro-Particle Phys.*, **2015**, 018

- Massey, R., Heymans, C., Bergé, J., et al. 2007, *Monthly Notices of the Royal Astronomical Society*, 376, 376
- Merten, J., Giocoli, C., Baldi, M., et al. 2019, *Mon. Not. R. Astron. Soc.*, 487, 104
- Meszaros, P. 1974, *Astron. Astrophys.*, 37, 225
- Micheletti, D., Iovino, A., Hawken, A. J., et al. 2014, *Astron. Astrophys.*, 570, A106
- Miralda-Escude, J. 1991, *Astrophys. J.*, 380, 1
- Miralda-Escude, J. & Babul, A. 1995, *The Astrophysical Journal*, 449, 449
- Moresco, M. & Marulli, F. 2017a, *Mon. Not. R. Astron. Soc.*, 471, L82
- Moresco, M. & Marulli, F. 2017b, *Mon. Not. R. Astron. Soc.*, 471, L82
- Motohashi, H., Starobinsky, A. A., & Yokoyama, J. 2013, *Phys. Rev. Lett.*, 110, 121302
- Mukhanov, V. 2005, *Physical Foundations of Cosmology* (Cambridge University Press)
- Mukherjee, S., Ghosh, A., Graham, M. J., et al. 2020, *arXiv e-prints*, arXiv:2009.14199
- Nadathur, S. & Hotchkiss, S. 2015a, *Mon. Not. R. Astron. Soc.*, 454, 2228
- Nadathur, S. & Hotchkiss, S. 2015b, *Mon. Not. R. Astron. Soc.*, 454, 889
- Nadathur, S., Hotchkiss, S., Diego, J. M., et al. 2015, *Mon. Not. R. Astron. Soc.*, 449, 3997
- Nadathur, S., Woodfinden, A., Percival, W. J., et al. 2020, *Monthly Notices of the Royal Astronomical Society*, 499, 499
- Naik, A. P., Puchwein, E., Davis, A.-C., & Arnold, C. 2018, *Mon. Not. R. Astron. Soc.*, 480, 5211
- Neyrinck, M. C. 2008, *Monthly Notices of the Royal Astronomical Society*, 386, 386
- Neyrinck, M. C., Gnedin, N. Y., & Hamilton, A. J. S. 2005, *Mon. Not. R. Astron. Soc.*, 356, 1222
- Nojiri, S. & Odintsov, S. D. 2007, *International Journal of Geometric Methods in Modern Physics*, 04, 115
- Nojiri, S. & Odintsov, S. D. 2008a, *Phys. Rev. D*, 78, 046006
- Nojiri, S. & Odintsov, S. D. 2008b, *Phys. Rev. D*, 77, 026007
- Nojiri, S. & Odintsov, S. D. 2011, *Phys. Rept.*, 505, 59
- Nojiri, S., Odintsov, S. D., & Sáez-Gómez, D. 2009, *Physics Letters B*, 681, 74
- Okabe, N., Takada, M., Umetsu, K., Futamase, T., & Smith, G. P. 2010, *Publ. Astron. Soc. Japan*, 62, 811
- Padmanabhan, T. 1993, *Structure Formation in the Universe*
- Paillas, E., Lagos, C. D. P., Padilla, N., et al. 2017, *Mon. Not. R. Astron. Soc.*, 470, 4434
- Paz, D., Lares, M., Ceccarelli, L., Padilla, N., & Lambas, D. G. 2013, *Monthly Notices of the Royal Astronomical Society*, 436, 436
- Peebles, P. J. E. 1980, *The large-scale structure of the universe*
- Peel, A., Pettorino, V., Giocoli, C., Starck, J.-L., & Baldi, M. 2018, *Astron. Astrophys.*, 619, A38
- Perico, Eder L. D., Voivodic, Rodrigo, Lima, Marcos, & Mota, David F. 2019, *AA*, 632, 632
- Perlmutter, S., Aldering, G., Goldhaber, G., et al. 1999, *Astrophys. J.*, 517, 565
- Perlmutter, S., Turner, M. S., & White, M. 1999, *Phys. Rev. Lett.*, 83, 83
- Petri, A., Haiman, Z., & May, M. 2016, *Phys. Rev. D*, 93, 93
- Petri, A., Haiman, Z., & May, M. 2017, *Phys. Rev. D*, 95, 95
- Piazza, F. & Vernizzi, F. 2013, *Classical and Quantum Gravity*, 30, 214007
- Pisani, A., Lavaux, G., Sutter, P. M., & Wandelt, B. D. 2014, *Mon. Not. R. Astron. Soc.*, 443, 3238
- Pisani, A., Massara, E., Spergel, D. N., et al. 2019, *Phys. Rev. D*, 100, 043511
- Pisani, A., Sutter, P., Lavaux, G., & Wandelt, B. 2016, in *The Zeldovich Universe: Genesis and Growth of the Cosmic Web*, ed. R. van de Weygaert, S. Shandarin, E. Saar, & J. Einasto, Vol. 308, 546–550
- Pisani, A., Sutter, P. M., Hamaus, N., et al. 2015, *Phys. Rev. D*, 92, 92

- Planck Collaboration, Ade, P. A. R., Aghanim, N., et al. 2016a, *Astron. Astrophys.*, **594**, A20
- Planck Collaboration, Ade, P. A. R., Aghanim, N., et al. 2016b, *Astron. Astrophys.*, **594**, A13
- Planck Collaboration, Ade, P. A. R., Aghanim, N., et al. 2016c, *AA*, **594**, 594
- Planck Collaboration, Aghanim, N., Akrami, Y., et al. 2020a, *Astron. Astrophys.*, **641**, A6
- Planck Collaboration, Aghanim, N., Akrami, Y., et al. 2020b, *Astron. Astrophys.*, **641**, A5
- Platen, E., Van De Weygaert, R., & Jones, B. J. T. 2007, *Monthly Notices of the Royal Astronomical Society*, **380**, 380
- Poulin, V., Boddy, K. K., Bird, S., & Kamionkowski, M. 2018, *Phys. Rev. D*, **97**, 123504
- Press, W. H. & Schechter, P. 1974, *Astrophys. J.*, **187**, 425
- Puchwein, E., Baldi, M., & Springel, V. 2013, *Mon. Not. R. Astron. Soc.*, **436**, 348
- Qin, J., Melia, F., & Zhang, T.-J. 2021, *Monthly Notices of the Royal Astronomical Society*, **502**, 502
- Refregier, A., Kacprzak, T., Amara, A., Bridle, S., & Rowe, B. 2012, *Mon. Not. R. Astron. Soc.*, **425**, 1951
- Riess, A. G., Casertano, S., Yuan, W., Macri, L. M., & Scolnic, D. 2019a, *Astrophys. J.*, **876**, 85
- Riess, A. G., Casertano, S., Yuan, W., Macri, L. M., & Scolnic, D. 2019b, *Astrophys. J.*, **876**, 85
- Riess, A. G., Filippenko, A. V., Challis, P., et al. 1998, *Astron. J.*, **116**, 1009
- Riess, A. G., Filippenko, A. V., Challis, P., Clocchiatti, A., & Diercks, A. e. o. 1998, *The Astrophysical Journal*, **116**, 116
- Roncarelli, M., Baldi, M., & Villaescusa-Navarro, F. 2018, *Mon. Not. R. Astron. Soc.*, **481**, 2497
- Roncarelli, M., Moscardini, L., Borgani, S., & Dolag, K. 2007, *Mon. Not. R. Astron. Soc.*, **378**, 1259
- Ronconi, T. & Marulli, F. 2017, *Astron. Astrophys.*, **607**, A24
- Ryden, B. 2016, Introduction to Cosmology
- Saito, S., Takada, M., & Taruya, A. 2008, *Phys. Rev. Lett.*, **100**, 100
- Sakstein, J. & Trodden, M. 2020, *Phys. Rev. Lett.*, **124**, 161301
- Sánchez, C., Clampitt, J., Kovacs, A., et al. 2017, *Mon. Not. R. Astron. Soc.*, **465**, 746
- Scaramella, R. 2014, in Building the Euclid Cluster Survey - Scientific Program, **1**
- Schäfer, B. M., Heisenberg, L., Kalovidouris, A. F., & Bacon, D. J. 2012, *Mon. Not. R. Astron. Soc.*, **420**, 455
- Schneider, P. 1996, in Examining the Big Bang and Diffuse Background Radiations, ed. M. C. Kafatos & Y. Kondo, Vol. 168, **209**
- Schneider, P. 1999, in Looking Deep in the Southern Sky, ed. R. Morganti & W. J. Couch, **51**
- Schneider, P., Asgari, M., Jozani, Y. N., et al. 2022, *Astron. Astrophys.*, **664**, A77
- Schneider, P., Ehlers, J., & Falco, E. E. 1992, Gravitational Lenses
- Schneider, P. & Seitz, C. 1995, *Astron. Astrophys.*, **294**, 411
- Schramm, D. N. & Turner, M. S. 1998, *Reviews of Modern Physics*, **70**, 303
- Schuster, N., Hamaus, N., Dolag, K., & Weller, J. 2023, *arXiv e-prints*, [arXiv:2312.11241](https://arxiv.org/abs/2312.11241)
- Seitz, C. & Schneider, P. 1995, *Astron. Astrophys.*, **297**, 287
- Seitz, C. & Schneider, P. 1997, *Astron. Astrophys.*, **318**, 687
- Seitz, S. & Schneider, P. 1998, *arXiv e-prints*, [astro](https://arxiv.org/abs/astro)
- Seljak, U., Slosar, A., & McDonald, P. 2006, *Journal of Cosmology and Astroparticle Physics*, **2006**, 2006
- Sereno, M. & Umetsu, K. 2011, *Mon. Not. R. Astron. Soc.*, **416**, 3187
- Sheth, R. K. & van de Weygaert, R. 2004, *Mon. Not. R. Astron. Soc.*, **350**, 517
- Shimasue, T., Osato, K., Oguri, M., Shimakawa, R., & Nishizawa, A. J. 2024, *Mon. Not. R. Astron. Soc.*, **527**, 5974

- Shirasaki, M., Nishimichi, T., Li, B., & Higuchi, Y. 2017, *Mon. Not. R. Astron. Soc.*, 466, 2402
- Smoot, G. F., Bennett, C. L., Kogut, A., et al. 1992, *The Astrophysical Journal Letters*, 396, 396
- Solà, J. 2013, *Journal of Physics: Conference Series*, 453, 453
- Song, H. & Lee, J. 2009, *Astrophys. J. Lett.*, 701, L25
- Springel, V. 2005, *Mon. Not. R. Astron. Soc.*, 364, 1105
- Springel, V., White, S. D. M., Tormen, G., & Kauffmann, G. 2001, *Mon. Not. R. Astron. Soc.*, 328, 726
- Starobinsky, A. A. 1980, *Physics Letters B*, 91, 99
- Starobinsky, A. A. 2007, *Soviet Journal of Experimental and Theoretical Physics Letters*, 86, 157
- Steigman, G. 2007, *Annual Review of Nuclear and Particle Science*, 57, 463
- Super-Kamiokande Collaboration, :, Abe, K., et al. 2023, *arXiv e-prints*, arXiv:2312.12907
- Suto, Y., Sato, K., & Sato, H. 1984, *Progress of Theoretical Physics*, 71, 938
- Sutter, P. M., Lavaux, G., Hamaus, N., et al. 2015, *Astronomy and Computing*, 9, 1
- Sutter, P. M., Lavaux, G., Hamaus, N., et al. 2014, *Mon. Not. R. Astron. Soc.*, 442, 462
- Tang, L., Lin, H.-N., & Liu, L. 2023, *Chinese Physics C*, 47, 47
- Tegmark, M., Strauss, M. A., Blanton, M. R., et al. 2004, *Phys. Rev. D*, 69, 103501
- Tessore, N., Winther, H. A., Metcalf, R. B., Ferreira, P. G., & Giocoli, C. 2015, *J. Cosm. Astro-Particle Phys.*, 2015, 036
- Thuan, T. X. & Izotov, Y. I. 2000, *arXiv e-prints*, astro
- Tormen, G., Moscardini, L., & Yoshida, N. 2004, *Mon. Not. R. Astron. Soc.*, 350, 1397
- Torrado, J. & Lewis, A. 2021, *J. Cosm. Astro-Particle Phys.*, 2021, 057
- Troxel, M. A. & Ishak, M. 2015, *Phys. Rept.*, 558, 1
- Tsujikawa, S. 2013, *Classical and Quantum Gravity*, 30, 214003
- Umetsu, K. 2013, *Astrophys. J.*, 769, 13
- Umetsu, K. 2020, *Astron. Astrophys. Rev.*, 28, 7
- Umetsu, K., Medezinski, E., Nonino, M., et al. 2014, *Astrophys. J.*, 795, 163
- Utiyama, R. & DeWitt, B. S. 1962, *Journal of Mathematical Physics*, 3, 3
- van de Weygaert, R. 2014, *Proceedings of the International Astronomical Union*, 11, 11
- van de Weygaert, R. & Schaap, W. 2009, in *Data Analysis in Cosmology*, ed. V. J. Martínez, E. Saar, E. Martínez-González, & M. J. Pons-Bordería, Vol. 665, 291–413
- van Waerbeke, L. 2000, *Mon. Not. R. Astron. Soc.*, 313, 524
- Velten, H. E. S., vom Marttens, R. F., & Zimdahl, W. 2014, *European Physical Journal C*, 74, 3160
- Verza, G., Pisani, A., Carbone, C., Hamaus, N., & Guzzo, L. 2019, *J. Cosm. Astro-Particle Phys.*, 2019, 040
- Viel, M., Haehnelt, M. G., & Springel, V. 2010, *J. Cosm. Astro-Particle Phys.*, 2010, 015
- Vielzeuf, P., Kovács, A., Demirbozan, U., et al. 2021, *Mon. Not. R. Astron. Soc.*, 500, 464
- Villaescusa-Navarro, F., Banerjee, A., Dalal, N., et al. 2018, *Astrophys. J.*, 861, 53
- Villaescusa-Navarro, F., Bird, S., Peña-Garay, C., & Viel, M. 2013, *Journal of Cosmology and Astroparticle Physics*, 2013, 2013
- Villaescusa-Navarro, F., Marulli, F., Viel, M., et al. 2014, *J. Cosm. Astro-Particle Phys.*, 2014, 011
- Voivodic, R., Rubira, H., & Lima, M. 2020, *J. Cosm. Astro-Particle Phys.*, 2020, 033
- Wagner, C., Verde, L., & Jimenez, R. 2012, *The Astrophysical Journal Letters*, 752, 752
- Wang, Y., Xu, L., & Zhao, G.-B. 2017, *Astrophys. J.*, 849, 84
- Weinberg, S. 1972, *Gravitation and Cosmology: Principles and Applications of the General Theory of Relativity* (New York,: Wiley)

- Weinberg, S. 1989, [Reviews of Modern Physics](#), **61**, 1
- Weinberg, S. 2008, *Cosmology*
- Weyl, H. 1918, [Sitzungsberichte der Königlich Preussischen Akademie der Wissenschaften](#), 465
- Weyl, H. 1923, *Gravitation und Elektrizität* (Wiesbaden: Vieweg+Teubner Verlag), 147–159
- Will, C. M. 2005, [Phys. Rev. D](#), **71**, 084027
- Winther, H. A., Schmidt, F., Barreira, A., et al. 2015, [Mon. Not. R. Astron. Soc.](#), **454**, 4208
- Woodard, R. 2007, *Avoiding Dark Energy with 1/R Modifications of Gravity*, ed. L. Pappantonopoulos (Berlin, Heidelberg: Springer Berlin Heidelberg), 403–433
- Woodfinden, A., Nadathur, S., Percival, W. J., et al. 2022, [Monthly Notices of the Royal Astronomical Society](#), 516, 516
- Wright, B. S., Winther, H. A., & Koyama, K. 2017, [J. Cosm. Astro-Particle Phys.](#), 2017, 054
- Yoo, J. & Watanabe, Y. 2012, [International Journal of Modern Physics D](#), **21**, 1230002
- Yèche, C., Palanque-Delabrouille, N., Baur, J., & du Mas des Bourboux, H. 2017, [Journal of Cosmology and Astroparticle Physics](#), 2017, 2017
- Zeldovich, I. B., Einasto, J., & Shandarin, S. F. 1982, [Nature](#), **300**, 407
- Zel'dovich, Y. B. 1970, [Astron. Astrophys.](#), **5**, 84
- Zeldovich, Y. B. 1972, [Mon. Not. R. Astron. Soc.](#), **160**, 1P
- Zennaro, M., Bel, J., Dossett, J., Carbone, C., & Guzzo, L. 2018, [Monthly Notices of the Royal Astronomical Society](#), 477, 477
- Zentner, A. R. 2007, [International Journal of Modern Physics D](#), **16**, 763
- Zhao, C., Tao, C., Liang, Y., Kitaura, F.-S., & Chuang, C.-H. 2016, [Mon. Not. R. Astron. Soc.](#), **459**, 2670
- Zwicky, F. 1937, [Astrophys. J.](#), **86**, 217

